3D MICROFLUIDICS FOR ENVIRONMENTAL PATHOGEN DETECTION AND SINGLE-CELL PHENOTYPE-TO-GENOTYPE ANALYSIS

Thesis by

Yanzhe Zhu

In Partial Fulfillment of the Requirements for

the degree of

Doctor of Philosophy

CALIFORNIA INSTITUTE OF TECHNOLOGY

Pasadena, California

2020

(Defended June 03, 2020)

Yanzhe Zhu
ORCID: 0000-0002-2260-1830

ACKNOWLEDGMENTS

Before coming to Caltech, I thought I was a chemical engineer who would never touch biology and fluid mechanics. I'd never imagined that I'd become passionate about the combination of both, which I'm grateful to have the opportunity to explore during my PhD.

Thank you to my advisor, Professor Michael R. Hoffmann, for being a wonderful advisor, allowing me to freely explore research directions, always being supportive, and providing guidance and feedback throughout my PhD. I also learned a lot from him about life, history, politics, etc.

I also want to thank my other committee members for offering advice and guidance on my thesis work: Professor Jared Leadbetter, Professor Victoria Orphan, and Dr. Kasthuri Venkateswaran. Thank you to Victoria for piquing my interest in the curious world of geobiology.

I am very grateful to the Bill and Melinda Gates Foundation for their generous funding support. I truly identify with the goal of the Foundation for human equality and admire the Foundation's amazing efforts and impacts. It's been an honor to have the opportunity to work on this project.

I want to thank my mentors, Dr. Xing Xie, Dr. Janina Bahnemann, Dr. Eric Huang, Dr. Xinyu Lin, and Dr. Jing Li. The work in this dissertation would never have been completed without your guidance and hard work. Many thanks to Xing for bringing me into the microbiology part of environmental engineering, being a helpful and responsible mentor even after he left for the faculty position at Georgia Tech, and being a role model scientist. Thank you to Eric and Xingyu for putting up with me when I was low on momentum, being encouraging, and getting me excited with new ideas. Thank you to Dr. Jing Li; other than always providing enlightening insights and feedbacks, your enthusiasm towards science, art, humanity, and life is contagious. This work would have been impossible without you.

It's been an honor to work with a great group of fellow grad students, postdoc scholars, and scientists: Stephanie O'Gara, Jieun Shin, Eunkyung Kim, Siwen Wang, Dr. Yang Yang, Dr. Cody Finke, Dr. Clément Cid, Dr. Katharina Urmann, Eitam Shafran, Dr.

Leda Katebian, Hugo Leandri, Léopold Dobelle, Dr. Lei Guo, Alan Gu, Sean Kim, Axl LeVan, Heng Dong, Dr. Su Young Ryu, Dr. A. J. Colussi, and many others.

During my PhD, I've had the chance to have helpful discussions with many great scientists. Special thanks to Professor Alireza Ghaffari, who taught me essential microfluidic skills, offered suggestions, and discussed potential collaborations on my own research project. I'm also very grateful for the insights provided by Professor Robert Damoiseaux, Professor Dino Di Carlo, and Professor Matt Thomson.

I am deeply grateful to Professor Young-Shin Jun, my undergrad research advisor, who provided my first lessons on doing independent research. She continues to fuel my passion for science. I wish I could be an inspiring woman scientist like her.

Thank you to my coffee break mates: Dr. Jing Li, Siwen Wang, and Sam Zhang. Sharing interesting science and daily chatting, of course mostly the latter, always made a quality time and empowered my days during G4 and G5.

Thank you to my best friends and roommates, Dr. Jing Li, (all soon to be Dr.) Sam Zhang, Stephanie Kong, Alison Wu, Hao Xie, and Siteng Fan. This whole PhD would be incomplete without those nights of drinking, eating with no tomorrow, playing stupid games, or silly talking. Special thanks to Stephanie, Alison, and Hao, who took wonderful care of my sons while I was away. Very special thanks to Stephanie, who also introduced me to the great lawyer Dr. Amis Pan and her exceptionally awe-inspiring cats.

Thank you to Dr. Jia He, Dr. Zhaoyi Shen, Yue Hui, Kun Miao, Dr. Yuanlong Huang, Dr. Yue Zhang, Dr. Ray Wang, Dr. Joyce Yu, Yaqing Gao, Jin Huang, Hongdou An, Kang Wang, Si Liu, and many other friends for scientific and non-scientific, serious and hilarious discussions, and more importantly for being in my life.

Thank you to Helen and Peter Fan, Qisheng Liu and Xiang Chen, and Dr. Robin Liu. You are like my family here in Los Angeles.

Special thanks to my beloved sons, HaHa, HengHeng, HeeHee, and HuhHuh. You were the cutest guinea pigs in the world, and I miss you all.

Finally, thank you to my parents and other family members for your love and support.

ABSTRACT

The emergence of microfluidic technologies has enabled the miniaturization of cell analysis processes, including nucleic acid analysis, single cell phenotypic analysis, single cell DNA and RNA sequencing, etc. Traditional chip fabrication *via* soft lithography cost thousands of dollars just in personnel training and capital cost. The design of these systems is also confined to two dimensions limited by their fabrication. To address the needs of smooth transition from technology to adoption by end-users, less complexity is urgently needed for microfluidics to be applied in pathogen detection under low-resource settings and more powerful integration of analyses to understand single cells. This dissertation presents my explorations in 3D microfluidics involving simulation-aided design of pretreatment devices for pathogen detection, fabrication through 3D printing, utilization of alternative commercial parts, and the combination with hydrogel material to link phenotypic analysis with *in situ* molecular detection for single cells. The main outputs of this dissertation are as follows:

1) COMSOL Multiphysics® was used to aid the design and understanding of microfluidic systems for environmental pathogen detection. In the development of an asymmetric membrane for concentration and digital detection of bacteria, the quantification requires Poisson distribution of cells into membrane pores; the flow field and particle trajectories were simulated to validate the cell distribution in capturing pores. In electrochemical bacterial DNA extraction, the hydroxide ion generation, species diffusion, and cation exchange were modeled to understand the pH gradient within the chamber. To address the overestimated risk by polymerase chain reactions (PCR) that detects all target nucleic acids regardless of cell viability, we developed a microfluidic device to carry out on-chip propidium monoazide (PMA) pretreatment. The design utilizes split-and-recombine (SAR) mixers for initial PMA-sample mixing and a serpentine flow channel containing herringbone structures for dark and light incubation. Ten SAR mixers were employed based on fluid flow and diffusion simulation. High-resolution 3D printing was used for

prototyping. On-chip PMA pretreatment to differentiate live and dead bacterial cells in buffer and natural pond water samples was experimentally demonstrated.

2) Water-in-oil droplet-based microfluidic platforms for digital nucleic acid analysis eliminates the need for calibration that is required for qPCR-based environmental pathogen detection. However, utilizing droplet microfluidics generally requires fabrication of sub-100 μm channels and complicated operation of multiple syringe pumps, thus hindering the wide adoption of this powerful tool. We designed a disposable centrifugal droplet generation device made simply from needles and microcentrifuge tubes. The aqueous phase was added into the Luer-Lock of the commercial needle, with the oil at the bottom of the tube. The average droplet size was tunable from 96 μm to 334 μm and the coefficient of variance (CV) was minimized to 5%. For droplets of a diameter of 175 μm, each standard 20 μL reaction could produce ~10^4 droplets. Based on this calculated compartmentalization, the dynamic range is theoretically from 0.5 to 3×10^3 target copies or cells per μL, and the detection limit is 0.1 copies or cells per μL.

3) Based on the disposable droplet generation device, we further developed a novel platform that enables both high-throughput digital molecular detection and single-cell phenotypic analysis, utilizing nanoliter-sized biocompatible polyethylene glycol (PEG) hydrogel beads. The crosslinked hydrogel network in aqueous phase adds additional robustness to droplet microfluidics by allowing reagent exchange. The hydrogel beads demonstrated enhanced thermal stability, and achieved uncompromised efficiencies in digital PCR, digital loop-mediated isothermal amplification (dLAMP), and single cell phenotyping. The crosslinked hydrogel network highlights the prospective linkage of various subsequent molecular analyses to address the genotypic differences between cellular subpopulations exhibiting distinct phenotypes. This platform has the potential to advance the understanding of single cell genotype-to-phenotype correlations.

4) For effective sorting of the hydrogel beads after single cell phenotyping, a gravity-driven acoustic fluorescence-based hydrogel beads sorter was developed. The design involves a 3D-printed microfluidic tube, two sequential photodetectors, acoustic actuator, and a control system. Instead of bulky syringe pumps used in traditional cell or droplet sorting, this invention drives beads suspended in heavier fluorinated oil simply by buoyancy force to have the beads float through a vertical channel. Along the channel, sequential photodetectors quantify the bead acceleration and inform the action of downstream acoustic actuator. Hydrogel beads with different fluorescence intensity level were led into different collection chambers. The developed sorter promises cheap instrumentation, easy operation, and low contamination for beads sorting, and thus the full establishment of the single cell phenotype-genotype link.

In summary, the work in this dissertation established a) the simulation-aided design and 3D printing to reduce the complexity of microfluidics, and thus lowered its barrier for environmental applications, b) a simple and disposable device using cheap commercial components to produce monodispersed water-in-oil droplets to enable easy adoption of droplet microfluidics by non-specialized labs, c) a hydrogel bead-based analysis platform that links single-cell phenotype and genotype to open new research avenues, and d) a gravity-driven portable bead sorting system that may extend to a broader application of hydrogel microfluidics to point of care and point of sample collection. These simple-for-end-user solutions are envisioned to open new research avenues to tackle problems in antibiotic heteroresistance, environmental microbial ecology, and other related fundamental problems.

PUBLISHED CONTENTS AND CONTRIBUTIONS

Zhu, Y., Huang, X., Xie, X., Bahnemann, J., Lin, X., Wu, X., Wang, S., and Hoffmann, M. R. (2018). Propidium monoazide pretreatment on a 3D-printed microfluidic device for efficient PCR determination of 'live versus dead' microbial cells. *Environmental Science: Water Research & Technology*, *4*(7), 956-963. https://doi.org/10.1039/C8EW00058A.

M.R.H., X.X., and J.B. conceived the concept for this study; X.X., J.B., and Y.Z. contributed to the chip design and 3D printing troubleshooting. X.H., X.X., and Y.Z. designed the study; Y.Z. performed experiments; X.L., X.W., and S.W. contributed to the interpretation of the results; X.H., X.X., and Y.Z. analyzed the data and wrote the paper; all authors provided critical feedback and edited the manuscript.

Zhu, Y., Li, J., Lin, X., Huang, X., and Hoffmann, M.R. (2019). A hydrogel beads based platform for single-cell phenotypic analysis and digital molecular detection. *bioRxiv*: 848168. https://doi.org/10.1101/848168 (A revised version is submitted for journal publication)

M.R.H, X.H., and Y.Z. conceived the concept for this study; J.L., X.H., X.L., and Y.Z. designed the study; Y.Z. performed experiments; J.L. and Y.Z. analyzed the data and wrote the paper.

Zhu, Y., Li, J., and Hoffmann, M.R. A gravity-driven acoustic-actuated fluorescence-based hydrogel bead sorter. *In preparation*.

M.R.H. and Y.Z. conceived the concept for this study; J.L. and Y.Z. designed the study; Y.Z. developed and ran the numerical simulation model and analyzed data; J.L. and Y.Z. wrote the manuscript.

Wang, S., Zhu, Y., Yang, Y., Li, J. and Hoffmann, M. R. (2020) Electrochemical cell lysis of gram-positive and gram-negative bacteria: DNA extraction from environmental water samples. *Electrochimica Acta,* 135864. https://doi.org/10.1016/j.electacta.2020.135864

Y.Z. developed and ran the numerical simulation model, and participated in the corresponding data analysis, result interpretation, and manuscript writing.

Lin, X., Huang, X., Zhu, Y., Urmann, K., Xie, X., & Hoffmann, M. R. (2018). Asymmetric membrane for digital detection of single bacteria in milliliters of complex water samples. *ACS Nano*, *12*(10), 10281-10290. https://pubs.acs.org/doi/abs/10.1021/acsnano.8b05384

Y.Z. participated in developing the numerical simulation model, analyzing simulation data, interpreting results, and editing the manuscript.

Wu, X., Huang, X., Zhu, Y., Li, J., and Hoffmann, M.R. (2020). Synthesis and application of superabsorbent polymer microspheres for rapid concentration and quantification of microbial pathogens in ambient water. *Separation and Purification Technology*: 116540. https://doi.org/10.1016/j.seppur.2020.116540

Y.Z. contributed to manuscript editing.

Li, J., Zhu, Y., Wu, X., and Michael R. Hoffmann. (2020) Rapid detection methods for bacterial pathogens in ambient waters at the point-of-sample collection: A brief review. *Clinical Infectious Diseases*. In Press.

Y.Z. reviewed biosensor-based technologies and contributed to compiling the technology summary table, manuscript writing, and editing.

TABLE OF CONTENTS

LIST OF ILLUSTRATIONS AND TABLES

Figures

Tables

Chapter 1

INTRODUCTION

1.1 Waterborne bacterial pathogen diseases: Problems and needs

Waterborne diseases, including diarrhea, cholera, typhoid, and polio, claim millions of lives every year (Troeger et al., 2018), especially in developing countries and countries in conflicts (**Figure 1.1**). In 2016, it was estimated that 829,000 deaths resulted from diarrhea, and 1.9% of the global burden of disease in Disability-Adjusted Life Years (DALY) were attributed to water, sanitation, and hygiene (Prüss-Ustün et al., 2019). Waterborne pathogens include bacteria, fungi, viruses, protozoa, and helminths (Nwachcuku & Gerba, 2004). Among them, gram-negative bacteria and viruses are most common causes of death for children and the elderly (**Figure 1.2**). Transmission of waterborne pathogens from a water environment may occur through direct contact or indirect consumption such as *via* fecal-oral route or inhalation of aerosols (Leclerc et al., 2002).

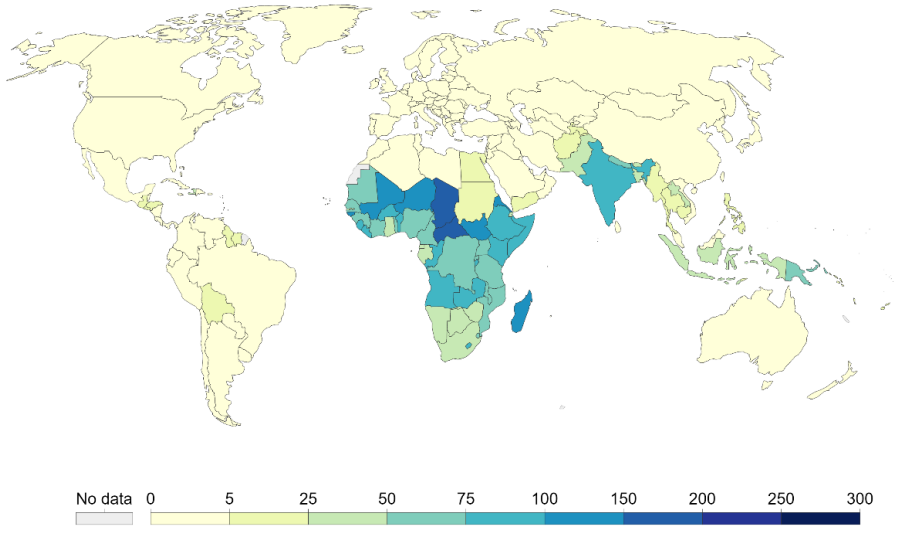

Figure 1.1 Annual death rate from diarrheal diseases per 100,000 people in 2017. Reproduced from *OurWorldInData.org* (Dadonaite et al., 2020), which is available under the terms of Creative Commons Attribution License (CC BY).

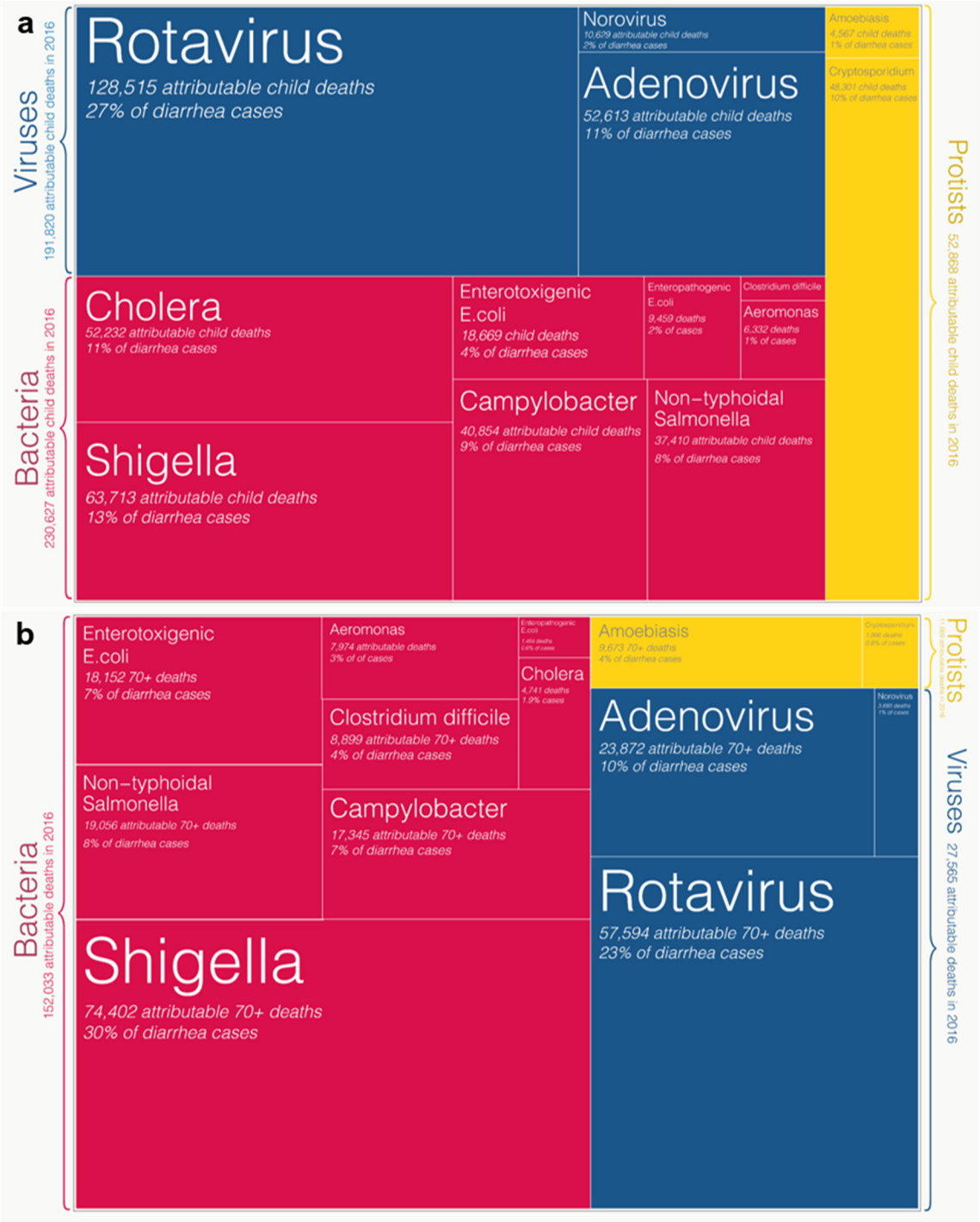

Figure 1.2 Number of death attributable to each pathogen in (**a**) children under 5 and (**b**) people aged 70+. Reproduced from *OurWorldInData.org* (Dadonaite et al., 2020), which is available under the terms of Creative Commons Attribution License (CC BY).

To decrease disease burden with the ultimate goal of eradication, there are global efforts in the development of vaccines and treatments, as well as in environmental monitoring (BMGF, 2019). However, despite advances in point-of-care diagnostics, there is a lack of sensitive, specific, and rapid tool for monitoring of bacterial pathogens at point-of-sample-collection where equipment and personnel are limited (Li et al., 2020). Such tools are essential for the water quality assessment and environmental surveillance, which are keys in understanding disease burden, preventing infectious disease outbreaks, improving strategy of vaccine distribution, and advising healthcare policy making (Carey et al., 2019).

As the most important treatment for bacterial infections, antibiotics are medications that selectively destroy or interfere with bacterial structures or functional molecules (Kohanski et al., 2010). The fast emergence and spread of antibiotic resistance (**Table 1.1**) hampers effective antibiotic treatment and causes increased mortality due to common bacterial infections, such as multidrug-resistant (MDR) *Acinetobacter* and methicillin-resistant *Staphylococcus aureus* (MRSA) (Baym et al., 2016; CDC, 2019; Ventola, 2015). It was estimated by WHO's Global Antimicrobial Surveillance System (GLASS) that antibiotic resistance widely occurred across 22 countries with suspected bacterial infections in 500,000 people (WHO, 2017). Many genes responsible for conveying the resistance have been identified (Frieri et al., 2017; Giedraitienė et al., 2011), however, we still lack a thorough understanding of how the resistance evolves and spreads.

The widely observed antibiotic heteroresistance phenomenon further complicates the issue (Andersson et al., 2019; Nicoloff et al., 2019). Within a cell community, impressive means of bacterial collaboration against antibiotic stress are being discovered. For example, *Vibrio cholerae* was observed to be able to 'grab' and incorporate a piece of exotic DNA fragment with pili (Ellison et al., 2018), implying potential hazards posed by antibiotic genes that are present in the environment (Martínez, 2008; Rodriguez-Mozaz et al., 2015). In another case, under exposure to an antibiotic, the subpopulation of cells that acquired resistant mutation was found to secret molecules to protect the non-resistant cells and gain nutrients from them to cover the additional fitness cost (Lee et al., 2010). Moreover,

accumulating evidence has shown that the genetic diversity and varying level of antibiotic resistance of clonal bacterial cells may increase resistance to antibiotic stress at a community level (Lee et al., 2010). Therefore, other than developing new antibiotics and characterizing newly evolved antibiotic resistance, it is imperative to understand the evolution of antibiotic resistance, in order to provide insights in our future efforts preventing the approach of the post-antibiotic era, where common bacterial pathogen kills again.

Antibiotic Approved or Released	Year Released	Resistant Germ Identified	Year Identified
Penicillin	1941	Penicillin-resistant *Staphylococcus aureus*[20, 21]	1942
		Penicillin-resistant *Streptococcus pneumoniae*[9,10]	1967
		Penicillinase-producing *Neisseria gonorrhoeae*[11]	1976
Vancomycin	1958	Plasmid-mediated vancomycin-resistant *Enterococcus faecium*[12,13]	1988
		Vancomycin-resistant *Staphylococcus aureus*[14]	2002
Amphotericin B	1959	Amphotericin B-resistant *Candida auris*[15]	2016
Methicillin	1960	Methicillin-resistant *Staphylococcus aureus*[16]	1960
Extended-spectrum cephalosporins	1980 (Cefotaxime)	Extended-spectrum beta-lactamase- producing *Escherichia coli*[17]	1983
Azithromycin	1980	Azithromycin-resistant *Neisseria gonorrhoeae*[18]	2011
Imipenem	1985	*Klebsiella pneumoniae* carbapenemase (KPC)-producing *Klebsiella pneumoniae*[19]	1996
Ciprofloxacin	1987	Ciprofloxacin-resistant *Neisseria gonorrhoeae*[20]	2007
Fluconazole	1990 (FDA approved)	Fluconazole-resistant *Candida*[21]	1988
Caspofungin	2001	Caspofungin-resistant *Candida*[22]	2004
Daptomycin	2003	Daptomycin-resistant methicillin-resistant *Staphylococcus aureus*[23]	2004

Table 1.1 Major types of resistance developed after approval and release of antibiotics or antifungals over time. Reproduced from CDC report (CDC, 2019).

1.2 Bacterial pathogen detection and analysis methods

Bacterial pathogen detection and analysis methods can usually be classified into phenotypic methods and molecular methods. Phenotypic methods in this context are mainly based on culture of bacteria and the observation of their growth. For detection of bacterial pathogens, culture-based methods that observe the occurrence and characteristics of colony formation remain the gold standard (Meals et al., 2013; Teunis & Schijven, 2019). Although generally cost-effective and low in requirement for training and instrumentation, culture-based methods often take days to give a qualitative positive result and even longer to confirm a negative one. For bacterial analysis with clinical relevance, antibiotic susceptibility tests (AST) are usually conducted to guide antibiotic prescription (Syal et al., 2017). Conventional AST used to help prescribe the type and concentration of antibiotic is based on bulk culture phenotyping. It takes days from sample collection to results, which only yield a population-averaged minimum inhibitory concentration (MIC). Such an MIC is not sensitive to rare but clinically more important resistant strains, leading to treatment failure and exacerbating the global AMR crisis. In addition, days of sample culture under antibiotic exposure may induce evolution of antibiotic resistance (Baym et al., 2016; Lee et al., 2010; Zhang et al., 2011), leading to biased AST results that do not accurately reflect the in-host antibiotic susceptibility.

Nucleic acid tests (NAT), as a representative class of molecular methods, target characteristic or functional nucleic acid molecules inside bacterial cells. The targeted gene sequences are specific to the target bacteria for detection purposes, or have been identified to be associated with antibiotic resistance for AST (Syal et al., 2017). NAT is becoming increasingly standardized for microbial monitoring since the advent of polymerase chain reaction (PCR) in 1980s (Kralik & Ricchi, 2017). NAT generally involves nucleic acid extraction, purification, amplification of the target sequence, and signal detection. PCR process creates copies of target amplicons by DNA denature, primer annealing, and extension, facilitated by thermocycling. PCR takes a few hours to generate enough amplification product for signal reading. The need for precise temperature manipulation

requires specialized instruments and hinders its easy adaptation for portable applications or in resource-limited settings. To address the problems above, a few isothermal amplification methods, including loop-mediated isothermal amplification (LAMP) (Hara-Kudo et al., 2005), and recombinase polymerase amplification (RPA) (Armes & Stemple, 2007), etc., have been developed to eliminate the need for thermocycling. These methods are innovative in primer design or employ novel enzymes to produce a much larger number of amplicons in a shorter period of time. Compared to traditional culture-based methods, NAT significantly improves the accuracy and sensitivity of pathogen detection. The analytical time is reduced from days to hours (Girones et al., 2010) and even possibly within 0.5 hour for novel isothermal amplifications (Lutz et al., 2010).

Other important molecular methods mainly include next-generation sequencing (NGS) and biosensors. NGS, which generates high-throughput sequence reading of DNA or RNA, has been an advanced nucleic acid analysis tool that accelerates discoveries in antibiotic resistance. Combining phenotypic screening and NGS, functional genomics and transcriptional profiling have shown success in identifying novel antibiotic resistance genes (ARGs) and thus facilitating resistance mechanism elucidation (Cui et al., 2005; Telke & Rolain, 2015; Torres-Cortés et al., 2011). NGS have also enabled discoveries of omnipresent ARGs by surveying environmental metagenomic DNA libraries, such as from aerosol (Li et al., 2018), soil (Allen et al., 2009), and wastewater (Guo et al., 2017). Biosensors, which are widely developed for pathogen detection, generally target specific protein molecules using recognition molecules and transducing the signal produced by the interaction between the recognition molecules and the specific target. Comprehensive reviews on biosensors for waterborne microbial pathogen detection are available (Justino et al., 2017; Kumar et al., 2018). In this dissertation, NGS and biosensors are not further discussed in detail.

For the methods discussed above, we have reviewed available technologies for point-of-sample-collection microbial pathogen detection (Appendix D).

1.3 Microfluidic toolbox

The emergence of microfluidic technologies has enabled the miniaturization of cell detection and analysis. Miniaturized cell analysis has the advantage of smaller reagent volumes, increased sensitivity, less liquid handling time, and less manual labor (Asiello & Baeumner, 2011; Castillo-León, 2015). **Figure 1.3** highlights the milestones in the field of microfluidics (that were deemed relevant for this dissertation), along with the development of key microfluidic fabrication technologies and biological analysis methods.

Since Manz et al. brought up the concept of miniaturized total chemical analysis systems (μ-TAS) (Manz et al., 1990), innovations in microfluidic designs have achieved a wide range of fluid manipulations including mixing, sorting, valving, etc. (Lee et al., 2011; Oh & Ahn, 2006; Zhang et al., 2016). The powerful fluid control capacity enabled the translation of newly developed biological assays onto lab-on-a-chip (LOC). For example,

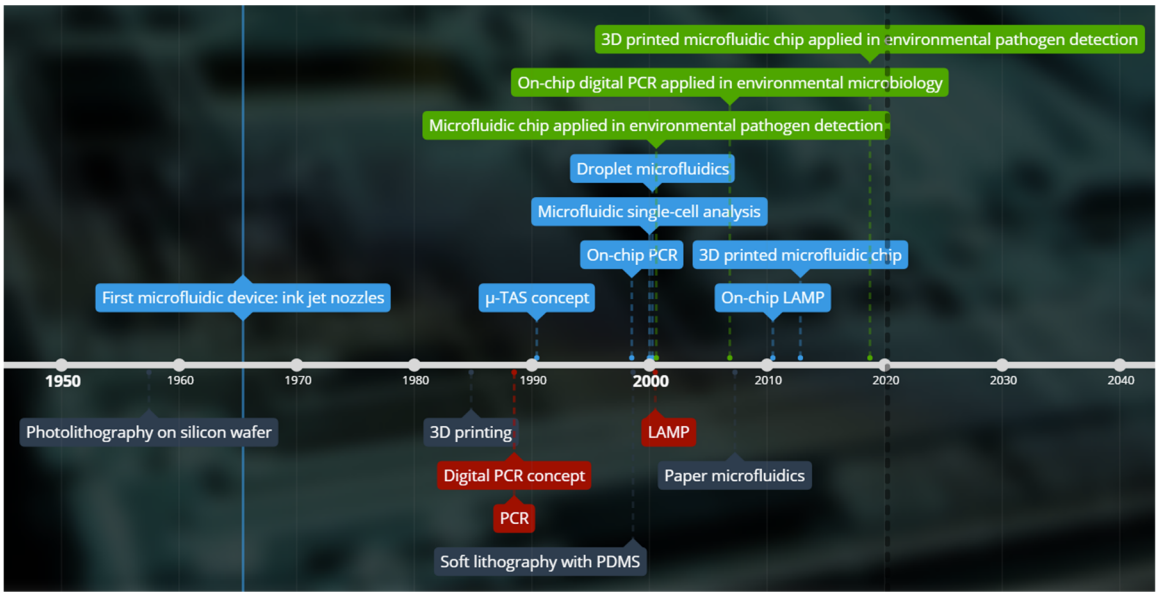

Figure 1.3 Timeline highlighting the emergence of key technologies in microfluidic fabrication, the main advances in biological analysis technology, the milestones in the field of microfluidics, and the first applications in environmental microbiology.

studies have demonstrated automated PCR and LAMP systems that integrate DNA extraction, thermal cycling or heating, and results reading (Huang et al., 2017; Kopp et al., 1998; Lee et al., 2006). These integrated nucleic acid analysis systems have shown great potential for microfluidics to be applied in waterborne pathogens analysis in low-resource settings. However, those technologies are still not widely applied due to the complicated fabrication and operation of such devices, as well as expensive and bulky instrumentation. The polydimethylsiloxane (PDMS) based technologies and traditionally fabricated lab-on-a-disc systems easily cost thousands of dollars just in personnel training and capital cost (Kim et al., 2014; Sun et al., 2015; Tian et al., 2015). Also, the designs of those systems are confined to two-dimensions limited by their fabrication.

3D printing microfluidics, instead, generally requires less personnel training in design and prototyping. The advent of 3D printing allows more freedom in design by the use of the third dimension in the design philosophy. Although initially the low resolution of 3D printing limited its applicability in microfluidic fabrication (Castillo-León, 2015), recent development in 3D printing techniques and materials has achieved micrometer-resolution (Lee et al., 2015; Sweet et al., 2017). A plethora of innovations have demonstrated powerful applications of 3D-printed microfluidics (Lee et al., 2015; Sweet et al., 2017), which shows potential of immediate application for end-users from diverse fields.

1.4 Towards minimal instrumentation

Microfluidics has developed from its origin in inkjet printing to a variety of fields, including biological analysis, over the past decades. However, it could take about 10 years to translate a new technology, such as PCR or LAMP, into the first PDMS-based microfluidic chip, and 10 more years to be adapted for environmental applications. For environmental microbial analysis, the adaptation of microfluidic technologies has enabled automated detection tools (Altintas et al., 2018; Besmer et al., 2014; Nguyen et al., 2018) and revealed new observations of intriguing phenomena (Ahmed et al., 2010; Deng et al., 2019; Singh & Olson, 2012). But these systems have shown little success in commercialization or they can be hard to be adopted for labs with a different range of expertise. Thus, microfluidics for end users in environmental microbiology has not reached its full potential.

Building upon the development of 3D printing technologies and the advanced understanding of microfluidic systems, increasing efforts in the field are focused on promoting the accessibility of microfluidics to potential end users. Specifically, through minimizing the required instrumentation, novel microfluidic systems are emerging to ease the demands in skills and facilities for design, fabrication, and operation. For example, the development of 3D printing allows end-users to easily tailor existing designs for their own specific purposes and produce prototype without cleanroom facilities (Hu & Jiang, 2017). Lab-on-a-disk (LOD) systems, as another example, incorporate fully integrated designs and are intended as pre-packed products (Huang et al., 2017; Kim et al., 2013; Sayad et al., 2018). The fluids in LOD systems are driven by centrifugal force, so that complicated operations of multiple syringe pumps are eliminated.

Another class of microfluidic innovation with minimal instrumentation drops the idea of using traditional microfluidic channels or wells. Novel substrates are used instead to realize the physics of traditional microfluidic systems. For example, the asymmetric membranes, developed by Lin et al. as discussed in detail in Chapter 2.3, achieved reliable compartmentalization, which is usually done by creating water-in-oil emulsions, using

commercially available membranes (Lin et al., 2018). Hydrogels provide another novel substrate. Hatori et al. used hydrogel particles as templates and produced water-in-oil emulsion for digital analysis via vortex emulsification (Hatori et al., 2018). Moreover, a variety of technologies has been developed to produce hydrogel beads with complex designed structures and/or preloaded contents, in order to enable advanced functions, such as cell shape-compatible cultivation and barcoding for single cell sequencing, and meanwhile allow easy adoption by end users (Wu et al., 2018; Wu et al., 2015; Zilionis et al., 2017).

1.5 Thesis overview

In this thesis, I explore novel microfluidic fabrication techniques that utilize 3D printing, the use of hydrogel materials, and numerical simulations to guide microbial analytical device design. The roadmap of this thesis is shown in **Figure 1.4**.

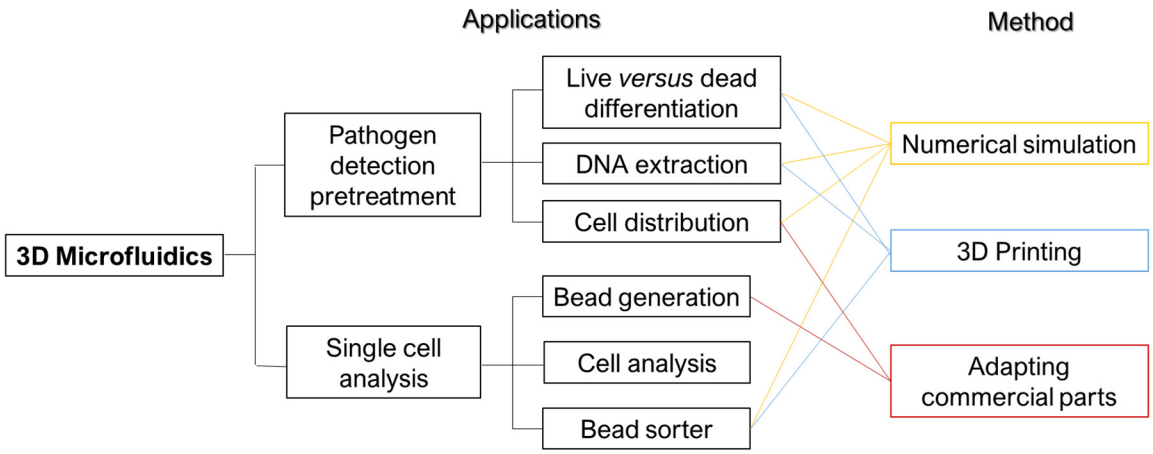

Figure 1.4 Roadmap of this dissertation.

Chapter 2 describes the use of multiphysics simulation in the development of several novel 3D microfluidic devices for nucleic acid-based pathogen detection in environmental water samples. The developed simulation models aided the design of a microfluidic chip for live *versus* dead cell differentiation, the understanding of DNA extraction performance in a milliliter-chamber device for electrochemical cell lysis, and the validation of cell distribution on an asymmetric membrane for integrated digital detection.

Chapter 3 describes the development of a hydrogel bead-based (Gelbead) platform that links single cell phenotypic and molecular analysis. In this chapter, I describe how needles and microcentrifuge tubes were adapted into 3D microfluidic devices for monodispersed droplet generation. The disposable device enabled the combination of fast-crosslinking biocompatible hydrogel with droplet microfluidics. The hydrogel bead-based

assays were established for cell viability assessment, digital PCR, digital LAMP, and *in situ* PCR, following cell viability assessment.

Chapter 4 describes the ongoing work of developing a bead sorter that is a portable and affordable solution for benchtop and potentially point-of-care bead analysis and sorting. The hydrogel beads are interrogated individually, and are sorted by acoustophoretic force based on the fluorescence intensity for downstream analysis such as PCR or sequencing. The sorter system has been designed and prototyped, and its feasibility was studied through COMSOL simulation.

Chapter 5 describes the provisional work based on the development reported in previous chapters. The proposed work includes the development of DropTube, which is a fully integrated centrifugal device for various in-field pathogen analysis, and the investigation of AMR evolution kinetics through the Gelbead platform.

References

Ahmed, T., Shimizu, T. S., & Stocker, R. (2010). Bacterial chemotaxis in linear and nonlinear steady microfluidic gradients. *Nano Letters, 10*(9), 3379-3385.

Allen, H. K., Moe, L. A., Rodbumrer, J., Gaarder, A., & Handelsman, J. (2009). Functional metagenomics reveals diverse β-lactamases in a remote Alaskan soil. *The ISME Journal, 3*(2), 243-251. doi:10.1038/ismej.2008.86

Altintas, Z., Akgun, M., Kokturk, G., & Uludag, Y. (2018). A fully automated microfluidic-based electrochemical sensor for real-time bacteria detection. *Biosensors and Bioelectronics, 100*, 541-548.

Andersson, D. I., Nicoloff, H., & Hjort, K. (2019). Mechanisms and clinical relevance of bacterial heteroresistance. *Nature Review Microbiology*. doi:10.1038/s41579-019-0218-1

Armes, N. A., & Stemple, D. L. (2007). Recombinase polymerase amplification. U.S. Patent 7270981B2.

Asiello, P. J., & Baeumner, A. J. (2011). Miniaturized isothermal nucleic acid amplification, a review. *Lab on a Chip, 11*(8), 1420-1430.

Baym, M., Lieberman, T. D., Kelsic, E. D., Chait, R., Gross, R., Yelin, I., & Kishony, R. (2016). Spatiotemporal microbial evolution on antibiotic landscapes. *Science, 353*(6304), 1147-1151.

Besmer, M. D., Weissbrodt, D. G., Kratochvil, B. E., Sigrist, J. A., Weyland, M. S., & Hammes, F. (2014). The feasibility of automated online flow cytometry for in-situ monitoring of microbial dynamics in aquatic ecosystems. *Frontiers in Microbiology, 5*, 265.

BMGF. (2019). Enteric and Diarrheal Diseases. Bill & Melinda Gates Foundation. Retrieved Mar 28, 2020, from https://www.gatesfoundation.org/what-we-do/global-health/enteric-and-diarrheal-diseases

Carey, M. E., Diaz, Z. I., Zaidi, A. K., & Steele, A. D. (2019). A global agenda for typhoid control—a perspective from the Bill & Melinda Gates Foundation. *Clinical Infectious Diseases, 68*(Supplement_1), S42-S45.

Castillo-León, J. (2015). Microfluidics and lab-on-a-chip devices: History and challenges. In *Lab-on-a-Chip Devices and Micro-Total Analysis Systems* (pp. 1-15): Springer.

CDC. (2019). *Antibiotic resistance threats in the United States*. Atlanta, GA: U.S. Department of Health and Human Services.

Cui, L., Lian, J.-Q., Neoh, H.-m., Reyes, E., & Hiramatsu, K. (2005). DNA microarray-based identification of genes associated with glycopeptide resistance in Staphylococcus aureus. *Antimicrobial Agents and Chemotherapy, 49*(8), 3404-3413.

Dadonaite, B., Ritchie, H., & Roser, M. (Producer). (2020, Mar 28, 2020). Diarrheal diseases. *Our World in Data*.

Deng, J., Zhou, L., Sanford, R. A., Shechtman, L. A., Dong, Y., Alcalde, R. E., Sivaguru, M., Fried, G. A., Werth, C. J., & Fouke, B. W. (2019). Adaptive evolution of escherichia coli to ciprofloxacin in controlled stress environments: Contrasting patterns of resistance in spatially varying *versus* uniformly mixed concentration conditions. *Environmental Science & Technology, 53*(14), 7996-8005.

Ellison, C. K., Dalia, T. N., Ceballos, A. V., Wang, J. C.-Y., Biais, N., Brun, Y. V., & Dalia, A. B. (2018). Retraction of DNA-bound type IV competence pili initiates DNA uptake during natural transformation in Vibrio cholerae. *Nature Microbiology, 3*(7), 773-780.

Frieri, M., Kumar, K., & Boutin, A. (2017). Antibiotic resistance. *Journal of Infection and Public Health, 10*(4), 369-378.

Giedraitienė, A., Vitkauskienė, A., Naginienė, R., & Pavilonis, A. (2011). Antibiotic resistance mechanisms of clinically important bacteria. *Medicina, 47*(3), 19.

Girones, R., Ferrus, M. A., Alonso, J. L., Rodriguez-Manzano, J., Calgua, B., Correa, A. D., Hundesa, A., Carratala, A., & Bofill-Mas, S. (2010). Molecular detection of pathogens in water - The pros and cons of molecular techniques. *Water Research, 44*(15), 4325-4339. doi:10.1016/j.watres.2010.06.030

Guo, J., Li, J., Chen, H., Bond, P. L., & Yuan, Z. (2017). Metagenomic analysis reveals wastewater treatment plants as hotspots of antibiotic resistance genes and mobile genetic elements. *Water Research, 123*, 468-478.

Hara-Kudo, Y., Yoshino, M., Kojima, T., & Ikedo, M. (2005). Loop-mediated isothermal amplification for the rapid detection of Salmonella. *FEMS Microbiology Letters, 253*(1), 155-161.

Hatori, M. N., Kim, S. C., & Abate, A. R. (2018). Particle-templated emulsification for microfluidics-free digital biology. *Analytical Chemistry, 90*(16), 9813-9820.

Hu, L., & Jiang, G. (2017). 3D printing techniques in environmental science and engineering will bring new innovation. In: ACS Publications.

Huang, X., Gowda, H. N., Wu, X., Dumas, S. L., Zhu, Y., Lin, X., Kido, H., Xie, X., Jiang, S., Madou, M., & Hoffmann, M. R. (2017). *Portable Pathogen Analysis System (PPAS) for microbial water quality analysis*. Paper presented at the 21st International Conference on Miniaturized Systems for Chemistry and Life Sciences (μTAS), Savannah, Georgia, USA.

Justino, C. I., Duarte, A. C., & Rocha-Santos, T. A. (2017). Recent progress in biosensors for environmental monitoring: A review. *Sensors, 17*(12), 2918.

Kim, T.-H., Abi-Samra, K., Sunkara, V., Park, D.-K., Amasia, M., Kim, N., Kim, J., Kim, H., Madou, M., & Cho, Y.-K. (2013). Flow-enhanced electrochemical immunosensors on centrifugal microfluidic platforms. *Lab on a Chip, 13*(18), 3747-3754.

Kim, T.-H., Park, J., Kim, C.-J., & Cho, Y.-K. (2014). Fully integrated lab-on-a-disc for nucleic acid analysis of food-borne pathogens. *Analytical Chemistry, 86*(8), 3841-3848.

Kohanski, M. A., Dwyer, D. J., & Collins, J. J. (2010). How antibiotics kill bacteria: From targets to networks. *Nature Reviews Microbiology, 8*(6), 423-435.

Kopp, M. U., De Mello, A. J., & Manz, A. (1998). Chemical amplification: Continuous-flow PCR on a chip. *Science, 280*(5366), 1046-1048.

Kralik, P., & Ricchi, M. (2017). A basic guide to real time PCR in microbial diagnostics: Definitions, parameters, and everything. *Frontiers in Microbiology, 8*, 108.

Kumar, N., Hu, Y., Singh, S., & Mizaikoff, B. (2018). Emerging biosensor platforms for the assessment of water-borne pathogens. *Analyst, 143*(2), 359-373.

Leclerc, H., Schwartzbrod, L., & Dei-Cas, E. (2002). Microbial agents associated with waterborne diseases. *Critical Reviews in Microbiology, 28*(4), 371-409.

Lee, C.-Y., Chang, C.-L., Wang, Y.-N., & Fu, L.-M. (2011). Microfluidic mixing: A review. *International Journal of Molecular Sciences, 12*(5), 3263-3287.

Lee, H. H., Molla, M. N., Cantor, C. R., & Collins, J. J. (2010). Bacterial charity work leads to population-wide resistance. *Nature, 467*(7311), 82-85.

Lee, J.-G., Cheong, K. H., Huh, N., Kim, S., Choi, J.-W., & Ko, C. (2006). Microchip-based one step DNA extraction and real-time PCR in one chamber for rapid pathogen identification. *Lab on a Chip, 6*(7), 886-895.

Lee, W., Kwon, D., Choi, W., Jung, G. Y., Au, A. K., Folch, A., & Jeon, S. (2015). 3D-printed microfluidic device for the detection of pathogenic bacteria using size-based separation in helical channel with trapezoid cross-section. *Scientific Reports, 5*, 7717.

Li, J., Cao, J., Zhu, Y.-g., Chen, Q.-l., Shen, F., Wu, Y., Xu, S., Fan, H., Da, G., & Huang, R.-j. (2018). Global survey of antibiotic resistance genes in air. *Environmental Science & Technology, 52*(19), 10975-10984.

Li, J., Zhu, Y., Wu, X., & Hoffmann, M. R. (2020). Rapid detection methods for bacterial pathogens in ambient waters at the point-of-sample collection: A brief review. *Clinical Infectious Diseases, In Press*.

Lin, X., Huang, X., Zhu, Y., Urmann, K., Xie, X., & Hoffmann, M. R. (2018). Asymmetric membrane for digital detection of single bacteria in milliliters of complex water samples. *ACS Nano, 12*(10), 10281-10290. doi:10.1021/acsnano.8b05384

Lutz, S., Weber, P., Focke, M., Faltin, B., Hoffmann, J., Müller, C., Mark, D., Roth, G., Munday, P., & Armes, N. (2010). Microfluidic lab-on-a-foil for nucleic acid analysis

based on isothermal recombinase polymerase amplification (RPA). *Lab on a Chip, 10*(7), 887-893.

Manz, A., Graber, N., & Widmer, H. á. (1990). Miniaturized total chemical analysis systems: A novel concept for chemical sensing. *Sensors and Actuators B: Chemical, 1*(1-6), 244-248.

Martínez, J. L. (2008). Antibiotics and antibiotic resistance genes in natural environments. *Science, 321*(5887), 365-367.

Meals, D., Harcum, J., & Dressing, S. (2013). Monitoring for microbial pathogens and indicators. *US Environmental Protection Agency*.

Nguyen, P. L., Sudheesh, P. S., Thomas, A. C., Sinnesael, M., Haman, K., & Cain, K. D. (2018). Rapid detection and monitoring of flavobacterium psychrophilum in water by using a handheld, field-portable quantitative PCR System. *Journal of Aquatic Animal Health, 30*(4), 302-311.

Nicoloff, H., Hjort, K., Levin, B. R., & Andersson, D. I. (2019). The high prevalence of antibiotic heteroresistance in pathogenic bacteria is mainly caused by gene amplification. *Nature Microbiology, 4*(3), 504-514. doi:10.1038/s41564-018-0342-0

Nwachcuku, N., & Gerba, C. P. (2004). Emerging waterborne pathogens: Can we kill them all? *Current Opinion in Biotechnology, 15*(3), 175-180.

Oh, K. W., & Ahn, C. H. (2006). A review of microvalves. *Journal of Micromechanics and Microengineering, 16*(5), R13.

Prüss-Ustün, A., Wolf, J., Bartram, J., Clasen, T., Cumming, O., Freeman, M. C., Gordon, B., Hunter, P. R., Medlicott, K., & Johnston, R. (2019). Burden of disease from inadequate water, sanitation and hygiene for selected adverse health outcomes: An updated analysis with a focus on low-and middle-income countries. *International journal of Hygiene and Environmental Health, 222*(5), 765-777.

Rodriguez-Mozaz, S., Chamorro, S., Marti, E., Huerta, B., Gros, M., Sànchez-Melsió, A., Borrego, C. M., Barceló, D., & Balcázar, J. L. (2015). Occurrence of antibiotics and antibiotic resistance genes in hospital and urban wastewaters and their impact on the receiving river. *Water Research, 69*, 234-242.

Sayad, A., Ibrahim, F., Uddin, S. M., Cho, J., Madou, M., & Thong, K. L. (2018). A microdevice for rapid, monoplex and colorimetric detection of foodborne pathogens using a centrifugal microfluidic platform. *Biosensors and Bioelectronics, 100*, 96-104.

Singh, R., & Olson, M. S. (2012). Transverse chemotactic migration of bacteria from high to low permeability regions in a dual permeability microfluidic device. *Environmental Science & Technology, 46*(6), 3188-3195.

Sun, Y., Quyen, T. L., Hung, T. Q., Chin, W. H., Wolff, A., & Bang, D. D. (2015). A lab-on-a-chip system with integrated sample preparation and loop-mediated isothermal amplification for rapid and quantitative detection of Salmonella spp. in food samples. *Lab on a Chip, 15*(8), 1898-1904.

Sweet, E. C., Chen, J. C.-L., Karakurt, I., Long, A. T., & Lin, L. (2017). *3D printed three-flow microfluidic concentration gradient generator for clinical E. coli-antibiotic drug screening.* Paper presented at the 2017 IEEE 30th International Conference on Micro Electro Mechanical Systems (MEMS).

Syal, K., Mo, M., Yu, H., Iriya, R., Jing, W., Guodong, S., Wang, S., Grys, T. E., Haydel, S. E., & Tao, N. (2017). Current and emerging techniques for antibiotic susceptibility tests. *Theranostics, 7*(7), 1795.

Telke, A. A., & Rolain, J.-M. (2015). Functional genomics to discover antibiotic resistance genes: the paradigm of resistance to colistin mediated by ethanolamine phosphotransferase in Shewanella algae MARS 14. *International Journal of Antimicrobial Agents, 46*(6), 648-652.

Teunis, P., & Schijven, J. (2019). Generic Guidance to Quantitative Microbial Risk Assessment for Food and Water. *National Institute for Public Health and the Environment.*

Tian, Q., Mu, Y., Xu, Y., Song, Q., Yu, B., Ma, C., Jin, W., & Jin, Q. (2015). An integrated microfluidic system for bovine DNA purification and digital PCR detection. *Analytical Biochemistry, 491*, 55-57.

Torres-Cortés, G., Millán, V., Ramírez-Saad, H. C., Nisa-Martínez, R., Toro, N., & Martínez‐Abarca, F. (2011). Characterization of novel antibiotic resistance genes identified by functional metagenomics on soil samples. *Environmental Microbiology, 13*(4), 1101-1114.

Troeger, C., Blacker, B. F., Khalil, I. A., Rao, P. C., Cao, S., Zimsen, S. R., Albertson, S. B., Stanaway, J. D., Deshpande, A., & Abebe, Z. (2018). Estimates of the global, regional, and national morbidity, mortality, and aetiologies of diarrhoea in 195 countries: A systematic analysis for the Global Burden of Disease Study 2016. *The Lancet Infectious Diseases, 18*(11), 1211-1228.

Ventola, C. L. (2015). The antibiotic resistance crisis: Part 1: Causes and threats. *Pharmacy and Therapeutics, 40*(4), 277.

WHO. (2017). *Global antimicrobial resistance surveillance system (GLASS) report: Early implementation 2016-2017*. Geneva, Switzerland: Licence: CC BY-NC-SA 3.0 IGO.

Wu, C.-Y., Stoecklein, D., Kommajosula, A., Lin, J., Owsley, K., Ganapathysubramanian, B., & Di Carlo, D. (2018). Shaped 3D microcarriers for adherent cell culture and analysis. *Microsystems & Nanoengineering, 4*(1), 1-9.

Wu, C. Y., Owsley, K., & Di Carlo, D. (2015). Rapid software-based design and optical transient liquid molding of microparticles. *Advanced Materials, 27*(48), 7970-7978.

Zhang, J., Yan, S., Yuan, D., Alici, G., Nguyen, N.-T., Warkiani, M. E., & Li, W. (2016). Fundamentals and applications of inertial microfluidics: A review. *Lab on a Chip, 16*(1), 10-34.

Zhang, Q. C., Lambert, G., Liao, D., Kim, H., Robin, K., Tung, C. K., Pourmand, N., & Austin, R. H. (2011). Acceleration of emergence of bacterial antibiotic resistance in connected microenvironments. *Science, 333*(6050), 1764-1767.

Zilionis, R., Nainys, J., Veres, A., Savova, V., Zemmour, D., Klein, A. M., & Mazutis, L. (2017). Single-cell barcoding and sequencing using droplet microfluidics. *Nature Protocols, 12*(1), 44.

Chapter 2

MULTIPHYSICS SIMULATION IN MICROFLUIDIC PATHOGEN DETECTION

3D microfluidic systems often involve multiple physics processes simultaneously. Laminar flow regimes and well-controlled fluidic conditions in 3D microfluidic systems allow for insightful theoretical analysis. The design of microfluidic devices and gaining an understanding of their performance capabilities can be facilitated by numerical simulation. COMSOL provides a powerful interface to conduct the multiphysics simulation for versatile 3D geometries. Herein, I have employed COMSOL Multiphysics® to simulate processes including fluid flow, ion diffusion, reaction, particle tracing, etc. The development of the simulation models contributed to the design of a 3D-printed microfluidic chip for PCR pretreatment that enables differentiation between live and dead cells, understanding the DNA extraction performance of an electrochemical cell lysis device, and validating key assumptions of uniform cell distributions on an asymmetric membrane for integrated digital detection.

2.1 Designing a 3D-printed microfluidic device for efficient PCR determination of 'live *versus* dead' microbial cells

Reproduced from the article below with permission from the Royal Society of Chemistry.

Zhu, Y., Huang, X., Xie, X., Bahnemann, J., Lin, X., Wu, X., Wang, S., and Hoffmann, M. R (2018). Propidium monoazide pretreatment on a 3D-printed microfluidic device for efficient PCR determination of 'live *versus* dead' microbial cells. *Environmental Science: Water Research & Technology*, *4*(7), 956-963. https://doi.org/10.1039/C8EW00058A.

2.1.1 Abstract

Waterborne microbial pathogen detection *via* nucleic acid analysis on portable microfluidic devices is a growing area of research, development, and application. Traditional polymerase chain reaction (PCR) based nucleic acid analysis detects total extracted DNA, but cannot differentiate live and dead cells. A propidium monoazide (PMA) pretreatment step before PCR can effectively exclude DNA from nonviable cells, as PMA can selectively diffuse through compromised cell membranes and intercalate with DNA to form DNA-PMA complex upon light exposure. The complex strongly inhibits the amplification of the bound DNA in PCR, and thus, only cells with intact cell membranes are detected. Herein, this study reports the development of a microfluidic device to carry out on-chip PMA pretreatment. Chip design was guided by computer simulations, and prototypes were fabricated using a high-resolution 3D printer. The optimized design utilizes split and recombine mixers for initial PMA-sample mixing and a serpentine flow channel containing herringbone structures for dark and light incubation. On-chip PMA pretreatment to differentiate live and dead bacterial cells in buffer and natural pond water samples was successfully demonstrated.

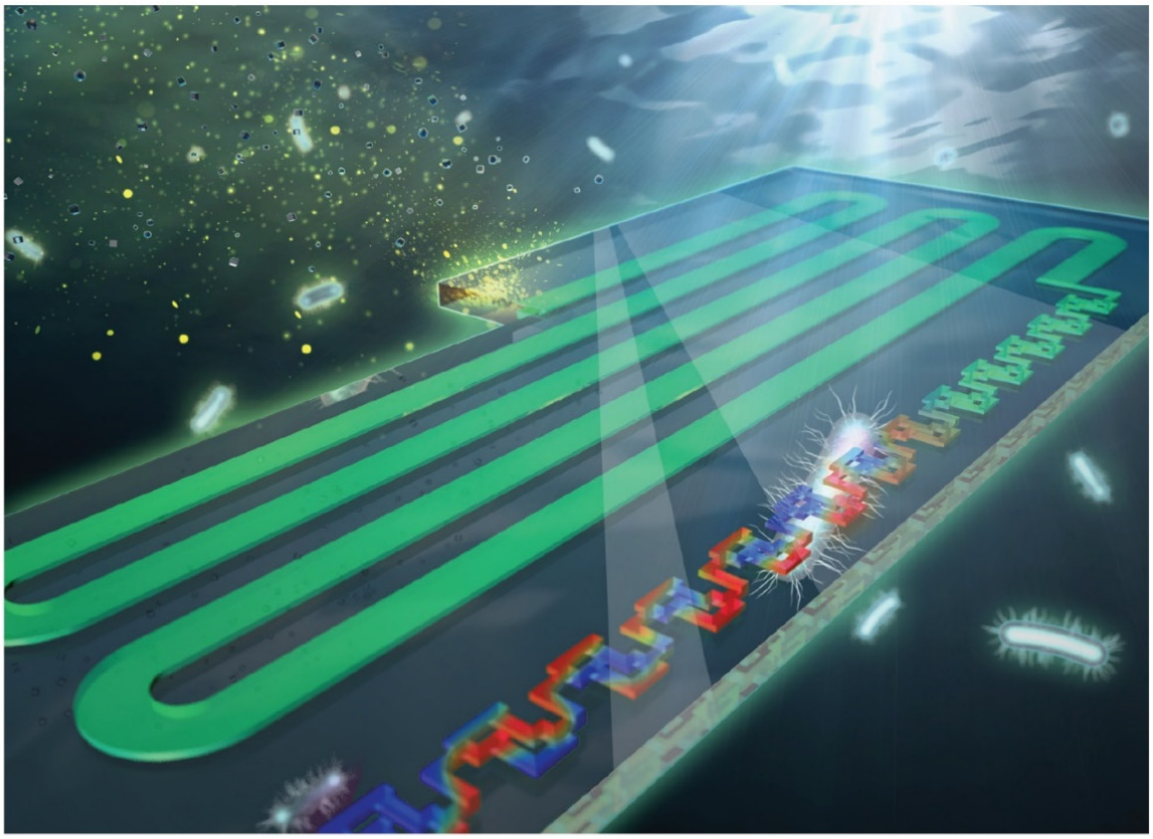

Featuring work from Dr. Michael R. Hoffmann and his team from the Department of Environmental Science and Engineering, California Institute of Technology, USA.

Propidium monoazide pretreatment on a 3D-printed microfluidic device for efficient PCR determination of 'live *versus* dead' microbial cells

A microfluidic chip for live/dead bacterial cell differentiation with propidium monoazide pretreatment has been developed. The study reports computer-aided design of microfluidic structures, prototyping by high-resolution 3D printing, and successful tests with lab and environmental samples.

As featured in:

See Michael R. Hoffmann *et al.*, *Environ. Sci.: Water Res. Technol.*, 2018, 4, 956.

Image reproduced by permission of Dr. Michael R. Hoffmann and the Royal Society of Chemistry from *Environmental Science: Water Research & Technology*, 2018, **4**, 956-963, https://doi.org/10.1039/C8EW00058A.

2.1.2 Introduction

Due to poor water and sanitation conditions, outbreaks of waterborne diseases claim millions of lives per year in many developing countries and countries in conflicts (e.g., the cholera epidemics in Yemen and Haiti) (Ashbolt, 2004; Gleick, 2002). Compared to traditional culture-based methods, polymerase chain reaction (PCR) technology significantly improves the accuracy and sensitivity of pathogen detection and it reduces the analytical time from days to hours (Girones et al., 2010). In recent years, the emergence of microfluidic technologies has enabled the miniaturization of PCR processes onto chip-based devices. Studies have demonstrated automated PCR systems that integrate DNA extraction, thermal cycling, and results reading (Huang et al., 2017; Kopp et al., 1998; Lee et al., 2006). These portable systems have shown great potential in waterborne pathogens detection and monitoring, especially in low-resource settings.

Bacterial cells, constituting a major category of waterborne pathogens, can exist in three states characterized by distinct cell behaviors in traditional culture-based methods. The three states are culturable, dead, and a dormancy state called viable but non-culturable (VBNC) (Oliver, 2005). Pathogenic bacterial cells in both culturable and VBNC states pose potential risks to public health, thus should be considered as "live" cells in environmental monitoring and microbial risk analysis. Culture-based methods obviously tend to underestimate the pathogen concentrations due to the presence of VBNC cells under various environmental stresses (Oliver et al., 2005; Oliver et al., 1995). However, the differentiation between live and dead cells is even more challenging without cultivation. Although PCR is becoming the new standard in environmental microbial detection, it cannot differentiate live and dead pathogens, since it indiscriminately detects all target DNA fragments in a sample. Studies have shown that a considerable fraction of pathogens in environmental water samples may have lost viability, but their DNA may still be present and detectable by PCR for several weeks. This would likely result in an overestimation of potential health risks (Josephson et al., 1993). A few studies showed that dielectrophoresis can separate live and dead cells based on the different induced electrophoretic forces on the cells (Lapizco-Encinas et al., 2004;

Markx et al., 1994; Shafiee et al., 2010). The viability of cells may also be assessed by the integrity of their plasma membranes. A combination of two fluorescent dyes SYTO-9 (stains all cells in green) and propidium iodide (only penetrates cells with damaged membranes and labels them in red) has been widely used for microscopic and flow-cytometric live *versus* dead cell determination (Berney et al., 2007; Boulos et al., 1999; Giao et al., 2009).

Using the membrane exclusion properties of live cells, propidium monoazide (PMA), a DNA intercalating dye, has been coupled with PCR to detect only live cells (Cawthorn & Witthuhn, 2008). The aforementioned dye is able to penetrate the compromised cell membranes of dead cells but not those of the live cells. With light exposure, the azide group on the dye molecule is converted into a reactive nitrene intermediate, which irreversibly forms C-N covalent bonds with adjacent DNA (Hixon et al., 1975). Dye-bound DNA loses its ability to bind PCR primers and thus cannot be amplified during PCR cycles. The excess dye molecules react with water during light incubation and lose their ability to bind amplified DNAs (Nocker et al., 2007). This method intrinsically enables selective detection of live cells including those in VBNC state. It should be noted that the efficacy of PMA pretreatment is not universal among all microorganisms. Some live cells, such as *Bacillus subtilis* and *Staphylococcus epidermidis*, have been shown to have a non-negligible PMA permeability, and thus the PMA method may underestimate the number of live cells of such species (Kobayashi et al., 2009; Xie et al., 2016). Moreover, not all dead cells exhibit a higher PMA permeability than the live ones. This is particularly true in the case of UV disinfection process, in which the cell death is mainly induced by damages to DNA/RNA instead of to cell membranes. The intact membranes of such dead cells could obstruct the permeation of PMA, leading to an overestimation of live cell concentration. Nevertheless, PMA pretreatment is still an applicable and possibly the most rapid method to differentiate live/dead cells when the assay is properly designed.

Traditional PMA pretreatment is performed in-tube by adding PMA into samples, followed by a brief vortex, a given time of dark incubation, and then a light incubation (Bae

& Wuertz, 2009). Performing PMA pretreatment on a microfluidic chip can eliminate the need of multiple manual pipetting steps with the advantage of accuracy and reproducibility. Moreover, an on-chip PMA pretreatment may also benefit for the future design of an integrated PMA-PCR microfluidic system. In a microfluidic chip with limited channel volume, sufficient incubation time requires relatively low flowrates. However, mass transport under these conditions is dominated by diffusion due to small Reynold's and Peclet numbers. To ensure the effective diffusion of PMA into compromised cells, a split and recombine (SAR) mixer can be used to shorten the mixing channel lengths (Lin, 2011). However, the multilayer structure of such mixers poses a major challenge for chip fabrication. Conventional fabrication methods such as soft lithography or direct etching are essentially 2-dimensional, which limit the multi-dimensional design. Furthermore, bonding of corresponding channels leads to low turnover rates and poor prototype consistency (Au et al., 2016).

The overall goal of this project is to develop a microfluidic chip to simplify PMA pretreatment in PCR-based live/dead bacterial cell differentiation. COMSOL Multiphysics® simulation software was employed to guide the chip design by modeling the fluidic behavior under experimental conditions. High-resolution 3D printing techniques were used to fabricate chips with complicated 3D structures without using traditional clean room facilities. PMA pretreatment to differentiate live and dead bacterial cells in buffer and natural pond water samples was successfully demonstrated using the prototype chip.

2.1.3 Materials and methods

2.1.3.1 Flow simulation

The number of split and recombine (SAR) mixer units required for adequate mixing were determined by flow simulation in COMSOL Multiphysics® (COMSOL Multiphysics, 2015). The inlet PMA concentration was set as 400 μM, while its concentration at the sample inlet side was set as zero. The fluid properties of bacterial suspension were assumed to be the same as water. The geometry of 15 SAR mixers was assembled in COMSOL and the cross-sectional PMA concentration profiles were simulated at the end of each mixer. COMSOL solves the laminar flow profile of the system and then solves the transport of dilute species. With a PMA to sample flowrate ratio set at 1:4, total flowrates of 7.5, 12.5, 25, 50, 100, and 150 μL/min were tested. At the cross-sections after each mixer unit, the values of $|C_{PMA}$ - 80 μM| were calculated and averaged for all mesh points in the plane, which represents the cross-sectional averaged absolute difference between actual PMA concentration (C_{PMA}) and target PMA concentration (80 μM). The effectiveness of mixing after certain number of mixers (N) was quantified by percentage mixing, calculated by **Equation 2.1**:

$$\%\ \text{Mixing}_N = 1 - \frac{(|C_{PMA} - 80\ \mu M|_{n=N})_{cross-sectional\ average}}{(|C_{PMA} - 80\ \mu M|_{n=0})_{cross-sectional\ average}} \qquad \textbf{(Eq. 2.1)}$$

The design of mixers is based on the simulated percentage of mixing values, which approaches 100% when the fluids are perfectly mixed.

2.1.3.2 Chip design, fabrication and characterization

The PMA pretreatment chip was fabricated using a high-resolution 3D printer (3D systems ProJet™ MJP 2500 Plus, Rock Hill, SC) with clear plastic 3D printing material (Visijet M2 RCL, 3D Systems). After printing was completed, the chip was cleaned in hot mineral oil bath and the channel was flushed with hot mineral oil to remove the supporting wax outside and inside the chip. A schematic diagram and a photograph of the chip are shown in **Figure 2.1a-d**. The microfluidic chip contains 10 SAR mixers followed by a serpentine-

shaped incubation channel. Herringbone structures were also incorporated into the incubation channel to reduce the residence time difference caused by the parabolic flow profile (Rajabi et al., 2014).

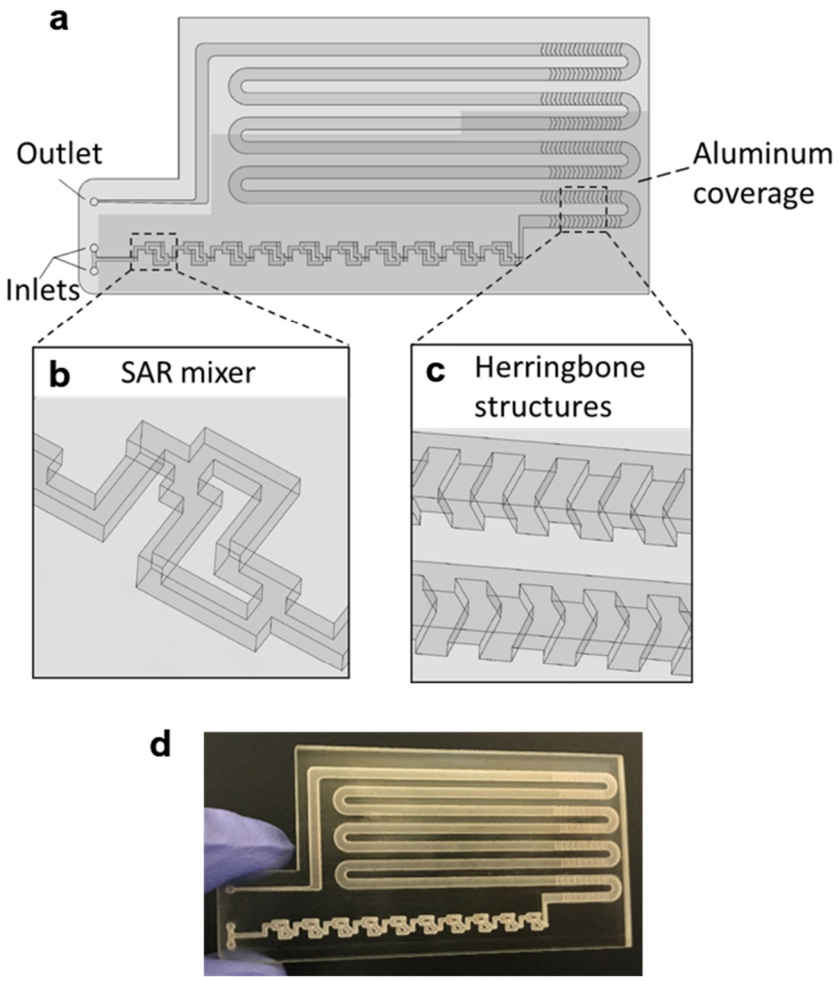

Figure 2.1 Microfluidic chip design and prototype. (**a–c**) Chip design: top view (**a**) with a zoomed-in 3D view of an SAR mixing unit (**b**) and the herringbone structures (**c**). The injected cell sample and PMA solution are continuously mixed in the SAR mixers and then enter the incubation channel with herringbone structures. The darker shade indicates that part of the chip is covered by aluminum foil for dark incubation. (**d**) Photo of the 3D-printed chip prototype.

The channel width of the SAR mixer is 500 μm, while that of the incubation section is 2 mm. The total void volume within the chip was calculated to be 138 μL. The thickness of the covering layer above the incubation channel was 0.8 mm. To test the channel integrity and quality, a 500 μm-thick slice was printed with square holes with sides of 500 μm and was viewed under a microscope (Leica M205FA, Buffalo Grove, IL). The light transmittance of the material was assessed by UV-vis spectrometer (Shimadzu UV-2101PC, Kyoto, Japan) over the wavelength range from 200 to 700 nm. A 0.8 mm-thick slide, which has the same thickness as the top cover layer over the channels, was printed. The slide was measured with one side rubbed with mineral oil facing the light source, in order to simulate the chip layer above the fluid during light incubation.

2.1.3.3 Cell cultures and natural water samples

Escherichia coli (*E. coli,* ATCC 10798) were employed as model bacteria and cultivated in Luria-Bertani (LB) broth in an incubator shaking at 200 rpm for ~16 h at 37 °C. *E. coli* cells were harvested and washed 3 times with 1× phosphate-buffered saline (PBS) and used as stock solution. Buffer samples were prepared with 7×10^8 CFU/mL live *E. coli* cells spiked in PBS, as estimated by plate counts. To prepare dead cell samples, the stock solution was heat-treated in 90°C water bath for 10 minutes, and the cell inactivation by this heating protocol was verified by Xie et al.

To investigate the performance of PMA chip in real water samples, environmental water samples were collected from the Turtle Pond in Caltech. The basic water quality parameters are presented in Table S1.

2.1.3.4 PMA pretreatment on the prototype chip

The inlets, SAR mixers, and part of the incubation channel were covered with aluminum foil for dark incubation, while the rest of the incubation channel was left uncovered for light exposure (1100 W/m^2, ABET Sun 2000, Milford, CA). The chip surface facing the light source was rubbed with mineral oil in order to enhance the light transmittance. 400 μM PMA solution (Biotium Inc.) and the water sample were introduced

into each inlet *via* microfluidic connectors (Dolomite M1 4-way linear connector, Royston, UK) with a flowrate ratio of 1:4, and the flows were controlled by syringe pumps (Cole-Parmer 74905-02, Vernon Hills, IL). Depending on the flow rate, usually 1-10 mL cell sample was loaded for each experiment. After injection, the PMA solution and *E. coli* were mixed in the SAR mixers, followed by dark incubation to allow the diffusion of PMA molecules through dead cell membranes, and then light exposure to induce the reaction between PMA and adjacent DNA. Samples (100 μL/sample) were collected from the outlet in triplicates after the flow reached steady state.

The on-chip PMA pretreatment was first tested with PBS buffer seeded with all dead cells at total flow rates of 7.5, 12.5, 25, 50, 100, and 150 μL/min, corresponding to light exposure time (1/2 total residence time) of 9.17, 5.50, 2.75, 1.38, 0.69, and 0.46 minutes. Control experiments without PMA treatment were performed, in which the PMA solution was substituted by Milli-Q water, with all other conditions kept the same. For in-tube PMA pretreatment, 20 μL 400 mM PMA solution was mixed with 80 μL cell solution. Then the samples were incubated in dark for a designated time before light incubation. The dark/light incubation conditions tested were the same as the on-chip experiments.

At the optimal flowrate for dead cell discrimination, live and dead *E. coli* cell mixtures (100% live, 10% live, and 100% dead) in PBS were tested on-chip and in-tube. For natural pond water, a mixed sample with 90% heat-treated pond water and 10% non-treated pond water is prepared. The mixed pond water samples were tested under the optimal flow condition on-chip with PMA, in-tube with PMA, and on-chip without PMA.

2.1.3.5 PCR assays

Sample DNAs were extracted with a commercial DNA extraction kit following the instructions (PureLink® Genomic DNA Mini Kit, ThermoFisher Scientific) and quantified by real-time PCR following the similar protocol as Xie et. al (Eppendorf 6300 Realplex 2, Hamburg, Germany). Each 20 μL reaction mixture consists of 10 μL PerfeCTa® qPCR ToughMix® (Quanta BioSciences Inc.), 0.25 μM forward primer, 0.25 μM reverse primer,

0.25 μM TaqMan probe, 2 μL DNA sample, and nuclease free water. The real-time PCR analysis was targeting the universal bacterial 16s rRNA gene. The sequences of the primers and the probe used are listed in SI.

The software (Eppendorf Inc.) accompanied the real-time PCR instrument was used to evaluate threshold cycle (C_t values). The sample DNA concentrations are reflected by threshold cycle (C_t) values, where larger C_t value indicates lower DNA concentration. The effectiveness of on-chip PMA pretreatment, as well as in-tube pretreatment, was showed by ΔC_t, which was calculated by subtracting the C_t value of the cell sample before PMA treatment ($C_{t_{in}}$) from the C_t values of the sample after PMA treatment ($C_{t_{\text{out}}}$) (corrected by the dilution ratio of 5/4), as represented by **Equation 2.2**:

$$\Delta C_t = (C_{t_{\text{out}}} - \log_2\left(\frac{5}{4}\right)) - C_{t_{in}} \qquad \textbf{(Eq. 2.2)}$$

2.1.4 Results and discussions

2.1.4.1 Simulation of PMA-sample mixing by SAR mixers

The SAR mixers aid diffusion by "folding" the joined flows, as demonstrated by **Figure 2.2a** (Glatzel et al., 2008). The mixers utilize the no-slip boundary characteristic of laminar flow to re-orient the split flows by a 90° turn, which forces the concentrated side to meet with the diluted side when the flows recombine. The required diffusion length to achieve a well-mixed state is then reduced to facilitate the diffusive transport of PMA molecules. The cross-sectional PMA concentration profiles after 1, 2, 5, 10, and 15 SAR mixers are shown in **Figure 2.2b**. The mixing effectiveness is visually represented by the uniformity of blue color. At the same geometric position (e. g, **Figure 2.2b**, N=2), fluids under a slower flowrate displayed better-mixed concentration profiles, but the time required to achieve good mixing was much longer.

The tradeoff between time effectiveness and number of mixing units required is demonstrated quantitatively in **Figure 2.2c-d**. Percentages of mixing extent were plotted against the number of mixing units passed and total retention time in the mixing section, respectively. For the same amount of time, higher flowrates result in more efficient mixing, due to more mixing units passed with enhanced advection. However, the optimal flowrate should also take residence time into consideration, since optimal pretreatment requires proper dark and light incubation times for PMA-DNA interaction. Ideally, the design of the mixers needs to provide complete mixing under a range of flow conditions. For the flowrate range of 7.5 to 150 μL/min, which corresponds to a reasonable incubation time range of 9.17 min to 0.46 min (Xie et al., 2016), at least 10 mixers were required to reach a plateau with a 98.5% mixing level. Therefore, 10 mixers were employed in our prototype for additional experiments.

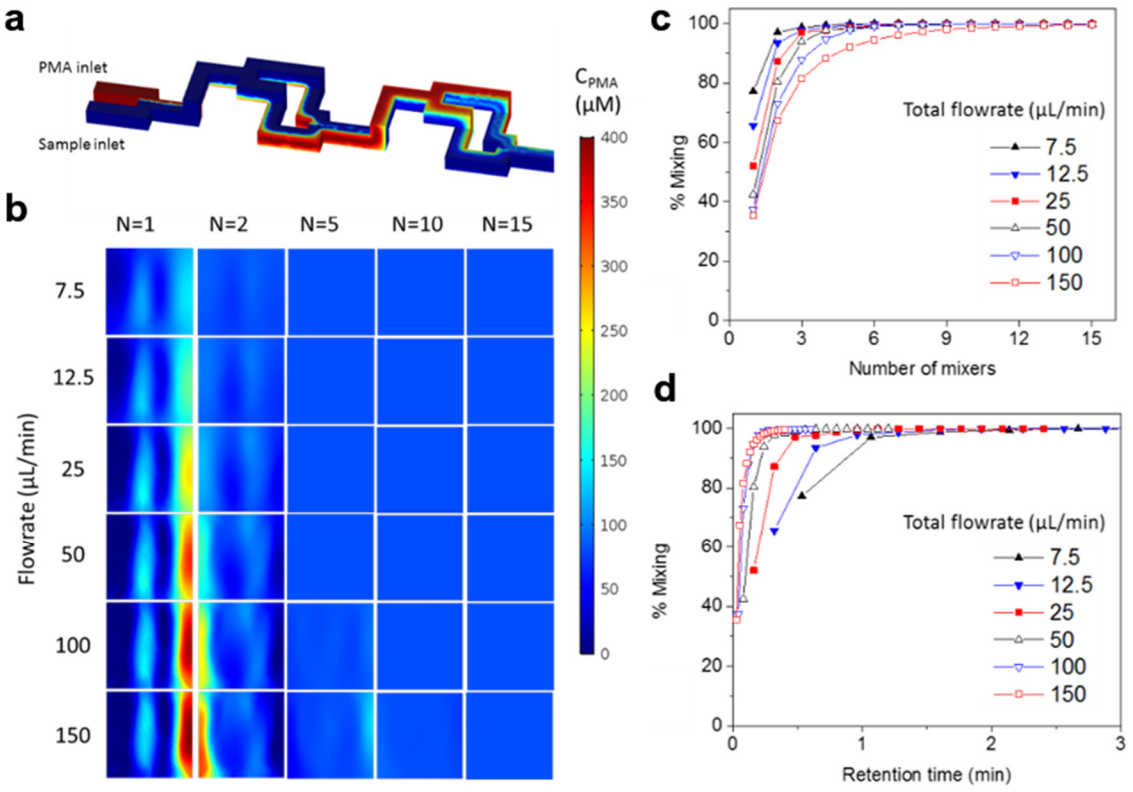

Figure 2.2 Simulation of SAR mixers. (**a**) Demonstration of SAR mixing mechanism: simulated cross-sectional concentration of inlet and the first two mixers at a flowrate of 150 μL/min. (**b**) Simulated PMA concentration profiles at cross sections after 1,2,5,10, and 15 SAR mixers at flowrates ranging from 7.5 to 150 μL/min. (**c-d**) Simulated percentage of mixing plotted over (**c**) number of mixing units passed and (**d**) total retention time in the mixers.

2.1.4.2 Chip fabrication

The resolution of the 3D printer is 800×900×790 DPI, which converts to approximate dimensions of 32×28×32 µm (3D Systems, 2017). The smallest feature of the chip is the SAR channels with 500 µm in size. As shown in **Figure 2.3a**, the 3D printer can create channels with sides as small as 400 µm and surface roughness less than 30 µm. This demonstrates the feasibility of using the 3D printer to realize the current design of the PMA pretreatment chip as well as some other chips with more complicated microscale structures.

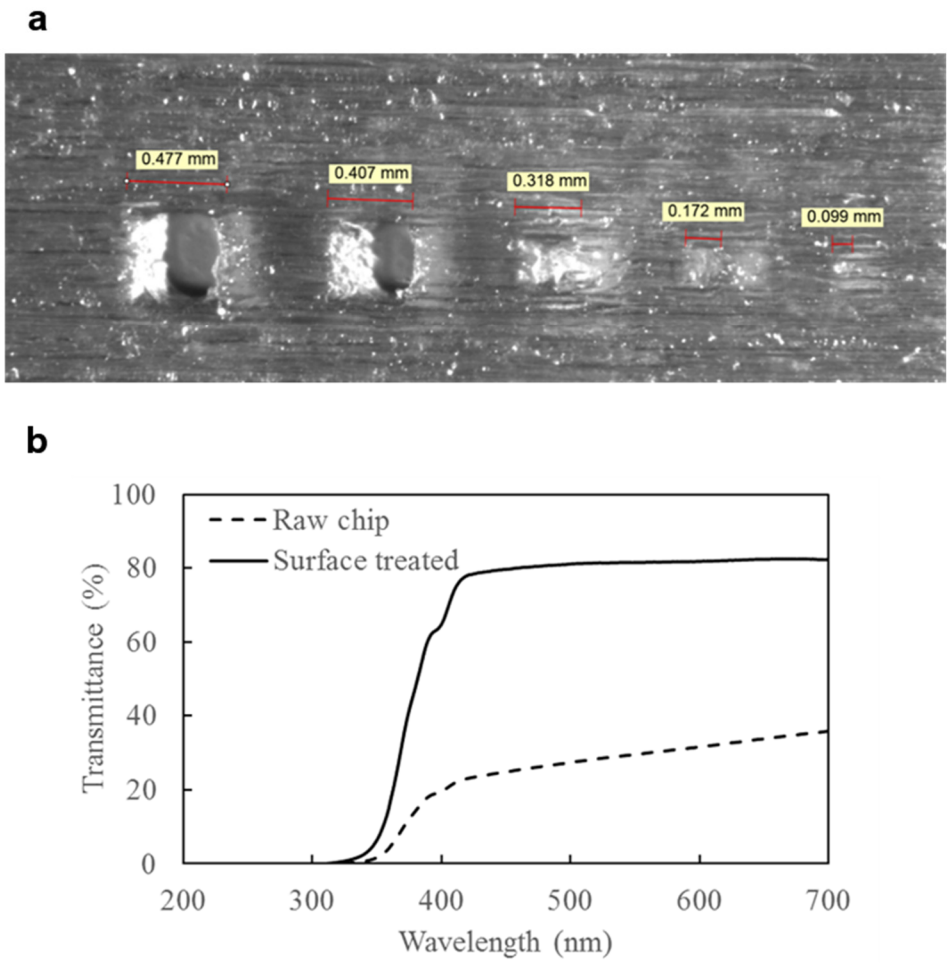

Figure 2.3 3D printing material characterization. (**a**) 3D printed channels at designed sizes of (from left to right) 500 µm, 400 µm, 300 µm, 200 µm, and 100 µm. (**b**) Light transmittance of the 3D printed chip, with and without rubbing mineral oil onto surface, over 200 to 700 nm wavelength range.

The light transmittance of the 3D printing material was characterized to test its effect on radiation available to the fluids. The freshly printed chip is visually opaque before any surface treatment, due to light scattering by the rough surface produced from 3D printing. Demonstrated in **Figure 2.3b**, the test chip without surface treatment allows less than 30% light transmitted at the optimum wavelength of 470 nm. In contrast, the surface-treated chip has enhanced light transmittance of approximately 80% at the same wavelength. With the surface roughness mostly overcome by applying an oil layer, the loss of transmitted radiation was likely due to absorption by the 3D printing material.

It should be noted that the device is not autoclavable, as the 3D printing material is subject to heat distortion at elevated temperatures. However, the material is resistant to common solvents like ethanol and isopropanol, which can be used for cleaning and sterilization purposes (3D Systems, 2017). The material cost of a single microfluidic chip is around $5. Compared to traditional microfluidic chip fabrication methods, 3D printing provides a fast and cost-effective way for prototyping.

2.1.4.3 Performance of on-chip PMA pretreatment

Figure 2.4 shows the dead cell discrimination was achieved with the designed chip. ΔC_t values for various dark/light incubation times are reported along with those acquired for in-tube and on-chip no-PMA control experiments. The higher ΔC_t value indicates larger PCR signal reduction (dead cells' DNA was successfully blocked). For in-tube experiments, the peak ΔC_t observed was at an incubation time of 1.38 minutes. A similar maximum ΔC_t value was also observed by Xie et al. at a light incubation time of 2 min, while the ΔC_t declines with extended light exposure likely due to the degradation of the PMA-DNA complexes. A similar trend was observed in on-chip experiments, with the optimal performance ($\Delta C_t = 7.41 \pm 0.85$) at the incubation time of 2.75 minutes (corresponding to the flowrate of 25 µL/min).

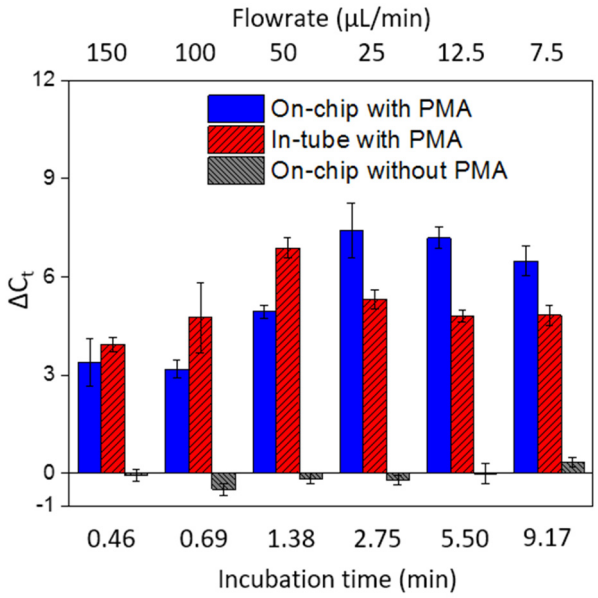

Figure 2.4 The effectiveness of dead cell discrimination with PMA treatment. The experimental results were quantified by real-time PCR and expressed as the differences in the cycle number (ΔC_t) for samples before and after PMA pretreatment. The performance was tested under various flowrates, which corresponds to different light incubation times. The error bars represent the Standard Error (SE) of ΔC_t.

The result was not significantly different (*t*-test, $p>0.5$) from the optimal performance in the in-tube pretreatment ($\Delta C_t = 6.88 \pm 0.31$ at 1.38 min). The slight delay in attainment of an optimal performance is likely related to the light exposure efficiency. The tubes employed in in-tube experiments were made of highly transparent polypropylene (Thermo Fisher Scientific, 2015), while the roughness and light absorbance of the 3D printing material compromised a small fraction of radiation, so that longer incubation time was required to obtain the optimal on-chip PMA pretreatment. In on-chip no-PMA control experiments, the ΔC_t values were close to 0. This result implies that very few dead cells were lost during on-chip treatment due to trapping and sedimentation. Therefore, the observed ΔC_t values in on-chip PMA treatment can be attributed to PMA pretreatment.

At the optimal flowrate (25 μL/min), the on-chip differentiation of live and dead bacterial cells in the spiked buffer samples and natural pond water samples is demonstrated in **Figure 2.5**. For 100% live cells, on-chip PMA treatment resulted in a ΔC_t of 1.77 ± 0.43. This value is significantly smaller (*t*-test, $p < 0.01$) in comparison to the ΔC_t observed in dead-cell-only samples ($\Delta C_t = 7.41 \pm 0.85$). This indicates that the on-chip pretreatment significantly discriminated dead cells while causing much smaller change in the reading of live cells. For a mixed cell sample with 10% live cells and 90% dead cells, deactivation of 90% initial DNA templates would result in a ΔC_t of 3.3 theoretically. The on-chip pretreatment leads to a ΔC_t of 4.57 ± 0.58, with the elevated ΔC_t likely attributed to the fact that some of the live cells were also blocked by PMA.

For the pond water, the total indigenous microbial population was analyzed as the PCR primers targeted at the universal bacterial 16s rDNA. The preliminary result showed that ΔC_t was in the range of 0.58 to 1.28, which may not be reliable as it runs close to the detection limit of the assay. Real-time PCR analysis can differentiate as little as two-fold target gene changes. In PMA pretreatment, this indicates that dead cells in the sample have to be more than 50% (total DNA: live cell DNA>2:1), corresponding to a ΔC_t increase larger than 1 after PMA pretreatment. Therefore, a mixture of heated and unheated (v/v =9:1) pond water sample was prepared to better demonstrate the on-chip PMA treatment. PMA

pretreatment on-chip yields ΔC_t of 2.88 ± 0.65, indicating dead cells constitute 89.6% - 91.3% of the total microbial population. This result generally agrees with the preliminary estimation that 90 - 96% cells were dead in the sample. The slight deviation from prediction might be due to insufficient PMA pretreatment as the pretreatment conditions were not optimized for the variety of bacterial species present. Hence, species-specific and matrix-specific optimization would benefit environmental application.

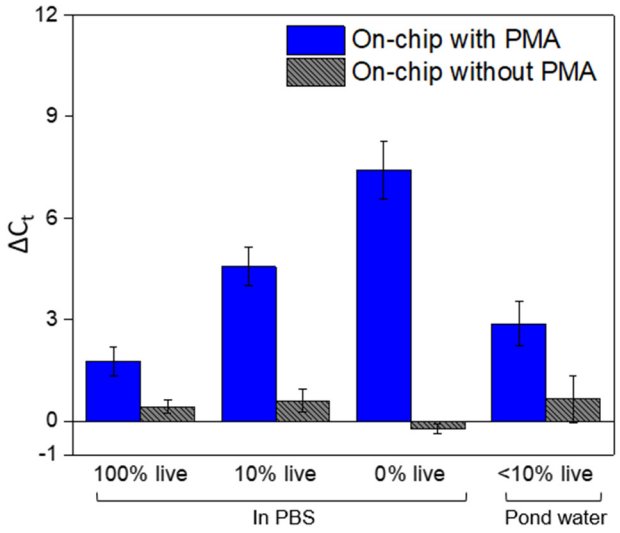

Figure 2.5 The on-chip PMA pretreatment performance, as well as no-PMA control, for live cells, dead cells, 10% live cell samples, and 10 % live pond water samples under the optimal incubation time as previously determined. The results for dead cells under the same condition are plotted as a comparison. The error bars represent the SE of ΔC_t.

2.1.5 Conclusions

The on-chip PMA pretreatment achieves effective dead cell discrimination against live cells in the tested buffer and environmental water samples. Despite discussed limitations, on-chip PMA pretreatment has the advantage of less manual labor required and the potential to be incorporated into an integrated microfluidic system for high throughput, accurate, sensitive, and efficient pathogen detection. The research presented here demonstrates the capability of high resolution 3D printing as a microfluidic prototyping method for new chip design and fabrication. The approach has the advantage of easy design and operation, high fidelity, and quick turnover rates (Au et al., 2016). However, wider microfluidic application of 3D printing would call for development of new materials, better knowledge of material properties, and standardization of surface treatment techniques to cater to various demands (Au et al., 2016; Bhattacharjee et al., 2016). The combination of COMSOL and 3D printing technologies reduces the complexity of microfluidic chip design and prototyping, and therefore lowers the barrier of microfluidics for environmental applications.

2.1.6 Acknowledgements

The authors acknowledge the financial support of the Bill and Melinda Gates Foundation (BMGF OPP1111246).

2.1.7 Supplementary Information

The PCR thermocycling involves 3 minutes of initialization at 95 °C, and 42 cycles of denaturation at 95 °c for 15 seconds followed by annealing/extension at 55 °C for 30 seconds. The primers and probe are targeting the universal bacterial 16s rRNA gene (Suzuki et al., 2000). The sequences are listed in **Table 2.1**.

	Sequence
Forward primer	5'CGGTGAATACGTTCYCGG3' where Y is either C or T
Reverse primer	5'GGWTACCTTGTTACGACTT3', where W is either A or T
TaqMan probe	FAM-5'CTTGTACACACCGCCCGTC3'

Table 2.1 The sequences of primers and probes.

For the tested pond water, the water quality parameters, including pH, electrical conductivity, UV254, and COD, are listed in **Table 2.2**.

pH	7.75	
Electrical Conductivity	925.9	µS/cm
UV254	0.003	
COD	74.7	mg/L

Table 2.2 Water quality parameters of the pond water tested.

2.2 Understanding DNA extraction performance of electrochemical lysis

Wang, S., Zhu, Y., Yang, Y., Li, J. and Hoffmann, M. R. (2020) Electrochemical cell lysis of gram-positive and gram-negative bacteria: DNA extraction from environmental water samples. *Electrochimica Acta,* 135864. https://doi.org/10.1016/j.electacta.2020.135864

2.2.1 Introduction

As a sample preparation step for PCR-based waterborne pathogen detection, cell lysis is required to release the nucleic acids from membrane-encapsulated cells. Membrane disruption or destruction can be achieved chemically (e.g. alkaline lysis), mechanically (e.g. beads beating), electrically (e.g. electroporation), etc. (Shehadul Islam et al., 2017). In this study, we focus on electrochemical cell lysis (ECL). ECL disrupts microbial cell membranes by generating hydroxide ions at the cathode, which creates a local high pH and breaks the fatty acid-glycerol ester bonds in membrane phospholipids (Di Carlo et al., 2005; Nevill et al., 2007). Compared to electroporation which generally requires a high voltage of 500 V (Wang et al., 2006), ECL uses a conveniently low voltage in the range of 2-5 V (Di Carlo et al., 2005; Jha et al., 2012; Jha et al., 2011; Lee et al., 2010; Nevill et al., 2007). The low working voltage avoids joule heating so as to better preserve the released nucleic acid molecules, and can be easily applied in resource limited settings. However, previous studies on ECL were mainly focused on clinical samples (Di Carlo et al., 2005; Nevill et al., 2007). Thus, the reported device development was with micro- or nano-liter throughput, and the validation was only in well-controlled systems with purified buffers. To adapt ECL for wider applications, such as in environmental or agricultural microbial analysis, it is essential to assess the performance of ECL for the interested type of cells in complex matrices with a throughput relevant to the application.

This work reports the development of a novel ECL device with ~1mL capacity that targets in-field application for environmental samples under resource-limited settings. With model gram-negative bacteria (*Escherichia coli* and *Salmonella* Typhi) and gram-positive bacteria (*Enterococcus durans* and *Bacillus subtilis*), the DNA extraction performance was characterized in lab buffer and environmental samples, including turtle pond water and untreated latrine wastewater. COMSOL Multiphysics simulation was employed to better understand the observed performance.

2.2.2 Device design and DNA extraction performance

The ECL device design is shown in **Figure 2.6a**. The design consists of a dimensionally stable IrO2/Ti anode (Yang et al., 2016), a Ti cathode, and a cation exchange membrane. The material of the reactor was polycarbonate. The configuration and the reactions involved in ECL are illustrated in **Figure 2.6b**. The cathodic chamber of 0.8 mL and the anodic chamber of 1.6 mL were separated by the cation exchange membrane. A gas ventilation outlet was located at the top of each chamber. For ECL reaction experiments, 50 mM Na_2SO_4 and bacterial suspensions were syringe-injected from the bottom into the anodic and cathodic chamber, respectively. A constant direct current of 40 mA was applied. The cathodic effluents were collected with syringes after each reaction for downstream PCR analysis.

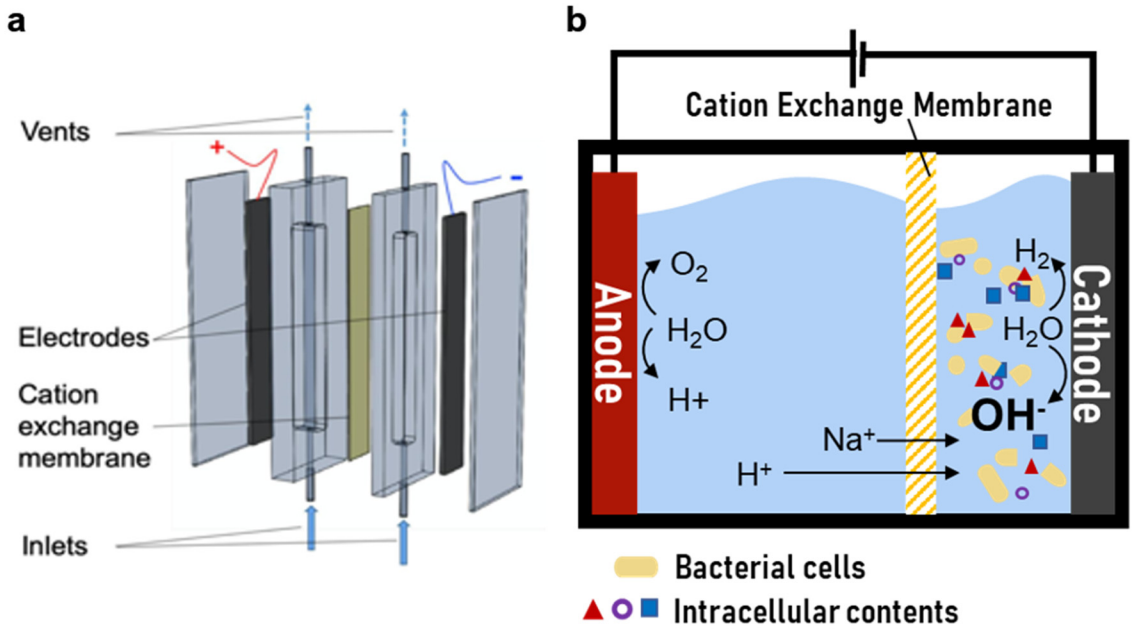

Figure 2.6 ECL device design. (**a**) Major structures of the ECL device shown in an exploded view. (**b**) Schematic of electrochemical cell lysis processes involved inside the device. Adapted from Wang et al.

The DNA extraction performance by ECL with treatment time varying from 30 s to 10 min was evaluated for the 4 model bacteria. The treated samples were further analyzed in qPCR, which reports the cycle number (C_T) that the fluorescence signal associated with the PCR amplification products exceeds the fluorescence threshold. The DNA extraction efficiency for each ECL run was quantified by ΔC_T, which was calculated by subtracting C_T values of the suspended DNA in the ECL treated samples from those in the untreated ones. For all 4 model bacteria, the highest ΔC_T values of the ECL were in the range of 6.5 - 9.8, and were observed with 1 min of ECL treatment. After this optimized treatment duration, the DNA extraction efficiencies generally decrease after 2 min of ECL. Since plausible PCR inhibition caused by electrolyzed cathodic effluents was ruled out experimentally (as discussed in the supporting information of the published article), it is supposed that the decreased efficiency in prolonged ECL could be mainly due to DNA damage by the high pH.

As a reference of the pH effect, direct alkaline lysis experiments were conducted for *E. coli* at varying pH created by homogenous NaOH at concentrations of 0.1 mM – 1 M. The results suggest that the optimal pH for DNA extraction of the tested bacteria lies between 12 and 13. This optimal pH range agrees with the previously reported optimal pH range of 11.5-12.5 for cell lysis (Harrison, 1991; Lee et al., 2010). The bulk pH (12.47-12.76) measured under optimized conditions for ECL extraction also sits within the optimal alkaline lysis pH range. With a pH higher than 13, the decrease in ΔC_T indicates that DNA might be damaged, which is consistent with the DNA damage observed in the samples treated by more than 2 min of ECL. The highest ΔC_T value achieved by alkaline lysis was at 4.2, far less than the ΔC_T of 9.8 with the optimized ECL treatment. ECL was also observed to be capable of lysing gram-positive bacteria *E. durans* while conventional alkaline lysis was not effective, with ΔC_T values all below 3.0. The results highlight that, compared to the most commonly used alkaline cell lysis, ECL is a faster and much more efficient DNA extraction method for gram-negative and gram-positive bacterial cells.

2.2.3 Understanding ECL performance through pH profile simulation

To gain more insight in the observed ECL performance, COMSOL Multiphysics® was employed to simulate the fluidic motion and pH distribution in the cathodic chamber solution. As indicated by the calculated flow field shown in the **Figure 2.7a**, gas evolution helps mixing the solution in the simulated cathodic chamber. In the superimposed 2D arrow plot of velocity field, it is observed that upward fluid momentum close to the electrode surface (the right edge) was induced by gas motion, and that downward motion on the other side was driven by mass conservation. The fluid in the upper volume was notably accelerated and would boost convective transport of OH- ions. Under the simulated flow fields, the pH profiles for the vertical mid-plane of the cathodic chamber were simulated for different contact times and are shown in **Figure 2.7b**. These simulations show that the local pH value near the cathode surface increases rapidly within 1 min of ECL and that an ideal pH range for cell lysis (pH 12-13) is predicted. The gas evolution-induced mixing leads to a larger volume that has a suitable pH for cell lysis after 30 s and 1 min of operation.

After 2 min of ECL operation, the pH in most of the upper volume reaches 13. This simulation is consistent with the DNA loss observed during ECL tests on different bacteria. Hydrogen gas is also generated, as protons are consumed and OH^- is produced at the cathode surface. The simulated pH profiles for the bulk-phase cathodic solutions as a function of time is shown in **Figure 2.7c**. The simulation results are in line with the measured bulk pH values of the cathodic effluents during different ECL tests. The results also highlight that there is a higher pH at the cathode surface than in the bulk electrolyte. It is speculated that cells were efficiently lysed near the cathode surface. The released DNA molecules with negative charge were likely repelled from the cathode, and subsequently preserved in the bulk electrolyte at a lower pH. This may explain the much more efficient DNA extraction by ECL than that by direct alkaline lysis (*vide supra*).

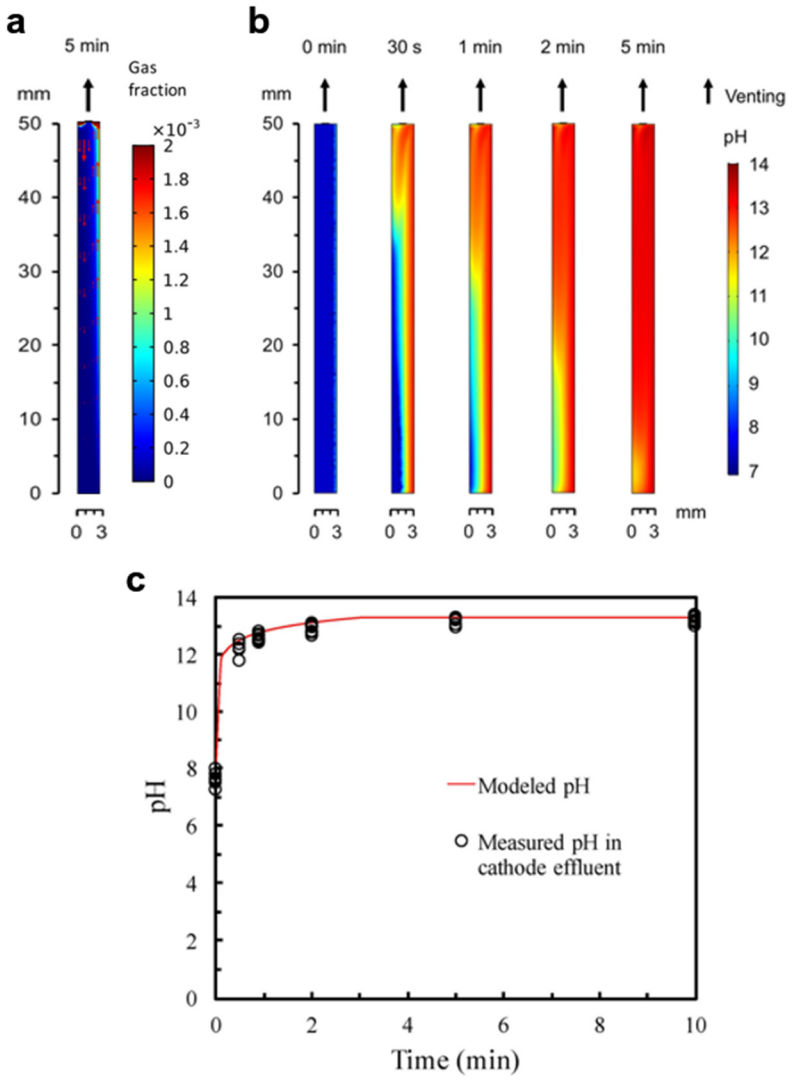

Figure 2.7 Simulation of gas evolution and pH profiles. (**a**) Simulated steady-state flow field of the vertical mid-plane across the electrode and the membrane. The gas fraction and velocity field shown in the plot rapidly reached steady-state within 0.1 s, the shortest time step in the simulation. The color surface represents the volume fraction of gas phase. (**b**) Simulation of pH value distribution for the vertical mid-plane in the cathodic chamber with the cation exchange membrane on the left and the cathode on the right. (**c**) Modeled and measured pH for the cathode effluents as a function of electrochemical reaction time. Adapted from Wang et al.

2.2.4 Simulation methods

COMSOL Multiphysics (COMSOL Multiphysics, 2015), a commercial finite element modeling software, was used to study the fate and transport of hydroxide ions inside the cathodic chamber. The fluid in the cathodic chamber was modeled as a $3 \times 5 \times 50$ mm^3 block, with the electrode surface and the cation exchange membrane represented by the two 5×50 mm^2 sides. The gas vent hole on the top was represented by a cylindrical extrusion with a diameter of 1 mm and a height of 0.1 mm. OH^- and H^+ are generated with the hydrogen and oxygen evolution reactions at the cathode and anode, respectively:

Anode: $2H_2O \rightleftharpoons 4H^+ + 4\bar{e} + O_2$ (**Eq. 2.3**)

Cathode: $4H_2O + 4\bar{e} \rightleftharpoons 4OH^-$ (**Eq. 2.4**)

The generation and venting of H_2 during electrolysis induce fluid movements in the cathodic chamber. The time-dependent flow field within the cathodic chamber was simulated by *laminar bubbly-flow* module, which calculates the fluid movement induced by the generation and venting of H_2 during electrolysis. The convective and diffusive OH^- transport under the calculated flow field was then modeled by *transport of dilute species* module. Free tetrahedral mesh calibrated for fluid dynamics was used with predefined element size, which was set as fine for all boundary surfaces and as normal for the rest of the geometry.

For flow field simulation, *laminar bubbly-flow* module uses Euler-Euler model to solve two-phase flow macroscopically by tracking phase averaged parameters and volume fraction of each phase (Vera & Ruiz, 2012). Molar influx of H_2 gas at the cathode surface was theoretically half of the OH^- generation rate R_{in}^{cat}, which was calculated by **Equation 2.5** (Bard et al., 1980):

$$R_{in}^{cat} = \frac{i}{nFA} \quad \text{(Eq. 2.5)}$$

where i is the supplied current (40 mA), n is the number of electrons used to generate a hydroxide ion, which is 1, F is the Faraday constant, and A is the surface area. The bubble

diameter was set at 100 μm which is a typical size reported in literature (Matsushima et al., 2006; Matsushima et al., 2009).

For *transport of dilute species* interface, OH^- generation from the cathodic electrode surface was represented by a uniform inward flux of R_{in}^{cat}, calculated by **Equation 2.5** at 1.66 × 10^{-3} mol/(s·m^2). Simultaneously, in the anodic chamber with 50 mM Na_2SO_4 buffer solution, H^+ ions were produced from the anode surface at the same rate as OH^- generation, and cations were forced across the cation exchange membrane. It was assumed that sodium ions were the dominant species transported across the membrane due to their concentration dominance over protons, until sodium ions were transferred down to a concentration comparable to the proton; at this point, protons are the preferred ions for membrane transport due to their smaller size. For the cathodic chamber, the influx of H^+ was considered as the sink of OH^- and the contribution of water dissociation was negligible to mass transfer through the membrane (Krol et al., 1999; Simons, 1979; Tanaka et al., 2012).Therefore, the flux of hydroxide ions at the membrane, R_{in}^{mem}, was approximated as a step function:

$$R_{in}^{mem} = \begin{cases} 0 & t < t_c \\ -R_{in}^{cat} & t \geq t_c \end{cases} \qquad \textbf{(Eq. 2.6)}$$

where t is time and t_c is the critical time when protons become favored for cross membrane transport. The value of t_c was approximated by the time of complete consumption of sodium ion in the anodic chamber. The initial pH was set at 7.5. The time-dependent concentration profile of OH^- was analyzed with the diffusion coefficient of OH^- in water set at 5×10^{-5} cm^2/s (Lee & Rasaiah, 2011). From the simulated hydroxide ion concentrations, the transient pH profiles of the cut plane across the electrode and the membrane were generated, while the bulk solution pH was estimated from the volume average of $[OH^-]$.

2.3 Validating cell distribution on an asymmetric membrane for integrated digital detection

Adapted from the article below with permission from American Chemical Society. Further permissions related to the material adapted should be directed to the ACS.

Lin, X., Huang, X., Zhu, Y., Urmann, K., Xie, X., & Hoffmann, M. R. (2018). Asymmetric membrane for digital detection of single bacteria in milliliters of complex water samples. *ACS nano*, *12*(10), 10281-10290. https://pubs.acs.org/doi/abs/10.1021/acsnano.8b05384

2.3.1 Asymmetric membrane for digital cell detection directly from environmental samples

Compartmentalization of cells of nucleic acid molecules is an essential step for digital detection, which runs the assay in thousands of parallel reactors with volumes of nano- or pico- liter. Common compartmentalization methods include emulsification into water-in-oil droplets, etching or machining wells or microchannels, hydrogel-based virtual microfluidics, etc. (Samiei et al., 2016; Xu et al., 2016). The complex operation and instrumentation involved in these methods hinder their application under resource-limited conditions. Furthermore, for in-field environmental applications, low concentration of pathogens present in environmental samples generally requires an additional step of sample concentration before successful nucleic acid detection (Wu et al., 2020). In this work, we developed a novel asymmetric membrane design that, besides being an easy compartmentalization solution, is capable of integrating bacterial cell capture, concentration, purification, and digital LAMP. With a sample size of 1 mL, absolute quantification of *E. coli* and *Salmonella* from 0.3 to 10,000 cell/mL was achieved in unprocessed environmental beach water and pond water within 1 hour.

The workflow of using the asymmetric membrane is shown in **Figure 2.8**. The asymmetric membrane is made of two pieces of commercial polycarbonate membranes, one

with dense vertical nanochannels and the other with uniform micropores. The two membranes could be assembled easily by heat treatment within 1 min. During filtration, a sacrificial pre-filter removes large particles and positively charged matters, while bacteria were forced through and captured homogeneously inside each micropore of the upper membrane layer. Meanwhile, the nanochannels on the bottom membrane layer allow elution of small molecules of amplification inhibitors in the environmental samples, such as proteins, organics, and heavy metals (Schrader et al., 2012). The strong sealing and vertical orientation of nanochannels ensure isolation of each pore without cross-contamination. After filtration, optimized assay reagents were introduced into an asymmetric membrane for rapid and isothermal amplification of target nucleic acids of single bacteria within each pore.

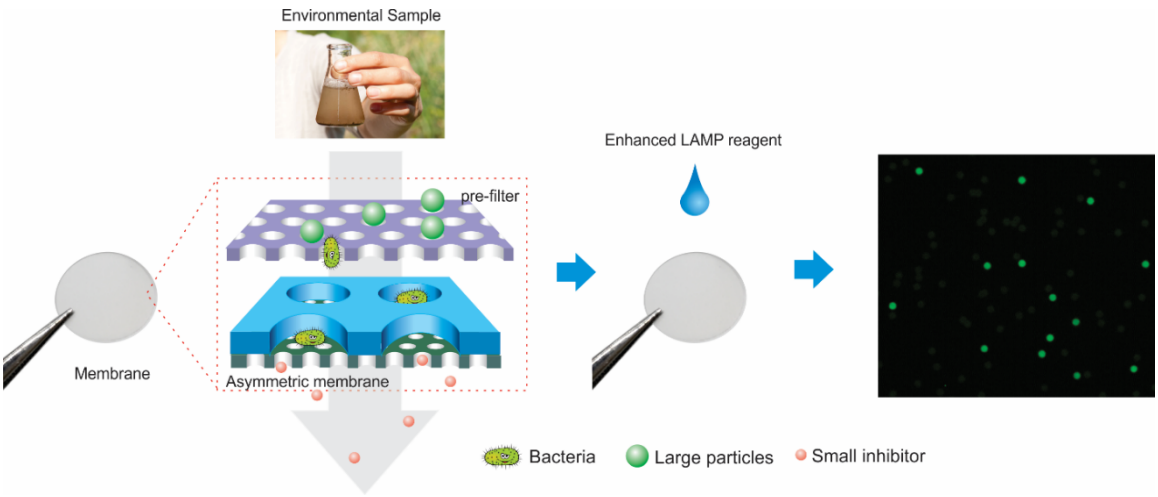

Figure 2.8 Schematic illustration of heterogeneous micro/nanochannel membrane for single bacteria detection from crude environmental samples.

2.3.2 Validating the random particle distribution assumption

The interpretation of the digital single cell detection and analysis using Poisson Distribution is based on the assumption that the targets are randomly distributed before the reaction. In this case, it means that the cell is assumed to disperse homogeneously on the entire membrane. To verify this assumption, we conducted finite element analysis using COMSOL to simulate fluid flow and particle trajectories through the asymmetric membrane.

The simulated flow field inside the filter is shown in **Figure 2.9a**. The fluid scattered across the asymmetric membrane before passing through. The transmembrane flow was then quantitatively investigated by comparing the flow rate at varying x-positions across the membrane, as shown in **Figure 2.9b**. The peaks represent the flow rate through one micropore. The flat-shaped peaks without any sign of bell-curve indicate that the flow rate was identical for all the micropores. Since bacterial cells experience additional drag force and inertial force compared to water or small molecules, the cell distribution was assessed by simulating particle trajectories under the calculated flow field. The particle properties were set to reflect those of *E. Coli* cells. A large number of particles were released at the inlet, and the portion of particles across the varying positions of the membrane is observed to be nearly constant (**Figure 2.9c**). The results indicate that theoretically the cells are distributed evenly across the asymmetric membrane, so that cells have an equal chance of partitioning into each micropore during filtration. With exceptional performance of concentrating cells from the water sample, the random distribution assumption is still fulfilled for valid downstream digital analysis.

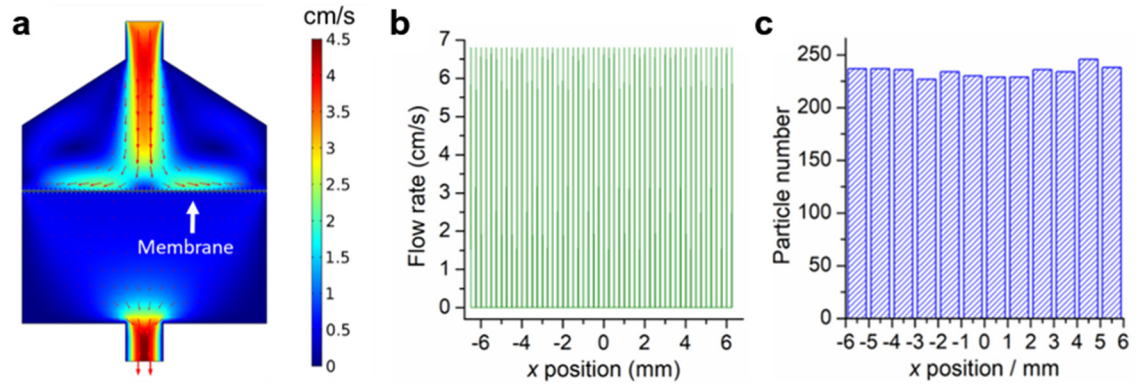

Figure 2.9 Simulation and experiments for the capture and partition of bacteria. (**a**) Numerical simulation of fluidic flow profile inside the filter when asymmetric membrane present. (**b**) Simulated flow rate at each *x* position of the asymmetric membrane. Each peak represents the flow rate through one micropore. (**c**) Simulated number of particles at each *x*-position range across the asymmetric membrane. Adapted from Lin et al.

2.3.3 Simulation methods

We performed finite element modeling using COMSOL Multiphysics® (COMSOL Multiphysics, 2015). The fluid regime above the asymmetric membrane was modeled to resemble the geometry inside the membrane fitter used in the experiments. A cylindrical fluid regime connected to the outlet was below the asymmetric membrane. The asymmetric membrane was modeled as two layers of fluid separator, each with a thickness of 25 μm and a diameter of 13 mm. The micropores in the upper layer are 25 μm diameter, with the center-to-center distance at 225 μm. For the bottom membrane layer, the nanochannels are 400 nm in diameter with the center-to-center distance at 2 μm. The fluid was simulated with properties of water, with a density of 1×10^3 kg·m^{-3}, and a dynamic viscosity μ of 1×10^{-3} Pa·s. The inlet fluid was set as a normal flow with a velocity of 0.0318 m/s, which was approximately calculated by the experimental rate of fluid injection *via* syringe.

The *laminar flow* module was used first to solve the steady-state Navier–Stokes equations. Under the calculated flow field throughout the modeled fluid regime containing the membrane, the time-dependent particle movement along the fluid was simulated using the *particle tracing under fluid flow* module. To qualitatively determine if the cells can be uniformly distributed into the micropores, thousands of particles were set to be released from the inlet, and their trajectories were calculated. The movement of the particles was dominated by the drag force exerted by the fluid flow. The particles were set to freeze upon contacting the walls inside the millipores, so that the distribution pattern of all the particles could be assessed by the final x-position. The particle diameter was set to 1.1 μm, and the density was set to 1100 kg/m^3, based on the properties of *E. coli (Martinez-Salas et al., 1981)*.

References

3D Systems. (2017). *MultiJet Plastic Printers Tech Specs*. Retrieved from https://www.3dsystems.com/sites/default/files/2017-03/3D-Systems_MJP_2500_Tech_Specs_USEN_2017.03.24_WEB.pdf

Ashbolt, N. J. (2004). Microbial contamination of drinking water and disease outcomes in developing regions. *Toxicology, 198*(1-3), 229-238. doi:10.1016/j.tox.2004.01.030

Au, A. K., Huynh, W., Horowitz, L. F., & Folch, A. (2016). 3D-printed microfluidics. *Angewandte Chemie International Edition, 55*(12), 3862-3881.

Bae, S. W., & Wuertz, S. (2009). Discrimination of viable and dead fecal bacteroidales bacteria by quantitative PCR with propidium monoazide. *Applied and Environmental Microbiology, 75*(9), 2940-2944. doi:10.1128/Aem.01333-08

Bard, A. J., Faulkner, L. R., Leddy, J., & Zoski, C. G. (1980). *Electrochemical Methods: Fundamentals and Applications* (Vol. 2): Wiley New York.

Berney, M., Hammes, F., Bosshard, F., Weilenmann, H. U., & Egli, T. (2007). Assessment and interpretation of bacterial viability by using the LIVE/DEAD BacLight Kit in combination with flow cytometry. *Applied Environmental Microbiology, 73*(10), 3283-3290. doi:10.1128/AEM.02750-06

Bhattacharjee, N., Urrios, A., Kang, S., & Folch, A. (2016). The upcoming 3D-printing revolution in microfluidics. *Lab on a Chip, 16*(10), 1720-1742. doi:10.1039/c6lc00163g

Boulos, L., Prevost, M., Barbeau, B., Coallier, J., & Desjardins, R. (1999). LIVE/DEAD (R) BacLight (TM): Application of a new rapid staining method for direct enumeration of viable and total bacteria in drinking water. *Journal of Microbiological Methods, 37*(1), 77-86.

Cawthorn, D. M., & Witthuhn, R. C. (2008). Selective PCR detection of viable Enterobacter sakazakii cells utilizing propidium monoazide or ethidium bromide monoazide. *Journal of Applied Microbiology, 105*(4), 1178-1185.

COMSOL Multiphysics. (2015). The platform for physics-based modeling and simulation. *Retrieved from: http://www.comsol.com/comsol-multiphysics*.

Di Carlo, D., Ionescu-Zanetti, C., Zhang, Y., Hung, P., & Lee, L. P. (2005). On-chip cell lysis by local hydroxide generation. *Lab on a Chip, 5*(2), 171-178.

Giao, M. S., Wilks, S. A., Azevedo, N. F., Vieira, M. J., & Keevil, C. W. (2009). Validation of SYTO 9/propidium iodide uptake for rapid detection of viable but noncultivable Legionella pneumophila. *Microbial Ecology, 58*(1), 56-62. doi:10.1007/s00248-008-9472-x

Girones, R., Ferrus, M. A., Alonso, J. L., Rodriguez-Manzano, J., Calgua, B., Correa, A. D., Hundesa, A., Carratala, A., & Bofill-Mas, S. (2010). Molecular detection of pathogens in water–the pros and cons of molecular techniques. *Water Research, 44*(15), 4325-4339. doi:10.1016/j.watres.2010.06.030

Glatzel, T., Litterst, C., Cupelli, C., Lindemann, T., Moosmann, C., Niekrawletz, R., Streule, W., Zengerle, R., & Koltay, P. (2008). Computational fluid dynamics (CFD) software tools for microfluidic applications–A case study. *Computers & Fluids, 37*(3), 218-235. doi:10.1016/j.compfluid.2007.07.014

Gleick, P. H. (2002). *Dirty-water: Estimated deaths from water-related diseases 2000-2020*: Citeseer.

Harrison, S. T. (1991). Bacterial cell disruption: A key unit operation in the recovery of intracellular products. *Biotechnology Advances, 9*(2), 217-240.

Hixon, S. C., White, W. E., Jr., & Yielding, K. L. (1975). Selective covalent binding of an ethidium analog to mitochondrial DNA with production of petite mutants in yeast by photoaffinity labelling. *Journal of Molecular Biology, 92*(2), 319-329.

Huang, X., Gowda, H. N., Wu, X., Dumas, S. L., Zhu, Y., Lin, X., Kido, H., Xie, X., Jiang, S., Madou, M., & Hoffmann, M. R. (2017). *Portable Pathogen Analysis System (PPAS) for microbial water quality analysis*. Paper presented at the 21st International Conference on Miniaturized Systems for Chemistry and Life Sciences (μTAS), Savannah, Georgia, USA.

Jha, S. K., Chand, R., Han, D., Jang, Y.-C., Ra, G.-S., Kim, J. S., Nahm, B.-H., & Kim, Y.-S. (2012). An integrated PCR microfluidic chip incorporating aseptic electrochemical cell lysis and capillary electrophoresis amperometric DNA detection for rapid and quantitative genetic analysis. *Lab on a Chip, 12*(21), 4455-4464.

Jha, S. K., Joo, G.-S., Ra, G.-S., Lee, H. H., & Kim, Y.-S. (2011). Development of PCR microchip for early cancer risk prediction. *IEEE Sensors Journal, 11*(9), 2065-2070.

Josephson, K. L., Gerba, C. P., & Pepper, I. L. (1993). Polymerase chain reaction detection of nonviable bacterial pathogens. *Applied Environmental Microbiology, 59*(10), 3513-3515.

Kobayashi, H., Oethinger, M., Tuohy, M. J., Hall, G. S., & Bauer, T. W. (2009). Improving clinical significance of PCR: Use of propidium monoazide to distinguish viable from dead Staphylococcus aureus and Staphylococcus epidermidis. *Journal of Orthopaedic Research, 27*(9), 1243-1247. doi:10.1002/jor.20872

Kopp, M. U., Mello, A. J., & Manz, A. (1998). Chemical amplification: Continuous-flow PCR on a chip. *Science, 280*(5366), 1046-1048. doi:10.1126/science.280.5366.1046

Krol, J., Wessling, M., & Strathmann, H. (1999). Concentration polarization with monopolar ion exchange membranes: Current–voltage curves and water dissociation. *Journal of Membrane Science, 162*(1-2), 145-154.

Lapizco-Encinas, B. H., Simmons, B. A., Cummings, E. B., & Fintschenko, Y. (2004). Dielectrophoretic concentration and separation of live and dead bacteria in an array of insulators. *Analytical Chemistry, 76*(6), 1571-1579. doi:10.1021/ac034804j

Lee, H. J., Kim, J.-H., Lim, H. K., Cho, E. C., Huh, N., Ko, C., Park, J. C., Choi, J.-W., & Lee, S. S. (2010). Electrochemical cell lysis device for DNA extraction. *Lab on a Chip, 10*(5), 626-633.

Lee, J. G., Cheong, K. H., Huh, N., Kim, S., Choi, J. W., & Ko, C. (2006). Microchip-based one step DNA extraction and real-time PCR in one chamber for rapid pathogen identification. *Lab on a Chip, 6*(7), 886-895. doi:10.1039/b515876a

Lee, S. H., & Rasaiah, J. C. (2011). Proton transfer and the mobilities of the H^+ and OH^- ions from studies of a dissociating model for water. *The Journal of Chemical Physics, 135*(12), 124505.

Lin, B. (2011). *Microfluidics: Technologies and Applications* (Vol. 304): Springer.

Markx, G. H., Talary, M. S., & Pethig, R. (1994). Separation of viable and non-viable yeast using dielectrophoresis. *Journal of Biotechnology, 32*(1), 29-37. doi:10.1016/0168-1656(94)90117-1

Martinez-Salas, E., Martin, J., & Vicente, M. (1981). Relationship of Escherichia coli density to growth rate and cell age. *Journal of Bacteriology, 147*(1), 97-100.

Matsushima, H., Fukunaka, Y., & Kuribayashi, K. (2006). Water electrolysis under microgravity: Part II. Description of gas bubble evolution phenomena. *Electrochimica Acta, 51*(20), 4190-4198.

Matsushima, H., Kiuchi, D., Fukunaka, Y., & Kuribayashi, K. (2009). Single bubble growth during water electrolysis under microgravity. *Electrochemistry Communications, 11*(8), 1721-1723.

Nevill, J. T., Cooper, R., Dueck, M., Breslauer, D. N., & Lee, L. P. (2007). Integrated microfluidic cell culture and lysis on a chip. *Lab on a Chip, 7*(12), 1689-1695.

Nocker, A., Sossa, K. E., & Camper, A. K. (2007). Molecular monitoring of disinfection efficacy using propidium monoazide in combination with quantitative PCR. *Journal of Microbiological Methods, 70*(2), 252-260. doi:10.1016/j.mimet.2007.04.014

Oliver, J. D. (2005). The viable but nonculturable state in bacteria. *J Microbiol, 43 Spec No*, 93-100.

Oliver, J. D., Dagher, M., & Linden, K. (2005). Induction of Escherichia coli and Salmonella typhimurium into the viable but nonculturable state following chlorination of wastewater. *Journal of Water and Health, 3*(3), 249-257. doi:10.2166/wh.2005.040

Oliver, J. D., Hite, F., McDougald, D., Andon, N. L., & Simpson, L. M. (1995). Entry into, and resuscitation from, the viable but nonculturable state by Vibrio vulnificus in an estuarine environment. *Applied Environmental Microbiology, 61*(7), 2624-2630.

Rajabi, N., Bahnemann, J., Tzeng, T. N., Barradas, O. P., Zeng, A. P., & Muller, J. (2014). Lab-on-a-chip for cell perturbation, lysis, and efficient separation of sub-cellular components in a continuous flow mode. *Sensors and Actuators A: Physical, 215*, 136-143. doi:10.1016/j.sna.2013.12.019

Samiei, E., Tabrizian, M., & Hoorfar, M. (2016). A review of digital microfluidics as portable platforms for lab-on a-chip applications. *Lab on a Chip, 16*(13), 2376-2396.

Schrader, C., Schielke, A., Ellerbroek, L., & Johne, R. (2012). PCR inhibitors–occurrence, properties and removal. *Journal of Applied Microbiology, 113*(5), 1014-1026.

Shafiee, H., Sano, M. B., Henslee, E. A., Caldwell, J. L., & Davalos, R. V. (2010). Selective isolation of live/dead cells using contactless dielectrophoresis (cDEP). *Lab on a Chip, 10*(4), 438-445. doi:10.1039/b920590j

Shehadul Islam, M., Aryasomayajula, A., & Selvaganapathy, P. R. (2017). A review on macroscale and microscale cell lysis methods. *Micromachines, 8*(3), 83.

Simons, R. (1979). Strong electric field effects on proton transfer between membrane-bound amines and water. *Nature, 280*(5725), 824-826.

Suzuki, M. T., Taylor, L. T., & DeLong, E. F. (2000). Quantitative analysis of small-subunit rRNA genes in mixed microbial populations via 5'-nuclease assays. *Applied Environmental Microbiology, 66*(11), 4605-4614.

Tanaka, Y., Moon, S.-H., Nikonenko, V. V., & Xu, T. (2012). Ion-exchange membranes. *International Journal of Chemical Engineering, 2012*.

Thermo Fisher Scientific. (2015). *Sterilin Single-Use Laboratory Plastics*. Retrieved from https://tools.thermofisher.com/content/sfs/brochures/Sterilin-Single-Use-Lab-Plastics-Catalog.pdf

Vera, E. A., & Ruiz, J. R. (2012). *Comparison Between Turbulent and Laminar Bubbly-Flow for Modeling H2/H2O Separation.* Paper presented at the COMSOL Conference, Milan.

Wang, H.-Y., Bhunia, A. K., & Lu, C. (2006). A microfluidic flow-through device for high throughput electrical lysis of bacterial cells based on continuous DC voltage. *Biosensors and Bioelectronics, 22*(5), 582-588.

Wu, X., Huang, X., Zhu, Y., Li, J., & Hoffmann, M. R. (2020). Synthesis and application of superabsorbent polymer microspheres for rapid concentration and quantification of microbial pathogens in ambient water. *Separation and Purification Technology*, 116540.

Xie, X., Wang, S. W., Jiang, S. C., Bahnemann, J., & Hoffmann, M. R. (2016). Sunlight-activated propidium monoazide pretreatment for differentiation of viable and dead bacteria by quantitative real-time polymerase chain reaction. *Environmental Science & Technology Letters, 3*(2), 57-61. doi:10.1021/acs.estlett.5b00348

Xu, L., Brito, I. L., Alm, E. J., & Blainey, P. C. (2016). Virtual microfluidics for digital quantification and single-cell sequencing. *Nature Methods, 13*(9), 759-762. doi:10.1038/nmeth.3955

Yang, Y., Shin, J., Jasper, J. T., & Hoffmann, M. R. (2016). Multilayer heterojunction anodes for saline wastewater treatment: Design strategies and reactive species generation mechanisms. *Environmental Science & Technology, 50*(16), 8780-8787.

Chapter 3

A HYDROGEL BEAD-BASED PLATFORM FOR LINKING SINGLE-CELL PHENOTYPIC ANALYSIS AND DIGITAL MOLECULAR DETECTION

Zhu, Y., Li, J., Lin, X., Huang, X., and Hoffmann, M.R. (2019). A hydrogel beads based platform for single-cell phenotypic analysis and digital molecular detection. *bioRxiv*: 848168. https://doi.org/10.1101/848168 (A revised version is submitted for journal publication.)

3.1 Abstract

Cell heterogeneity such as antibiotic heteroresistance and cancer cell heterogeneity has been increasingly observed. To probe the underlying molecular mechanisms in the dynamically changing heterogeneous cells, high throughput platform is urgently needed to establish single cell genotype-phenotype correlations. Herein, we report on the development of an analytical platform that combines single-cell viability phenotypic analysis with digital molecular detection for bacterial cells. The platform utilizes biocompatible polyethylene glycol hydrogel beads (Gelbeads) produced by a novel disposable droplet generation device. Gelbead-based single cell viability and molecular detection assays were established. Enhanced thermal stability and uncompromised efficiency were achieved in digital polymerase chain reaction (PCR) and digital loop-mediated isothermal amplification. The reagent exchange for *in situ* PCR following viability phenotypic analysis was demonstrated. The combined analyses may address the genotypic differences between cellular subpopulations exhibiting distinct phenotypes. The platform promises new perspectives in mechanism elucidation of environment-evolution interaction, and might be extended to other cell types for medical research.

3.2 Introduction

Microfluidic single cell techniques have enabled observations of rare genotypes or phenotypes within a cell population and thus ubiquitous cell heterogeneity (Buenrostro et al., 2015; Cheow et al., 2016; F. J. Lyu et al., 2018). The phenotypic diversity exhibited by supposedly genetically identical cells boosts the population adaptability under selection pressures, and thus raises concerns in fields spanning from clinical practice to medical research on infectious diseases and cancers, etc. (Ben-David et al., 2018; Claudi et al., 2014) For example, less susceptible pathogenic bacterial subpopulations originally consist 10^{-2} to 10^{-6} of the overall population that can be amplified during antibiotic exposure. The subsequent increase in the resistant subpopulation may eventually lead to the failure of an antibiotic treatment (Andersson et al., 2019). Hypotheses for the underlying molecular mechanisms involving the stochasticity of genetic mutation, gene expression, and protein regulation (Avery, 2006; Ben-David et al., 2018; Nicoloff et al., 2019), however, remain hard to test in dynamically changing cell subpopulations, partly due to the absence of an appropriate single cell experimental technique (Takhaveev & Heinemann, 2018). The need to better understand cell heterogeneity motivates the development of new techniques that link the single-cell viability phenotype with its *in situ* molecular information.

As an emerging class of technologies, water-in-oil droplet-based microfluidic platforms have been well developed for high-throughput phenotypic and molecular analyses at single cell or single molecule resolution (F. Lyu et al., 2018; F. J. Lyu et al., 2018; Ottesen et al., 2006). Nonetheless, due to the rare and transient nature of cell heterogeneity events, population-averaged molecular analyses would most likely fail to directly explain the characterized phenotypes, even if all analyses are conducted at single cell or molecular resolution (Andersson et al., 2019; Marusyk et al., 2012). Meanwhile, incorporating a crosslinked hydrogel network into the aqueous phase theoretically provides a droplet-based platform with additional robustness by allowing reagent exchange (Li et al., 2018). This strategy, therefore, has been explored for a range of hydrogel materials and crosslinking chemistry, including cooling-induced formation of agarose beads for digital droplet

polymerase chain reaction (ddPCR) (Zhu et al., 2012), ionic crosslinking of alginate beads for cell encapsulation and DNA extraction (Tan & Takeuchi, 2007; Zimny et al., 2018), and UV-initiated polyethylene glycol (PEG) beads for cell encapsulation (Young et al., 2012). Such platforms have demonstrated to be effective in either phenotyping or molecular analysis, while the material and/or initiation method would be intrinsically incompatible with the combination of both. For example, temperature manipulation or UV radiation might affect the phenotype and genotype of encapsulated cells (Ikehata & Ono, 2011), and alginate is a well-known PCR inhibitor (Wadowsky et al., 1994). PEG crosslinked by a thiol-Michael addition reaction between the bioinert acrylate and thiol groups has been attempted in bulk analyses and is among the most promising solutions (Huang et al., 2018; Xu et al., 2016), but it is yet to be developed for our specific purpose. The main obstacle may lie in the fast and spontaneous gelation, which would be detrimental to traditional expensive microfluidic droplet generation approaches.

Herein, we report a novel PEG hydrogel bead-based platform for linking single-cell phenotypic analysis and *in situ* molecular detection (**Figure 3.1a-b**). To solve the challenge posed by the fast thiol-Michael addition gelation chemistry, we developed a disposable centrifugal device for droplet generation (**Figure 3.1c**). With generated droplets further spontaneously crosslinked into PEG hydrogel beads (Gelbeads), we established single cell encapsulation and effective viability phenotyping within 4 hours for the tested bacteria. Gelbead-based assays were also developed for nucleic acid amplification detections, including PCR and loop-mediated isothermal amplification (LAMP). Compared to droplet digital PCR and LAMP (ddPCR and ddLAMP), Gelbead-based digital PCR and LAMP (gdPCR and gdLAMP) exhibited enhanced thermal stabilities and uncompromised amplification efficiencies. Phase transfer and reagent infusion for *in situ* PCR following Gelbead-based viability phenotyping were successfully conducted. The Gelbead platform reported here has the potential to extend to study of other types of cells and promises unprecedented capabilities for investigation of cell heterogeneity, and thus will be of broad interest to many fundamental biological research fields.

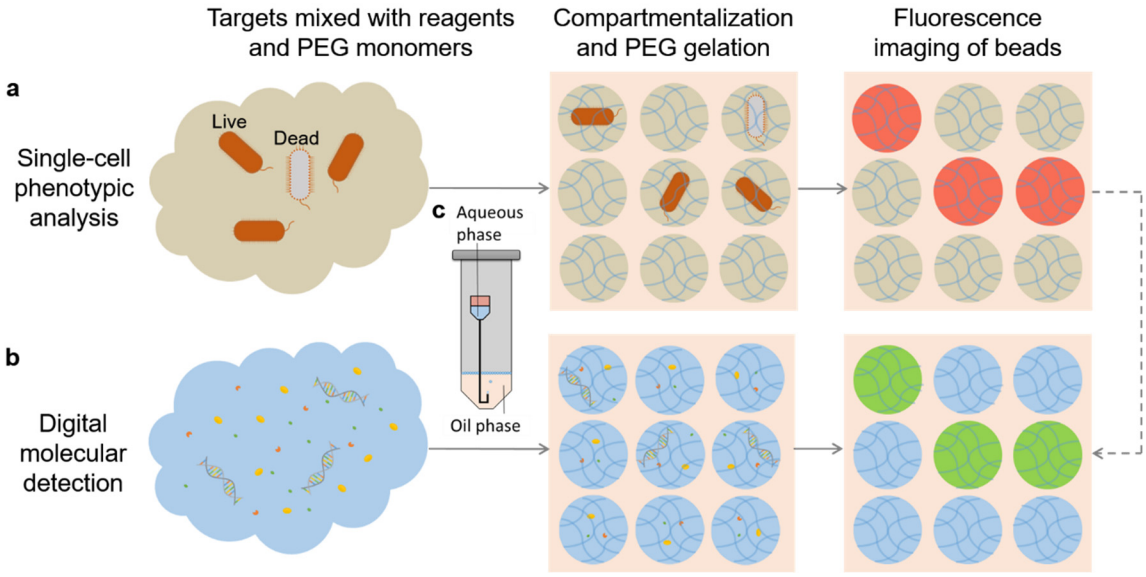

Figure 3.1 Schematic of this study. A hydrogel bead (Gelbeads)-based cell analysis platform was developed for (**a**) single-cell phenotypic analysis and (**b**) digital molecular detection including PCR and LAMP. The compartmentalization was realized by (**c**) a disposable centrifugal droplet generation device. The dashed-line arrow indicates that the immediate potential of linking cell phenotype with *in situ* DNA/RNA characterization at single-cell resolution.

3.3 Results

3.3.1 Development of the disposable droplet generation device

Microfluidic-based droplet generation methods generally require special fabrication facilities to fabricate sub-100 μm channels and involve complicated operations, such as syringe pump-driven T-junctions fabricated by photolithography and centrifugally driven labs-on-a-disc fabricated by micro milling and hot embossing (Schuler et al., 2015; Tan et al., 2006). These traditional methods are not compatible with the Gelbead generation due to fast clogging imposed by the thiol-Michael addition chemistry. The bulk PEG crosslinking experiments showed that the time frame for droplet generation before gelation was as short as 8.5 min with the chosen hydrogel concentration at 7.5 w/v% (**Supplementary Note 3.7.1, Table 3.1**). In order to easily generate Gelbeads within minutes without clogging the expensive microfluidic equipment, we designed a disposable device using affordable commercial components (**Figure 3.2a**). The device utilized a dispensing blunt needle with a bent tip. The bent-tipped needle was then set into a 1.5-mL microcentrifuge tube with oil to establish the physics for centrifugal droplet generation. With centrifugal acceleration, the aqueous phase is forced into the fluorinated oil phase by the elevated pressure difference between the reservoir surface and the narrow inlet. The fluorinated oil phase with a higher density pinches off the aqueous droplets, which then float to the air-oil interface. Ten needles were randomly selected after droplet generation, and the length of the bent tip was measured to be 1.8±0.1 mm, indicating that this manual fabrication could actually be fairly consistent.

Standard 20 μL LAMP mix with unquenched calcein was dispersed in fluorinated oil (see methods) and characterized using a fluorescence microscope to study the droplet generation performance of the device (**Figure 3.2b**). The average droplet size was tunable from 99 μm to 334 μm and the coefficient of variance (CV) was minimized to 5%, by varying the oil phase volume, centrifugal acceleration, and the needle gauge as shown in **Figure 3.2c-f**. Smaller droplets with slightly larger size distribution (**Figure 3.2e**) were produced by increasing the centrifugal acceleration, which provided a greater pressure difference to drive

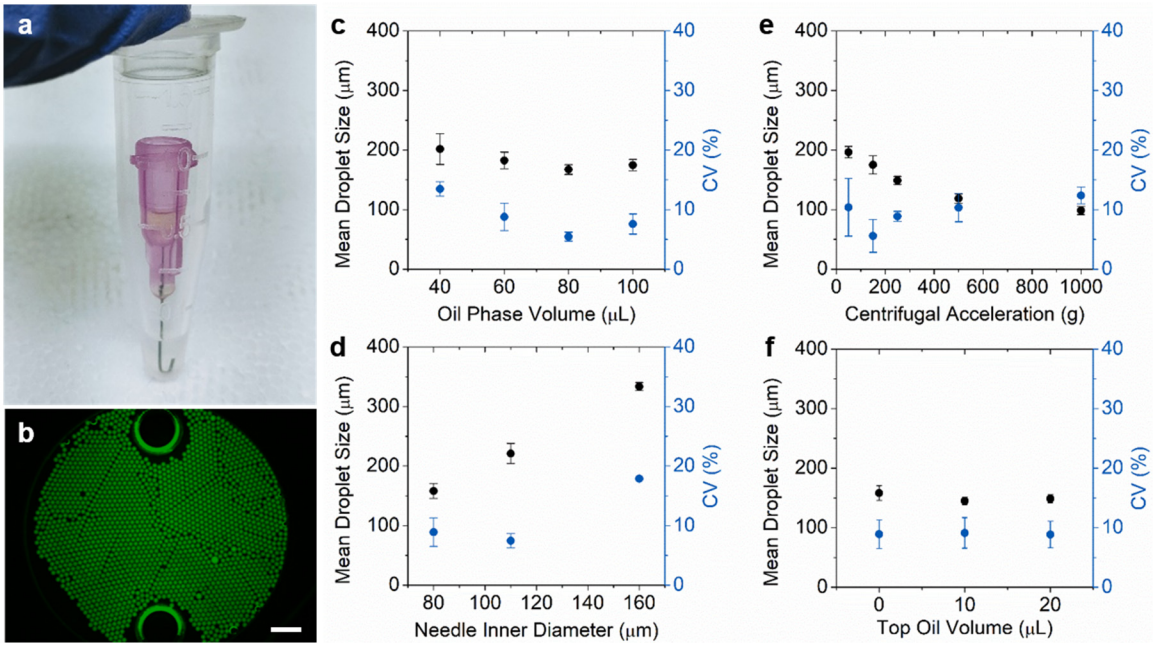

Figure 3.2 Development and evaluation of disposable microfluidics for centrifugal droplet generation. (**a**) The device setup consisting of a 1.5-mL microcentrifuge tube holding the oil phase and a needle with bent tip holding the aqueous reaction mixture in the Luer-lock. (**b**) A representative fluorescence microscope image of generated droplets extracted into a viewing chamber. The two large bright circles are ports on the viewing chamber for liquid loading Scale bar, 1 mm. (**c-f**) Mean droplet size (black circles) and CV (blue circles) of droplets produced under varying parameters including (**c**) oil phase volume, (**d**) needle inner diameter, (**e**) centrifugal acceleration, and (**f**) oil volume added to the Luer-lock. Error bars represent standard deviation from independent triplicates.

the aqueous phase inflow. The larger CV in **Figure 3.2e** was likely due to the unstable flow during initial acceleration, which can be alleviated by adding more oil (**Figure 3.2c**) to reduce the oil phase height variation and limit the amount of aqueous phase inlet during acceleration. Among all tested conditions, the optimal CV was found to be a combination of 34 Ga needles, 80 μL oil phase, and 150 g centrifugation run for 5 min and droplets were produced at an average diameter of 175 μm in 5 min with minor trial-to-trial difference, which was found to be comparable to other microfluidic methods such as centrifugal lab-on-

a-disk (Schuler et al., 2015) and polymer-tube micronozzles (**Supplementary Note 3.7.2**) (Haeberle et al., 2008). The average diameter of 175 μm is a reasonable size for this study, as droplets of 100 to 200 μm diameters are commonly used for cell analysis (Brouzes et al., 2009; Schuler et al., 2015). For droplets with this size, each standard 20 μL reaction could theoretically produce ~10^4 droplets. Based on this calculated compartmentalization, the dynamic range is theoretically from 0.5 to 3×10^3 target copies or cells per μL, and the detection limit is 0.1 copies or cells per μL (Kreutz et al., 2011). It should be noted that the bent needle tip, the viscosity of water phase, and the volume of water phase may also affect the droplet size generated from this device. The application of this device thus may need optimization for new aqueous and oil phase recipes.

3.3.2 Gelbead generation and thermal stability characterization

The Gelbead and droplet generation performance were assessed using various reaction matrices including culture media, PCR mix, and LAMP mix, under the optimized condition reported in the previous section (**Figure 3.3a**). The average diameter of generated Gelbeads was found to range from 145 μm to 217 μm with a CV from 3.6 % to 7.6 %. The observed variations were likely due to viscosity differences and interfacial property changes in different reaction matrices. It should be noted that the culture media alone was not able to be sustained as droplets or Gelbeads in the fluorinated oil by 5% FluoroSurfactant. Bovine serum albumin (BSA), a protein commonly used as an additive to protect essential molecules (fatty acids, amino acids, etc.) in culture media (Francis, 2010), was added to the aqueous phase as an additional surfactant to modify interfacial properties and thus prevent the droplet merging. For the PCR reaction matrix, the generated Gelbeads had a larger CV than droplets. We assume that the presence of PEG hydrogel may have disturbed the surfactant-stabilized aqueous-oil interface, by inducing interfacial adsorption of additional charged species such as thiolate, magnesium ions, etc. In summary, the observed sizes and CVs of droplets and Gelbeads were considered acceptable for our assays. In general, this generation device fulfills the requirements for Gelbead generation. The simple generation device may be used for applications for which a simple yet powerful compartmentalization method is needed.

The effect of PEG crosslinking on stabilizing the aqueous-in-oil compartments was evaluated. Thermodynamic instability of water-in-oil droplets may impair the reliability of amplification processes such as PCR and LAMP that require extensive heating (Schuler et al., 2016). Heating accelerates droplet merging and evaporation, which would affect the fluorescence reading by modifying concentrations of targets and reagents (e.g., salts and fluorescent dyes). In this context, the compartmental heat stability manifests through the dispersion of droplet/Gelbead sizes before and after heating. The sizes were investigated for droplets and Gelbeads before and after common heating protocols respectively for PCR and LAMP (see methods, **Figure 3.3b**). Compared to those before heating, droplets that had undergone PCR and LAMP heating increased in their CVs by 6.2% and 3.5%, respectively.

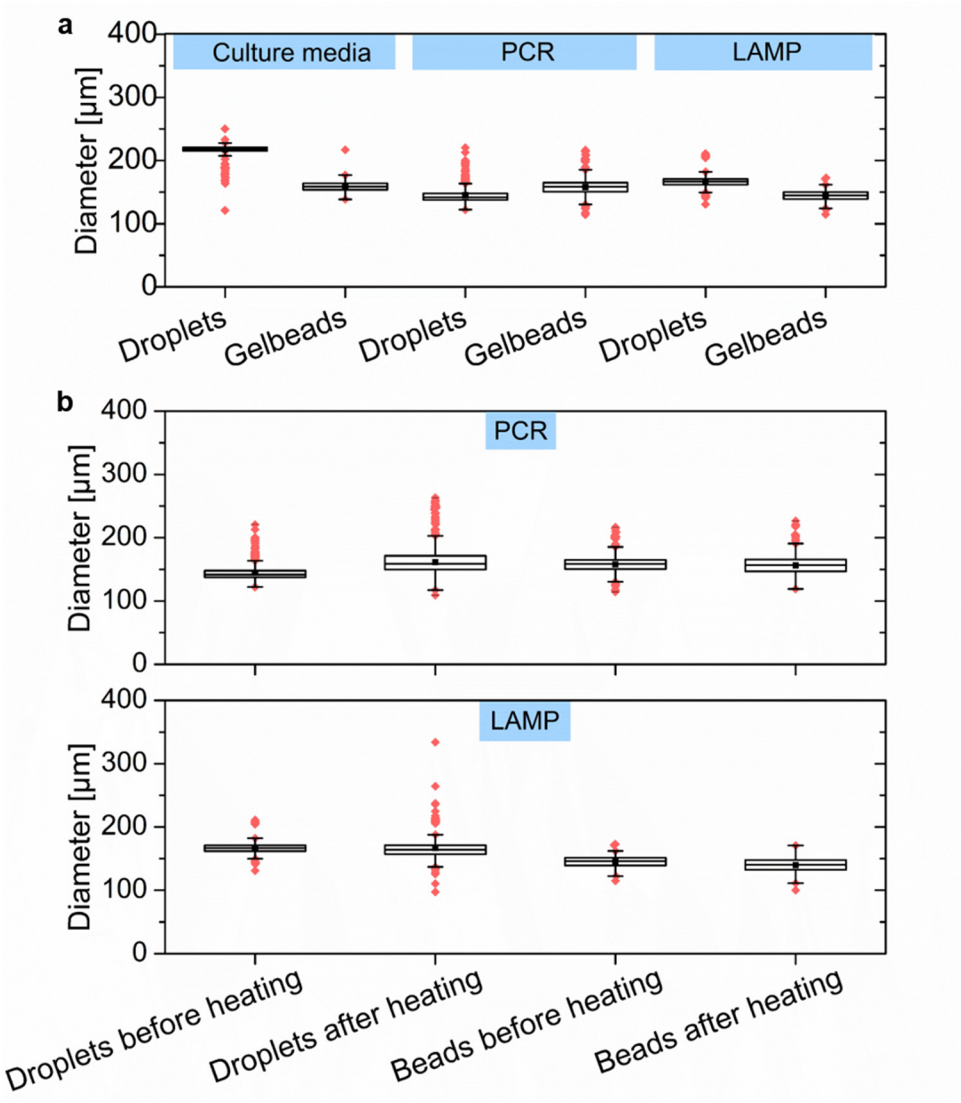

Figure 3.3 Size characterization of droplets and Gelbeads. The size distribution of droplets and Gelbeads (**a**) generated in reaction matrices including PCR mix, LAMP mix, and culture media mix, and (**b**) before and after heating program designated for PCR and LAMP. The line inside each box represents the mean diameter; the lower and upper edges of each box respectively represent 25% and 75% percentiles; the vertical bars below and above each box respectively indicate 90th and 10th percentiles. The lower and upper red dots stand for outliers, which are points located outside the whiskers.

In addition, the heating resulted in a noticeably larger population with both larger and smaller outlier sizes implying that extensive merging and evaporation had occurred. Following the same heating protocol as for the droplets, the Gelbeads exhibited much less of a change in size distribution (CV increased by 1.9% for PCR and 1.6% for LAMP). However, the average Gelbead diameter decreased slightly. These results indicate that the stabilization effect achieved by crosslinked PEG was mainly by preventing merging of compartments, and lessen the extent of aqueous evaporation. The effect of mild aqueous evaporation in Gelbeads can be compensated by optimization of assay recipes. Gelbeads used for the LAMP procedure had a more significant improvement in thermal stability due to PEG crosslinking than for the PCR procedure. We assume that, in the case of the PCR recipe, the combination of SuperMix and the oil phase from BioRad were chemically well-optimized for interfacial stability, leaving limited room for improvement. This result therefore indicates that, other than modifying the surfactant composition or increasing surfactant concentration, hydrogel crosslinking could be an alternative strategy for maintaining the emulsion. Our results demonstrate that Gelbeads are a reliable platform for standalone heated digital analysis in terms of enhanced individual compartment integrity.

3.3.3 Gelbeads for cell viability phenotyping

To obtain the optimal single cell encapsulation efficiency, we first characterized the distribution of cells in Gelbeads using *Salmonella* Typhimurium with green fluorescent protein (*S.* Typhimurium GFP). The cells were diluted to an average of 1 cell per Gelbead for counting the number of cells in each Gelbead (**Figure 3.4b**). At this cell concentration, theoretically, 34% of the compartments were occupied by single cells, which was the maximum following a Poisson distribution, 29% of the compartments encapsulated more than 1 cell, and 37% of the compartments contained no cells. As shown in **Figure 3.4a**, the observed number of encapsulated cells was close to the theoretical distribution. The number of Gelbeads containing high cell numbers was slightly less than predicted, possibly because some cells were located out of focus when imaged in spherical compartments at a high microscope objective. Since high throughput detection of stained cells within spherical compartment droplets or Gelbeads was challenging for fluorescence microscope imaging, we then employed cell metabolism indicator dye in Gelbead viability phenotyping experiments.

Gelbead-based viability phenotyping performance was investigated by co-incubation of alamarBlue and *S.* Typhi in the culture media. As a resazurin-based dye used in bulk phenotyping assays of a wide range of cell lines, alamarBlue can be reduced by actively metabolizing cells into resorufin, whose bright red fluorescence can stain the whole compartment for visualization (Xu et al., 2015). The fluorescence of Gelbeads was monitored during the incubation for up to 4 hrs (**Figure 3.4d-h)**. It was observed that Gelbeads appeared to be much brighter than the droplets were before incubation (**Figure 3.7**); this was possibly due to additional reduction of resazurin by thiol group (Neufeld et al., 2018). We suppose that the interference by thiol groups would not affect the phenotyping results since the monomers were rigorously mixed and evenly distributed into Gelbeads. Gelbeads containing live cells would exhibit even brighter fluorescence in the presence of sufficient AlamarBlue.

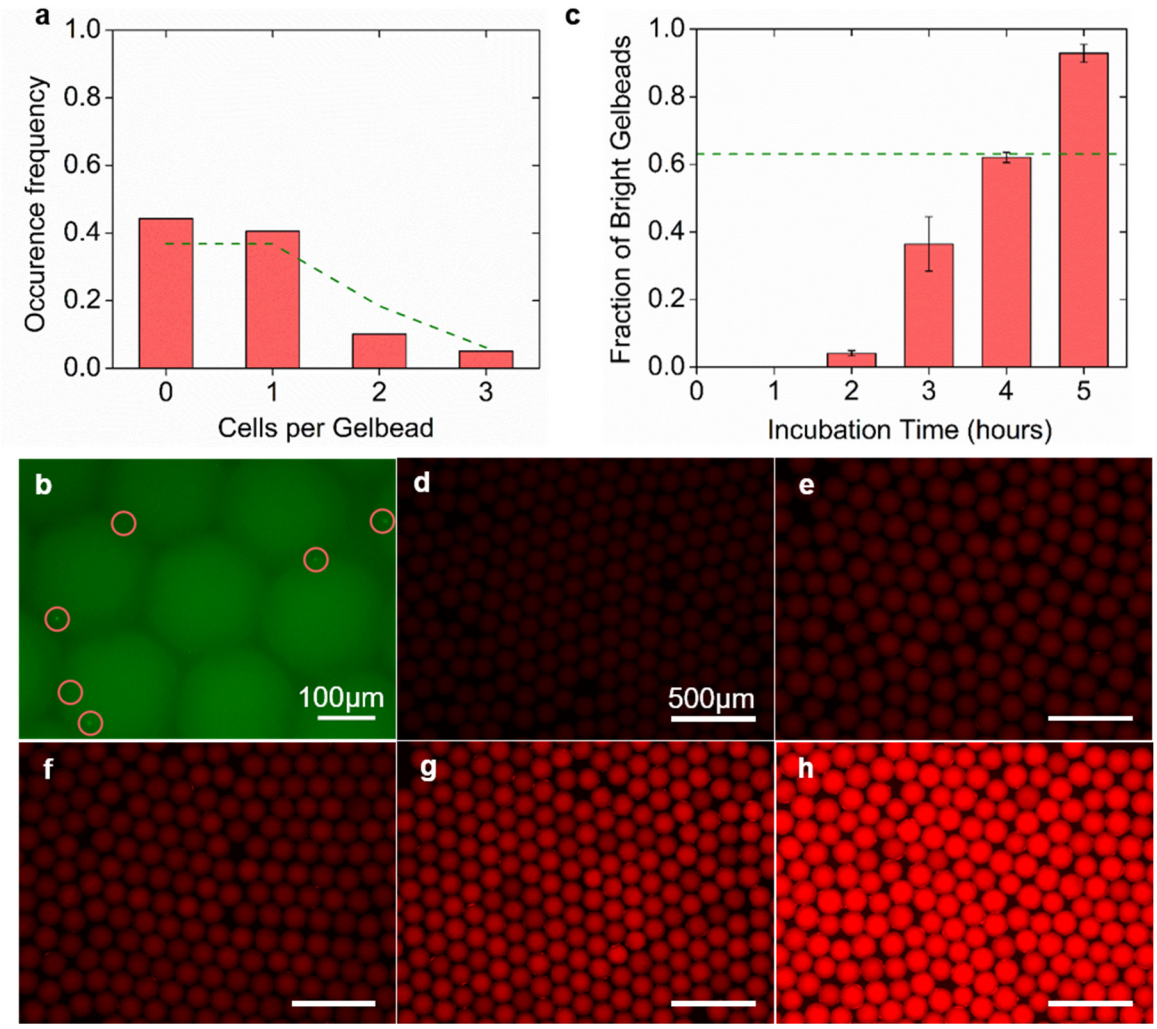

Figure 3.4 Single cell encapsulation validation and viability phenotyping performance in Gelbeads. (**a**) Number of cells encapsulated in each Gelbead counted and represented by occurrence frequency. The dashed lines represent theoretical values based on Poisson distribution. (**b**) Example fluorescence image of encapsulated *S.* Typhimurium GFP cells (circled) for counting. Scale bar, 100 μm. (**c**) The observed fraction of bright Gelbeads with varying incubation time, with the dashed line representing 63% as Poisson distribution predicted based on the input cell concentration. Error bars represent standard deviation from independent triplicates. (**d-h**) Example images of Gelbeads containing *S.* typhi at the same input concentration incubated for 0, 2, 3, 4, 5 hrs. Scale bars, 500 μm.

The quantitative performance of viability phenotyping with Gelbeads was assessed by analysis of observed fractions of bright fluorescent Gelbeads (see methods and **Figure 3.8** for thresholding) compared to the theoretical value, as shown in **Figure 3.4c**. According to theoretical estimation, 63% of Gelbeads were supposed to contain greater than or equal to 1 cell and thus to be bright. The observed positive fraction of 62.0±1.5% after 4 hours of incubation matched well with the theoretical value of 63%. It was also noticed that, after 3 hours of incubation, the positive Gelbead fraction was 36.4±8.1%, which corresponds well with the theoretical fraction of Gelbeads (26%) encapsulating more than 1 cell. Based on the linear response of alamarBlue to the number of cells within the compartment (Shemesh et al., 2014), our results reasonably indicate that effective single cell phenotyping in Gelbeads is achievable within 4 hrs. However, 5 hr incubation lead to overly bright fluorescence and 92.9±2.7% bright Gelbeads, which was likely attributed to excessive incubation and the diffusion of metabolized fluorescent resorufin across the aqueous-oil interfacial barrier. This observation indicates that the optimization of incubation time is a race between cross-talking and cell proliferation. Considering the intrinsic difference in proliferation rate between bacterial species, the observed incubation time for distinction of positive and negative compartments was comparable to the results by Lyu et al., who achieved *Escherichia coli* (*E. coli*) phenotyping with alamarBlue in 85 pL droplets with a 2 hr incubation.

In summary, Gelbeads synthesized in this study could act as a platform for characterizing phenotypic cell heterogeneity if co-encapsulated with antibiotics or drugs. The cell viability detection strategy demonstrated with Gelbeads has been proven to apply well to a wide range of cells in bulk assays and droplet microfluidics (F. J. Lyu et al., 2018; Shemesh et al., 2014; Xu et al., 2015). We note that here the single cell encapsulated Gelbeads were at the highest yield under Poisson distribution so that they theoretically comprised the majority (59%) of the bright Gelbeads in the current set up. The input cell concentration can be diluted to increase the single cell encapsulation among positive Gelbeads to above 99% (Collins et al., 2015), or the single cell encapsulated Gelbeads could

potentially be sorted out through on-chip imaging of the Gelbeads to count the fluorescence labeled cells (Cao et al., 2013).

3.3.4 Gelbead digital PCR (gdPCR)

To establish a reliable gdPCR assay, we investigated the amplification efficiency of gdPCR compared to digital PCR performed in droplets generated from a commercial recipe (represented as ddPCR, hereinafter) with DNA extracted from cultured *Salmonella* Typhi (*S.* Typhi). Previous use of hydrogels and PCR utilized polyacrylamide in the form of either a bulk phase hydrogel membrane as a quasi-digital PCR platform (Mitra & Church, 1999) or using hydrogel beads as a substrate for surface coating of primers (Spencer et al., 2016; Zilionis et al., 2017), which is an approach different from our concept. To the best of our knowledge, performing PCR inside crosslinked hydrogel beads has not been reported to date. Even in bulk membrane form, only 80% amplification efficiency was observed, which may be partially attributed to template damage by free radicals as suggested (Mitra & Church, 1999). In this study, a similar drop in amplification efficiency was observed in the Gelbeads compared to that in droplets (**Figure 3.5a**), even though the Michael addition chemistry between acrylate and thiol used in this study does not involve free radical formation. In this case, the crosslinked hydrogel network may be responsible for the observed inhibition by limiting the diffusion of functional components such as ions, nucleic acids, and proteins, where the extent of the limitation relates to the size and charge of the component (Weber et al., 2009; Wu et al., 2009).

From effective diffusivity modeling (**Figure 3.9**), we reasoned that the most affected functional component might be DNA polymerase, which is the relatively large protein (~6 nm) responsible for building amplicons. For a fixed template concentration of 200 copies/μL estimated by ddPCR, gdPCR assay performance was assessed with additional OneTaq polymerase supplied at varying concentrations of 0.025, 0.05, 0.1, 0.2 Units per reaction, as shown in **Figure 3.5a.** Results showed that an additional 0.025 Unit per reaction, 5% of the recommended OneTaq polymerase concentration per reaction, boosted the amplification

efficiency the most. OneTaq polymerase concentrations supplied more or less than that showed inhibition to amplification efficiency, and gdPCR assay with additional 0.2 Unit per reaction was shown to be completely inhibited. We speculate that the observed trend was mainly due to the commercial SuperMix buffer conditions not optimized for the supplied OneTaq polymerase. While some additional polymerase compensated the reduced diffusivity of the SuperMix polymerase in hydrogel, the excess additional OneTaq polymerase might scavenge the essential ions for the original polymerase from SuperMix leading to amplification failure.

With the optimized additional polymerase, gdPCR assays for serially diluted DNA with concentrations ranging from 2.5 to 600 copies/μL were then performed; typical images are shown in **Figure 3.5c-h** (**Supplementary Note 3.7.3**). The image analysis results demonstrated that the amplification efficiency of gdPCR was comparable ($k = 0.98 \pm 0.02$, $R^2 = 0.9979$) to that of ddPCR with the recipe adjustment (**Figure 3.5b**). The quantification results also correlated well with input DNA concentration (**Figure 3.10a**). It should be noted that the crosslinking inhibition effect eliminated in this case was for a 131 bp target gene (Tran et al., 2010), a typical size for detection of specific bacteria. Further optimization in polymerase or Supermix concentration would be required for other applications if a larger DNA fragment is targeted.

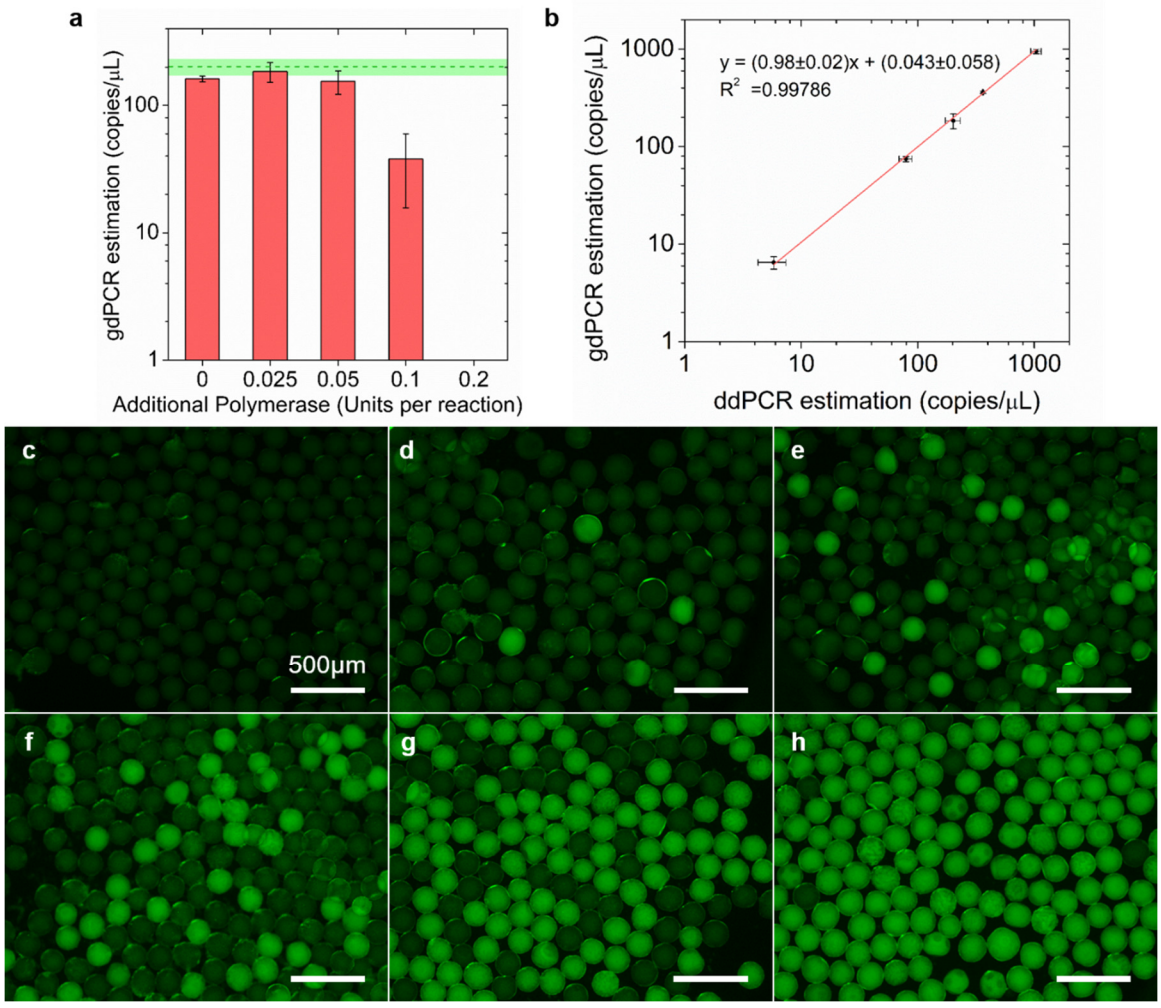

Figure 3.5 Optimization and performance of gdPCR. (**a**) The concentration estimations of gdPCR assays for a fixed input S. Typhi DNA concentration (200 copies/μL) with varying concentrations of additional polymerase. The green dashed line and the green area represent mean concentration estimation with standard deviation of ddPCR assays from independent triplicates. (**b**) With the optimized additional polymerase concentration (0.025 Units per reaction), the correlation between gdPCR and ddPCR estimation for serial diluted target templates. Error bars represent standard deviations from independent triplicates. (**c-h**) Example gdPCR fluorescent images for no DNA input, and with 24000, 1500, 600, 300, 100 times dilution of harvested S. Typhi DNA. Scale bars, 500 μm.

3.3.5 Gelbeads digital LAMP (gdLAMP)

Gelbead-based molecular analysis with LAMP was also investigated. LAMP has been an attractive emerging platform for molecular detection since it eliminates the need for thermocycling by utilizing a combination of 4 or 6 primers to achieve fast and specific detection (Notomi et al., 2000). The heating protocol of LAMP was fairly mild, however, severe Gelbead aggregation occurred for samples with target DNA but not for no-template controls (**Figure 3.11**) in preliminary experiments. This was supposedly due to the fact that LAMP produces a much larger amount of amplification products than PCR (Notomi et al., 2000).The negatively charged amplified DNA may have affected interfacial tension when adsorbed to the interface. Aggregated Gelbeads showed apparent crosstalking, which rendered the assay invalid since the compartment independence assumption required for Poisson statistics was contradicted. The problem was relieved by adding 1.5 mg/mL BSA, a common real-time PCR additive, to prevent surface adsorption. However, it was still observed that positive Gelbeads tended to stick next to each other (**Figure 3.6a)**. The observed radiative patterns in Gelbeads manifested the differential diffusivity of amplification products of varying size in crosslinked hydrogel network. A similar radiative pattern was observed by Huang et al. in LAMP performed in a hydrogel membrane (Huang et al., 2018). In our case, neither of the two radiative centers were at the connected interface, indicating that the stickiness may not have led to false positive Gelbeads within the time frame tested. The connection of positive Gelbeads was most likely the result of a change in interfacial tension caused by large amount of the negatively charged DNA produced during amplification. Further crosslinking breaking through the oil barrier would only occur when the positive Gelbeads encounter each other. In summary, the connected interface should not affect the quantification results.

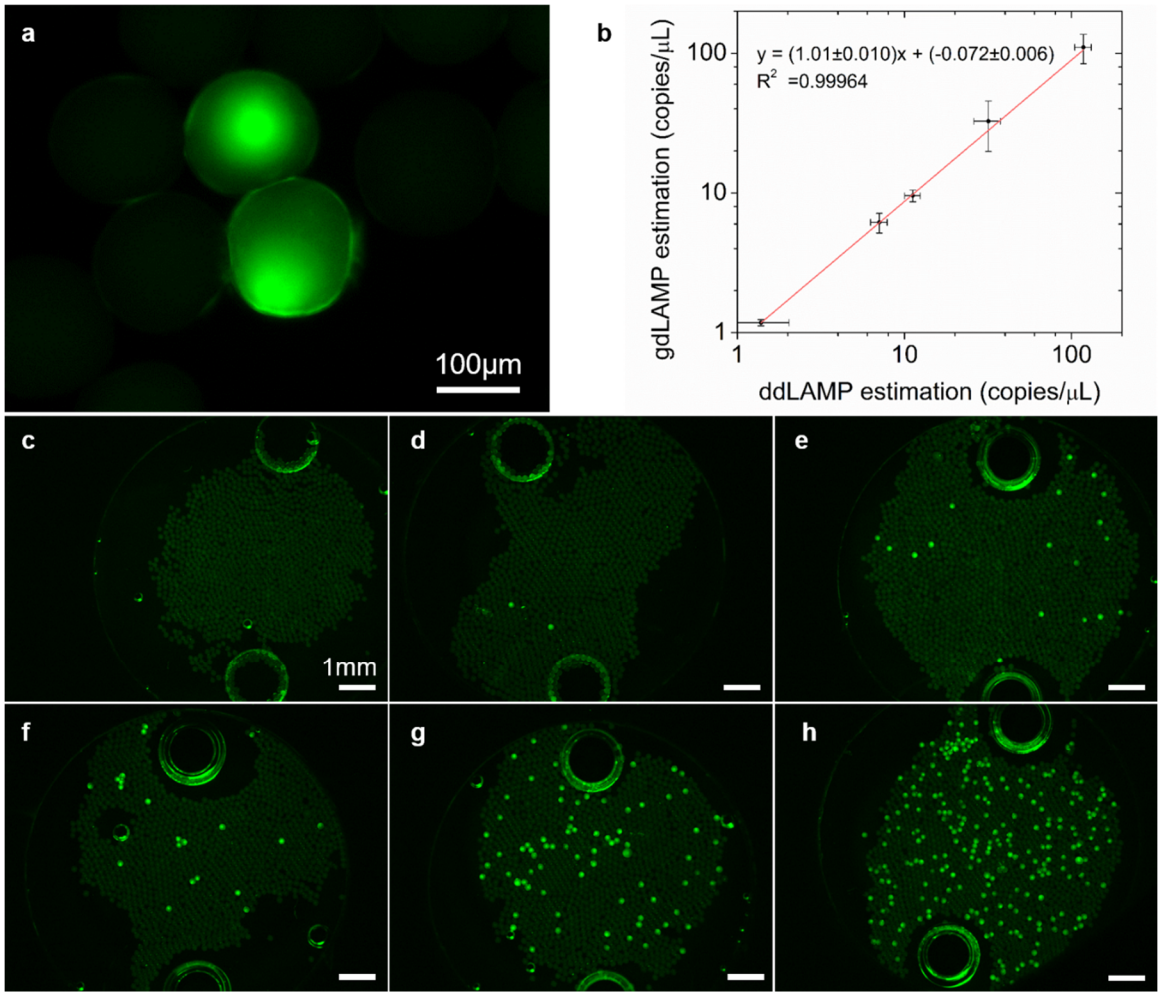

Figure 3.6 Performance of gdLAMP. (**a**) Connection of two positive Gelbeads after the gdLAMP assay. Scale bar, 100 µm. (**b**) The correlation between concentration estimations of gdLAMP and ddLAMP assays for serial diluted target templates. Error bars represent standard deviation from independent triplicates. (**c-h**) Example gdLAMP fluorescent images for no DNA input, and with 200, 100, 50, 20, 5 times dilution of harvested *S.* Typhi DNA. The two large bright circles on each image are ports on the viewing chamber for liquid loading. Scale bars, 1 mm.

The gdLAMP quantifications for no-template control and serial diluted *S.* Typhi DNA ranging from 300 to 1.2×10^4 copies/μL were then verified. Example images are shown in **Figure 3.6c-h**. The image analysis results demonstrated that the amplification efficiency of gdLAMP was similar ($k = 1.01 \pm 0.01$, $R^2 = 0.9996$) to that of ddLAMP (**Figure 3.6b**). However, both ddLAMP and gdLAMP gave concentration estimations lower than input DNA concentration (**Figure 3.10b**). Further increases in the amplification efficiency would likely require an improved primer design, which is out of the scope of this study. In summary, the results confirmed our hypothesis that the stickiness of positive Gelbeads do not considerably affect gdLAMP quantification, and demonstrated that the hydrogel network had a negligible inhibition effect on the digital LAMP assays that were performed.

3.3.6 Reagent exchange for in situ PCR following viability phenotyping

With reagent exchange enabled by the crosslinked network of hydrogel, our Gelbead-based platform has the immediate potential to link phenotyping and *in situ* molecular detection for single cells. Here we develop the reagent exchange protocol to demonstrate the feasibility to combine Gelbead-based *S.* Typhi viability phenotyping and *in situ* PCR for S. Typhi-specific STY0201 gene using assays established in previous sections. The key to linking the analyses lies in the effective phase transfer and reagent infusion. After single cell phenotyping (**Figure 3.12a**), successful phase transfer was conducted (**Figure 3.12b-h**) with little loss of Gelbeads and minimal emulsified aqueous reagent leftover. The challenge posed by the possibly denser interfacial hydrogel network, which might have hindered the inward diffusion of essential PCR macromolecules, was overcome by a freeze-thaw treatment (**Supplementary Note 3.7.4**). Resuspended Gelbeads remained intact after subsequent PCR and allowed for fluorescence analysis (**Figure 3.12i**). The fluorescence intensity profiles for randomly analyzed 5 positive and 5 negative Gelbeads were statistically distinguishable, with 40% significant difference ($p < 0.001$, one-way ANOVA) in mean fluorescence intensity (**Figure 3.13**, **Supplementary Note 3.7.5**). The results suggest that, after phase transfer protocol, the PCR reagents were successfully infused into Gelbeads for target amplification to proceed inside. It is thus feasible to combine single cell phenotype-genotype analysis using

our developed platform. However, to generate new knowledge and deepen our phenotype-genotype understanding such as probing the correlation of an antibiotic-resistant phenotype and the presence or absence of a gene that might be essential to resistance, bead sorting that separates varying phenotypes prior to molecular analysis would be indispensable.

3.4 Discussion

The developed Gelbeads platform promises a robust analysis tool that could potentially link single-cell phenotypic analysis with *in situ* molecular detection. Besides the advantages presented, we acknowledge the following limitations. First, the dynamic range in our study was restricted by the size of the compartments generated by our device. Further reductions in size would result in larger size variations, and the surfactant might have to be changed or adjusted if higher uniformity is required. Second, given the use of fluorescence microscopic imaging of the compartments inside a viewing chamber, the Gelbead imaging approach employed could probe only a limited viewing area, and the resolution could be affected by the focus. The fluorescence characterization may be further improved by interrogating single Gelbead with fluorescence-activated bead sorter or in double emulsion with flow cytometry.

In this work, a disposable centrifugal device was developed for Gelbead generation using highly biocompatible PEG monomers spontaneously crosslinked with no free-radical, UV-induced or heat-induced initiation. Our design allows for easy adoption of droplet microfluidics without expensive and complicated equipment, which could be useful for applications other than Gelbeads generation. In addition to single cell phenotyping, the Gelbeads showed enhanced thermal stability coupled with high amplification efficiency for dPCR and dLAMP. Widely available qPCR and LAMP assays can therefore be easily transferred into digital assays by this Gelbead approach. The unique structural stability of the hydrogel network allows for easy manipulation of the Gelbeads that may have many possibilities for other upstream and downstream analyses. The reagent exchange protocol was developed for *in situ* PCR following Gelbead single cell viability phenotyping to

demonstrate the feasibility of combining multiple analyses with Gelbeads. The Gelbead platform will be further developed for fluorescence-based Gelbead sorting and downstream sequencing, etc. Since the cells are encapsulated into individual compartments, the viability phenotype can be observed independent of intercellular collaboration, which is common for bacterial cells under pressure (Lee et al., 2010; Yurtsev et al., 2016). After the Gelbeads containing cells of similar phenotype are sorted together, the differential genotypic trait may then be directly analyzed *in situ* with high throughput. We envision that the potential of our Gelbeads platform in generating genetic and gene expression data with phenotyped single cells will help narrow the genotype-phenotype knowledge gap, and thus offer exciting new insights in cell heterogeneity studies.

3.5 Materials and methods

3.5.1 PEG crosslinking and characterizations

PEG hydrogel monomers included 4-arm PEG-acrylate [molecular weight (MW) of 10 000, Laysan Bio, Arab, AL, USA] and thiol-PEG-thiol (MW of 3400; Laysan Bio), with acrylate and thiol mixed at a molar ratio of 1:1 for crosslinking. For sol-gel transition time characterization, 7.5 w/v% and 10 w/v% PEG hydrogel were respectively tested in PCR mix, LAMP mix, and culture media mix. PEG monomers were weighed to make 10× monomer solutions for PEG-acrylate and PEG-thiol separately. The weighed monomers were then dissolved either in water (Molecular Biology Grade Water™, Corning, Acton, MA, USA) for PCR and LAMP mix, or in TSB (BD™ Bacto™ Tryptic Soy Broth, Becton Dickinson and Company, Franklin Lakes, NJ, USA) for culture media mix. In addition to 2 μL of each 10× PEG monomer solution, for each 20 μL reaction mix, PCR mix contained 10 μL ddPCR™ Supermix for Probes (BioRad, Hercules, CA, USA) and 6 μL water; LAMP mix contained 10 μL 2×WarmStart® LAMP Mastermix (New England Biolabs, Ipswich, MA, USA) and 6 μL water; culture media mix contained 16 μL TSB. The reaction mix was briefly vortexed. The sol-gel transition was considered to have started when lifting the pipette tip

could draw filaments out of the reaction mix, and the transition was considered to have ended when the reaction mix formed a gelatinous lump.

3.5.2 Development of the disposable droplet generation device

Each droplet generation device consisted of a 1.5 mL DNA LoBind tube (Eppendorf, Hamburg, Germany) and a blunt tip dispensing needle (LAOMA Amazon, Seattle, WA, USA) with the tip bent by a tweezer (VWR, Radnor, PA, USA). The tweezer and the needles were autoclaved (2540EP, Heidolph Brinkmann, Schwabach, Germany) prior to use. The oil phase was added to the bottom of the microcentrifuge tube, and the aqueous reaction mix was added to the Luer-lock of the needle. The device was then centrifuged (Centrifuge 5430R, Eppendorf) for 5 min. For optimization of droplet generation, fluorinated oil (HFE-7500 3M® Novec® Engineering Fluid, 3M, Maplewood, MN, USA) supplied with 5% FluoroSurfactant (RAN Biotechnologies, Beverly, MA, USA) was added into the oil phase. The 20-μL aqueous phase contained 1×WarmStart® LAMP Mastermix and 50 μM calcein (Sigma-Aldrich, St. Louis, MO, USA). Four parameters including oil phase volume, needle inner diameter, centrifugal acceleration and oil volume added to the Luer-lock were investigated. Specific variables in details were as follows: 1) the oil phase volume of 40, 60, 80, and 100 μL, respectively, at the bottom of the tube in 34 Ga needles under 250 g centrifugation; 2) needles of 30, 32, and 34 Ga (corresponding to an inner diameter of around 160, 110, and 80 μm) under the condition of 250 g centrifugation and 80 μL oil phase volume; 3) the centrifugal accelerations of 50, 150, 250, 500, 1000 g with 34 Ga needles and 80 μL oil phase; 4) additional oil phase added into the Luer-lock of 0, 10, and 20 μL in 34 Ga needles under 250 g centrifugation with 80 μL oil phase. Ten needles that generated droplets were randomly selected to measure the length of the bent tip by a ruler.

3.5.3 Gelbead generation and thermal stability characterization

In all the following experiments, the device configuration was fixed with 34 Ga needles, 80 μL oil phase, no additional oil at the Luer-lock, and 150 g centrifugation run for 5 min. The droplet and Gelbead generation using the described device was respectively

characterized with PCR mix, LAMP mix, and culture media mix. In each 20 μL reaction, the PCR mix contained 1× ddPCR™ Supermix and 50 μM calcein; the LAMP mix contained 1×WarmStart® LAMP Mastermix, and 50 μM calcein; the culture media mix was TSB with 1 mg/mL BSA (New England Biolabs®) and 50 μM calcein. The mix was briefly pipette-mixed. The reaction mix for Gelbead generation contained 7.5 w/v% PEG hydrogel, added as 10× PEG monomers. For dispersion of PCR mix as droplets and Gelbeads, Droplet Generation Oil for Probes (BioRad) was used instead of fluorinated oil with 5% FluoroSurfactant.

For thermal stability characterizations, generated droplets or Gelbeads were extracted into PCR tubes (0.2 mL individual PCR tubes, BioRad) and incubated in a thermal cycler (T100, BioRad). The thermocycling protocol for PCR included 10 min of initiation at 95 °C, followed by 40 cycles of denaturation at 94 °C for 30 s, annealing at 52 °C for 60 s, and extension at 65 °C for 30 s. For LAMP heating, droplets or Gelbeads were incubated at 65 °C for 1 hour.

3.5.4 Bacterial cell culture and DNA preparation

Salmonella Typhi (*S.* Typhi, CVD 909), obtained from American Type Culture Collection (ATCC, Manassas, VA, USA), was employed as the model strain. *S.* Typhi was cultivated in TSB supplied with 1 mg/L of 2,3-dihydroxybenzoate (DHB, Sigma-Aldrich) in an incubator (Innova® 42, New Brunswick Scientific, Edison, NJ, USA) shaking at 200 rpm at 35 °C for 14-16 hours. The concentration of cultivated cells was estimated by OD 600 (NanoDrop™ 2000c Spectrophotometer, Thermo Scientific™, Barrington, IL, USA). DNA was harvested using PureLink® Genomic DNA Mini Kits (Fisher Scientific, Waltham, MA, USA) following the manufacturer's instructions. For the single cell encapsulation test, *Salmonella* Typhimurium GFP (ATCC 14028GFP) was cultivated in nutrient broth (Difco™ 23400, Becton Dickinson and Company) supplied with 100 mcg/ml Ampicillin (Sigma-Aldrich) in an incubator shaking at 200 rpm at 37 °C for 14-16 hours. The cell concentration

was estimated by counting under a fluorescence microscope (Leica DMi8, Wetzlar, Germany).

3.5.5 Gelbeads for cell viability phenotyping

For the single cell encapsulation efficiency test, the cultivated *Salmonella* Typhimurium GFP (*S.* Typhimurium GFP) was diluted 600 times for Gelbeads generation. The dilution factor was estimated from prior knowledge of harvested cell concentration and Gelbead volume. The number of cells encapsulated in each Gelbead was analyzed by fluorescence microscope imaging with a 20× objective. 79 Gelbeads were analyzed from 15 fluorescent images. For phenotyping experiments, 1mL of overnight cultured *S.* Typhi was freshly cultivated for 3 hours in 5mL TSB supplied with 1 mg/L of DHB in an incubator shaking at 200 rpm at 35 °C. The cell concentration was verified to be around 0.135 by OD 600. AlamarBlue™ (Invitrogen, Carlsbad, CA, USA) was employed as the cell viability indicator. To address the fluctuation of excitation intensity and emission detection within a microscopic view, calcein was used as a reference dye. Each 20 μL reaction consisted of 1× AlamarBlue, 50 μM calcein, 1 mg/mL BSA, diluted *S.* Typhi cells, and the rest of the volume filled with DHB supplied TSB. 7.5 w/v% PEG hydrogel was added as 10× PEG monomers dissolved in DHB supplied TSB. After Gelbead generation, the Gelbeads were incubated at 37 °C for 0-5 hrs, and were extracted for imaging after 0, 1, 2, 3, 4 hrs of incubation.

3.5.6 Gelbead digital PCR (gdPCR) assay

The thermocycling protocol of gdPCR assay was the same as described in the thermal stability characterization. Each 20 μL reaction consisted of 1× ddPCR Supermix, 900 nM forward primer, 900 nM reverse primer, 250 nM probe, and 2 μL DNA sample or water. Additional 7.5 w/v% PEG hydrogel was added as 10× PEG monomers for gdPCR assays. The primers and probe were ordered from Integrated DNA Technologies (IDT, Coralville, IA, USA), with sequences (**Supplementary Table S1**) designed for specific detection of *S.* Typhi, targeting a region in gene STY0201 for an amplicon size of 131 bp (Tran et al., 2010). For gdPCR optimization, the same DNA template concentration (600 times dilution from

harvested) was added for gdPCR assays and ddPCR control. Optimal concentration of additional polymerase (OneTaq® DNA polymerase, New England Biolabs) was investigated by supplying various concentrations to the described reaction mix incrementally at 0.025, 0.5, 0.1, and 0.2 U/reaction. For quantification assays, harvested DNA sample were serial diluted 100, 300, 600, 1500, and 24000 times for ddPCR and gdPCR. The reactions were prepared on iceblock (Carolina® Chill Block, Burlington, NC, USA) and centrifugation temperature was set at 4 °C. Droplets or Gelbeads were generated in BioRad droplet generation oil, and were then extracted into PCR tubes for thermocycling. No-template controls were examined for each tested condition.

3.5.7 Gelbead digital LAMP (gdLAMP) assay

The reagents for LAMP were acquired from New England BioLabs if not indicated otherwise. Each 20 μL of modified LAMP mix for digital single bacteria LAMP contained 1× isothermal buffer, 6 mM total MgSO4, 1.4 mM dNTP, 640 U/mL Bst 2.0 WarmStart® polymerase, 1.6 μM FIB and BIP, 0.2 μM F3 and B3, 0.8 μM LF and LB, 1.5 mg/mL BSA, 1× LAMP dye (Lin et al., 2019; Lin et al., 2018). For gdLAMP assays, 7.5 w/v% PEG hydrogel was added as 10× PEG monomers. The primers, ordered from IDT with the sequences shown in **Supplementary Table S1**, were targeting a 196 bp region within the *S.* Typhi specific gene STY1607 (Fan et al., 2015). For gdLAMP and ddLAMP assays, harvested DNA was serial diluted 5, 20, 50, 100, and 200 times. The reactions were prepared on iceblock and centrifuged into 5% FluoroSurfactant supplied fluorinated oil at 4 °C. Droplets or Gelbeads were then extracted into PCR tubes for 30 min heating at 65 °C followed by 5 min polymerase deactivation at 80 °C. No-template controls were examined under the same protocol.

3.5.8 Combined phenotyping and gdPCR for antibiotic resistance analysis

S. Typhi cells were cultivated, encapsulated, and phenotyped following the same procedure as described in the section of Gelbeads for cell viability phenotyping. The phenotyped Gelbeads were subject to phase transfer and reagent infusion in preparation for

in situ PCR. The chemical emulsion breaker was prepared by diluting 1H,1H,2H,2H-perfluorooctanol (PFO, Sigma-Aldrich) with HFE 7500 oil to make 20 vol % PFO stock. Excess oil below the Gelbeads was extracted and discarded. After 10 μL PBS was added and briefly vortexed, 40 μL of 20 vol % PFO was added to the top and the tube was mildly vortexed for 10 sec. The mixture was then briefly centrifuged. All the liquids were drained with a pipette sticking to the bottom of the tube. Then 40 μL of water was added to the Gelbeads and the mixture was frozen at -20 °C for approximately 16 hours. After thawing, the volume of the Gelbeads was roughly estimated by comparing the interface level of the total mixture and the pipette-removed water with the interface level of known volume. Concentrated PCR reagent mixture was added to the drained Gelbeads at twice their estimated volume. The concentrated PCR mixture was prepared 1.5 times the final component concentrations, which were similar to the recipe in gdPCR with doubled primers and probe concentration. The aqueous mixture of Gelbeads and PCR reagents was allowed to sit for 60 min. Gelbeads were then washed with oil for 3 times to eliminate remaining free aqueous phase. During each washing cycle, the mixture was pipette-mixed with additional 20 μL BioRad droplet generation oil, and the fluids were pipette-drained. The washed Gelbeads were resuspended in 80 μL of BioRad droplet generation oil for PCR thermocycling. Before imaging, the Gelbeads were washed again with the oil to eliminate possible interference from the remaining aqueous droplets.

3.5.9 Droplets and Gelbeads imaging and analysis

The droplets or Gelbeads to be analyzed were transferred into a viewing chamber made by adhering SecureSeal™ Hybridization Chamber (9 mm DIA × 1.0 mm Depth, Grace Bio-Labs, Bend, OR, USA) to a glass slide (VistaVision® Microscope slides, VWR). The chambers were imaged under the fluorescence microscope using a 1.25× objective for droplets/Gelbeads generation, characterizations, and gdLAMP. For each sample in gdPCR and single cell phenotyping, five images of different area in the viewing chamber were taken using a 5× objective. Fluorescein isothiocyanate (FITC) filter was used, except for phenotyping experiments where Texas Red (TXR) filter was used in addition. In phenotyping

experiments, the image data collected through TXR channel was normalized using the image data collected through FITC channel. For analysis of bright Gelbeads fraction, the data of each pixel was the intensity ratio of TXR channel to FITC channel. All images were analyzed using customized MATLAB scripts (**Supplementary Files**). For droplets and Gelbeads generation as well as thermal stability characterizations, the images were analyzed for individual compartment diameters. The diameters were further analyzed to calculate average compartment diameter and coefficient of variation (CV). For gdPCR, gdLAMP, and phenotyping assays, in addition to size analysis, the images were also analyzed for number of positive and negative compartments by setting a bright-dark threshold. Using the ratio of negative compartments to total compartments, the input DNA or cell concentrations were estimated by Poisson distribution (Pinheiro et al., 2012). For images from phenotyping assays, since the distinction of dark and bright Gelbeads was hard to inspect visually, Gaussian fitting was used to advise the threshold (**Figure 3.8**).

3.6 Acknowledgements

General: We thank Dr. Katharina Urmann for helpful discussions. **Funding:** The authors acknowledge the financial support provided by the Bill and Melinda Gates Foundation (grant nos. OPP1111252 and OPP1192379).

3.7 Supplementary notes

3.7.1 Characterization of PEG hydrogel crosslinking

To identify the reasonable time frame for Gelbead generation, PEG gelation time in our targeted reaction matrices by bulk phase sol-gel transition experiments (see methods) was first measured. Ideally the compartmentalization process should be completed before the sol-gel transition starting, after which further crosslinking would considerably alter fluid properties such as viscosity and surface tension. For the three types of reaction matrix examined, results showed that the sol-gel transition start time spanned from 4.5 min to 43.0 min, and the crosslinking was accelerated by higher pH and higher monomer concentration (**Table 3.1**). Accordingly, the gelation time might be further extended by decreasing the crosslinking temperature (Pritchard et al., 2011). We then estimated if the lower gel concentration considerably affects the hydrogel properties. The theoretical pore sizes for our crosslinked PEG were close for 7.5% and 10% gel (**Table 3.1**). Both would allow diffusion of functional molecules in our applications including water, ions, small DNA fragments, and proteins that size from below an angstrom to ~ 6 nm (Wu et al., 2009). This estimation neglects non-ideality such as dangling ends or monomer self-interlinking, which might result in larger actual pore size (Raeber et al., 2005). Using the same PEG monomers, 10 w/v% hydrogel concentration has been utilized in cell encapsulation, multiple displacement amplification (MDA), and LAMP (Huang et al., 2018; Xu et al., 2016). We reason that lowering the hydrogel concentration to 7.5 w/v% would benefit our applications by allowing more time for Gelbead generation and creating looser hydrogel network for reagent diffusion. Therefore, 7.5 w/v% PEG was used in further experiments.

3.7.2 Droplet generation performance and sources of error

To achieve high throughput analysis of droplets with limited available instruments, we chose to analyze droplets through fluorescence imaging. As in the reported protocol, droplets were extracted into a viewing chamber, made by bonding a commercial plastic chamber onto a glass slide, for fluorescence imaging at 1.25× objective. We acknowledge that this protocol might have introduced systematic error in size characterizations by 1) pipetting droplets from the microcentrifuge tube into the viewing chamber, 2) noise difference from focus point to the edges within an image, and 3) image processing bias by MATLAB when identifying the circular-shaped edges. These sources of error would lead to overestimation of size distribution. Therefore, it is anticipated that the actual CV of the generated droplets or Gelbeads should be lower than reported. Generally, the reported sizes and CVs of generated droplets, optimized at 175 μm diameter with CV of 5%, are comparable to those generated by centrifugal microfluidics reported in literature. For example, Haeberle et al. used polymer-tube micronozzles for alginate bead generation, and reported beads generated at diameters tunable from 180 to 800 μm with CV of 7–16%. As another example, using a lab-on-a-disk centrifugal droplet generation, Schuler et al. reported droplet diameters of 120 to 170 μm with CV of 2–4%. It should be noted that these values represent only 20 measurements of droplet under high microscope objective.

3.7.3 Microscope objective choice

For ddPCR and gdPCR, 5× objective was used in fluorescent microscope imaging to more accurately capture the assay quantification performance. Taqman probe, commonly used in PCR for enhanced detection specificity by hydrolysis upon encounter of specific sequence target, was employed in our PCR assay recipe. In this case, the fluorescence exhibited by negative compartments was too low to be distinguishable from the oil phase under 1.25× objective. To be able to count negative compartments, a zoomed-in view using 5× objective had to be used instead of 1.25× objective, which was employed to image ddLAMP and gdLAMP results. A commercial DNA-intercalating dye was used in LAMP so that the higher background fluorescence was observed in negative compartments. 1.25× objective could image an area of 0.785 cm^2 to include the whole viewing chamber at one image shot. The smaller view at 5× objective was compensated by taking 5 images of different areas in the viewing chamber. A similar strategy was applied in Gelbeads imaging for phenotyping experiments to better distinguish the Gelbeads with varying fluorescence levels.

3.7.4 Overcoming challenges of PCR reagent infusion for Gelbeads

Initial attempts on PCR reagent infusion for phenotyped Gelbeads failed to yield any bright Gelbeads, despite the visually successful Gelbead phase transfer from oil to aqueous phase and then back to the oil phase. Hydrogel network has been reported to possibly form smaller pores on the side of higher interfacial tension (Savina et al., 2011). It was thus suspected that, during Gelbead crosslinking in fluorinated oil, the aqueous-oil interface might have smaller pore sizes. The surface barrier then might have hindered the inward diffusion of essential PCR macromolecules when the Gelbeads were transferred into aqueous phase. To overcome the Gelbead surface barrier, we performed a freeze-thaw treatment on the phenotyped Gelbeads prior to reagent infusion. The overnight freezing of the Gelbeads in water was intended for expanding the pores through ice crystal formation, which has been utilized to fabricate macroporous hydrogel for biomedical applications (Oxley et al., 1993). After adding the freeze-thaw treatment while other protocols remained unchanged, the Gelbead *in situ* PCR showed successful amplification.

It was observed that the contrast between positive and negative Gelbeads was less visually apparent than in direct gdPCR (**Figure 3.5d-h**), likely due to enlarged pore size. In our experiments, the fluorescence intensity difference was distinguishable for positive and negative Gelbeads, but the larger pore size might cause potential problems. For example, the viability phenotyping assay with other fluorescence dyes, such as PrestoBlue, that are more soluble in fluorinated oil thus easier to cross the interfacial barrier might have more crosstalking. It was also observed that, after phase transfers even without freeze-thaw treatment, the diameter of the Gelbead increased approximately from 160 μm to 220 μm. Gelbead swelling during the phase transfer process should not affect the interpretation of downstream PCR results, since the positive or negative reading on a Gelbead only reveals the molecular information of its own encapsulated cells since phenotyping. However, the actual volume of the swollen Gelbeads needs to be cautiously estimated while preparing the concentrated PCR reagent mixture, so that the final component concentrations can be achieved accurately.

3.7.5 In situ PCR results

The fraction of positive Gelbeads was observed to be 43%, which falls below the theoretical value of 63%, the percentage of Gelbeads containing at least one *S.* Typhi cell. Imminent systematic optimization of the recipe is needed to establish the quantitative accuracy of downstream *in situ* molecular analysis.

3.8 Supplementary illustrations

3.8.1 Tables

		LAMP mix	PCR mix	TSB media
pH		8.8	8.3	7.3
7.5 w/v%	Sol-Gel transition time [min]	7.0	11.5	43.0
		8.5	13.5	53.0
	Pore size	27nm		
10 w/v%	Sol-Gel transition time [min]	4.5	8.5	18.0
		5.5	10.0	23.5
	Pore size	25nm		

Table 3.1 PEG hydrogel crosslinking characterization in bulk for LAMP mix, PCR mix, and TSB media. Sol-Gel transition time was experimentally determined (See Methods). The pH values were supplied by the manufacturers. The pore sizes were theoretically estimated for our gel concentration by scaling from experimentally measured mesh sizes, assuming a simplified hydrogel architecture (Raeber et al., 2005).

PCR	
Forward primer	5’ CGCGAAGTCAGAGTCGACATAG 3’
Reverse primer	5’ AAGACCTCAACGCCGATCAC 3’
Probe	5’ FAM AAGACCTCAACGCCGATCAC 3’

LAMP	
FIP	5’ AACTTGCTGCTGAAGAGTTGGACCGAATGACTCGACCATC 3’
BIP	5’ CCTGGGGCCAAATGGCATTATGCACTAAGTAAGGCTGG 3’
F3	5’ GACTTGCCTTTAAAAGATACCA 3’
B3	5’ AGAGTGCGTTTGAACACTT 3’
LF	5’ TCGGATGGCTTCGTTCCT 3’
LB	5’ CAAGGGTTTCAAGACTAAGTGGTTC 3’

Table 3.2 Sequences of primers and probe for PCR and LAMP assays. PCR primers and probes target a region in gene STY0201 specific for *S.* Typhi for an amplicon size of 131 bp (Tran et al., 2010). LAMP primers target a 196 bp region within the *S.* Typhi specific gene STY1607 (Fan et al., 2015). The target regions for PCR and LAMP were both found to occur at one copy per cell, by searching the sequences within the complete genome of *S.* Typhi strain CT18 (Accession no. NC_003198) using Basic Local Alignment Search Tool (BLAST) (Coordinators, 2018).

3.8.2 Figures

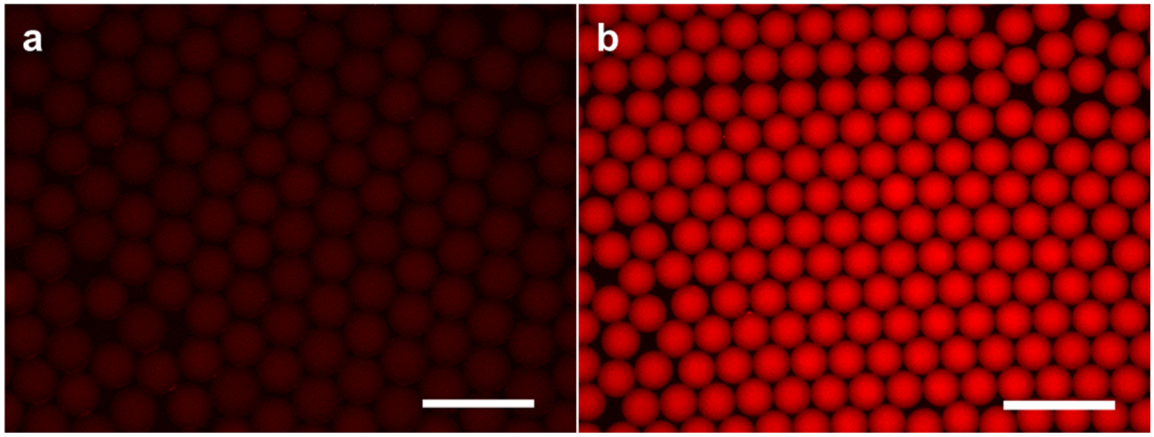

Figure 3.7 Example images of preliminary cell phenotyping experiments. With alamarBlue and media only and without incubation, Gelbeads appeared to be much brighter than (**a**) droplets even though (**b**) Gelbeads were imaged under a lower fluorescence (300 ms exposure for droplets and 25 ms exposure for Gelbeads). Scale bars, 500 μm.

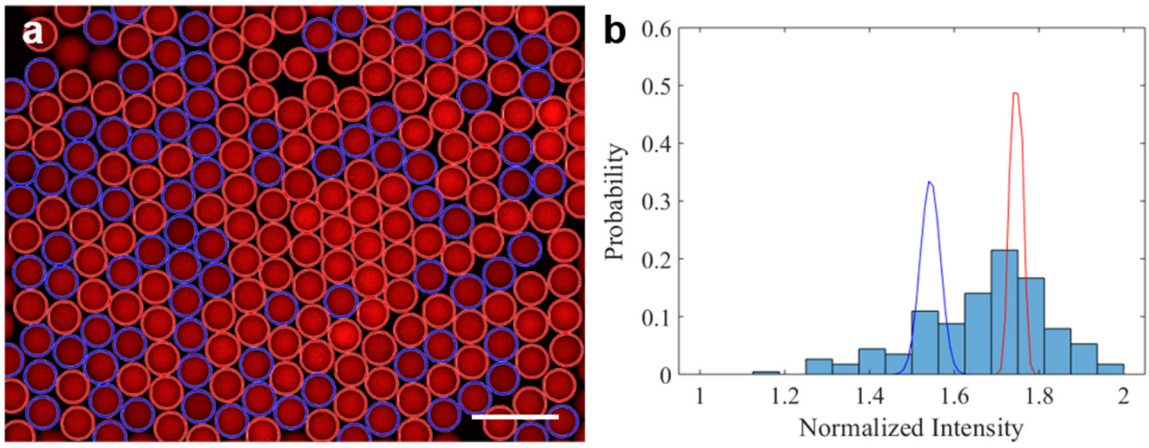

Figure 3.8 MATLAB analysis and threshold setting for images from phenotyping experiments. (**a**) An example image of phenotyping assay analyzed in MATLAB. Scale bar, 500 μm. The blue circles represent identified dark Gelbeads, and the red circles represent identified bright Gelbeads. (**b**) The histogram presents the occurrence probability of mean normalized intensity of Gelbeads analyzed based on the source image of (a). Gaussian fitting of the occurrence probability data generated two peaks, represented by the blue and red curves. The threshold suggested by this MATLAB script was set as the average of the mean (μ) of two peaks. This threshold was used to categorize negative and positive Gelbeads and produced the identification results on the left. We note that for 2 hours and 5 hours of incubation, the differences in normalized intensity of Gelbeads were too small for this thresholding method. In these cases, threshold enumeration and visual inspection were used instead for an approximately appropriate threshold.

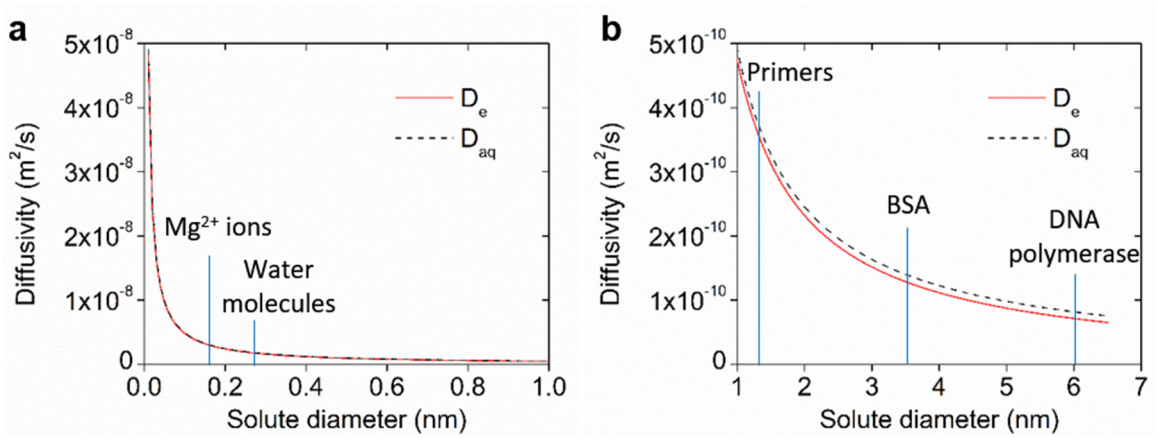

Figure 3.10 Calculated effective diffusivity (D_e) of solute in 7.5 w/v% PEG hydrogel matrix based on Weber et al. (Weber et al., 2009) and diffusivity in aqueous phase (D_{aq}) at 37 °C based on Stokes-Einstein equation as a function of solute hydrodynamic radius (**a**) from 0-1 nm and (**b**) from 1-7 nm. For functional molecules in the molecular assays, approximate sizes reported in or calculated from literature (Wu et al., 2009; Fujimoto et al., 1994) are indicated on the plots.

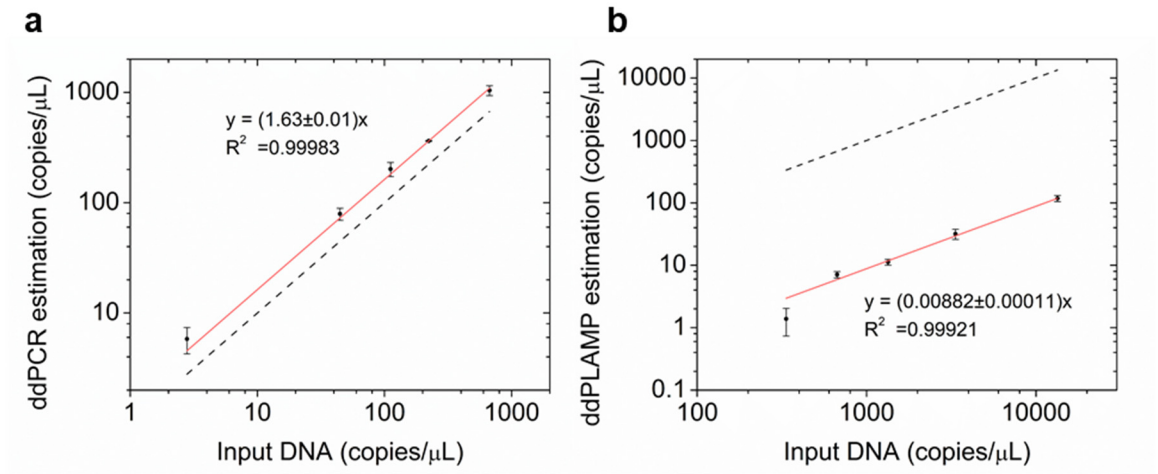

Figure 3.9 Estimated DNA concentration by (**a**) ddPCR for 24000, 1500, 600, 300, 100 times dilution of harvested *S.* Typhi DNA and (**b**) ddLAMP for 200, 100, 50, 20, 5 times dilution of harvested *S.* Typhi DNA compared with input DNA concentration. Input DNA concentration was calculated from dilution factor and OD600 measurement of cultured cells before DNA extraction using commercial kit. The dashed lines reference an exact match with input DNA concentration.

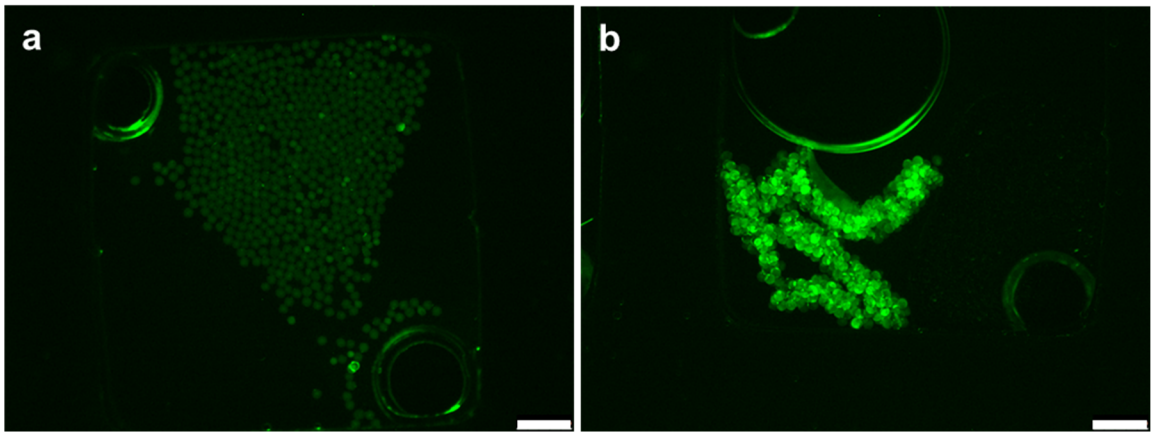

Figure 3.11 Gelbead aggregation was observed exclusively in positive samples during preliminary gdLAMP experiments. Example fluorescent images of Gelbeads with (**a**) no target template and (**b**) 100 times dilution of harvested *S*. Typhi DNA. Scale bars, 1 mm. For preliminary gdLAMP experiments, LAMP MasterMix was used (New England BioLabs) instead of the customizable LAMP recipe specified in Materials and Methods. Each 20 μL of reaction mix contained 1× LAMP MasterMix, 1.6 μM FIB and BIP, 0.2 μM F3 and B3, 0.8 μM LF and LB, 1× LAMP dye. 7.5 w/v% PEG hydrogel was added as 10× PEG monomers. The heating protocol involved 65 °C for 30 min and then 80 °C for 5 min. Aggregation of Gelbeads observed for positive samples, but not for no-template controls. The extent of aggregation indicates occurrence of severe crosstalking.

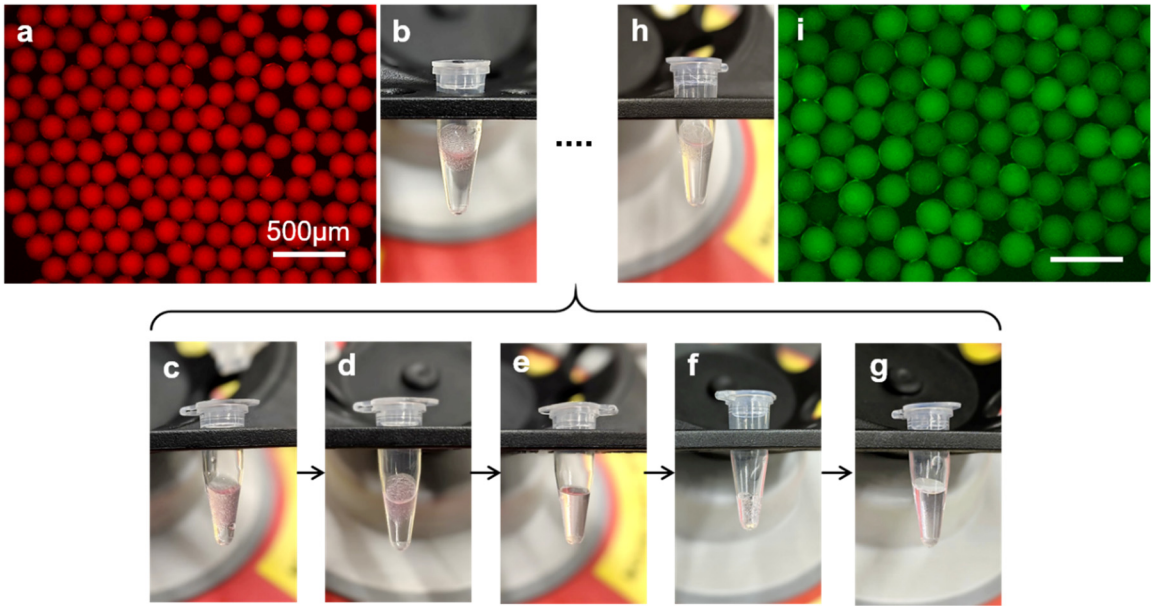

Figure 3.12 Combined phenotyping and *in situ* PCR. (**a**) Example fluorescence image of the Gelbeads after phenotyping. (**b**) The phenotyped Gelbeads were subject to reagent exchange, involving (**c**) breaking the emulsion with PFO, (**d**) facilitating phase separation by centrifugation, (**e**) removing all the liquid and adding water to freeze overnight, (**f**) draining the water with pipette, (**g**) incubating with concentrated PCR reagents, and (**i**) washing the Gelbeads with BioRad oil and resuspending for PCR. (**j**) Example fluorescence image of the Gelbeads that were further analyzed through *in situ* gdPCR. Scale bars, 500 μm.

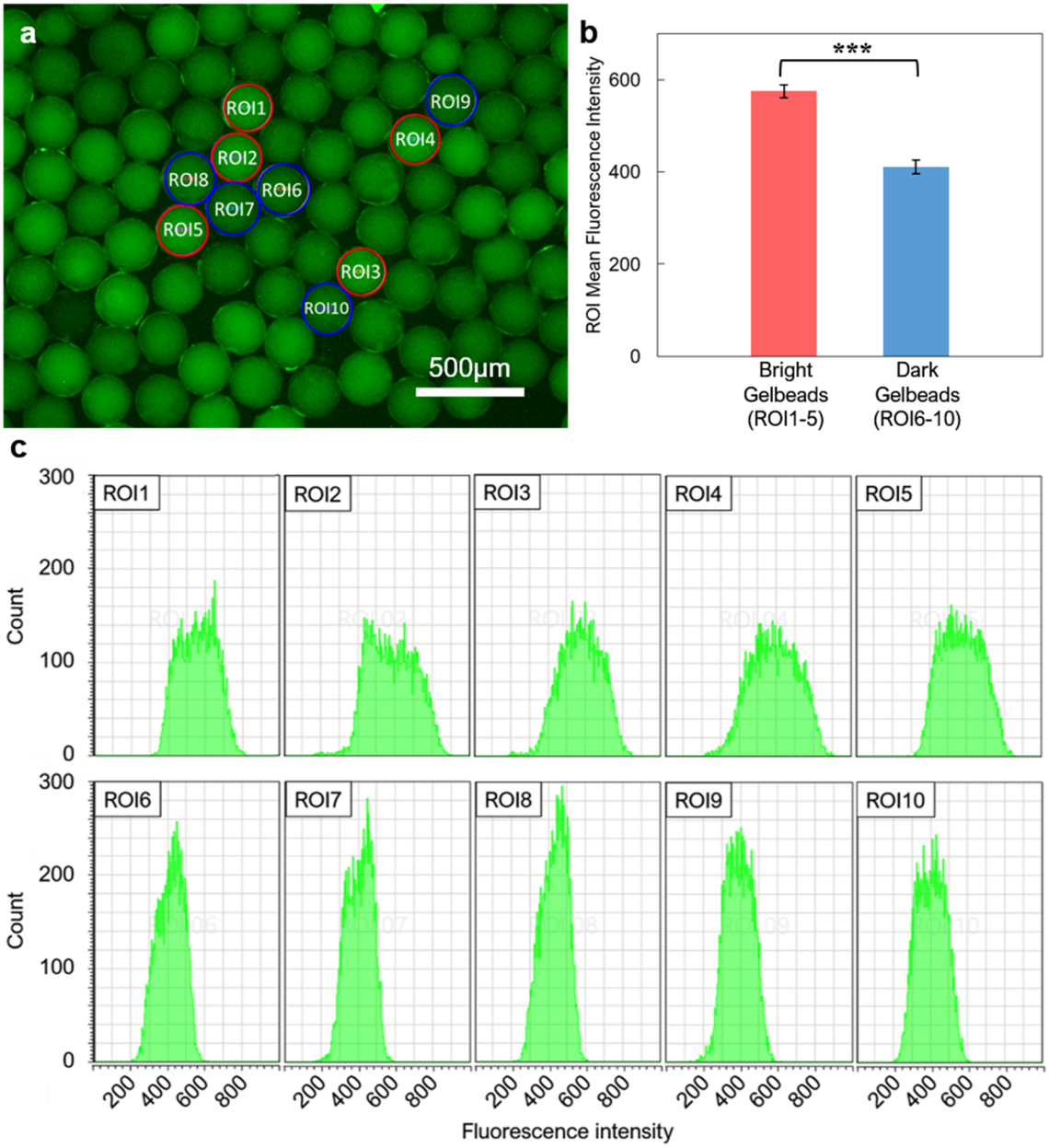

(Captions next page)

Figure 3.13 Fluorescence analysis of Gelbeads after *in situ* PCR. A fluorescence image was analyzed in the software (Leica Application Suite X) accompanied by the fluorescence microscope. (**a**) The fluorescence image with 10 bright and dark Gelbeads circled as region of interest (ROIs) to be analyzed. Bright Gelbeads (ROI1-5) are marked by red circles, and the dark ones (ROI6-10) are marked by blue circles. The ROIs were selected as pairwise neighboring bright and dark Gelbeads to limit the interference of the focus effect. Scale bar, 500 μm. (**b**) The mean fluorescence intensity within the ROIs were significantly different ($p < 0.001$, one-way ANOVA) for the analyzed bright and dark Gelbeads. The averaged mean fluorescence intensity of the bright Gelbeads was 40% higher than the dark ones. Error bars represent standard deviation for the 5 ROIs in each group. (**c**) Histograms of fluorescence intensity counts for the ROIs.

References

Andersson, D. I., Nicoloff, H., & Hjort, K. (2019). Mechanisms and clinical relevance of bacterial heteroresistance. *Nature Reviews Microbiology,* 1. doi:10.1038/s41579-019-0218-1

Avery, S. V. (2006). Microbial cell individuality and the underlying sources of heterogeneity. *Nature Reviews Microbiology, 4*(8), 577-587. doi:10.1038/nrmicro1460

Ben-David, U., Siranosian, B., Ha, G., Tang, H., Oren, Y., Hinohara, K., Strathdee, C. A., Dempster, J., Lyons, N. J., Burns, R., Nag, A., Kugener, G., Cimini, B., Tsvetkov, P., Maruvka, Y. E., O'Rourke, R., Garrity, A., Tubelli, A. A., Bandopadhayay, P., Tsherniak, A., Vazquez, F., Wong, B., Birger, C., Ghandi, M., Thorner, A. R., Bittker, J. A., Meyerson, M., Getz, G., Beroukhim, R., & Golub, T. R. (2018). Genetic and transcriptional evolution alters cancer cell line drug response. *Nature, 560*(7718), 325-330. doi:10.1038/s41586-018-0409-3

Brouzes, E., Medkova, M., Savenelli, N., Marran, D., Twardowski, M., Hutchison, J. B., Rothberg, J. M., Link, D. R., Perrimon, N., & Samuels, M. L. (2009). Droplet microfluidic technology for single-cell high-throughput screening. *Proceedings of the National Academy of Sciences, 106*(34), 14195-14200.

Buenrostro, J. D., Wu, B., Litzenburger, U. M., Ruff, D., Gonzales, M. L., Snyder, M. P., Chang, H. Y., & Greenleaf, W. J. (2015). Single-cell chromatin accessibility reveals principles of regulatory variation. *Nature, 523*(7561), 486-490. doi:10.1038/nature14590

Cao, Z., Chen, F., Bao, N., He, H., Xu, P., Jana, S., Jung, S., Lian, H., & Lu, C. (2013). Droplet sorting based on the number of encapsulated particles using a solenoid valve. *Lab on a Chip, 13*(1), 171-178.

Cheow, L. F., Courtois, E. T., Tan, Y., Viswanathan, R., Xing, Q., Tan, R. Z., Tan, D. S., Robson, P., Loh, Y. H., Quake, S. R., & Burkholder, W. F. (2016). Single-cell multimodal profiling reveals cellular epigenetic heterogeneity. *Nature Methods, 13*(10), 833-836. doi:10.1038/nmeth.3961

Claudi, B., Sprote, P., Chirkova, A., Personnic, N., Zankl, J., Schurmann, N., Schmidt, A., & Bumann, D. (2014). Phenotypic variation of Salmonella in host tissues delays eradication by antimicrobial chemotherapy. *Cell, 158*(4), 722-733. doi:10.1016/j.cell.2014.06.045

Collins, D. J., Neild, A., DeMello, A., Liu, A.-Q., & Ai, Y. (2015). The Poisson distribution and beyond: Methods for microfluidic droplet production and single cell encapsulation. *Lab on a Chip, 15*(17), 3439-3459.

Coordinators, N. R. (2018). Database resources of the National Center for Biotechnology Information. *Nucleic Acids Research, 46*(D1), D8-D13. doi:10.1093/nar/gkx1095

Fan, F. X., Yan, M. Y., Du, P. C., Chen, C., & Kan, B. (2015). Rapid and sensitive *Salmonella* Typhi detection in blood and fecal samples using reverse transcription loop-mediated isothermal amplification. *Foodborne Pathogens and Disease, 12*(9), 778-786. doi:10.1089/fpd.2015.1950

Francis, G. L. (2010). Albumin and mammalian cell culture: Implications for biotechnology applications. *Cytotechnology, 62*(1), 1-16. doi:10.1007/s10616-010-9263-3

Haeberle, S., Naegele, L., Burger, R., Von Stetten, F., Zengerle, R., & Ducree, J. (2008). Alginate bead fabrication and encapsulation of living cells under centrifugally induced artificial gravity conditions. *Journal of Microencapsulation, 25*(4), 267-274. doi:10.1080/02652040801954333

Huang, X., Lin, X., Urmann, K., Li, L., Xie, X., Jiang, S., & Hoffmann, M. R. (2018). Smartphone-based in-gel loop-mediated isothermal amplification (gLAMP) system enables rapid coliphage MS2 quantification in environmental waters. *Environmental Science & Technology, 52*(11), 6399-6407. doi:10.1021/acs.est.8b00241

Ikehata, H., & Ono, T. (2011). The mechanisms of UV mutagenesis. *Journal of Radiation Research, 52*(2), 115-125. doi:10.1269/jrr.10175

Kreutz, J. E., Munson, T., Huynh, T., Shen, F., Du, W., & Ismagilov, R. F. (2011). Theoretical design and analysis of multivolume digital assays with wide dynamic range validated experimentally with microfluidic digital PCR. *Analytical Chemistry, 83*(21), 8158-8168. doi:10.1021/ac201658s

Lee, H. H., Molla, M. N., Cantor, C. R., & Collins, J. J. (2010). Bacterial charity work leads to population-wide resistance. *Nature, 467*(7311), 82-85.

Li, M., van Zee, M., Riche, C. T., Tofig, B., Gallaher, S. D., Merchant, S. S., Damoiseaux, R., Goda, K., & Di Carlo, D. (2018). A gelatin microdroplet platform for high-throughput sorting of hyperproducing single-cell-derived microalgal clones. *Small, 14*(44), e1803315. doi:10.1002/smll.201803315

Lin, X., Huang, X., Urmann, K., Xie, X., & Hoffmann, M. R. (2019). Digital loop-mediated isothermal amplification on a commercial membrane. *ACS Sensors, 4*(1), 242-249. doi:10.1021/acssensors.8b01419

Lin, X., Huang, X., Zhu, Y., Urmann, K., Xie, X., & Hoffmann, M. R. (2018). Asymmetric membrane for digital detection of single bacteria in milliliters of complex water samples. *ACS Nano, 12*(10), 10281-10290. doi:10.1021/acsnano.8b05384

Lyu, F., Blauch, L. R., & Tang, S. K. (2018). Quantifying phenotypes in single cells using droplet microfluidics. *Methods in Cell Biology* (Vol. 148, pp. 133-159): Elsevier.

Lyu, F. J., Pan, M., Patil, S., Wang, J. H., Matin, A. C., Andrews, J. R., & Tang, S. K. Y. (2018). Phenotyping antibiotic resistance with single-cell resolution for the detection of heteroresistance. *Sensors and Actuators B-Chemical, 270*, 396-404. doi:10.10196/j.snb.2018.05.047

Marusyk, A., Almendro, V., & Polyak, K. (2012). Intra-tumour heterogeneity: A looking glass for cancer? *Nature Reviews Cancer, 12*(5), 323-334. doi:10.1038/nrc3261

Mitra, R. D., & Church, G. M. (1999). In situ localized amplification and contact replication of many individual DNA molecules. *Nucleic Acids Research, 27*(24). doi:ARTN e34 10.1093/nar/27.24.e34

Neufeld, B. H., Tapia, J. B., Lutzke, A., & Reynolds, M. M. (2018). Small molecule interferences in resazurin and MTT-based metabolic assays in the absence of cells. *Analytical Chemistry, 90*(11), 6867-6876. doi:10.1021/acs.analchem.8b01043

Nicoloff, H., Hjort, K., Levin, B. R., & Andersson, D. I. (2019). The high prevalence of antibiotic heteroresistance in pathogenic bacteria is mainly caused by gene amplification. *Nature Microbiology, 4*(3), 504-514. doi:10.1038/s41564-018-0342-0

Notomi, T., Okayama, H., Masubuchi, H., Yonekawa, T., Watanabe, K., Amino, N., & Hase, T. (2000). Loop-mediated isothermal amplification of DNA. *Nucleic Acids Research, 28*(12), E63. doi:10.1093/nar/28.12.e63

Ottesen, E. A., Hong, J. W., Quake, S. R., & Leadbetter, J. R. (2006). Microfluidic digital PCR enables multigene analysis of individual environmental bacteria. *Science, 314*(5804), 1464-1467. doi:10.1126/science.1131370

Oxley, H., Corkhill, P., Fitton, J., & Tighe, B. (1993). Macroporous hydrogels for biomedical applications: Methodology and morphology. *Biomaterials, 14*(14), 1064-1072.

Pinheiro, L. B., Coleman, V. A., Hindson, C. M., Herrmann, J., Hindson, B. J., Bhat, S., & Emslie, K. R. (2012). Evaluation of a droplet digital polymerase chain reaction format for DNA copy number quantification. *Analytical Chemistry, 84*(2), 1003-1011. doi:10.1021/ac202578x

Pritchard, C. D., O'Shea, T. M., Siegwart, D. J., Calo, E., Anderson, D. G., Reynolds, F. M., Thomas, J. A., Slotkin, J. R., Woodard, E. J., & Langer, R. (2011). An injectable thiol-acrylate poly(ethylene glycol) hydrogel for sustained release of methylprednisolone sodium succinate. *Biomaterials, 32*(2), 587-597. doi:10.1016/j.biomaterials.2010.08.106

Raeber, G. P., Lutolf, M. P., & Hubbell, J. A. (2005). Molecularly engineered PEG hydrogels: A novel model system for proteolytically mediated cell migration. *Biophysical Journal, 89*(2), 1374-1388. doi:10.1529/biophysj.104.050682

Savina, I. N., Gun'Ko, V. M., Turov, V. V., Dainiak, M., Phillips, G. J., Galaev, I. Y., & Mikhalovsky, S. V. (2011). Porous structure and water state in cross-linked polymer and protein cryo-hydrogels. *Soft Matter, 7*(9), 4276-4283.

Schuler, F., Schwemmer, F., Trotter, M., Wadle, S., Zengerle, R., von Stetten, F., & Paust, N. (2015). Centrifugal step emulsification applied for absolute quantification of

nucleic acids by digital droplet RPA. *Lab on a Chip, 15*(13), 2759-2766. doi:10.1039/c5lc00291e

Schuler, F., Trotter, M., Geltman, M., Schwemmer, F., Wadle, S., Domínguez-Garrido, E., López, M., Cervera-Acedo, C., Santibáñez, P., & von Stetten, F. (2016). Digital droplet PCR on disk. *Lab on a Chip, 16*(1), 208-216.

Shemesh, J., Ben Arye, T., Avesar, J., Kang, J. H., Fine, A., Super, M., Meller, A., Ingber, D. E., & Levenberg, S. (2014). Stationary nanoliter droplet array with a substrate of choice for single adherent/nonadherent cell incubation and analysis. *Proceedings of the National Academy of Sciences of the United States of America, 111*(31), 11293-11298. doi:10.1073/pnas.1404472111

Spencer, S. J., Tamminen, M. V., Preheim, S. P., Guo, M. T., Briggs, A. W., Brito, I. L., Weitz, D. A., Pitkanen, L. K., Vigneault, F., Virta, M. P. J., & Alm, E. J. (2016). Massively parallel sequencing of single cells by epicPCR links functional genes with phylogenetic markers. *ISME Journal, 10*(2), 427-436. doi:10.1038/ismej.2015.124

Takhaveev, V., & Heinemann, M. (2018). Metabolic heterogeneity in clonal microbial populations. *Current Opinion in Microbiology, 45*, 30-38. doi:10.1016/j.mib.2018.02.004

Tan, W. H., & Takeuchi, S. (2007). Monodisperse alginate hydrogel microbeads for cell encapsulation. *Advanced Materials, 19*(18), 2696-+. doi:10.1002/adma.200700433

Tan, Y. C., Cristini, V., & Lee, A. P. (2006). Monodispersed microfluidic droplet generation by shear focusing microfluidic device. *Sensors and Actuators B-Chemical, 114*(1), 350-356. doi:10.1016/j.snb.2005.06.008

Tran, V. T. N., Karkey, A., Dongol, S., Hang, N. T., Dunstan, S., Holt, K., Le, T. P. T., Campbell, J. I., Tran, T. C., Nguyen, V. V. C., Arjyal, A., Koirala, S., Basnyat, B., Dolecek, C., Farrar, J., & Baker, S. (2010). The sensitivity of real-time PCR amplification targeting invasive Salmonella serovars in biological specimens. *BMC Infectious Diseases, 10*. doi:10.1186/1471-2334-10-125

Wadowsky, R. M., Laus, S., Libert, T., States, S. J., & Ehrlich, G. D. (1994). Inhibition of PCR-based assay for Bordetella pertussis by using calcium alginate fiber and aluminum shaft components of a nasopharyngeal swab. *Journal of Clinical Microbiology, 32*(4), 1054-1057.

Weber, L. M., Lopez, C. G., & Anseth, K. S. (2009). Effects of PEG hydrogel crosslinking density on protein diffusion and encapsulated islet survival and function. *Journal of Biomedical Materials Research Part A, 90a*(3), 720-729. doi:10.1002/jbm.a.32134

Wu, Y. B., Joseph, S., & Aluru, N. R. (2009). Effect of Cross-Linking on the Diffusion of Water, Ions, and Small Molecules in Hydrogels. *Journal of Physical Chemistry B, 113*(11), 3512-3520. doi:10.1021/jp808145x

Xu, L., Brito, I. L., Alm, E. J., & Blainey, P. C. (2016). Virtual microfluidics for digital quantification and single-cell sequencing. *Nature Methods, 13*(9), 759-762. doi:10.1038/nmeth.3955

Xu, M. L., McCanna, D. J., & Sivak, J. G. (2015). Use of the viability reagent PrestoBlue in comparison with alamarBlue and MTT to assess the viability of human corneal epithelial cells. *Journal of Pharmacological and Toxicological Methods, 71*, 1-7. doi:10.1016/j.vascn.2014.11.003

Young, C. J., Poole-Warren, L. A., & Martens, P. J. (2012). Combining submerged electrospray and UV photopolymerization for production of synthetic hydrogel microspheres for cell encapsulation. *Biotechnology and Bioengineering, 109*(6), 1561-1570. doi:10.1002/bit.24430

Yurtsev, E. A., Conwill, A., & Gore, J. (2016). Oscillatory dynamics in a bacterial cross-protection mutualism. *Proceedings of the National Academy of Sciences of the United States of America, 113*(22), 6236-6241.

Zhu, Z., Zhang, W. H., Leng, X. F., Zhang, M. X., Guan, Z. C., Lu, J. Q., & Yang, C. J. (2012). Highly sensitive and quantitative detection of rare pathogens through agarose droplet microfluidic emulsion PCR at the single-cell level. *Lab on a Chip, 12*(20), 3907-3913. doi:10.1039/c2lc40461c

Zilionis, R., Nainys, J., Veres, A., Savova, V., Zemmour, D., Klein, A. M., & Mazutis, L. (2017). Single-cell barcoding and sequencing using droplet microfluidics. *Nature Protocols, 12*(1). doi:10.1038/nprot.2016.154

Zimny, P., Juncker, D., & Reisner, W. (2018). Hydrogel droplet single-cell processing: DNA purification, handling, release, and on-chip linearization. *Biomicrofluidics, 12*(2). doi:Artn 02410710.1063/1.5020571

C h a p t e r 4

SORTING HYDROGEL BEADS WITH A GRAVITY DRIVEN FLUORESCENCE ACTIVATED ACOUSTIC ACTUATED BEAD SORTING

This chapter is in preparation for publication.

4.1 Abstract

Hydrogel beads, which combine water-in-oil droplets and structurally stabilizing hydrogel materials, have been developed for encapsulation and analysis of various cells and molecules. However, a portable, affordable, and easy-to-operate system is not yet available to decentralize fluorescence-activated sorting of beads in oil. Herein, we developed a versatile fluorescence-activated bead sorter with minimal instrumentation (MiniFABS) that uses gravity as the fluid driving force and acoustic actuation for high-throughput bead manipulation. We demonstrate via numerical simulation that simply using gravity as a driving force allows for predictable particle spacing. Furthermore, application of acoustic pressure forces the beads into a separate collection chamber within the spacing defined by gravity. With the fabricated MiniFABS prototype, we will perform extensive characterization and optimization of its sorting performance. The sorting accuracy and throughput will be experimentally optimized and characterized. The effect of the piezoelectric voltage on potential targets, including cells, nucleic acids, and proteins, will also be tested.

4.2 Introduction

Hydrogel microfluidics, which is the combination of hydrogel material and water-in-oil droplet microfluidics, have been widely developed for cell encapsulation, single cell analysis, and single molecule analysis (Li et al., 2018; Zhu et al., 2019; Zhu & Yang, 2017). To investigate the cells or molecules encapsulated in the hydrogel beads, fluorescent dyes and probes are usually employed as indicators of interested characteristics, such as high cell metabolism (Zhu et al., 2019) or proliferation rate (Li et al., 2018) and secretion of proteins (Chokkalingam et al., 2013; Hsu et al., 2018). The reagent exchange capacity of the crosslinked hydrogel network promises *in situ* downstream analysis (Zhu et al., 2019). Therefore, the capability of selecting sub-populations of beads from the carrying oil based on their fluorescence intensity could provide more robust hydrogel microfluidic tools for use in mechanistic studies, drug screening, diagnostics, etc. (Le Goff et al., 2015; Zhu et al., 2019; Zimny et al., 2018).

Fluorescence-activated cell sorting (FACS) is a commercially available standard technique for fluorescent particle separation (Naeem et al., 2017; Tang et al., 2019). However, FACS is generally incompatible with an oil phase, making it unsuitable for our targeted application, since the oil phase is responsible for holding the fluorescent dyes within each bead. In addition, FACS primarily handles particle diameters below 50 μm (Yang et al., 2018), while hydrogel microfluidics may often deal with compartments of larger diameters above 100 μm. A few commercial FACS systems handle larger particles, but the high capital costs (>$250,000), high maintenance cost, and intricate operation limit their application into centralized facilities with highly trained personnel (Aubry et al., 2015; Li et al., 2018). Miniaturization of FACS onto microfluidic chips (μFACS) has shown successes on high-throughput, low cost, and convenient separation of cells as well as droplets (Lee et al., 2017; Xi et al., 2017). Although such devices theoretically could be adapted for bead sorting, the distinctive structural stability of hydrogel beads may allow further advance in the miniaturized sorting.

Other than an apparatus for fluorescence excitation and detection, a fluorescence-based particle sorting system needs to be powered in order to exert a driving force, an actuating force for fluid control, and particle manipulation, respectively. Hydrodynamic fluid control by syringe pumps, most commonly used in traditional μFACS, focuses the sample flow with 1-2 continuous phase inflow to achieve an accurate known velocity of particles and spacing in between. Researchers have been pushing for more convenience by utilizing passive fluid control with capillary force (Cho et al., 2003; Tirapu-Azpiroz et al., 2017), gravity (Huh et al., 2007; Yao et al., 2004), and vacuum (Xu et al., 2015). Among the strategies above, gravity as a driving force has the advantage of requiring no power input, but can process less than 100 cells per min (Yao et al., 2004). In our case, the larger density difference in a bead-in-oil system than in a cell-buffer system promises higher throughput. For the particle manipulation, no-contact actuation strategies using magnetic force (Yang et al., 2016), electrophoretic force (Fiedler et al., 1998), optical tweezer (Landenberger et al., 2012), surface acoustic wave (Jakobsson et al., 2014), and acoustophoretic force (Yang & Soh, 2012) have been explored. Recently, Bachman et al. has demonstrated cell manipulation in an open well using low frequency flexural wave generated by cheap commercial buzzers (Bachman et al., 2020). This acoustic actuation technique represents a simple, low-cost, portable option for hydrogel bead sorting.

Herein, we present a novel combination of gravitational driving force and acoustic actuation for high-throughput fluorescence-based bead sorting with minimal instrumentation and training required (MiniFABS, schematic shown in **Figure 4.1**). The hydrogel beads suspended in heavier fluorinated oil are driven by buoyancy force to float through a vertical channel. We suppose that the challenge for using gravity as the driving force in high-throughput bead sorting lies in imposing the downstream actuation with accurate timing and strength. Two sequential photodetectors are thus employed along the channel, in order to detect the fluorescence intensity, quantify the bead acceleration, and inform downstream actuation. The piezoelectric transducer provides the necessary acoustophoretic force deflection of the targeted bead into a different collection chamber. We have designed a

MiniFABS system and conducted a feasibility study through numerical simulation. The design was prototyped by assembly of in-house designed parts fabricated by high-resolution 3D printing and commercially available components. MiniFABS provides a portable and affordable solution for potentially point-of-care and point-of-sample-collection analysis and sorting of hydrogel beads.

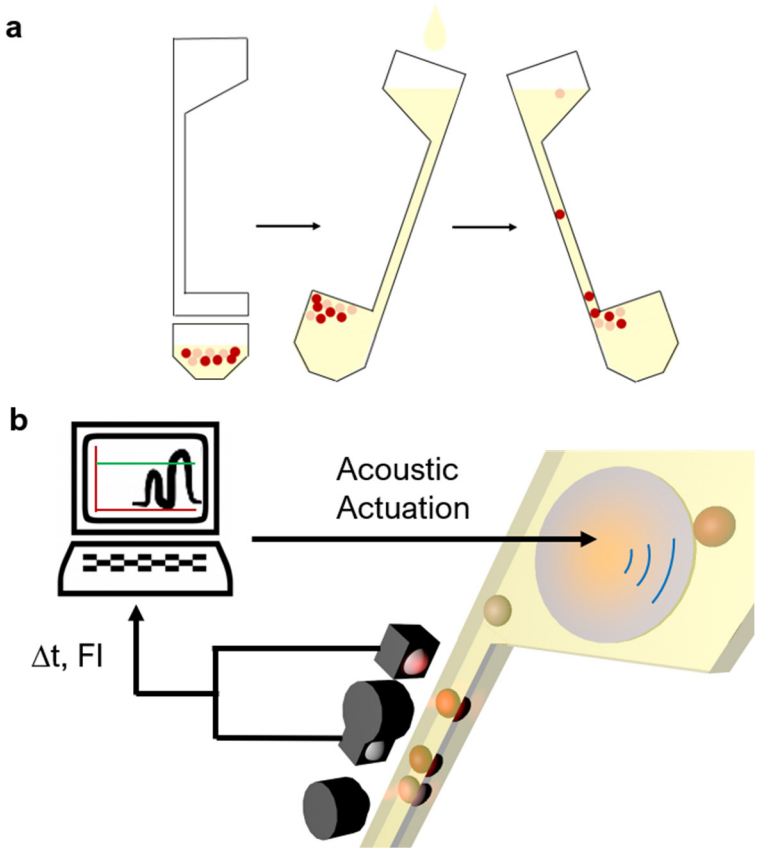

Figure 4.1 Schematic of the MiniFABS system. (**a**) Illustrations of sample loading, oil addition, and tube tilting to initiate floating of beads. (**b**)The fluorescence intensity (FI) of each bead is detected by two sequential photodetectors. The time difference (Δt) of the same bead passing through, along with the FI are analyzed to actuate the acoustic actuator for a bead with FI above a certain threshold. The positive bead moves in the direction perpendicular to the channel so that it enters a different collection chamber.

4.3 Results and discussion

4.3.1 Design and prototype of MiniFABS

The system involves a microfluidic tube (design shown in **Figure 4.2a**), two sequential photodetectors, two excitation lasers, an acoustic actuator, and a control system. The hydrogel beads suspended in heavier fluorinated oil are held in the bottom of the microfluidic tube. After sealing with the upper part and resting tilted at the position shown in **Figure 4.2b**, sorting can be initiated by adding oil and reversing the tube tilting direction (**Figure 4.2c**). The hydrogel beads are individually driven by buoyancy force through the channel, which has a side length of 800 μm. Along the channel, the sequential photodetectors monitor the fluorescence intensity (FI) for the control system to detect the passing bead, quantify its bead acceleration, and determine when the piezoelectric transducer is triggered if the FI of the bead exceeds the set threshold. The main hub and the microfluidic tubes were fabricated in house by high-resolution 3D printing, which can create channels with sizes larger than 400 μm on each side with high fidelity (Zhu et al., 2018). For red fluorescence-based sorting as our model system, the MiniFABS prototype has been assembled (photo shown in **Figure 4.2d**) with commercial light emitted diodes (LEDs), avalanche photodiodes (APDs), and a piezoelectric transducer all connected to a Raspberry Pi computer. The total cost of the prototype was below $500.

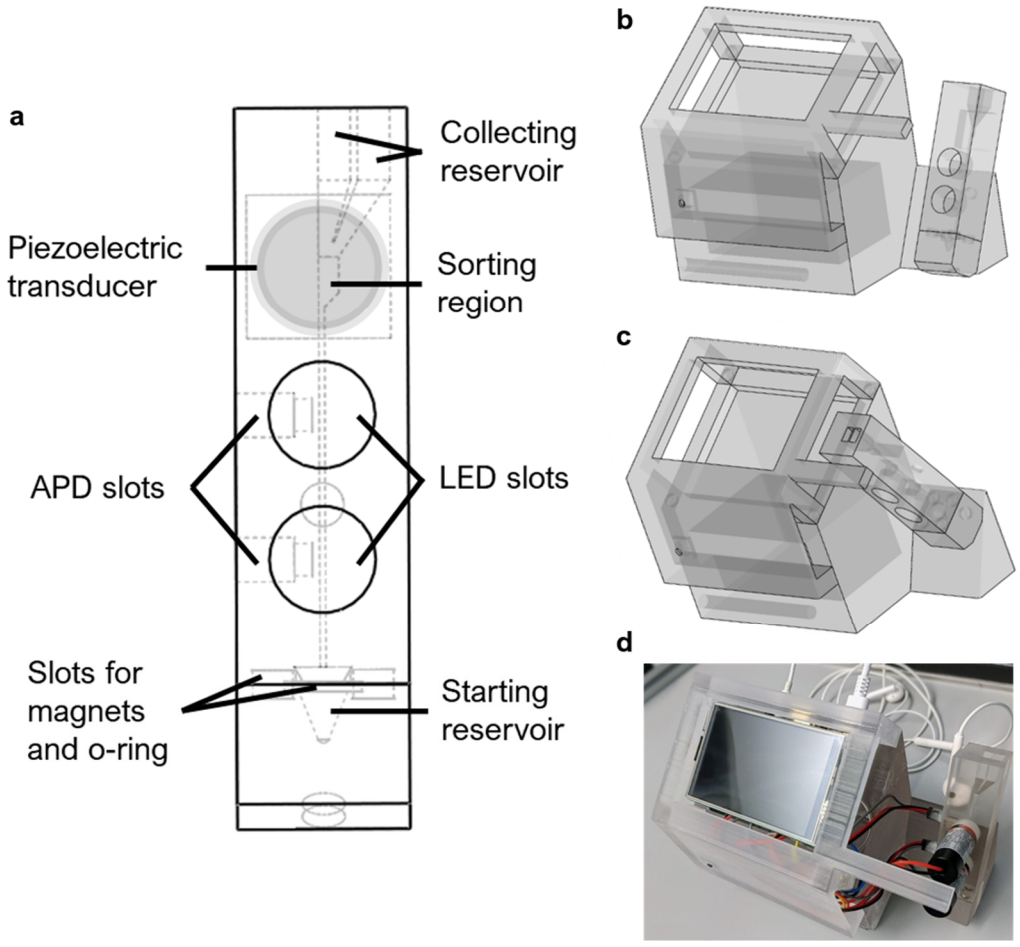

Figure 4.2 Detailed design of the MiniFABS prototype. (**a**) The microfluidic tube consisting of a bottom part for sample loading and an upper part for sorting and sample collection. The two parts are sealed with O-ring and magnets. (**b-c**) The system design containing the main hub for holding the control system with the microfluidic tube resting in (**b**) pre-initiation position and (**c**) sorting position. (**d**) Photo of the 3D printed prototype with LEDs, APDs etc.

4.3.2 Bead spacing in MiniFABS

The feasibility of the MiniFABS design was first investigated by exploring the bead spacing enabled by gravitational acceleration. The particle trajectories driven by gravity and drag force were simulated for two beads that are sequentially released from the bottom of the channel, as shown in **Figure 4.3a-b**. With a total channel length of 30 mm, the distance between the two beads is near linearly increased, and reaches ~6 mm when the first particle exits. This Δz grants a reasonable length for the sorting region, so that the particle deflection force could actuate without affecting the next bead. The results also indicate that the channel may be extended should more spacing be needed for sufficient acoustic deflection.

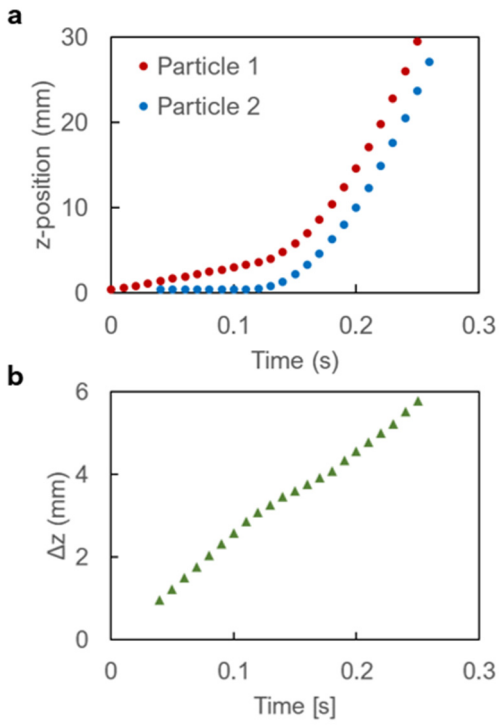

Figure 4.3 Temporal profiles (**a**) of vertical positions of two sequentially released beads under drag force and gravity and (**b)** of vertical distance between the two particles.

4.3.3 Acoustic actuation in MiniFABS

The feasibility of the MiniFABS design was first investigated by exploring the acoustic pressure field exerted by the piezoelectric transducer and its effect on a passing particle. For a particle moving upward into the sorting region, the acoustophoretic force ideally would move the particle in x-direction during the timeframe of particle crossing the sorting region. Therefore, it is essential for the piezoelectric transducer to generate a pressure gradient within the region. For the fluid in the sorting region and the solid of the underlying 3D printing material, the acoustic pressure induced by the piezoelectric transducer was simulated with varying frequencies including 40 kHz, 113 kHz, and 1.65 MHz as shown in **Figure 4.4a-c**. According to the simulation results, the 40 kHz transducer fails to impose noticeable acoustic pressure and pressure gradient in the fluid regime due to the low flexural wave energy. The high frequency (1.65 MHz) transducer generates a chaotic pressure field likely due to the densely packed pressure nodes (Bachman et al., 2020). The intermediate frequency of 113 kHz provides a pressure gradient. Moreover, this gradient would plausibly

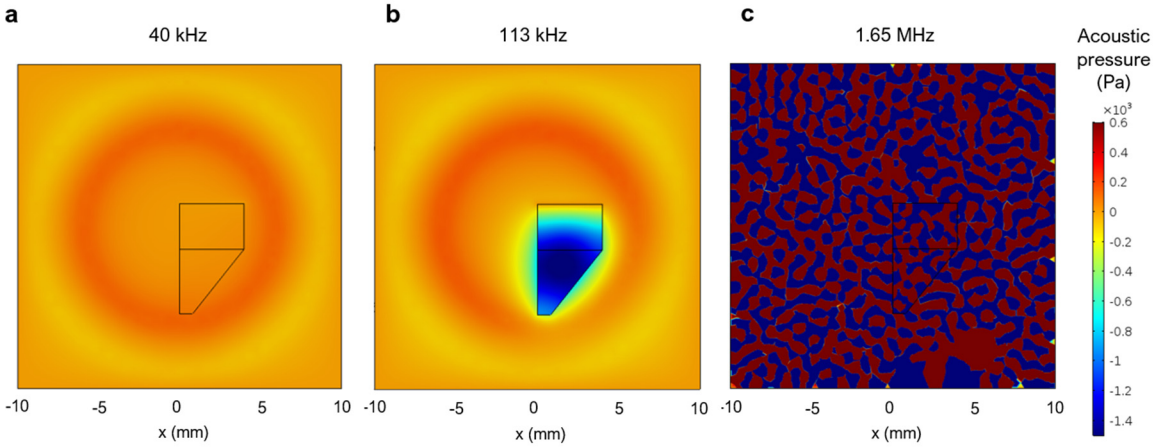

Figure 4.4 Simulated acoustic pressure field for the fluid in the sorting region exerted by applying 5V voltage on (**a**) 40 kHz, (**b**) 113 kHz, and (**c**) 1.65 MHz piezoelectric transducer. The square area represents the 1-mm thick wall.

favor particle deflection towards +x direction, with the current relative position of the sorting region fluid and the underlying transducer (invisible in this view).

The particle trajectory under the acoustic pressure (**Figure 4.5a-b**) was calculated with the simulated acoustic pressure fields. In this set of simulations, the particle under the acoustic pressure of 1.65 MHz transducer did not enter the sorting region, so its trajectory is not shown. The negligible particle deflection caused by the 40 kHz transducer was expected due to the lack of pressure gradient generated. For the 113 kHz transducer, the pressure field exerted is able to exert a discernible particle deflection in x-direction. If the sorting region length is taken as 5 mm, which is the bead spacing granted by gravitational acceleration after the ~24 mm channel, the simulated deflection (Δx) is at 2 mm. This deflection informs the upper limit of the distance between the collection chamber divider and the wall on the left. The designs will be experimentally tested and optimized for sorting accuracy.

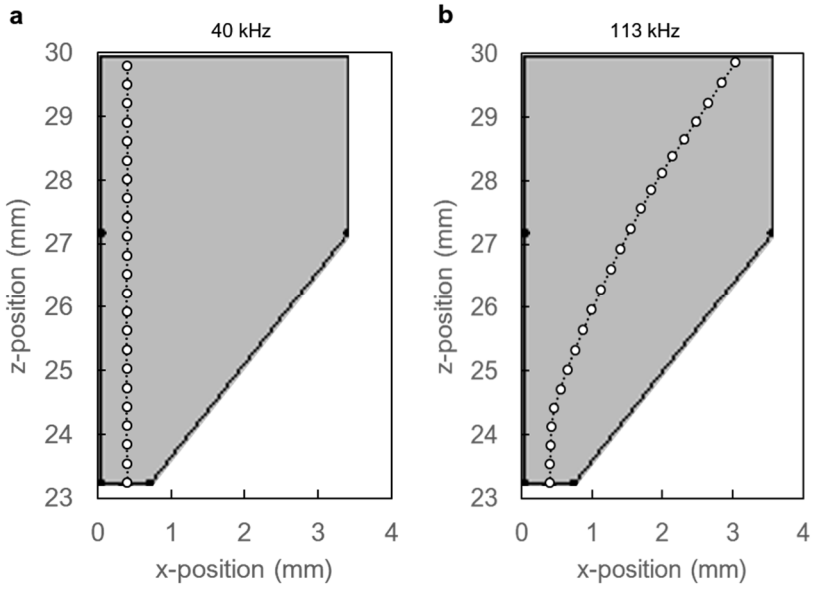

Figure 4.5 Particle trajectory simulated in the sorting region under drag force and acoustophoretic force under the simulated acoustic pressure fields for (**a**) 40 kHz and (**b**) 113 kHz piezoelectric transducers. The underlying grey area represents the corresponding front view of the sorting region.

4.4 Conclusions

We have demonstrated through numerical simulation that gravity, as a driving force, is capable of predictable particle spacing. Moreover, given the timeframe for the bead to cross the sorting region, the applied acoustic pressure can force the bead into a separate collection chamber. A full system prototype has been assembled. The control algorithm for fluorescence analysis and acoustic actuation is under development, and the bead sorting performance of the MiniFABS will be tested experimentally. The MiniFABS system promises cheap instrumentation, easy operation, and low contamination risk for hydrogel beads sorting. By connecting with other processes, MiniFABS has the potential to extend the application of hydrogel microfluidics to a point of care or in field.

4.5 Experimental section

4.5.1 Numerical simulation for gravity-driven bead movement

The spacing between two sequential particles while moving along the channel was studied by simulation in COMSOL Multiphysics® (COMSOL Multiphysics, 2015). The channel geometry was created with square cross-section of 800 μm sides and a total length of 30 mm. The *particle tracing for fluid flow* module was used to solve the time-dependent particle trajectory. Two particles were set to consecutively release from the center of the channel bottom with zero initial velocity. The particle diameter was set to 200 μm. It was assumed that the density of the bead resembles that of water. The dynamic viscosity and density of the oil phase was set to 1614 $kg \cdot m^3$ and 7.7×10^{-7} Pa·s, respectively, based on properties of HFE 7500 oil (Rausch et al., 2015). The drag force exerted by the stationary oil phase was calculated by Stoke's Law, and the gravity force was set based on the tilt angle of 60°. For mesh setting, predefined fine-sized free tetrahedral mesh calibrated for fluid dynamics was used for all boundary surfaces, and normal-sized one was used for the rest of the geometry.

4.5.2 Numerical simulation for acoustic actuation in the sorting region

The acoustic actuation of particles was studied by COMSOL simulation. The acoustic pressure field generated by the piezoelectric transducer was first simulated using the multiphysics module *acoustic-piezoelectric interaction, frequency domain*. The geometry of the sorting region fluid, the underlying 3D printing material, and a piezoelectric transducer at bottom, as shown in **Figure 4.6a**. The thickness of the three layers were 800 μm, 1mm, and 300 μm, respectively. The module first simulates the piezoelectric effect of the transducer by solving the coupled constitutive equations with the *Solid mechanics* and *electrostatics* modules. For the transducer geometry (**Figure 4.6b**), an electric potential of 5V was supplied to the center region of its bottom and the outer circle was grounded. The multiphysics module then solves the scalar wave equation and the Helmholtz equation with

the *pressure acoustics, frequency domain* module for the geometries of the fluid and 3D printing material. The properties involved were approximated by the built-in materials, using acrylic plastic for the proprietary 3D printing material and aluminum nitride for the piezoelectric transducer. The speed of sound for the sorting region fluid was set to 658.8 $m \cdot s^{-1}$ according to experimental measurement of HFE 7500 oil (Muñoz-Rujas et al., 2017).

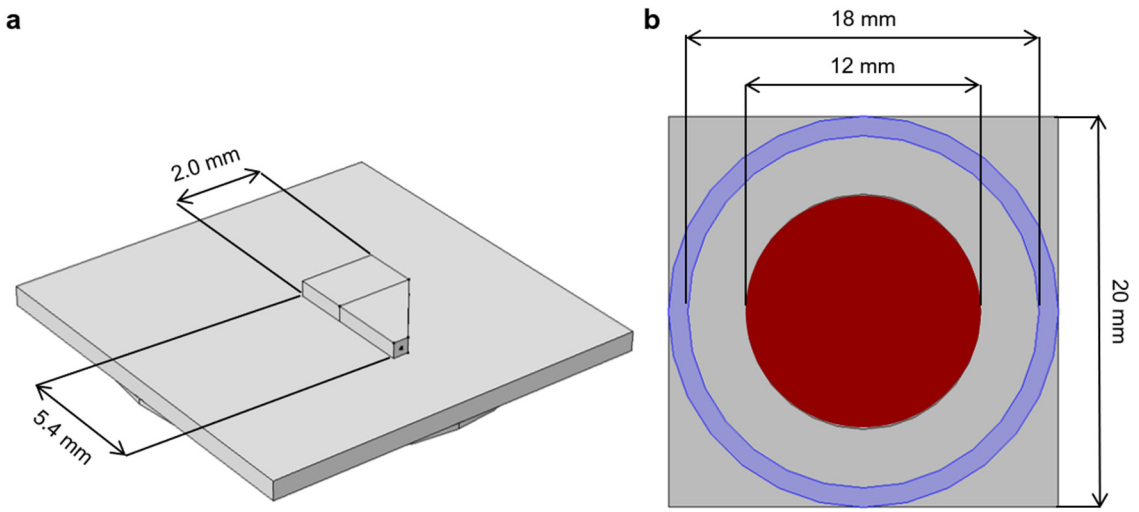

Figure 4.6 The geometry with key parameters for the simulation of acoustic actuation of particles. (**a**) isometric view including the sorting region fluid on top, underlying 3D printing material, and a piezoelectric transducer at bottom. (**b**) Bottom view of the geometry showing the piezoelectric transducer with concentric regions marked for imposing electric potential of 5V (red) and ground (purple).

The particle trajectory under the simulated acoustic pressure field was then modeled by *particle trajectory for fluid flow* module. Acoustophoretic force was calculated in addition to the drag force exerted by the stationary oil phase and gravity for the tilted tube. The particle inlet velocity in z-direction was approximated by a constant velocity of 0.3 $m \cdot s^{-1}$, which is the particle velocity after upward transporting for 24 mm in the channel as simulated in *Section 4.5.2*.

4.5.3 Prototype fabrication

The main hub and the two microfluidic tube parts were fabricated using a high-resolution 3D printer (3D systems ProJet™ MJP 2500 Plus, Rock Hill, SC) with clear plastic 3D printing material (Visijet® M2 RCL, 3D Systems). After printing was completed, the chip was cleaned in hot mineral oil bath and the channel was flushed with hot mineral oil to remove the supporting wax outside and inside the parts. The two microfluidic tube parts were sealed with O-ring and 4 ⌀2mm magnets. The steady positioning of the tube was facilitated by another 4 ⌀2mm magnets that held the tube at the two tilted positions against the supporting structures of the main hub. The assembly of prototype also included a Raspberry Pi (4, model B) with a 3.5" LCD touchscreen (UCTRONICS, Nanjing, China) as a control system and a power source for the electrical parts. The general-purpose input/output (GPIO) pins of the Pi were connected to two 650 nm red laser modules (Light99 Amazon, Seattle, WA, USA), two silicon Avalanche Photodiodes (Si APDs, S12053-02, Hamamatsu, Hamamatsu City, Japan), and a piezoelectric transducer (20mm 113KHz ultrasonic atomizer, WHDTS Amazon, Seattle, WA, USA). The LEDs and APDs were carefully wrapped with parafilm to ensure a tight fit into their slots.

4.6 Acknowledgements

The authors acknowledge the financial support provided by the Bill and Melinda Gates Foundation (grant nos. OPP1111252 and OPP1192379).

References

Aubry, G., Zhan, M., & Lu, H. (2015). Hydrogel-droplet microfluidic platform for high-resolution imaging and sorting of early larval Caenorhabditis elegans. *Lab on a Chip, 15*(6), 1424-1431.

Bachman, H., Gu, Y., Rufo, J., Yang, S., Tian, Z., Huang, P.-H., Yu, L., & Huang, T. J. (2020). Low-frequency flexural wave based microparticle manipulation. *Lab on a Chip, 20*(7), 1281-1289.

Cho, B. S., Schuster, T. G., Zhu, X., Chang, D., Smith, G. D., & Takayama, S. (2003). Passively driven integrated microfluidic system for separation of motile sperm. *Analytical Chemistry, 75*(7), 1671-1675.

Chokkalingam, V., Tel, J., Wimmers, F., Liu, X., Semenov, S., Thiele, J., Figdor, C. G., & Huck, W. T. (2013). Probing cellular heterogeneity in cytokine-secreting immune cells using droplet-based microfluidics. *Lab on a Chip, 13*(24), 4740-4744.

COMSOL Multiphysics. (2015). The platform for physics-based modeling and simulation. *Retrieved from: http://www.comsol.com/comsol-multiphysics*.

Fiedler, S., Shirley, S. G., Schnelle, T., & Fuhr, G. (1998). Dielectrophoretic sorting of particles and cells in a microsystem. *Analytical Chemistry, 70*(9), 1909-1915.

Hsu, M. N., Wei, S. C., Guo, S., Phan, D. T., Zhang, Y., & Chen, C. H. (2018). Smart hydrogel microfluidics for single-cell multiplexed secretomic analysis with high sensitivity. *Small, 14*(49), 1802918.

Huh, D., Bahng, J. H., Ling, Y., Wei, H.-H., Kripfgans, O. D., Fowlkes, J. B., Grotberg, J. B., & Takayama, S. (2007). Gravity-driven microfluidic particle sorting device with hydrodynamic separation amplification. *Analytical Chemistry, 79*(4), 1369-1376.

Jakobsson, O., Grenvall, C., Nordin, M., Evander, M., & Laurell, T. (2014). Acoustic actuated fluorescence activated sorting of microparticles. *Lab on a Chip, 14*(11), 1943-1950.

Landenberger, B., Höfemann, H., Wadle, S., & Rohrbach, A. (2012). Microfluidic sorting of arbitrary cells with dynamic optical tweezers. *Lab on a Chip, 12*(17), 3177-3183.

Le Goff, G. C., Srinivas, R. L., Hill, W. A., & Doyle, P. S. (2015). Hydrogel microparticles for biosensing. *European Polymer Journal, 72*, 386-412.

Lee, W., Tseng, P., & Di Carlo, D. (2017). Microfluidic cell sorting and separation technology. In *Microtechnology for Cell Manipulation and Sorting* (pp. 1-14): Springer.

Li, M., van Zee, M., Riche, C. T., Tofig, B., Gallaher, S. D., Merchant, S. S., Damoiseaux, R., Goda, K., & Di Carlo, D. (2018). A gelatin microdroplet platform for high-throughput sorting of hyperproducing single-cell-derived microalgal clones. *Small, 14*(44), 1803315.

Muñoz-Rujas, N., Bazile, J. P., Aguilar, F., Galliero, G., Montero, E., & Daridon, J. L. (2017). Speed of sound and derivative properties of hydrofluoroether fluid HFE-7500 under high pressure. *The Journal of Chemical Thermodynamics, 112*, 52-58.

Naeem, A., James, N., Tanvir, M., Marriam, M., & Nathaniel, S. (2017). Fluorescence activated cell sorting (FACS): An advanced cell sorting technique. *PSM Biological Research, 2*(2), 83-88.

Rausch, M. H., Kretschmer, L., Will, S., Leipertz, A., & Fröba, A. P. (2015). Density, surface tension, and kinematic viscosity of hydrofluoroethers HFE-7000, HFE-7100, HFE-7200, HFE-7300, and HFE-7500. *Journal of Chemical & Engineering Data, 60*(12), 3759-3765.

Tang, W., Jiang, D., Li, Z., Zhu, L., Shi, J., Yang, J., & Xiang, N. (2019). Recent advances in microfluidic cell sorting techniques based on both physical and biochemical principles. *Electrophoresis, 40*(6), 930-954.

Tirapu-Azpiroz, J., Temiz, Y., & Delamarche, E. (2017). Dielectrophoretic microbead sorting using modular electrode design and capillary-driven microfluidics. *Biomedical Microdevices, 19*(4), 95.

Xi, H.-D., Zheng, H., Guo, W., Gañán-Calvo, A. M., Ai, Y., Tsao, C.-W., Zhou, J., Li, W., Huang, Y., & Nguyen, N.-T. (2017). Active droplet sorting in microfluidics: A review. *Lab on a Chip, 17*(5), 751-771.

Xu, L., Lee, H., Jetta, D., & Oh, K. W. (2015). Vacuum-driven power-free microfluidics utilizing the gas solubility or permeability of polydimethylsiloxane (PDMS). *Lab on a Chip, 15*(20), 3962-3979.

Yang, A. H., & Soh, H. T. (2012). Acoustophoretic sorting of viable mammalian cells in a microfluidic device. *Analytical Chemistry, 84*(24), 10756-10762.

Yang, R.-J., Fu, L.-M., & Hou, H.-H. (2018). Review and perspectives on microfluidic flow cytometers. *Sensors and Actuators B: Chemical, 266*, 26-45.

Yang, R.-J., Hou, H.-H., Wang, Y.-N., & Fu, L.-M. (2016). Micro-magnetofluidics in microfluidic systems: A review. *Sensors and Actuators B: Chemical, 224*, 1-15.

Yao, B., Luo, G.-a., Feng, X., Wang, W., Chen, L.-x., & Wang, Y.-m. (2004). A microfluidic device based on gravity and electric force driving for flow cytometry and fluorescence activated cell sorting. *Lab on a Chip, 4*(6), 603-607.

Zhu, Y., Huang, X., Xie, X., Bahnemann, J., Lin, X., Wu, X., Wang, S., & Hoffmann, M. R. (2018). Propidium monoazide pretreatment on a 3D-printed microfluidic device for efficient PCR determination of 'live versus dead' microbial cells. *Environmental Science: Water Research & Technology, 4*(7), 956-963.

Zhu, Y., Li, J., Lin, X., Huang, X., & Hoffmann, M. R. (2019). A hydrogel beads-based platform for single-cell phenotypic analysis and digital molecular detection. *bioRxiv*, 848168.

Zhu, Z., & Yang, C. J. (2017). Hydrogel droplet microfluidics for high-throughput single molecule/cell analysis. *Accounts of Chemical Research, 50*(1), 22-31.

Zimny, P., Juncker, D., & Reisner, W. (2018). Hydrogel droplet single-cell processing: DNA purification, handling, release, and on-chip linearization. *Biomicrofluidics, 12*(2), 024107. doi:10.1063/1.5020571

C h a p t e r 5

PROSPECTIVE DEVELOPMENT AND APPLICATIONS

5.1 DropTube: Integrated centrifugal device for in-field pathogen analysis

5.1.1 Introduction

The development of a disposable device for centrifugal droplet and Gelbead generation was described in **Chapter 3**. The device uses a needle with a bent tip and a microcentrifuge tube, and the droplet generation can be conveniently driven by a common lab centrifuge. The successful generation of monodispersed water-in-oil droplets with the needle-in-a-tube geometry demonstrates the potential to develop a centrifuge-driven DropTube. Other than a long channel acting like the bent-tip needle, a variety of 3D microfluidic structures may be contained in DropTube to perform integrated fluid handling for digital nucleic acid analysis of waterborne pathogen. Therefore, we propose a further development of this platform, with a model application of in-field *S.* Typhi analysis. Specifically, the proposed work focuses on serovar-specific quantitative detection and antimicrobial resistance (AMR) characterization of *S.* Typhi. However, the development of this idea will be contingent upon the progress of 3D printing technologies, which is essential for prototyping the DropTube designs. Efforts of prototyping with various methods of 3D printing all failed due to the inability to produce the long narrow channel for droplet generation. However, mass production using injection molding should be feasible through injection molding (McCormick et al., 1997), upon successful design optimization with 3D printed prototypes. It is envisioned that this microfluidic DropTube can be developed into a simple, yet highly robust and versatile platform, which will finally eliminate the barriers for researchers to utilize microfluidics.

5.1.2 Integration of functional structures in DropTube

An in-tube droplet reading platform would significantly improve the applicability of the microfluidic tube since it eliminates multiple pipetting steps and avoids DNA contamination caused by opening the tube. The additional reading platform is designed to be a flat sidewall of the tube above the top of the liquid-air interface after droplet generation. After heating the droplets in-tube for LAMP, the tube can be laid flat so that the droplets, along with the carrier oil, would be drawn into the droplet reading platform, the rectangular slice of space, by capillary force. The droplets are gathered into single layer arrays, and can then be easily imaged by a fluorescent microscope or smartphone. The integrated design is created in Solidworks, as shown in **Figure 5.1a-c**, and is ready to be fabricated by 3D printing.

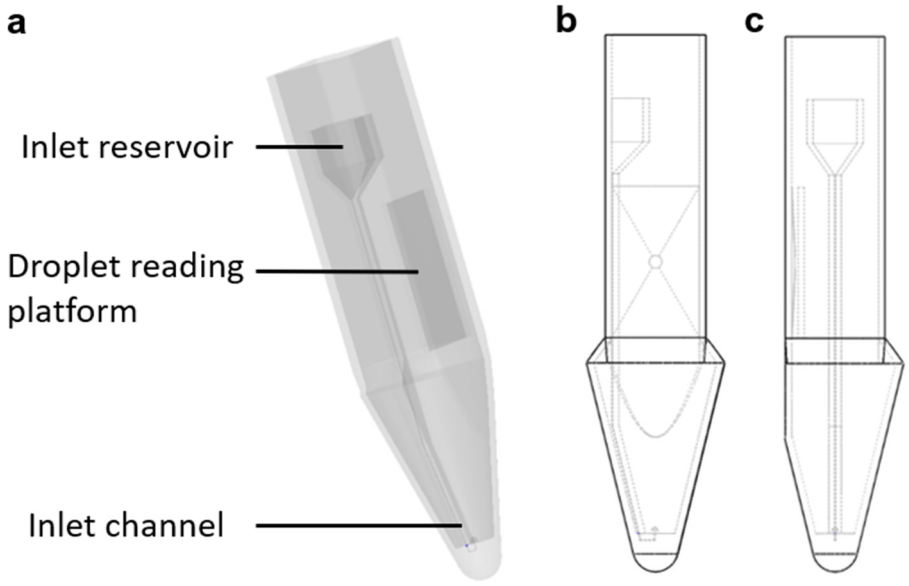

Figure 5.1 3D model of the design incorporating droplet generation structure and droplet reading platform: (**a**) isometric view, (**b**) front view, and (**c**) side view.

5.1.3 DropTube for serovar-specific quantitative detection

Serovar-specific detection is crucial in environmental surveillance because typhoidal *Salmonella* poses distinctive risks when compared to other *Salmonella* serovars. Typhoidal *Salmonella* is characteristic of being non-diarrheal and human-restricted. Salmonella carries the *inv*A gene that codes for proteins responsible for invading intestinal epithelial mediated by M-cell (Crump, 2015). For non-typhoidal *Salmonella*, invasion of epithelial cells stimulates the release of cytokines which induce an inflammatory reaction causing diarrhea (Dougan & Baker, 2014). Typhoidal *Salmonella*, after entering mucosa tissue, cover the surface antigens with Vi-antigen when interacting with human macrophage cells (Dougan & Baker, 2014). *S.* Typhi rapidly becomes nonmotile, noninvasive, and capsulated after its transition through the intestinal epithelium into the mucosal tissue. From there, it enters the bloodstream and disseminates all over the body. It is human-restricted mainly due to specific interactions with human cells in the aforementioned pathogenic process. *S.* Typhi survives in human macrophages, but not in other species. Moreover, *S.* Typhi expresses the *pil*V gene to synthesize type IVB pili, which specifically interact with the human cystic fibrosis transmembrane conductance receptor (CFTR) proteins. These proteins act as a chloride channel on the membrane of human epithelial cells in many organs (Pier et al., 1998). Also, when *S.* Typhi enters human cells, it starts to upregulate typhoid toxin production which is highly immunogenic and pyrogenic. Some individuals who are infected with S. Typhi or recover from typhoid may become asymptomatic life-long carriers that serve as the reservoir for these pathogens.

There is a lack of easy and field-ready methods capable of *S.* Typhi detection at serovar-level in environmental samples. The existing methods that detect at serovar-level are very time consuming, and involve complicated steps that require a fully equipped laboratory and corresponding expertise. The USEPA's standard analysis of *S.* Typhi in drinking water involves multiple steps of enrichment culturing and selective culturing, followed by at least 5 tests for serovars verification, taking more than 5 days to confirm a positive strain (EPA.,

2010). Molecular analysis has been widely researched and commercial kits are available to detect *Salmonella* at a genus level, which shortens the sample-to-result time to 2-3 days (Abirami et al., 2016; Francois et al., 2011; George, 2011; Hara-Kudo et al., 2005; Lim et al., 2015; Ohtsuka et al., 2005). Commercial kits are available, but generally target the *inv*A gene common for all *Salmonella* serovars. Differentiation of species and serovars by molecular analysis are rarely reported, likely due to the genetic similarity within the genus. Also, the main limitation in environmental sample molecular analysis lies in the enrichment step. Enrichment by culture is slow and is highly likely limited by background microbiota (Abirami et al., 2016; Lim et al., 2015).

Here we propose to develop a DropTube device for quantitative serovar-specific *S.* Typhi detection, building upon the integrated digital LAMP DropTube (as described in **Section 5.1.2**). The established integrated digital LAMP DropTube will perform DNA extraction, purification, droplet generation, and digital LAMP. An additional enrichment step before cell lysis may enable selective concentration of *S.* Typhi from 1ml to ~5 µl, which is a typical sample volume. While keeping the cells intact for molecular analysis, it is possible to perform serovar-selective enrichment by specific recognition of certain cell membrane proteins by aptamer coated magnetic beads or antibody coated porous materials (Davies & Wray, 1997; Jyoti et al., 2011). The serovar-specific enrichment step, as an addition to the digital LAMP microfluidic tube, will enable quantitative serotype level detection of typhoidal *Salmonella*. The design will have the potential to be used broadly since it can easily be adapted for the detection of other serovars, species, etc. with modifications to the capturing aptamer or antibody.

5.1.4 DropTube for AMR characterization

Another great challenge in controlling typhoid outbreaks lies in the emergence and fast spreading of antibiotic resistant *S.* Typhi strains. Multidrug resistant H58 lineages of *S.* Typhi (resistant to 1st line antibiotics amoxicillin, chloramphenicol, and cotrimoxazole) has rapidly gained domination over other clades since its first isolation in 1970s (Crump, 2015;

Feasey et al., 2015; Olarte & Galindo, 1973; Yan et al., 2016). The shift of treatment strategy to 3rd generation antibiotics was followed by the emergence of strains displaying reduced susceptibility to fluoroquinolones (Wain et al., 1997). Antibiotic resistance can be characterized by phenotyping or genotyping. Phenotyping involves cultivation of *S.* Typhi on antibiotic-containing media and is usually time-consuming, taking several days to confirm a resistant strain. Genetic detection of the antibiotic resistance genes (ARG) shortens the time to hours, but is highly relying on available knowledge of the ARG sequences and risks missing new resistant strains due to mutation. Fast and reliable antibiotic resistance characterization remains a challenge.

To overcome these barriers, DropTube can also be adapted into a digital AMR characterization device. Schoepp et. al demonstrated AMR characterization of *E. coli* enabled by PCR recognition of DNA replication after 15 min incubation with antibiotics (Schoepp et al., 2016). The DropTube for digital LAMP can be modified to generate hydrogel droplets, which could encapsulate cells while remaining permeable to small molecules and biological reagents. Gelled droplets, compared to liquid droplets, enable the exchange of reagents, are more stable for amplification inside, and grant the possibility of downstream analysis of specific droplets of interest. The cell-containing sample will be compartmentalized into hydrogel droplets with the target antibiotic to incubate shortly. Subsequently, reagents will be exchanged before molecular detection of RNA production to indicate the live/dead status of the cells.

5.2 Gelbead-based AMR evolution kinetics study

5.2.1 Mutation induced fast emergence and evolution of AMR

Ubiquitous cell heterogeneity, such as antibiotic heteroresistance and cancer stem cell heterogeneity, has long been observed and raises concerns in various fields. Microfluidic single cell techniques have enabled identification of rare genotypes or phenotypes within a cell population. To understand the cell heterogeneity and tackle the problem it poses, it would

be essential to identify single cell genotype-to-phenotype correlations. However, the analysis tool capable of establishing such correlations is not available yet.

The PEG hydrogel bead-based platform (Gelbeads) was validated for both single-cell phenotypic analysis and molecular detection, with demonstrated potential of linking both for single cell analysis (as described in **Chapter 3**). Here we propose to probe the molecular mechanism of antibiotic resistance evolution using the Gelbead platform. Bacteria are known to exhibit remarkable adaptability under exposure to antibiotics. Previous studies have shown that the genetic and phenotypic diversity of bacterial cells led to increased resistance to antibiotic stress as a community (Lee et al., 2010; Yurtsev et al., 2016). Under exposure to antibiotic, the subpopulation acquired resistant mutation was found to secret molecules to protect the non-resistant and gain nutrients from them to cover the additional fitness cost (Lee et al., 2010). A few possibly functional alleles have been identified for resistance evolution (Zhang et al., 2011). However, these studies only reported phenotypic observations of such evolution and deduced mechanism through sequencing of the end-point bacterial isolates. The kinetics of the SNP emergence and its correlation with the cell community dynamics during antibiotic resistance evolution remain poorly understood.

5.2.2 Provisional study workflow

During co-incubation of bacteria and target antibiotic, the proposed study will investigate the emergence of resistant subpopulation and corresponding temporal profiles of significant SNPs. *Salmonella* Typhimurium can be employed as a model strain, with ciprofloxacin as a model fluoroquinolone antibiotic. The study involves the following milestones: a) determine single nucleotide polymorphisms (SNPs) significant in antibiotic resistance evolution by end point single cell sequencing, b) design and test PCR primers specifically targeting the SNPs, c) develop the fluorescence activated beads sorter and validate Gelbead multiplex PCR after sorting, and d) antibiotic resistance evolution experiments. The schematic of the study is shown in **Figure 5.2**.

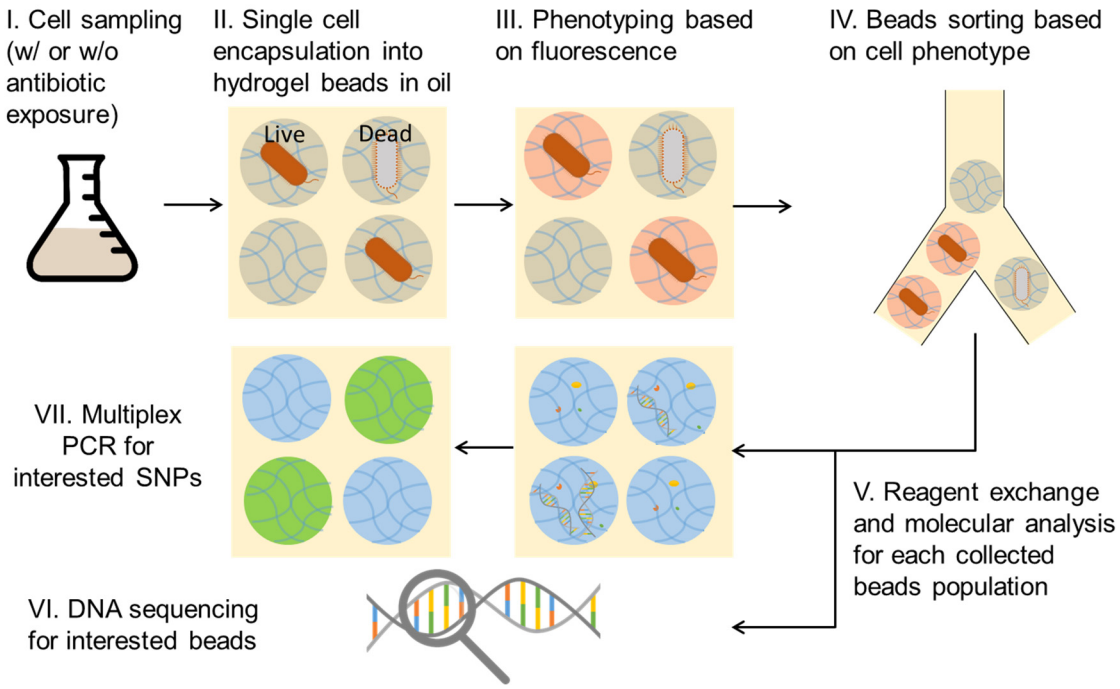

Figure 5.2 Schematic of the proposed study on antibiotic resistance evolution kinetics.

Target SNPs will be identified using methods similar to literature (Zhang et al., 2011). Bacteria and antibiotic will be co-incubated, and a small portion of the cells will be

tested for viability. After acquired resistance is observed, the whole genome sequence will be examined to understand what mutations occurred and spread within the population. The sequences of single cells phenotyped in Gelbeads will also be examined to exclude mutations induced by the Gelbead phenotyping process. SNP will be identified by comparing the sequencing data with wild-type bacteria sequences. The significant SNPs (ideally one seems directly related to resistance and one seems irrelevant) will be selected as the targets of PCR assays. The primers amplifying the genes containing the SNP will be either found in literature or designed using BLAST. Molecular beacon specifically targeting the SNPs will be designed (Mhlanga & Malmberg, 2001). The assays will be optimized with qPCR and verified in gdPCR. Multiplexing will be attempted to include 16s rDNA detection as a reference for cell presence.

For the experiments, during the co-incubation of bacteria and the antibiotic, cell samples will be extracted and washed prior to entering the single cell analysis workflow. The sampling time points will be determined based on the timeframe observed in 2.1. The cell samples will be resuspended in the mixture for phenotyping and compartmentalized into Gelbeads, which then are sorted into positive and negative beads. Each population of beads is then analyzed by PCR for SNPs. The results will be collectively analyzed for temporal profiles of quantitative resistance phenotype emergence and the presence of SNPs in each phenotypic population. The analysis will likely generate information as shown in **Figure 5.3**. The PCR profiles would inform which SNP appears first. The timing of emergence SNPs relative to the temporal profile of the resistant subpopulation may inform the role of SNP in antibiotic resistance and single cell fitness. Collectively, the above information may suggest the role of these molecular variations in antibiotic resistance evolution as a community.

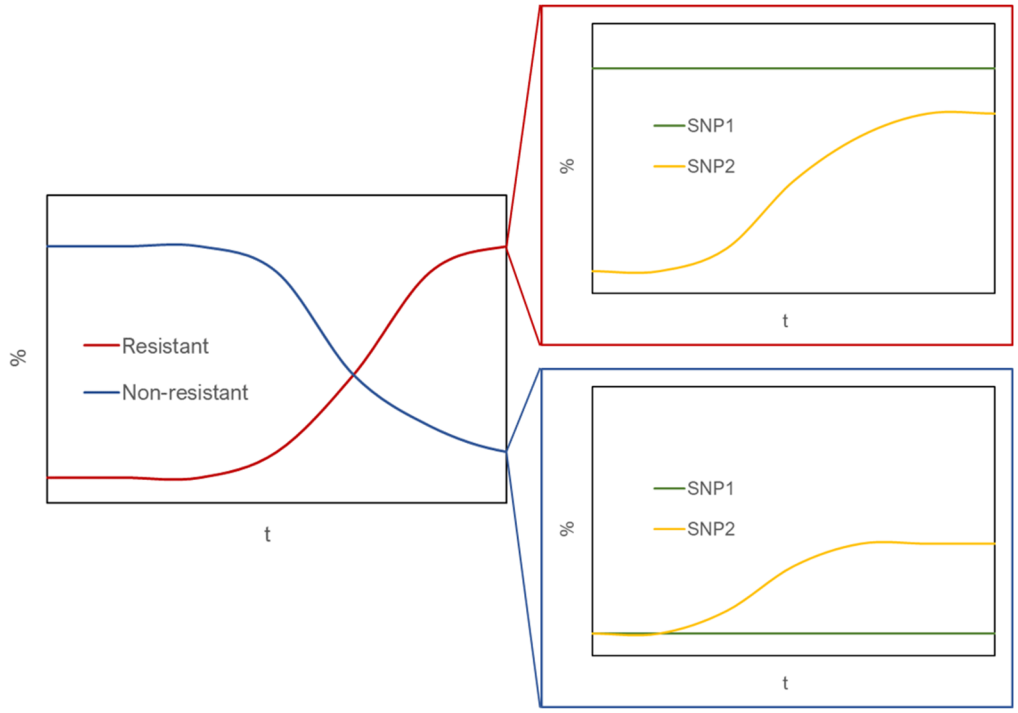

Figure 5.3 Provisional obtainable information from the designed experiments.

The completion of this study will hopefully be able to answer the following questions about the crucial SNPs during antibiotic heteroresistance evolution: a) What is the order of their occurrence during the evolution, and are their kinetics interdependent? b) what are their roles in cell fitness? and c) what are their roles in the evolving community? The answers to these questions will have implications in modulation of antibiotic treatments for enhanced efficacy and resistance prevention. Once the workflow is established, its application can be extended to studies of complicated heterogeneous cell systems such as in microbial ecology and oncology.

References

Abirami, N., Nidaullah, H., Chuah, L.-O., Shamila-Syuhada, A. K., Chandraprasad, S., Huda, N., Hasmaizal, H., & Rusul, G. (2016). Evaluation of commercial loop-mediated isothermal amplification based kit and ready-to-use plating system for detection of Salmonella in naturally contaminated poultry and their processing environment. *Food Control, 70*, 74-78.

Crump, J. (2015). Sjö lund-Karlsson M, Gordon MA, Parry CM. Epidemiology, clinical presentation, laboratory diagnosis, antimicrobial resistance, and antimicrobial management of invasive Salmonella infections. *Clinical Microbiology Reviews, 28*, 901-937.

Davies, R., & Wray, C. (1997). Use of antibody-coated cellulose sponges for enhanced isolation of salmonella. *Letters in Applied Microbiology, 25*(4), 246-248.

Dougan, G., & Baker, S. (2014). Salmonella enterica serovar Typhi and the pathogenesis of typhoid fever. *Annual Review of Microbiology, 68*, 317-336.

EPA., U. S. (2010). Standard Analytical Protocol for Salmonella Typhi in Drinking Water. Washington, DC: U.S. Environmental Protection Agency.

Feasey, N. A., Gaskell, K., Wong, V., Msefula, C., Selemani, G., Kumwenda, S., Allain, T. J., Mallewa, J., Kennedy, N., & Bennett, A. (2015). Rapid emergence of multidrug resistant, H58-lineage Salmonella typhi in Blantyre, Malawi. *PLoS Neglected Tropical Diseases, 9*(4).

Francois, P., Tangomo, M., Hibbs, J., Bonetti, E.-J., Boehme, C. C., Notomi, T., Perkins, M. D., & Schrenzel, J. (2011). Robustness of a loop-mediated isothermal amplification reaction for diagnostic applications. *FEMS Immunology & Medical Microbiology, 62*(1), 41-48.

George, D. (2011). Adaptive finite volume methods with well-balanced Riemann solvers for modeling floods in rugged terrain: Application to the Malpasset dam-break flood (France, 1959). *International Journal for Numerical Methods in Fluids, 66*(8), 1000-1018.

Hara-Kudo, Y., Yoshino, M., Kojima, T., & Ikedo, M. (2005). Loop-mediated isothermal amplification for the rapid detection of Salmonella. *FEMS Microbiology Letters, 253*(1), 155-161.

Jyoti, A., Vajpayee, P., Singh, G., Patel, C. B., Gupta, K. C., & Shanker, R. (2011). Identification of environmental reservoirs of nontyphoidal salmonellosis: aptamer-assisted bioconcentration and subsequent detection of Salmonella typhimurium by quantitative polymerase chain reaction. *Environmental Science & Technology, 45*(20), 8996-9002.

Lee, H. H., Molla, M. N., Cantor, C. R., & Collins, J. J. (2010). Bacterial charity work leads to population-wide resistance. *Nature, 467*(7311), 82-U113. doi:10.1038/nature09354

Lim, H. S. Y., Zheng, Q., Miks-Krajnik, M., Turner, M., & Yuk, H.-G. (2015). Evaluation of commercial kit based on loop-mediated isothermal amplification for rapid detection of low levels of uninjured and injured Salmonella on duck meat, bean sprouts, and fishballs in Singapore. *Journal of Food Protection, 78*(6), 1203-1207.

McCormick, R. M., Nelson, R. J., Alonso-Amigo, M. G., Benvegnu, D. J., & Hooper, H. H. (1997). Microchannel electrophoretic separations of DNA in injection-molded plastic substrates. *Analytical Chemistry, 69*(14), 2626-2630.

Mhlanga, M. M., & Malmberg, L. (2001). Using molecular beacons to detect single-nucleotide polymorphisms with real-time PCR. *Methods, 25*(4), 463-471. doi:10.1006/meth.2001.1269

Ohtsuka, K., Yanagawa, K., Takatori, K., & Hara-Kudo, Y. (2005). Detection of Salmonella enterica in naturally contaminated liquid eggs by loop-mediated isothermal amplification, and characterization of Salmonella isolates. *Applied Environmental Microbiology, 71*(11), 6730-6735.

Olarte, J., & Galindo, E. (1973). Salmonella typhi resistant to chloramphenicol, ampicillin, and other antimicrobial agents: strains isolated during an extensive typhoid fever epidemic in Mexico. *Antimicrobial Agents and Chemotherapy, 4*(6), 597-601.

Pier, G. B., Grout, M., Zaidi, T., Meluleni, G., Mueschenborn, S. S., Banting, G., Ratcliff, R., Evans, M. J., & Colledge, W. H. (1998). Salmonella typhi uses CFTR to enter intestinal epithelial cells. *Nature, 393*(6680), 79-82.

Schoepp, N. G., Khorosheva, E. M., Schlappi, T. S., Curtis, M. S., Humphries, R. M., Hindler, J. A., & Ismagilov, R. F. (2016). Digital quantification of DNA replication and chromosome segregation enables determination of antimicrobial susceptibility after only 15 minutes of antibiotic exposure. *Angewandte Chemie International Edition, 55*(33), 9557-9561.

Wain, J., Hoa, N. T., Chinh, N. T., Vinh, H., Everett, M. J., Diep, T. S., Day, N. P., Solomon, T., White, N. J., & Piddock, L. J. (1997). Quinolone-resistant Salmonella typhi in Viet Nam: molecular basis of resistance and clinical response to treatment. *Clinical Infectious Diseases, 25*(6), 1404-1410.

Wu, X., Huang, X., Zhu, Y., Li, J., & Hoffmann, M. R. (2020). Synthesis and application of superabsorbent polymer microspheres for rapid concentration and quantification of microbial pathogens in ambient water. *Separation and Purification Technology*, 116540.

Yan, M., Li, X., Liao, Q., Li, F., Zhang, J., & Kan, B. (2016). The emergence and outbreak of multidrug-resistant typhoid fever in China. *Emerging Microbes & Infections, 5*(1), 1-6.

Yurtsev, E. A., Conwill, A., & Gore, J. (2016). Oscillatory dynamics in a bacterial cross-protection mutualism. *Proceedings of the National Academy of Sciences of the United States of America, 113*(22), 6236-6241. doi:10.1073/pnas.1523317113

Zhang, Q. C., Lambert, G., Liao, D., Kim, H., Robin, K., Tung, C. K., Pourmand, N., & Austin, R. H. (2011). Acceleration of emergence of bacterial antibiotic resistance in connected microenvironments. *Science, 333*(6050), 1764-1767. doi:10.1126/science.1208747

Chapter 6

CONCLUSIONS AND OUTLOOKS

The work in this dissertation sets forth an exploration in the nexus of 3D printing, polymer engineering, microfluidics, and life science, with potential applications that transcend disciplines. In an effort to develop simple solutions for environmental bacterial detection and analysis, this dissertation delivers:

(1) Simulation-aided designs and understanding of 3D microfluidic systems on unconventional substrates. The development of the simulation models supported the design of a 3D-printed microfluidic chip for live and dead cell differentiation prior to PCR detection, understanding of the DNA extraction performance observed for an electrochemical lysis device, and the validation of homogeneous cell dispersion onto an asymmetric membrane for integrated digital detection.

(2) A disposable droplet generation solution. The droplet generation device made simply from needles and microcentrifuge tubes was capable of producing monodispersed water-in-oil droplets. It demonstrates the potential of developing fully integrated microfluidic tubes that run in common lab centrifuges and incorporate sample preparation steps, digital results reading, etc.

(3) A hydrogel bead-based platform for probing single cell phenotype-to-genotype correlations. The hydrogel bead-based cell analysis platform, along with the bead sorter, establishes single-cell genotype-phenotype correlations, which would help answer important scientific questions in cell heterogeneity, including the mutation dynamics and their functions in the fitness of individual cells and cell communities. The understanding of these questions is indispensable in the combat against the global AMR crisis.

(4) A bead sorting system complementary to the hydrogel bead-based platform. The design minimizes instrumentation requirements by utilizing gravity as driving force and

commercial acoustic buzzer as actuator. The developed bead sorter provides a portable, affordable, and easy-to-operate solution to decentralize fluorescence-activated sorting of beads in oil.

In summary, our work shows the robustness of 3D microfluidics that uses novel materials, alternative fabrication methods, etc., often with advanced understanding through numerical simulations, to achieve fast, sensitive microbial detection and analysis with minimal instrumentation.

The approach explored in this dissertation also highlights a few remaining problems to be solved in the future. One such problem is that the standardization of these 3D microfluidic devices might be compromised due to the nature of the simple and non-standard fabrication process. For example, the consistency of the disposable devices from trial to trial may need to be more rigorously characterized and improved. The improvement of consistency may be achieved through stringent quality control of the commercial starting materials, such as the porous membranes discussed in Chapter 2.3 and the needles discussed in Chapter 3, and through automated robotic fabrication. However, these efforts may complicate the processes involved in using 3D microfluidics, which is against the essential goal of making the technologies effortless to use for end users. Moreover, wide adoption of technologies requires mass production. The most common mass fabrication of traditional microfluidic chip is through injection molding, which molds the chip material and then bond to the other layer to assemble into a closed chip. Thus, scaling up might not be guaranteed feasible for some of the 3D microfluidic systems with convoluted structures. Collective efforts in mass production method innovation might be needed to boost the field of microfluidics.

The interdisciplinary research of environmental microbiology and 3D microfluidics remains a thriving field with exciting upcoming advances and developments. It has been a great pleasure to have made this expedition, which intrigued me in how microbial life evolves, and potentially utilize this understanding to solve modern health problems.

A p p e n d i x A

ELECTROCHEMICAL CELL LYSIS OF GRAM-POSITIVE AND GRAM-NEGATIVE BACTERIA: DNA EXTRACTION FROM ENVIRONMENTAL WATER SAMPLES

Wang, S., Zhu, Y., Yang, Y., Li, J. and Hoffmann, M. R. (2020) Electrochemical cell lysis of gram-positive and gram-negative bacteria: DNA extraction from environmental water samples. *Electrochimica Acta,* 135864. https://doi.org/10.1016/j.electacta.2020.135864

Electrochimica Acta 338 (2020) 135864

Contents lists available at ScienceDirect

Electrochimica Acta

journal homepage: www.elsevier.com/locate/electacta

Electrochemical cell lysis of gram-positive and gram-negative bacteria: DNA extraction from environmental water samples

Siwen Wang , Yanzhe Zhu , Yang Yang , Jing Li , Michael R. Hoffmann *

Linde+Robinson Laboratories, California Institute of Technology, Pasadena, CA 91125, USA

ARTICLE INFO

Article history:
Received 28 October 2019
Received in revised form
4 February 2020
Accepted 5 February 2020
Available online 6 February 2020

Keywords:
Electrochemical cell lysis (ECL)
DNA extraction
Gram-positive and gram-negative bacteria
Environmental water samples

ABSTRACT

Cell lysis is an essential step for the nucleic acid-based surveillance of bacteriological water quality. Recently, electrochemical cell lysis (ECL), which is based on the local generation of hydroxide at a cathode surface, has been reported to be a rapid and reagent-free method for cell lysis. Herein, we describe the development of a milliliter-output ECL device and its performance characterization with respect to the DNA extraction efficiency for gram-negative bacteria (*Escherichia coli* and *Salmonella* Typhi) and gram-positive bacteria (*Enterococcus durans* and *Bacillus subtilis*). Both gram-negative and gram-positive bacteria were successfully lysed within a short but optimal duration of 1 min at a low voltage of ~5 V. The ECL method described herein, is demonstrated to be applicable to various environmental water sample types, including pond water, treated wastewater, and untreated wastewater with DNA extraction efficiencies similar to a commercial DNA extraction kit. The ECL system outperformed homogeneous chemical lysis in terms of reaction times and DNA extraction efficiencies, due in part to the high pH generated at the cathode surface, which was predicted by simulations of the hydroxide transport in the cathodic chamber. Our work indicates that the ECL method for DNA extraction is rapid, simplified and low-cost with no need for complex instrumentation. It has demonstrable potential as a prelude to PCR analyses of waterborne bacteria in the field, especially for the gram-negative ones.

1. Introduction

During water electrolysis, the micro-environment at the electrode/electrolyte interface has different properties compare to that of the bulk electrolyte. The cathodic proton reduction to hydrogen significantly increases the pH at the surface of cathode. This mechanism plays important roles in various physio-chemical processes such as NH_3 stripping [1], phosphate recovery [2] and enhanced CO_2 reduction [3]. However, the application of this mechanism in biomolecular analysis, especially the detection of waterborne bacteria was relatively less explored.

In recent years, the application of biomolecular techniques such as polymerase chain reaction (PCR) has resulted in rapid, accurate, and sensitive methods for the quantification of waterborne bacteria [4–6]. The initial step before actual PCR analysis is cell lysis for the extraction of nucleic acids. One of the most common cell lysis technique for microbial quantification is chemical lysis, which employs an alkaline buffer or other lytic reagents to disrupt cell walls. This technique requires an array of essential instruments and multi-step reagent additions which are time-consuming and labor-intensive. In addition, removal of the reagents after cell lysis is required in order to avoid interference with downstream detection [7,8]. Electroporation uses the sharp potential gradient to break down cell membrane. It is fast and agent-free, and it is able to leave intracellular components intact [9–18]. The downside of electroporation, however, is the use of high electric fields to achieve irreversible electroporation (*e.g.*, 10 kV/cm [14]). High power and voltage required to generate the high electric field, also leads to joule heating of the fluid [14,19–22]. Lower electroporation voltages can be realized using nano-structured electrodes coupled with microfluidic devices. However, this approach would require a complicated fabrication process and precise operation [11,13–15,17,23–25].

Electrochemical cell lysis (ECL) relies on the cathodically generated hydroxide (*i.e.*, localized high pH) to disrupt microbial cell membranes by breaking fatty acid-glycerol ester bonds in phospholipids [7,26]. In contrast to high-voltage electroporation (*e.g.*, 500 V [27]), ECL requires significantly lower voltages (*e.g.*, 2–5 V [7,8,26,28,29]), which avoids joule heating, and thereby, can

* Corresponding author.
E-mail address: mrh@caltech.edu (M.R. Hoffmann).

https://doi.org/10.1016/j.electacta.2020.135864

be easily applied under resource limited conditions encountered in remote field sampling locations. However, we note that the aforementioned studies of ECL were mainly focused on clinical samples (*e.g.*, human cells [7,26]), and conducted in well-controlled systems with purified buffers. Furthermore, all of these studies highlighted in the development of micro-scale devices with microliter or even nanoliter throughput. It is important to understand if ECL can be used for other target cells with more common throughput that are related to more extensive applications, *e.g.,* environment, food and agriculture, *etc.*

Herein, we now report on the development and application of an ECL device that functions using a small sample volume (~1 mL). Our overarching goal is to determine the DNA extraction efficiencies as a function of the key operational parameters (*i.e.*, pH ranges with varied treatment durations) for the use of ECL, as applied to DNA extraction and PCR amplification of gram-positive and gram-negative bacteria in real surface water and wastewater.

2. Experimental

2.1. Reagents

Sodium sulfate (Na_2SO_4) was purchased from EMD Millipore Corporation (Germany). Hydrochloric acid (HCl) and sodium hydroxide (NaOH) were purchased from Sigma-Aldrich (USA). 50 mM Na_2SO_4, HCl with varied concentrations (0.1 mM, 1 mM, 10 mM, 100 mM and 1 M) and NaOH with varied concentrations (0.1 mM, 1 mM, 10 mM, 100 mM and 1 M) were prepared using $\geq$ 18 MΩ Milli-Q water produced from a Millipore system (Millipore Co., USA). PBS (Gibco™, 1×, pH 7.2) was purchased from Thermo Fisher Scientific (USA). Luria-Bertani (LB) Broth, Tryptic Soy Broth (TSB), Brain Heart Infusion (BHI) Broth and Nutrient Broth (NB) were purchased from Becton, Dickinson and Company (USA). Nuclease free water for PCR was purchased from Promega Corporation (USA).

2.2. Bacterial sample preparation

The gram-negative bacteria species, *Escherichia coli* (ATCC 10798, *E. coli*), *Salmonella* Typhi (ATCC CVD909, *S.* Typhi), and gram-positive bacteria species, *Bacillus subtilis* (ATCC 6051, *B. subtilis*) and *Enterococcus durans* (ATCC 6056, *E. durans*) were cultivated at 200 rpm (Innova 42 Incubator Shaker, New Brunswick Scientific, USA) for 12–14 h to log-phase growth at the optical density at $\lambda = 600$ nm (OD_{600}) of 0.6–1.0. *E. coli, S.* Typhi and *E. durans* were grown at 37 °C in LB, TSB and BHI media, respectively. *B. subtilis* was grown at 30 °C in NB media. After incubation, the bacterial cells were harvested by centrifugation (Eppendorf, Germany) at 5000 rpm, washed twice and resuspended in 50 mM Na_2SO_4 to a concentration of ~10^8 cells/mL (estimated by OD_{600} values).

2.3. Electrochemical cell lysis experiment

The ECL device consists of a dimensionally stable IrO_2/Ti anode (synthesis was reported previously [30]), a Ti cathode, and a cation exchange membrane (Nafion 117, Dupont, USA), as shown in Fig. 1a. This is a typical configuration for water electrolysis. The reactor was made of polycarbonate and a photograph of the ECL device is also shown in Fig. S1. The mechanism on the breakdown of microbial cell membrane by ECL is illustrated in Fig. 1b and c. The membrane separates the device into an anodic chamber (1.6 mL) and a cathodic chamber (0.8 mL). One outlet was added on the top of each chamber to enable gas ventilation. For ECL reactions, 50 mM Na_2SO_4 and bacterial suspensions were injected from the bottom into the anodic and cathodic chamber, respectively, using syringes. A constant direct current of 40 mA (16 mA/cm^2, Potentiostat, BioLogic Science Instruments, France) was applied for 30 s – 10 min. The cathodic effluents were collected, using syringes, after each reaction and the chambers were washed three times with DI water between each reaction. The pH values were measured for all cathodic effluents and initial samples with a pH meter (Orion Star A215, Thermo Fisher Scientific, USA) containing a semi-micro pH probe (Orion 9110DJWP, Thermo Fisher Scientific, USA).

2.4. Analysis of cell lysis by fluorescent microscope

Following ECL reaction, a 500 μL aliquot of each bacterial sample was harvested by centrifugation at 10,000g for 10 min at 20 °C. The resulting pellets were then washed with PBS three times and resuspended in PBS to a final volume of 500 μL. The Live/Dead Baclight Viability kit (Invitrogen by Thermo Fisher Scientific, USA) was used for bacterial staining. Two staining dyes are included in this kit, the green-fluorescent nucleic acid stain Syto9, which stains both live and dead cells, and the red-fluorescent nucleic acid stain propidium iodide (PI), which can penetrate and stain only dead cells due to their compromised membrane [31]. The viability of bacterial cells was monitored by these two dyes. PI-staining of dead cells does not indicate the complete rupture of cell membranes, but merely their permeability for PI. Since completely lysed cells cannot be stained by Syto9, the extent of cellular lysis was measured by counting cells stained by Syto9 before and after ECL, as shown in Eq. (1) below:

$$\textit{Lysis efficiency}\ (\%) = \frac{N_{\textit{total cells in initial sample}} - N_{\textit{total cells in ECL sample}}}{N_{\textit{total cells in initial sample}}} \times 100 \quad (1)$$

where N is the counted number of the cells that stained by Syto9. According to the manufacturer's instruction, equal volumes (1.5 μL) of Syto9 (0.33 mM) and PI (2 mM) were added into each 100 μL sample. Each stained sample was added onto a glass slide with cover and examined under a fluorescence microscope (Leica DMi8, Germany). An objective with × 20 magnification was used for analyses. Five images were randomly taken from different areas on each slide and counted by ImageJ software (National Institute of Health, USA).

2.5. DNA quantification by qPCR

To measure the DNA released by ECL, the suspended DNA was collected from the supernatant of each sample by centrifugation at 10,000g for 10 min. As a negative control, an aliquot of the initial sample without ECL was treated in the same way to remove all the cells. Another aliquot of the initial sample was extracted for each bacterial strain using a commercial DNA extraction kit (PureLink® Genomic DNA Mini Kit, Invitrogen by Thermo Fisher Scientific, USA) as a positive control. Real-time PCR (qPCR, MasterCycler RealPlex 4, Eppendorf, USA) was used to quantify the presence of the universal bacterial 16S rRNA gene and to analyze DNA extraction efficiency for all the above samples. Each sample was tested in triplicates, using a similar protocol as reported previously [3,32]. The protocol was also briefly described in the Supporting Information, along with other necessary information for qPCR quantification including amplification curves (Fig. S2), qPCR standard curves and PCR efficiencies (Fig. S3). The cycle numbers above the background fluorescence threshold (C_T) were directly measured and analyzed after PCR reaction, using instrument specific software (Eppendorf, USA). The higher the DNA concentration in the template, the lower the C_T value because the background threshold can be reached with less

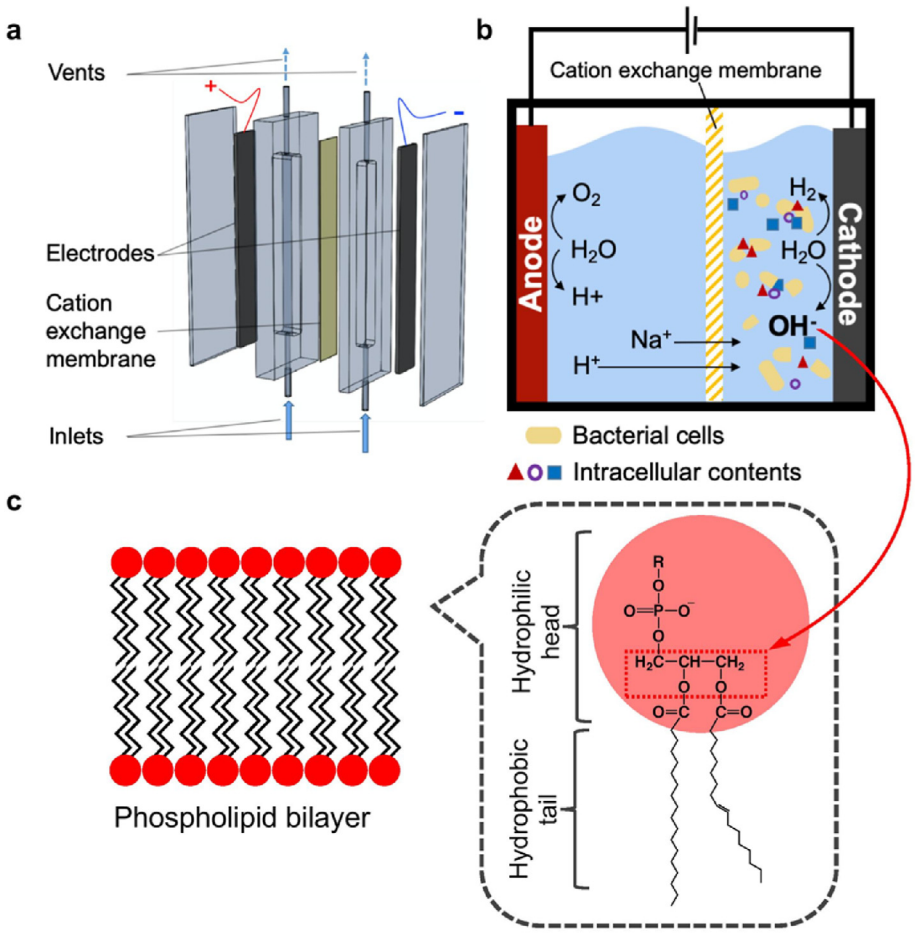

Fig. 1. Device and mechanism of electrochemical cell lysis. (a) Electrochemical cell lysis device. (b) Schematics of electrochemical cell lysis with cation exchange membrane between anodic and cathodic chambers. (c) Phospholipid bilayer, the major component of bacterial cell membranes, and the chemical structure of phospholipids. The fatty acid-glycerol ester bonds in phospholipids (highlighted in red box) can be hydrolyzed by the locally generated OH^- at cathode. (For interpretation of the references to colour in this figure legend, the reader is referred to the Web version of this article.)

cycles of PCR amplification. To evaluate the DNA extraction efficiency, ΔC_T values of the ECL treated samples were calculated by subtracting C_T values of the suspended DNA in the ECL treated samples from those in the untreated ones. With a comparison, ΔC_T values of the samples extracted by the commercial kit were calculated similarly, by subtracting C_T values of the total DNA extracted by the commercial kit from those of the suspended DNA in the untreated samples. For each bacterial strain, the higher ΔC_T values were expected for higher DNA extraction efficiency.

2.6. pH effect tests

The investigation of pH effects on cell lysis was conducted for one gram-negative bacterial species (*E. coli*) and one gram-positive species (*E. durans*) without ECL reaction. *E. coli* and *E. durans* were cultivated as described above. Then, several aliquots of 1 mL bacteria suspensions were harvested by centrifugation at 5000 rpm to obtain pellets. After removal of the culture media, 500 μL of NaOH with different concentrations (0.1 mM, 1 mM, 10 mM, 100 mM and 1 M) were directly added to the cell pellets, respectively, and resuspended immediately. As a negative control, 1 mL of 50 mM Na_2SO_4 was added to the cell pellets of initial samples for both species and mixed well. 500 μL of HCl with varied concentrations (0.1 mM, 1 mM, 10 mM, 100 mM and 1 M) were then added to neutralize the alkaline samples, correspondingly, after different sample contact times with alkaline solution (30 s, 1 min, 2 min, 5 min and 10 min). All the neutralized samples were centrifuged at 10,000g for 10 min to remove all the intact cells. The supernatants were then purified by the PureLink® Genomic DNA Mini Kit. An aliquot of the control was extracted by the same commercial DNA extraction kit as a comparison. Another aliquot was treated the same as other samples after alkaline lysis. Then all the purified samples were quantified by qPCR and ΔC_T values were calculated with the same methods described in the section of DNA quantification by qPCR.

2.7. Electrochemical cell lysis of bacteria in environmental water samples

Three different environmental water samples were tested to evaluate the performance of the ECL technique on DNA extraction of bacteria from ambient environmental water. Pond water was collected from the turtle pond at Caltech campus (Pasadena, CA). The treated and untreated latrine wastewater was collected from a previously described solar-powered recycling electrochemical toilet system located at Caltech with 550 mg/L of chemical oxygen demand (COD) and 28 mM NH_4^+ as major pollutants [33,34]. The latrine wastewater was treated by an electrochemical oxidation process to remove >90% of NH_4^+ and COD. Effluent was collected and denoted as “treated water” in this study. Pond water was

directly added into the cathodic chamber for ECL reaction, without any pretreatment while 50 mM Na_2SO_4 was added into the anodic chamber. Both types of wastewater samples were first filtered, using sterilized filter papers with 8.0 μm pore size (diameter, 55 mm; Cat No., 1002 055; Whatman) to remove big particles and to enhance the reproducibility between each experiment. Then the filtered wastewater was added into cathodic chamber for ECL reaction while 50 mM Na_2SO_4 was added into the anodic chamber. The suspended DNA of total bacteria from all the environmental water samples were then collected by centrifugation at 10,000g for 10 min. All the above environmental water samples were also extracted by the same commercial DNA extraction kit (PureLink® Genomic DNA Mini Kit) as the positive control. The same qPCR method was used for DNA quantification and evaluation of DNA extraction efficiency.

3. Theory and simulations

COMSOL Multiphysics (COMSOL Inc., USA), a commercial finite element modeling software, was used to study the fate and transport of hydroxide ions inside the cathodic chamber. The fluid in the cathodic chamber was modeled as a $3 \times 5 \times 50$ mm^3 block, with the electrode surface and the cation exchange membrane represented by the two 5×50 mm^2 sides. The gas vent hole on the top was represented by a cylindrical extrusion with a diameter of 1 mm and a height of 0.1 mm. OH^- and H^+ are generated with the hydrogen and oxygen evolution reactions at the cathode and anode, respectively:

$$\text{anode: } 2H_2O \leftrightarrow 4H^+ + 4e^- + O_2 \quad (2)$$

$$\text{cathode: } 4H_2O + 4e^- \leftrightarrow 4OH^- + 2H_2 \quad (3)$$

The generation and venting of H_2 during electrolysis induces fluid movements in the cathodic chamber. The resulting flow field was first calculated and then, the convective and diffusive OH^- transport was simulated. Molar influx of H_2 gas at the cathode surface was theoretically half of the OH^- generation rate R_{in}^{cat}, which was calculated by Ref. [35]:

$$R_{in}^{cat} = \frac{i}{nFA} \quad (4)$$

where i is the supplied current (40 mA), n is the number of electrons used to generate a hydroxide ion, which is 1, F is the Faraday constant, and A is the surface area. Simultaneously, H^+ was produced at the anode surface at the same rate as OH^- was generated, and cations were forced across the cation exchange membrane. It was assumed that sodium ions were the dominant species transported across the membrane due to their concentration dominance over protons, until sodium ions were depleted to a concentration comparable to the protons; at this point protons were the preferred ions for membrane transport due to their smaller size. For the cathodic chamber, the influx of H^+ was considered as the sink of OH^- and the contribution of water dissociation was negligible to mass transfer trough the membrane [36–38]. With the initial pH set at 7.5, time-dependent OH^- concentration profiles were simulated over the whole geometry. The transient pH profiles of the vertical mid-plane across the electrode and the membrane were generated, while the bulk solution pH was estimated from the volume average of [OH^-]. More details on the modules and equations used in this simulation are shown in the Supporting Information.

4. Results and discussion

4.1. Electrochemical cell lysis of different bacteria

Four different bacteria, *E. coli*, *S.* Typhi, *B. subtilis* and *E. durans*, with the initial concentrations of approximately 10^8 cells/mL were effectively lysed using the ECL method at different durations. ΔC_T values of 4 different bacteria treated by ECL with 30 s-10 min are shown in Fig. 2, along with a comparison of those extracted by the commercial kit. After 30 s of ECL, the averaged ΔC_T values of all the bacterial strains were significantly increased to 3.6–8.1. The highest ΔC_T values of the ECL treated bacterial samples all lied in the duration of 1 min as the optimized ECL condition, with the range of 6.5–9.8. In general, the DNA extraction efficiencies of all the bacterial cells decreases after 2 min of ECL. This could be mainly due to DNA damage during ECL process (*e.g.*, the local high pH which will be further discussed later with simulation in this study), as we preclude PCR inhibition caused by electrolyzed cathodic effluents. The details are described in Supporting Information, Fig. S4 and Fig. S5. The pH of the catholyte increased rapidly from the average of 7.4 (±0.2) to 12.5 (±0.1) after 1 min of ECL, which is consistent with the increase of ΔC_T values. It confirms that the generation of OH^- at cathode is the mechanism of ECL. All the PCR mixtures containing cathodic effluents (after ECL) were able to be adjusted to a pH range of 8.4–8.7 by the PCR reagents prior to qPCR measurements. Thus no additional neutralization step was necessary before detection. The optimized ECL duration of 1 min is much faster than most of the commercial DNA extraction kits based on chemical lysis (*e.g.*, at least 30 min for lysis step with the PureLink® Genomic DNA Mini Kit) [39]. The optimal processing time by ECL is also faster than the typical processing time of 5–30 min by the bead beating method, when using a flat pad vortex mixer, which is the least expensive bead beating technique [40,41]. In addition, the required voltage input is *ca.* 5 V, which is ~10–1000 fold lower than that of electrical lysis, reported previously [17,42–44].

DNA extraction by ECL was especially efficient for the 2 gram-negative bacterial strains. The averaged ΔC_T values increased to 9.8 and 9.7 with 1 min of ECL for *E. coli* and *S.* Typhi, respectively. There is no significant difference between the ΔC_T values of the samples treated by 1 min of ECL and of those extracted by the commercial kit ($P = 0.72$ for *E. coli* and $P = 0.48$ for *S.* Typhi). Lower DNA extraction efficiencies were observed for the 2 gram-positive bacterial strains with the optimized 1 min of ECL. Compared to the samples extracted by the commercial kit, the differences of ΔC_T values ($= \Delta C_{T,\text{ commercial kit}} - \Delta C_{T,\text{ 1 min of ECL}}$) are 1.8 and 2.9 for *B. subtilis* and *E. durans*, respectively. However, the ΔC_T values after 1 min of ECL were still increased significantly to 7.9 and 6.5 for *B. subtilis* and *E. durans*, respectively, which was sufficient for downstream qPCR detection in this study. The lower lysis efficiency for gram-positive bacteria than for gram-negative bacteria was not only observed by using ECL in our present study, but also by other lysis methods reported previously. For example, a lysis method based on cold atmospheric-pressure plasma was reported to have only 0.6 $\log_{10}$ reduction for *B. subtilis* after 10 min treatment, while 3.3–3.6 $\log_{10}$ reduction for other 3 gram-negative bacteria with the same treatment duration [45]. And 10–100 times higher detection limits were determined for gram-positive bacteria than for gram-negative bacteria by applying a hybrid chemical/mechanical lysis method on a microfluidic chip [46]. The differences in DNA extraction efficiency between the gram-positive and gram-negative bacteria can be explained by their different cell wall structures. The cell walls of gram-negative bacteria are composed of phospholipid bilayers (*i.e.*, cell membranes) that can be readily hydrolyzed by hydroxide ions, while the cell walls of the gram-positive bacteria are predominantly composed of multilayers of peptidoglycan,

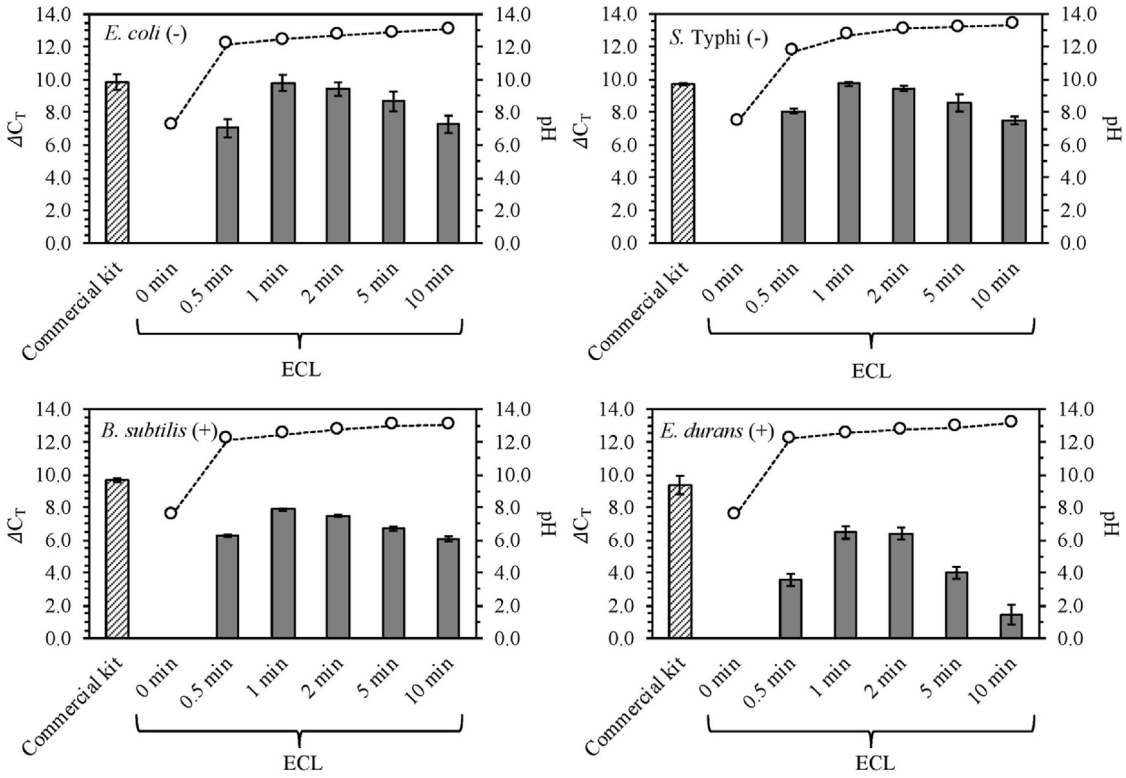

Fig. 2. ΔC_T values of 4 different bacterial cells lysed by ECL as a function of times (▭) and of those extracted by a commercial DNA extraction kit (▨) as a comparison; and the average pH values measured in the cathodic effluents (-○-). For the ECL treated samples, ΔC_T values were calculated by subtracting C_T values of the suspended DNA in ECL treated samples from those in the untreated samples. For the samples extracted by the commercial kit, ΔC_T values were calculated by subtracting C_T values of the total DNA extracted by the commercial kit from those of the suspended DNA in the untreated samples.

which provide stronger protection for gram-positive bacteria [47–49]. In addition, the cell wall thickness of gram-positive bacteria (*e.g.*, ~55.4 nm for *B. subtilis* [50–52]) is generally much higher than that of gram-negative bacteria (*e.g.*, ~8.2 nm for *Enterobacter cloacae* [53,54]) as well.

The successful cell lysis by ECL was further confirmed for all the bacteria via fluorescence microscopy. The fluorescence images visualizing the bacteria viability with ECL treatment, monitored by PI (in red) and Syto9 (in green), are shown for *E. coli* as an example in Fig. 3. It was observed clearly that cells were completely lysed by ECL after the cell death. Because the number of dead cells (in red) significantly increased after only 30 s of ECL, but reduced after 1 min. So did most of the total intact cells (in green) disappear after 1 min, which is an evidence for complete cell wall breakdown. The images in fluorescent green also show that the number of total intact cells decreased significantly after 30 s of ECL and only a few can be observed after 1 min, which has an agreement with the increase of ΔC_T values measured by qPCR. The cell numbers for both live and dead cells were calculated for all the bacteria with different ECL durations and are shown in Fig. S6. For gram-negative bacteria, the lysis efficiencies are close to 100% after 2 min of ECL, while efficiencies over 50% for both of the gram-positive bacteria were

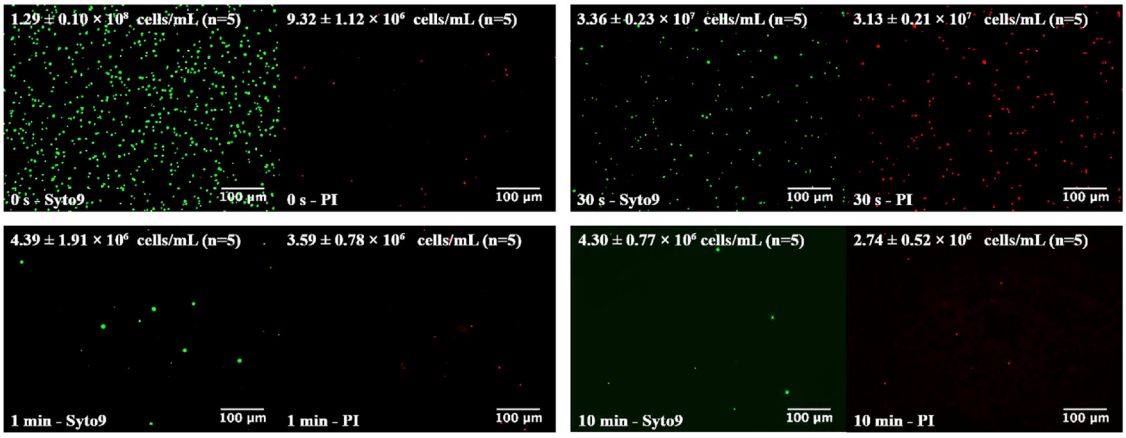

Fig. 3. Fluorescent microscope images of *E. coli* cells stained by Syto9 (green) and PI (red) with different durations of ECL. (For interpretation of the references to colour in this figure legend, the reader is referred to the Web version of this article.)

obtained after 5 min. The lysis efficiencies keep increasing over time until an apparent equilibrium is achieved. Apparently, the cell number measurement by fluorescent microscope showed the efficient performance of ECL on cell lysis more straightforwardly, due to the absence of complex factors related to DNA detection, *e.g.*, potential DNA damage after release from cells and PCR inhibition.

4.2. pH effects on cell lysis and DNA extraction

To further understand how pH affects cell lysis and DNA extraction, bacterial cells were treated by homogeneous alkaline lytic reagent at various pH values, *i.e.*, NaOH with varied concentrations of 0.1 mM−1 M, without ECL. *E. coli* and *E. durans* were selected as models for gram-negative and gram-positive bacteria, respectively. Homogeneous alkaline lysis is not efficient for *E. durans* at all investigated pH values (10−14). The ΔC_T values of *E. durans* treated by NaOH were all lower than 3.0 (data not shown), while those extracted by the commercial kit were 11.6 as an average. The ΔC_T values of *E. coli* cells treated by NaOH at varied pH from 10 to 14 as a function of contact times, are shown in Fig. 4. *E. coli* cells were barely lysed at pH 10 with ΔC_T values close to 0, while higher DNA extraction efficiency was observed at pH 11 with ΔC_T values around 2. Among all the conditions, the highest DNA extraction efficiency for *E. coli* cells was achieved at pH 13 with an averaged ΔC_T value of 5.6 at 2 min contact time. However, ΔC_T values decreased at contact times longer than 2 min. When pH increased to an even higher level, *i.e.*, at pH 14, C_T values of NaOH treated cells were even lower than initial samples after 2 min of contact time, although the samples were neutralized after a defined contact time. Consequently, ΔC_T values were negative and cannot be seen in Fig. 4. This suggests that the DNA might be damaged by high pH conditions above pH 13, which has an agreement with the DNA damage observed in the ECL experiments with longer durations than 2 min. On the other hand, there was no decrease of ΔC_T values observed for NaOH treated *E. coli* cells at pH 12 within contact times of 10 min. The ΔC_T values at pH 12 were quite close to those at pH 13 after 5 min of contact time and even out performed those at pH 13 later on. Therefore, it appears that a pH between 12 and 13 may provide optimal conditions for DNA extraction from bacterial cells; this result is consistent with a previously reported optimal pH range of 11.5−12.5 for cell lysis [8,55]. Plasmid DNA isolation via alkaline lysis was also previously reported to be most efficient within a pH range of 12.0−12.6 [56,57]. These values are also in good agreement with the bulk pH (12.47−12.76) measured under optimized conditions during ECL extraction.

As a comparison, the highest averaged ΔC_T value achieved by alkaline lysis (pH 13, 2 min) is 4.2 less than of that measured after 1 min of ECL, as highlighted in Fig. 4. And *E. coli* cells extracted by the commercial kit in this pH test were detected as similar ΔC_T values (9.7 ± 0.3) to those treated by 1 min of ECL. Besides, ECL is also capable of lysing gram-positive bacteria while conventional alkaline lysis cannot. Although the released DNA could be damaged by the high pH raised with longer ECL duration, the lysis of bacterial cells could also be benefited from the local high pH generated at cathode during ECL process. These results emphasize that the ECL method is faster and much more efficient for DNA extraction from gram-negative and gram-positive bacterial cells, compared to alkaline cell lysis.

4.3. Simulations of pH profiles at the cathode

To gain more mechanistic insight of the ECL process, pH profiles for the vertical mid-plane of the cathodic chamber were simulated for different contact times and are shown in Fig. 5a. These simulations show that the local pH value near the cathode surface increases rapidly within 1 min of ECL and that an ideal pH range for cell lysis (pH 12−13) is predicted. After 2 min of ECL operation, the pH in most of the upper volume reaches 13. This simulation is consistent with the DNA loss observed during ECL tests on different bacteria. Hydrogen gas is also generated, as protons are consumed and OH^- is produced at the cathode surface. Gas evolution helps mixing the solution (the calculated flow field is shown in Fig. S7), which in turn leads to a larger volume that has a suitable pH for cell lysis after 30 s and 1 min of operation (Fig. 5a). The simulated pH profiles for the bulk-phase cathodic solutions as a function of time is shown in Fig. 5b. The simulation results are in line with the measured bulk pH values of the cathodic effluents during different ECL tests. The results also highlight that there is a higher pH at the cathode surface than in the bulk electrolyte. It is speculated that cells were efficiently lysed near the cathode surface as we discussed earlier in this study. The released DNA molecules with negative charge were likely repelled from the cathode, and subsequently preserved in the bulk electrolyte at a lower pH. This may explain the much more efficient DNA extraction by ECL than that by direct alkaline lysis, which was found in the pH effect tests (*vide supra*). Detailed understanding of this phenomenon awaits further study.

4.4. Electrochemical cell lysis in environmental water

Fig. 6 shows the optimal ΔC_T values of total bacteria in natural pond water, treated and untreated latrine wastewater treated by ECL, with the comparison of those of *E. coli* (~10^8 cells/mL) in 50 mM Na_2SO_4 treated by ECL (*vide supra*). The initial cell concentrations of total bacteria were approximately 8.0 × 10^5,

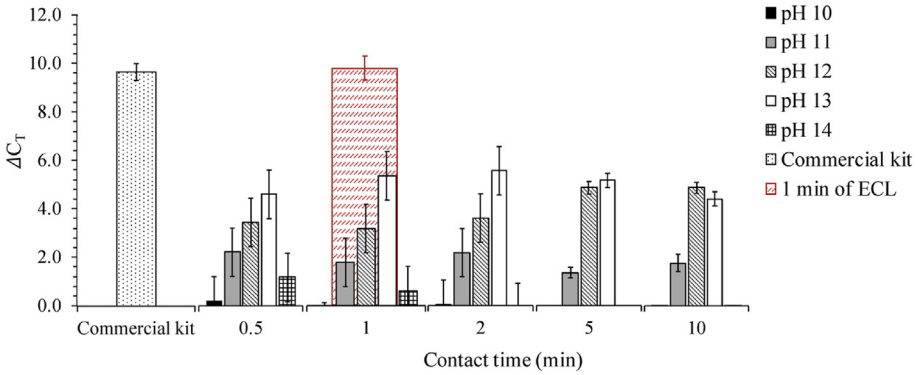

Fig. 4. ΔC_T values of *E. coli* cells under varied pH conditions as a function of contact times, with comparison of those extracted by the commercial DNA extraction kit and 1 min of ECL.

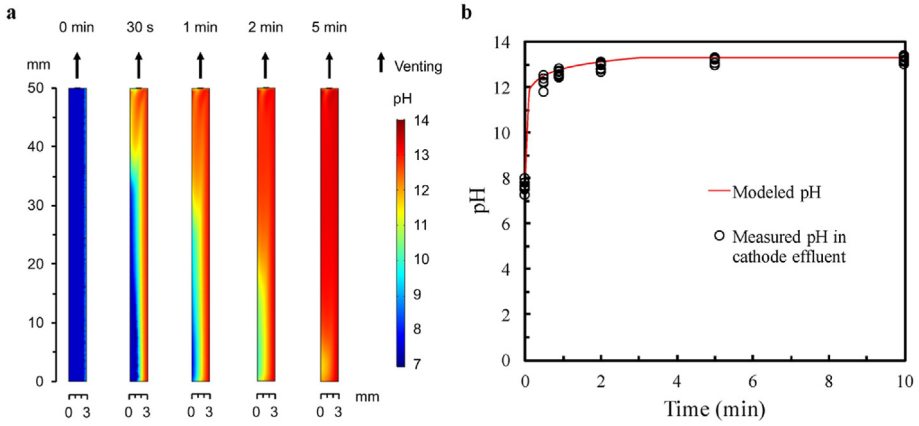

Fig. 5. Computational simulation results for the distribution of pH in the cathodic ECL chamber and corresponding pH values of cathodic effluents. (a) Simulation of pH value distribution for the vertical mid-plane in the cathodic chamber with the cation exchange membrane on the left and the cathode on the right. (b) Modeled and measured pH for the cathode effluents as a function of electrochemical reaction time.

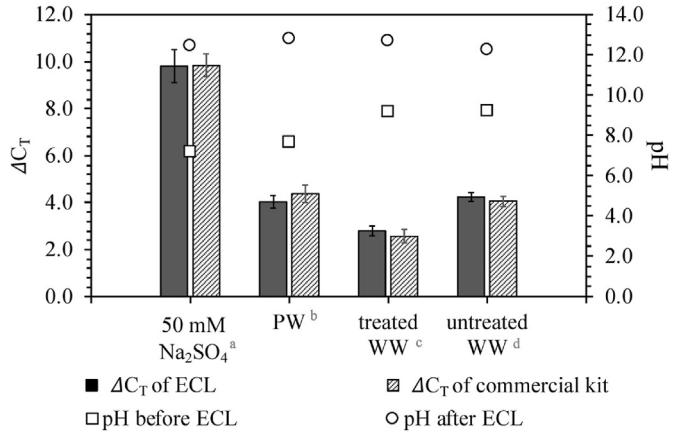

[a] ΔC_T of *E.coli* cells (~ 1×10^8 cells/mL) in 50 mM Na_2SO_4 with 1 min of ECL.
[b] ΔC_T of total bacteria in pond water with 1 min of ECL.
[c] ΔC_T of total bacteria in treated wastewater with 10 min of ECL.
[d] ΔC_T of total bacteria in untreated wastewater with 15 min of ECL.

Fig. 6. ΔC_T values of bacterial cells in 50 mM Na_2SO_4, pond water (PW), treated wastewater (treated WW) and untreated wastewater (untreated WW) extracted by ECL and the commercial kit.

3.0×10^6, 2.1×10^7 cells/mL for pond water, treated and untreated wastewater, respectively, as measured by qPCR with the calibration curve of *E. coli* (shown in Fig. S3). The optimal DNA extraction efficiency achieved ΔC_T values of 4.4 ± 0.4 for pond water after 1 min of ECL. For the treated and the untreated wastewater samples, the optimal ΔC_T values of 2.6 ± 0.3 and 4.1 ± 0.2 were obtained after 10 min and 15 min of ECL, respectively. These results show that the bacteria in both pond water and wastewater were rapidly and efficiently lysed by ECL with ΔC_T values comparable to those obtained with the commercial kit. The differences of ΔC_T values between ECL and the commercial kit are generally less than 0.3 for different water types. Clearly, the required lysis/extraction times for environmental water samples are longer than those for pure cell samples reported herein. It could be mainly taken account of the more complex composition in real environmental water samples which has buffer capacity. Therefore, it takes longer reaction time to achieve the ideal pH range for cell lysis in the cathodic chamber. For example, it was reported previously that there was 17 mM of $HCO_3^- + CO_3^{2-}$, 0.6 mM of total phosphate and 13 mM of NH_4^+, with buffer capacity of 0.79, 0.09 and 2.71 mequiv/(L· pH), respectively, for the wastewater collected from the same onsite electrochemical wastewater treatment system as this study [58]. However, the ECL process is still much faster than most of the conventional DNA extraction kits (*vide supra*), additionally with much more simplified operational procedure.

The optimized DNA extraction efficiencies for the environmental water samples by ECL treatment were in a pH range from 12 to 13. These results suggest that the pH can be used as an indicator to determine the optimal residence time of ECL for DNA extraction in the field. Additionally, in this study, a centrifugation step (at 10,000g for 10 min) was applied after each ECL reaction because the cell lysis by PCR process needs to be excluded for measuring the DNA extraction efficiency by ECL *per se*. The thermal cycling process of PCR could also cause some of the cells lysed and thereby increased the DNA extraction efficiency. Fig. S8 shows that the qPCR C_T values are 0.4–1.0 lower for different environmental water samples without any further treatment after the optimized ECL than with the centrifugation step. This result is somewhat counter-intuitive since higher C_T values (lower DNA concentrations) were expected for the samples without post-ECL treatment due to the potential inhibitors in environmental samples. However, any post-treatments after lysis could also cause sample loss, which might explain the lower C_T values (higher DNA concentrations) detected in this study. Therefore, for application of ECL in the field, the centrifugation after ECL might not be necessary. In case that a treatment might be necessary to reduce PCR inhibition, a filtration step with a 0.2 μm syringe filter (13 mm, nylon, Pall Corporation, USA) was also tested after ECL as an alternative post-treatment to centrifugation. Because it is much easier to be realized in the field. Centrifugation and filtration as a post-ECL step resulted in no significant differences of qPCR C_T values ($P = 0.62$, 0.25 and 0.48 for pond water, treated and untreated wastewater, respectively) for the three different types of environmental water samples (shown in Fig. S8).

5. Conclusion

In summary, we developed an ECL device for the rapid extraction of DNA from waterborne bacteria, using low-cost materials. The efficient cell lysis by ECL was demonstrated for both gram-positive and gram-negative bacteria with a short but optimal lysis duration of 1 min, at a constant DC of 40 mA (~5 V of voltage). Extraction by ECL was more efficient and quicker than direct

alkaline lysis. The successful application of ECL on different environmental water samples suggests the potential application of ECL as a rapid and reagent-free sample preparation technique with a low voltage requirement for microbial monitoring in the field. In addition, ECL as applied to cell lysis has the potential to significantly reduce the overall cost for nucleic acid-based microbial monitoring. For example, a conventional DNA extraction kit, based on chemical lysis, *e.g.*, PureLink® Genomic DNA Mini Kit, costs approximately $3 per preparation, using the required instrumentation (*e.g.*, centrifuge ($2000–20,000 provided by Eppendorf) and vortex mixer (>$300 available through VWR)). The bead beating method costs *ca.* $2 per sample prep using 0.1 mm diameter beads (Gene Rite, LLC) and a bead milling instrument with a price range from $300 to $12,000 [59–63]. The ECL device developed in this study, on the other hand, can be produced for as little as $4.20 per unit. The estimated total cost includes a) polycarbonate reactor ($0.44), b) an anode ($0.8 for an IrO_2/Ti anode with an estimated lifetime of 4.3 yrs at 25 mA/cm^2, as reported previously [30]), c) $0.54 for the Ti-cathode and, d) a cation exchange membrane ($2.42 for Nafion 117 with estimated lifetime of >60,000 h [64,65]). For field sampling, the ECL device can be powered by 4 AA batteries that should cost less than $1 for typical alkaline batteries.

Declaration of competing interest

There are no conflicts of interest to declare.

CRediT authorship contribution statement

Siwen Wang: Investigation, Data curation, Formal analysis, Writing - original draft. **Yanzhe Zhu:** Methodology, Software, Writing - original draft. **Yang Yang:** Conceptualization, Methodology, Writing - review & editing. **Jing Li:** Writing - review & editing. **Michael R. Hoffmann:** Supervision, Funding acquisition, Writing - review & editing.

Acknowledgements

This research was supported by the Bill and Melinda Gates Foundation, Seattle, WA [OPP1111252].

The authors acknowledge Xingyu Lin, Katharina Urmann and Jared R. Leadbetter, for their helpful discussion and critical reviews of our manuscript. We also thank Clement Cid and Nissim Gore-Datar for their help on the sampling of latrine wastewater.

Appendix A. Supplementary data

Supplementary data to this article can be found online at https://doi.org/10.1016/j.electacta.2020.135864.

References

[1] C. Zhang, J. Ma, D. He, T.D. Waite, Capacitive membrane stripping for ammonia recovery (CapAmm) from dilute wastewaters, Environ. Sci. Technol. Lett. 5 (2018) 43–49.
[2] C.A. Cid, J.T. Jasper, M.R. Hoffmann, Phosphate recovery from human waste via the formation of hydroxyapatite during electrochemical wastewater treatment, ACS Sustain. Chem. Eng. 6 (2018) 3135–3142.
[3] H.T. Ahangari, T. Portail, A.T. Marshall, Comparing the electrocatalytic reduction of CO_2 to CO on gold cathodes in batch and continuous flow electrochemical cells, Electrochem. Commun. 101 (2019) 78–81.
[4] X. Xie, S. Wang, S.C. Jiang, J. Bahnemann, M.R. Hoffmann, Sunlight-activated propidium monoazide pretreatment for differentiation of viable and dead bacteria by quantitative real-time polymerase chain reaction, Environ. Sci. Technol. Lett. 3 (2016) 57–61.
[5] C.A. Heid, J. Stevens, K.J. Livak, P.M. Williams, Real time quantitative PCR, Genome Res. 6 (1996) 986–994.
[6] J. Kim, J. Lim, C. Lee, Quantitative real-time PCR approaches for microbial community studies in wastewater treatment systems: applications and considerations, Biotechnol. Adv. 31 (2013) 1358–1373.
[7] D. Di Carlo, C. Ionescu-Zanetti, Y. Zhang, P. Hung, L.P. Lee, On-chip cell lysis by local hydroxide generation, Lab Chip 5 (2005) 171–178.
[8] H.J. Lee, J.-H. Kim, H.K. Lim, E.C. Cho, N. Huh, C. Ko, J. Chan Park, J.-W. Choi, S.S. Lee, Electrochemical cell lysis device for DNA extraction, Lab Chip 10 (2010) 626–633.
[9] S. Jaikla, T. Maturos, T. Pogfay, C. Neatpisarnvanit, P. Sritongkham, A. Tuantranont, On-chip Irreversible Electroporation for Bacterial Cell Membrane Rupture, IEEE, 2012, pp. 1–5.
[10] T.Y. Tsong, Electroporation of cell membranes, Biophys. J. 60 (1991) 297–306.
[11] H. Lu, M.A. Schmidt, K.F. Jensen, A microfluidic electroporation device for cell lysis, Lab Chip 5 (2005) 23–29.
[12] T. Geng, C. Lu, Microfluidic electroporation for cellular analysis and delivery, Lab Chip 13 (2013) 3803–3821.
[13] M. Shahini, J.T. Yeow, Cell electroporation by CNT-featured microfluidic chip, Lab Chip 13 (2013) 2585–2590.
[14] M. Poudineh, R.M. Mohamadi, A. Sage, L. Mahmoudian, E.H. Sargent, S.O. Kelley, Three-dimensional, sharp-tipped electrodes concentrate applied fields to enable direct electrical release of intact biomarkers from cells, Lab Chip 14 (2014) 1785–1790.
[15] C.M. Gabardo, A.M. Kwong, L. Soleymani, Rapidly prototyped multi-scale electrodes to minimize the voltage requirements for bacterial cell lysis, Analyst 140 (2015) 1599–1608.
[16] N. de Lange, T.M. Tran, A.R. Abate, Electrical lysis of cells for detergent-free droplet assays, Biomicrofluidics 10 (2016), 024114.
[17] J. Experton, A.G. Wilson, C.R. Martin, Low-voltage flow-through electroporation in gold-microtube membranes, Anal. Chem. 88 (2016) 12445–12452.
[18] H. Sedgwick, F. Caron, P.B. Monaghan, W. Kolch, J.M. Cooper, Lab-on-a-chip technologies for proteomic analysis from isolated cells, J. R. Soc. Interface 5 (2008) S123–S130.
[19] T. Kotnik, W. Frey, M. Sack, S. Haberl Meglič, M. Peterka, D. Miklavčič, Review: electroporation-based applications in biotechnology, Trends Biotechnol. 33 (2015) 480–488.
[20] U. Pliquett, Joule heating during solid tissue electroporation, Med. Biol. Eng. Comput. 41 (2003) 215–219.
[21] R.V. Davalos, B. Rubinsky, Temperature considerations during irreversible electroporation, Int. J. Heat Mass Tran. 51 (2008) 5617–5622.
[22] J. Gao, X.-F. Yin, Z.-L. Fang, Integration of single cell injection, cell lysis, separation and detection of intracellular constituents on a microfluidic chip, Lab Chip 4 (2004) 47–52.
[23] L. Nan, Z. Jiang, X. Wei, Emerging microfluidic devices for cell lysis: a review, Lab Chip - Miniaturisation Chem. Biol. 14 (2014) 1060.
[24] M. Shehadul Islam, A. Aryasomayajula, R.P. Selvaganapathy, A Review on Macroscale and Microscale Cell Lysis Methods, Micromachines vol 8 (2017).
[25] D.W. Graham, S. Olivares-Rieumont, C.W. Knapp, L. Lima, D. Werner, E. Bowen, Antibiotic resistance gene abundances associated with waste discharges to the almendares river near havana, Cuba, Environ. Sci. Tech. 45 (2011) 418–424.
[26] J.T. Nevill, R. Cooper, M. Dueck, D.N. Breslauer, L.P. Lee, Integrated microfluidic cell culture and lysis on a chip, Lab Chip 7 (2007) 1689–1695.
[27] H.-Y. Wang, A.K. Bhunia, C. Lu, A microfluidic flow-through device for high throughput electrical lysis of bacterial cells based on continuous dc voltage, Biosens. Bioelectron. 22 (2006) 582–588.
[28] S.K. Jha, G.-S. Joo, G.-S. Ra, H.H. Lee, Y.-S. Kim, Development of PCR microchip for early cancer risk prediction, IEEE Sensor. J. 11 (2011) 2065–2070.
[29] S.K. Jha, R. Chand, D. Han, Y.-C. Jang, G.-S. Ra, J.S. Kim, B.-H. Nahm, Y.-S. Kim, An integrated PCR microfluidic chip incorporating aseptic electrochemical cell lysis and capillary electrophoresis amperometric DNA detection for rapid and quantitative genetic analysis, Lab Chip 12 (2012) 4455–4464.
[30] Y. Yang, J. Shin, J.T. Jasper, M.R. Hoffmann, Multilayer heterojunction anodes for saline wastewater treatment: design strategies and reactive species generation mechanisms, Environ. Sci. Tech. 50 (2016) 8780–8787.
[31] L. Boulos, M. Prévost, B. Barbeau, J. Coallier, R. Desjardins, LIVE/DEAD®BacLight™: application of a new rapid staining method for direct enumeration of viable and total bacteria in drinking water, J. Microbiol. Methods 37 (1999) 77–86.
[32] Y. Zhu, X. Huang, X. Xie, J. Bahnemann, X. Lin, X. Wu, S. Wang, M.R. Hoffmann, Propidium monoazide pretreatment on a 3D-printed microfluidic device for efficient PCR determination of 'live versus dead' microbial cells, Environ. Sci.: Water Res. Tech. 4 (2018) 956–963.
[33] Y. Yang, M.R. Hoffmann, Synthesis and stabilization of blue-black TiO2 nanotube Arrays for electrochemical oxidant generation and wastewater treatment, Environ. Sci. Tech. 50 (2016) 11888–11894.
[34] J.T. Jasper, Y. Yang, M.R. Hoffmann, Toxic byproduct formation during electrochemical treatment of latrine wastewater, Environ. Sci. Tech. 51 (2017) 7111–7119.
[35] A.J. Bard, L.R. Faulkner, J. Leddy, C.G. Zoski, Electrochemical Methods: Fundamentals and Applications, Wiley New York, 1980.
[36] R. Simons, Strong electric field effects on proton transfer between membrane-bound amines and water, Nature 280 (1979) 824.
[37] J.J. Krol, M. Wessling, H. Strathmann, Concentration polarization with monopolar ion exchange membranes: current–voltage curves and water dissociation, J. Membr. Sci. 162 (1999) 145–154.
[38] Y. Tanaka, S.-H. Moon, V.V. Nikonenko, T. Xu, Ion-exchange membranes, Int. J. Chem. Eng. (2012), 2012.

[39] Invitrogen by Life Technologies, User Guide for PureLink® Genomic DNA Kit, For purification of genomic DNA, 2012.
[40] J.A.H. van Burik, R.W. Schreckhise, T.C. White, R.A. Bowden, D. Myerson, Comparison of six extraction techniques for isolation of DNA from filamentous fungi, Med. Mycol. 36 (1998) 299–303.
[41] C.W. Ho, W.S. Tan, W.B. Yap, T.C. Ling, B.T. Tey, Comparative evaluation of different cell disruption methods for the release of recombinant hepatitis B core antigen from Escherichia coli, Biotechnol. Bioproc. Eng. 13 (2008) 577–583.
[42] D.W. Lee, Y.-H. Cho, A continuous electrical cell lysis device using a low dc voltage for a cell transport and rupture, Sensor. Actuator. B Chem. 124 (2007) 84–89.
[43] M.M. Bahi, M.N. Tsaloglou, M. Mowlem, H. Morgan, Electroporation and lysis of marine microalga Karenia brevis for RNA extraction and amplification, J. R. Soc. Interface 8 (2010).
[44] S. Haberl, M. Jarc, A. Štrancar, M. Peterka, D. Hodžić, D. Miklavčič, Comparison of alkaline lysis with electroextraction and optimization of electric pulses to extract plasmid DNA from Escherichia coli, J. Membr. Biol. 246 (2013) 861–867.
[45] A. Mai-Prochnow, M. Clauson, J. Hong, A.B. Murphy, Gram positive and Gram negative bacteria differ in their sensitivity to cold plasma, Sci. Rep. 6 (2016) 38610.
[46] M. Mahalanabis, H. Al-Muayad, M.D. Kulinski, D. Altman, C.M. Klapperich, Cell lysis and DNA extraction of gram-positive and gram-negative bacteria from whole blood in a disposable microfluidic chip, Lab Chip 9 (2009) 2811–2817.
[47] L. Bruslind, Bacteria: Cell Walls, Microbiology (2018) 28–33. Chapter 4: Bacteria - cell walls.
[48] J.M. Ghuysen, R. Hakenbeck, Bacterial Cell Wall, Elsevier, 1994.
[49] S.M. Hammond, P.A. Lambert, A. Rycroft, The Bacterial Cell Surface, Springer Science & Business Media, 2012.
[50] V.R.F. Matias, T.J. Beveridge, Cryo-electron microscopy reveals native polymeric cell wall structure in Bacillus subtilis 168 and the existence of a periplasmic space, Mol. Microbiol. 56 (2005) 240–251.
[51] E.J. Hayhurst, L. Kailas, J.K. Hobbs, S.J. Foster, Cell wall peptidoglycan architecture in Bacillus subtilis, Proc. Natl. Acad. Sci. Unit. States Am. 105 (2008) 14603–14608.
[52] W. Vollmer, D. Blanot, M.A. De Pedro, Peptidoglycan structure and architecture, FEMS Microbiol. Rev. 32 (2008) 149–167.
[53] J.E. Coward, H.S. Rosenkranz, Electron microscopic appearance of silver sulfadiazine-treated Enterobacter cloacae, Chemotherapy 21 (1975) 231–235.
[54] G. Eumkeb, S. Chukrathok, Synergistic activity and mechanism of action of ceftazidime and apigenin combination against ceftazidime-resistant Enterobacter cloacae, Phytomedicine 20 (2013) 262–269.
[55] S.T.L. Harrison, Bacterial cell disruption: a key unit operation in the recovery of intracellular products, Biotechnol. Adv. 9 (1991) 217–240.
[56] H.C. Birnboim, J. Doly, A rapid alkaline extraction procedure for screening recombinant plasmid DNA, Nucleic Acids Res. 7 (1979) 1513–1523.
[57] H.C. Birnboim, A Rapid Alkaline Extraction Method for the Isolation of Plasmid DNA, Methods in Enzymology, Academic Press, 1983, pp. 243–255.
[58] C.A. Cid, J.T. Jasper, M.R. Hoffmann, Phosphate recovery from human waste via the formation of hydroxyapatite during electrochemical wastewater treatment, ACS Sustain. Chem. Eng. 6 (2018) 3135–3142.
[59] MP Biomedicals, LLC. website. FastPrep-24 5G™ high speed homogenizer. https://www.mpbio.com/.
[60] Biospec product Inc. website: mini bead beater. https://biospec.com.
[61] OMNI Inc. website. bead ruptor. https://www.omni-inc.com.
[62] Qiagen website. TissueLyser II. https://www.qiagen.com.
[63] T.R. Hopkins, Physical and chemical cell disruption for the recovery of intracellular proteins, Bioprocess Technol. (N. Y.) 12 (1991) 57–83.
[64] J. Rozière, D.J. Jones, Non-fluorinated polymer materials for proton exchange membrane fuel cells, Annu. Rev. Mater. Res. 33 (2003) 503–555.
[65] X. Cheng, C. Peng, M. You, L. Liu, Y. Zhang, Q. Fan, Characterization of catalysts and membrane in DMFC lifetime testing, Electrochim. Acta 51 (2006) 4620–4625.

Appendix B

ASYMMETRIC MEMBRANE FOR DIGITAL DETECTION OF SINGLE BACTERIA IN MILLILITERS OF COMPLEX WATER SAMPLES

Lin, X., Huang, X., Zhu, Y., Urmann, K., Xie, X., & Hoffmann, M. R. (2018). Asymmetric membrane for digital detection of single bacteria in milliliters of complex water samples. *ACS Nano*, *12*(10), 10281-10290. https://pubs.acs.org/doi/abs/10.1021/acsnano.8b05384

ACS NANO

Cite This: *ACS Nano* 2018, 12, 10281−10290

www.acsnano.org

ARTICLE

Asymmetric Membrane for Digital Detection of Single Bacteria in Milliliters of Complex Water Samples

Xingyu Lin,[†] Xiao Huang,[†] Yanzhe Zhu,[†] Katharina Urmann,[†] Xing Xie,[†,‡] and Michael R. Hoffmann*[,†]

[†]Linde + Robinson Laboratories, California Institute of Technology, Pasadena, California 91125, United States

[‡]School of Civil and Environmental Engineering, Georgia Institute of Technology, Atlanta, Georgia 30332, United States

Supporting Information

ABSTRACT: **In this work, we introduce an asymmetric membrane as a simple and robust nanofluidic platform for digital detection of single pathogenic bacteria directly in 10 mL of unprocessed environmental water samples. The asymmetric membrane, consisting of uniform micropores on one side and a high density of vertically aligned nanochannels on the other side, was prepared within 1 min by a facile method. The single membrane covers all the processing steps from sample concentration, purification, and partition to final digital loop-mediated isothermal amplification (LAMP). By simple filtration, bacteria were enriched and partitioned inside the micropores, while inhibitors typically found in the environmental samples (*i.e.*, proteins, heavy metals, and organics) were washed away through the nanochannels. Meanwhile, large particles, indigenous plankton, and positively charged pollutants in the samples were excluded by using a sacrificial membrane stacked on top. After initial filtration, modified LAMP reagents, including NaF and lysozyme, were loaded onto the membrane. Each pore in the asymmetric membrane functioned as an individual nanoreactor for selective, rapid, and efficient isothermal amplification of single bacteria, generating a bright fluorescence for direct counting. Even though high levels of inhibitors were present, absolute quantification of *Escherichia coli* and *Salmonella* directly in an unprocessed environmental sample (seawater and pond water) was achieved within 1 h, with sensitivity down to single cell and a dynamic range of 0.3−10000 cells/mL. The simple and low-cost analysis platform described herein has an enormous potential for the detection of pathogens, exosomes, stem cells, and viruses as well as single-cell heterogeneity analysis in environmental, food, and clinical research.**

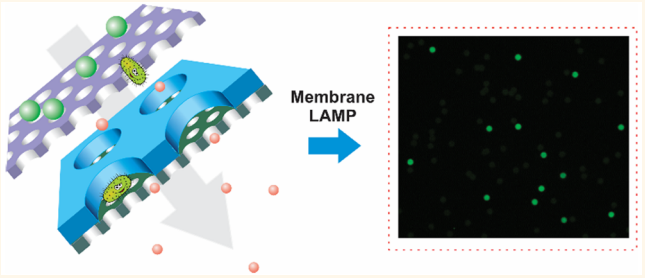

KEYWORDS: *asymmetric membrane, nanofluidics, pathogen detection, digital LAMP, single-molecule counting*

Intestinal parasitic infections and diarrheal diseases, which are caused by waterborne pathogens, have become a leading cause of morbidity and mortality, owing to insufficient hygiene and poor sanitation.[1,2] More than 2.2 million people die each year because of waterborne pathogen infections, with a resulting economic loss of nearly 12 billion U.S. dollars annually worldwide.[3] Given the low infectious dose of many waterborne pathogens, the presence of even a single bacterium in the environment may pose a serious health risk.[4] According to the U.S. Environmental Protection Agency (EPA), the concentration of *Escherichia coli* (*E. coli*) and *Enterococci* in environmental recreational samples should be less than 1.26 and 0.35 CFU/mL, respectively.[5] These strict standards require a detection method that is not only ultrasensitive but also quantitative and precise.

Culture-based methods remain the "gold standard" for bacteria identification and titration, although they require days to obtain the results and hardly differentiate bacteria at the species levels.[6] Quantitative real-time polymerase chain reactions (PCR) can shorten the time to several hours, but it requires expensive instrumentation and is poorly suited for absolute quantification.[7] Droplet-based microfluidics have emerged as promising methods for digital cell quantification, as well as single-cell heterogeneity analysis.[8,9] In this case, each cell is encapsulated into an individual droplet, and the specific cell information (*e.g.*, specific DNA,[10−18] RNA,[19−23] proteins,[24−26] enzymes,[27] metabolism,[28,29] and antibodies[30,31])

Received: July 17, 2018
Accepted: September 13, 2018
Published: September 13, 2018

DOI: 10.1021/acsnano.8b05384
ACS Nano 2018, 12, 10281−10290

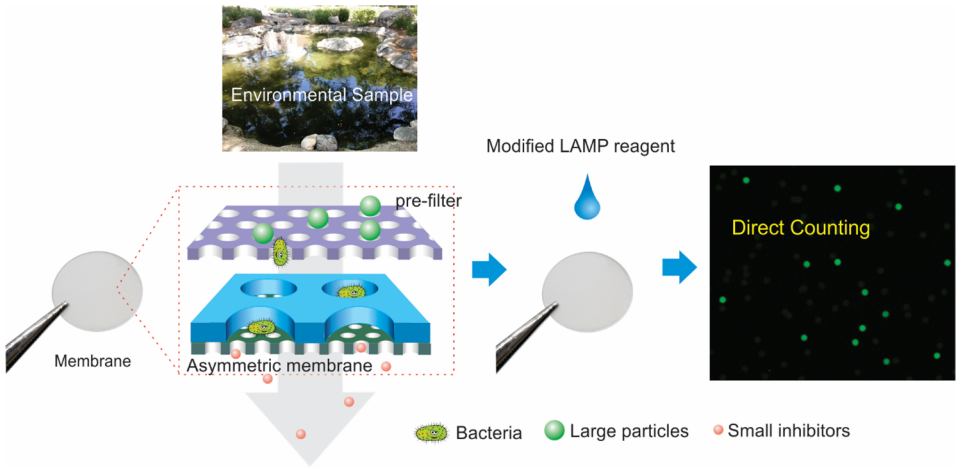

Figure 1. Schematic illustration of heterogeneous membrane for digital bacteria detection from complex environmental samples.

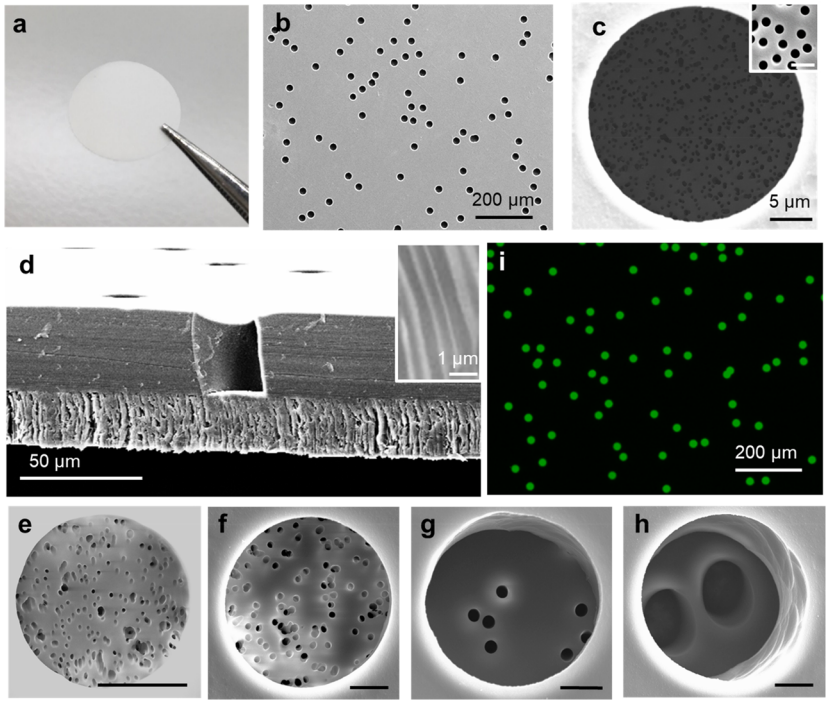

Figure 2. (a) Photograph of the asymmetric membrane. (b) SEM top-view image of the asymmetric membrane. (c) High-magnification top-view SEM image of one micropore. The inset shows the magnified image with a scale bar of 1 μm. (d) Cross-sectional SEM image of the asymmetric membrane. The inset shows the magnified image of the vertically aligned nanochannels. (e–h) Top-view SEM images of asymmetric membranes with other pore size combinations, 10 μm/200 nm (e), 25 μm/1 μm (f), 25 μm/2 μm (g), and 25 μm/8 μm (h). The scale bars are 5 μm. (i) Fluorescence microscope image of an asymmetric membrane after sample loading.

will be converted to a fluorescence signal and thus enable direct counting.[32] This "digital format" allows simple, rapid, and multiplexed detection of specific cell strains in the samples from commensal ones.[33] However, the concentration of pathogenic bacteria in environmental samples is typically beyond the detection limit of most microfluidic devices due to their limitation to microliter samples. To detect bacteria less than 1 cell per mL, at least several milliliters of samples have to be analyzed, no matter how sensitive the detection method is. For most chips, it would take several hours or days for bulk sample loading (even more for nanofluidics), which is not only a waste of time and precious bioreagents but also inactivate biochemical reaction.[34,35] In addition, multiple sample pretreatment steps are still required for crude samples to remove inhibitors, exclude particles, enrich bacteria, or extract DNA before ultimate analysis. Furthermore, accessing microfluidics, especially nanofluidics, typically calls for elaborate chip fabrication and sophisticated fluid control (*e.g.*, pump, vacuum, centrifuge, or valve), limiting their accessibility to users without related expertise and instruments.[36]

In this work, instead of using conventional micro/nanofluidic chips, we report on the use of a membrane for the digital detection of single bacteria in 10 mL of unprocessed environmental water samples within 1 h. The complete heterogeneous membrane system is composed of a sacrificial prefilter and an asymmetric micro/nanochannel membrane, as illustrated in Figure 1. The asymmetric membrane, containing highly ordered micropores (25 μm) on the top and a high

DOI: 10.1021/acsnano.8b05384
ACS Nano 2018, 12, 10281–10290

density of vertically aligned nanochannels (400 nm) on the bottom, was prepared within 1 min by glass-transition-induced bonding. The strong sealing and vertical orientation of nanochannels ensure the perfect isolation of each pore without cross-contamination. During the filtration, large particles and positively charged pollutants are removed by the sacrificial prefilter on the top, while bacterial cells can pass through and then concentrate inside the micropores. Meanwhile, small inhibitors typically found in environmental samples, such as proteins, humic acids, organics, and heavy metals, passed through the nanochannels and washed away. After initial filtration, modified loop-mediated isothermal amplification (LAMP) or reverse transcription-LAMP (RT-LAMP) reagents, including NaF and lysozyme, are loaded into the asymmetric membrane for direct, rapid, and efficient amplification of a single bacterium within the isolated pores. By direct counting of positive pores, absolute quantification of *E. coli* and *Salmonella* in unprocessed seawater and pond water samples was achieved within 1 h, with a dynamic range from 0.3 to 10000 cells/mL. In contrast, direct bacteria detection in these environmental samples by conventional methods completely failed. Furthermore, the membranes are inexpensive (less than 0.1 U.S. dollar) and easily prepared on a large scale. Therefore, they can be thrown away (disposable) after each use, avoiding subsequent LAMP contamination.

RESULTS AND DISCUSSION

Asymmetric Membrane Preparation. The asymmetric membrane with large micropores on one side and high-density nanochannel arrays on the other side is the key component of the complete heterogeneous membrane system. To function as a nanofluidic system for digital bacteria counting, the asymmetric membrane should share the following features: (i) All the uniform micro/nanochannels should be vertically aligned without interconnection. (ii) The micropores on one side of membrane should be large enough (>20 μm) for visual counting, and the nanochannels on other side should be smaller than 400 nm for bacteria capture. (iii) A strong bonding is necessary between the microchannels and nanochannels. (iv) To enable rapid manual filtration, a high density of nanochannels was required to lower the applied pressure and increase the flow rate. (v) The membrane should possess excellent mechanical/chemical/thermal stability.

Track-etching technique has become the main route for preparing symmetric membranes containing numerous vertically aligned nanochannels.[37] To obtain asymmetric membranes, many strategies have been employed, such as asymmetric etching,[38,39] asymmetric modification,[40,41] or asymmetric combination.[42,43] However, most preparation processes are complicated and not suitable for conventional laboratories. Herein, we report a simple and robust method for the preparation of asymmetric membranes utilizing conventional symmetric track-etched membranes. Two symmetric track-etched polycarbonate (PC) membranes (commercially available) are stacked together and then heated at 165 °C on a hot plate for 1 min (see schematic illustration in Figure S1 and details in the Experimental Section). After the short heating duration, the two membranes are irreversibly bonded together. Figure 2a shows a photograph of an asymmetric membrane with perfect sealing. We attribute the bonding mechanism to the glass transition properties of the thermoplastic material. The polycarbonate has a glass transition temperature of ∼150 °C.[44] Above this temperature, the membranes undergo a transition from a glassy state to a rubbery state, where they become soft while the micro/nanostructure remains unchanged. The long-range motion of the polymer chains in the rubbery state facilitates the tight adhesion of two membranes. Figure 2b shows a top-view scanning electron microscopy (SEM) image of the asymmetric membrane, confirming the presence of uniform micropores on its top surface. The pore size was measured to be 25 μm, and the pore density was about 10^4 pores/cm^2. The pore size was uniform, as confirmed by the size distribution results (see Figure S2). Magnification of the images reveals the high density of nanochannels, with diameters of 400 nm, within each micropore (Figure 2c). Compared to the original membranes, the morphology of micropores and nanochannels has not changed after the heat treatment (see detailed characterization in Figure S3). The cross-sectional view SEM image of the asymmetric membrane also demonstrates the presence of micropores on the top and vertically aligned nanochannels at the bottom, as shown in Figure 2d. The two membranes were indeed bonded tightly without any gap. It should be noted that, in these experiments, a strong bonding is crucial for the asymmetric membrane to prevent it from splitting during filtration with applied pressure. The successful sealing and parallel perpendicular nanochannels ensure the isolation of each pore and prevent cross-contamination. In addition to the mentioned size and materials, the asymmetric membranes combined with other pore size (range from 200 nm to 30 μm) and other materials (polyester) could also be successfully prepared, as shown in Figure 2e–h and Figure S4.

The wettability of membranes before and after thermal treatments was also tested, as shown in Table S1. The contact angle of LAMP solution on PC membranes increased slightly after thermal bonding, from 40 ± 3 to 50 ± 2° for membranes with 25 μm pore size and from 47 ± 3 to 54 ± 4° for membranes with 400 nm pore size. The low contact angles indicate that solutions can easily enter the micropores and nanochannels. Reagents could be loaded into each pore of the prepared asymmetric membrane, as illustrated in Figure S5 (see also the Experimental Section for details). Twenty-five microliters of sample was added onto the asymmetric membrane. Due to the capillary forces, the pores were easily wetted. The wetted membrane was then sealed between two polydimethylsiloxane (PDMS) films to remove residual reagents from the membrane surface. In order to prevent water evaporation, the top piece of PDMS was peeled off, followed by addition of mineral oil to cover the whole membrane. As shown in the fluorescence image (Figure 2i), each pore was filled with 13 pL of sample solution. A wide-view image is also shown in Figure S6, illustrating the successful loading and partitioning of the sample. To verify that no cross-contamination exists between pores, photobleaching tests were conducted.[12] Membranes loaded with fluorescent solution were exposed to UV light for 3 min, resulting in a patterned area with relatively weak fluorescence (see Figure S7). If cross-contamination occurred, dye molecules would diffuse between pores and the bleached pattern would vanish with time. However, in our case, the pattern did not change after the illumination and an extended period of observation. We repeated these experiments several times, using different membranes at different positions, and similar results were obtained. The perfect isolation of pores can also be proven by the following LAMP experiments on

DOI: 10.1021/acsnano.8b05384
ACS Nano 2018, 12, 10281–10290

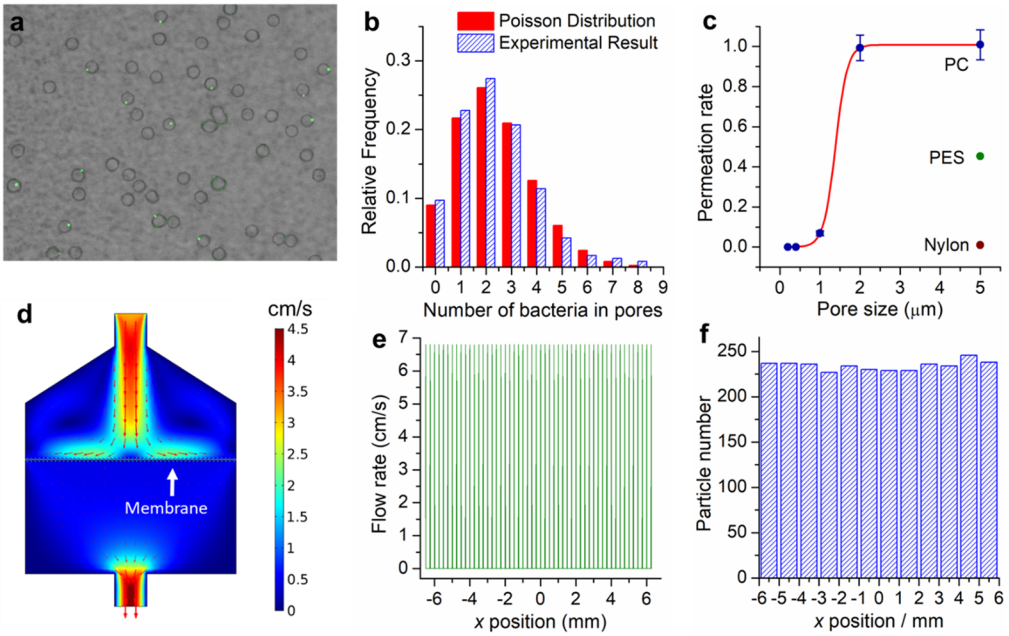

Figure 3. Bacteria capture, purification, and partition by sample filtration. (a) *E. coli* capture images. Green dots represent the stained *E. coli*, and the circles are the micropores. (b) Comparison between theoretical Poisson distribution and experimental *E. coli* distribution results in each pore. (c) *E. coli* permeation rate *versus* pore size. The blue points refer to PC membranes, and the green and brown points refer to PES and Nylon membranes, respectively. (d) Numerical simulation of fluidic flow profile inside the filter through the asymmetric membrane. (e) Simulated flow rate at each *x* position of the asymmetric membrane. Each peak represents the flow rate through one micropore. (f) Simulated statistical number of particles at each *x* position of the asymmetric membrane.

asymmetric membranes, as discussed later, at low bacteria concentration (see Figure S8).

Filtration. The asymmetric membrane was applied for the filtration of an *E. coli* sample using a syringe pushed by hand. Due to the high density of microchannels and nanochannels, water passed through the membrane rapidly, and a 1 mL sample was filtered within 5 s. The air in the syringe behind the solution could push all the sample out of the filter without a dead volume. Meanwhile, the numerous parallel nanochannels in the membrane also alleviated clogging, as the occlusion of any single nanopore resulted in the diversion of the flow to nearby pores.[45] After filtration, *E. coli* were randomly captured inside each micropore, whereas proteins, organics, nucleic acid, ions, and other small molecules passed through the nanochannels and were washed away.[46,47] Figure 3a shows stained *E. coli* (green dots) within the circular micropores. All the bacteria were captured and distributed randomly inside the micropores. No bacteria were found outside the pores, even if a relatively high concentration was used (Figure S9). At this concentration, an average of 2.2 *E. coli* were trapped in a single pore, and the statistic number of *E. coli* in each pore was also fit well with Poisson distribution (see Figure 3b). To test the capture efficiency, we measured the concentration of *E. coli* in the original sample, as well as in the filtrate, by standard bacteria culture and fluorescence enumeration (see Experimental Section). Results show that nearly 99.9% of *E. coli* were captured on the membrane (Figure S10). This excellent capture efficiency resulted from the outstanding size exclusion and electrostatic repulsion of the nanochannels, even under high flow rates.

In addition to bacterial enrichment, the membrane also provides an easy way for sample purification. During filtration, small inhibitors or interference molecules in the samples could be washed away through the nanochannels. However, for complex environmental samples, the presence of various large particles and organisms would easily block the asymmetric membrane or inhibit the following enzyme-driven nucleic acid amplification processes. To solve this challenge, a sacrificial track-etched PC membrane with uniform microchannels and negatively charged channel surface was introduced and stacked above the asymmetric membrane for sample prefiltration. The function of this sacrificial layer was to exclude all large particles and adsorb positively charged matters but not to obstruct the passage of target bacteria. Therefore, we tested the *E. coli* permeation rate through the prefilter. As shown in Figure 3c (blue circles), the track-etched PC membranes exhibit a nearly 100% permeation rate for *E. coli*, even when their pore size was only 2 μm, which was only slightly larger than the size of *E. coli* (~1 μm). Upon further decrease of the pore size to 1 μm, the permeation of *E. coli* was significantly decreased to 5%, exhibiting a perfect cutoff curve for bacterial sieving. This sharp cutoff property was indeed a characteristic behavior of isoporous membranes (membranes with highly ordered channels),[48] as track-etched PC membranes have ideal cylinder channel arrays and well-defined pore sizes. In contrast, conventional nylon membranes and PES membranes, which have irregular and intercrossed pore structures, show a poor cutoff performance. Bacteria were easily trapped within the pore networks of the nylon and PES membranes even when 5 μm pore size membranes were used (see Figure 3c). The sharp cutoff provided by PC membranes also offers the opportunity to collect bacteria/viruses/exosomes at different layers if membranes with different channel sizes were to be connected in sequence.[49]

For digital single-cell detection and analysis, the cells should be dispersed homogeneously on the entire asymmetric membrane. To verify this, we conducted finite element analysis, using COMSOL to compute the flow field, as well

DOI: 10.1021/acsnano.8b05384
ACS Nano 2018, 12, 10281−10290

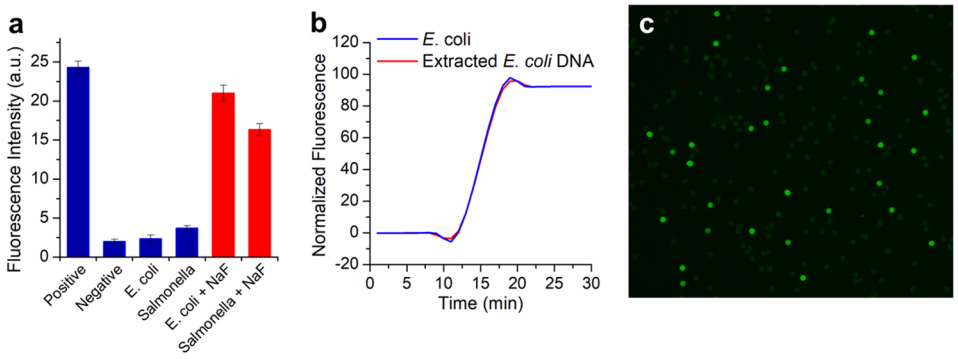

Figure 4. Single bacteria LAMP. (a) Fluorescence intensity after LAMP reaction in tube with different targets. Positive control used purified *E. coli* DNA, and negative control had no template. (b) Real-time fluorescence measurements of the LAMP reaction in a tube with *E. coli* or extracted DNA (by bead beating). Lysozyme was included in this reaction with a concentration of 0.1 mg/mL. (c) End-point fluorescence image of membrane after LAMP using modified reagents.

as particle trajectories when a solution passes through the asymmetric membrane. Figure 3d shows the flow profile inside the filter. The fluidic flow was dispersed before being passed through the asymmetric membrane. To quantitatively investigate the transmembrane flow, the flow rates across the membrane were recorded at each position. As shown in Figure 3e, a pulse-shaped curve was found, which can be attributed to the water flow through the porous membrane. Each peak represents the flow rate through one micropore. It can be seen that the fluidic flow rate through all the pores was found to be equal. However, other than water or small molecules, the cells in the fluid are subject to additional drag force and inertial force, resulting in different cell motion profiles. Therefore, particle trajectories were also simulated. The size of particles was set to 1 μm, and density was 1100 kg/m^3, similar to the parameters of *E. coli*.[50] After particles were introduced at the inlet, they dispersed well under the flow profile and were captured inside the micropores (see Movie S1). The particle counts along the membrane are almost constant, indicating uniform distribution (Figure 3f). All of the results above demonstrate that the micro/nanochannel membrane can be applied for bacterial capture, concentration, purification, and homogeneous partition *via* one-step simple filtration. In typical droplet-based assays, cell encapsulation requires several hours, especially for large sample volumes, causing cell sedimentation, protein inactivation, or cell damage.[34] The membrane filtration here was completed within 5 s, which significantly reduces the waiting time and circumvents these problems.

Digital Single Bacteria LAMP. After initial one-step filtration, the prefilter was thrown away, and a LAMP reagent mix (25 μL) was loaded inside each pore of the asymmetric membrane as discussed above for *in situ E. coli* LAMP (see Experimental Section). During 65 °C incubation, each pore of the asymmetric membrane functioned as an individual nanoreactor for template amplification, generating a bright fluorescence if a target bacterium was inside. We chose LAMP because it is fast and robust, without the need for thermal cycling.[51,52] However, as opposed to PCR, which applies a preheating (95 °C) step to denature proteins or lyse cells, the *Bst* polymerase used in the LAMP cannot withstand high temperature. Therefore, single *E. coli* LAMP in an ultrasmall nanoreactor was easily inhibited (Figure S11). Herein, we report a modified assay for one-step single bacteria LAMP within each pore.

To investigate in detail, we performed real-time LAMP experiments in a tube, followed by polyacrylamide gel electrophoresis. In order to mimic the concentration of bacteria inside the pores, samples with high concentrations of 10^8 cells/mL were used. As seen in Figure 4a, the reaction for *E. coli* shows a very weak fluorescence, similar to that of the negative control background. However, the gel electrophoresis results indicate the target *E. coli* DNA was indeed successfully amplified (Figure S12). A similar phenomenon was also observed when attempting to detect *Salmonella* (Figure 4a). Thus, false-negative results were likely caused by inhibitors in the bacterial lysate, which attenuates the fluorescence signal. In our current LAMP assay, a calcein-Mn^{2+} indicator was employed for fluorescence reading because of its high signal-to-background ratio. Before amplification, the calcein dye was quenched by the Mn^{2+} and a weak fluorescence was observed. After successful amplification, a large amount of DNA was synthesized, yielding a substantial pyrophosphate as a by-product. The pyrophosphate ions cause the precipitation of Mn^{2+} and the subsequent release of calcein, thus generating a bright fluorescence. We suppose that the false-negative results were attributed to the pyrophosphatase found in bacteria. The pyrophosphatase is a ubiquitous enzyme existing in most organisms for energy metabolism.[53] It is capable of hydrolyzing pyrophosphate ions to phosphate ions, and thus Mn^{2+} will no longer be precipitated.[54] Therefore, the fluorescence of calcein was always quenched. This assumption was confirmed by the observation that no turbidity was observed for bacteria LAMP, although its DNA was successfully amplified. The activity of pyrophosphatase can be inhibited by fluoride ions.[55] As shown in Figure 4a, fluorescence was restored for *E. coli* and *Salmonella* samples after including 2 mM NaF into the LAMP reaction, which is nearly 10-fold higher compared to the nontemplate negative control.

Robust single bacteria LAMP also requires efficient cell lysis. Lysozyme is known for its ability to degrade the peptidoglycans of the bacteria cell wall.[56] However, the presence of lysozyme in the reaction inhibits the PCR process and should be removed before amplification.[57] By including lysozyme into the LAMP reaction, the bacterial lysis proceed simultaneously during the isothermal amplification. Effective lysis was proved by the real-time fluorescence results, which shows a coincident amplification curve and the same time-to-detection value for *E. coli* and its extracted DNA when lysozyme was included (Figure 4b). Meanwhile, the

DOI: 10.1021/acsnano.8b05384
ACS Nano 2018, 12, 10281−10290

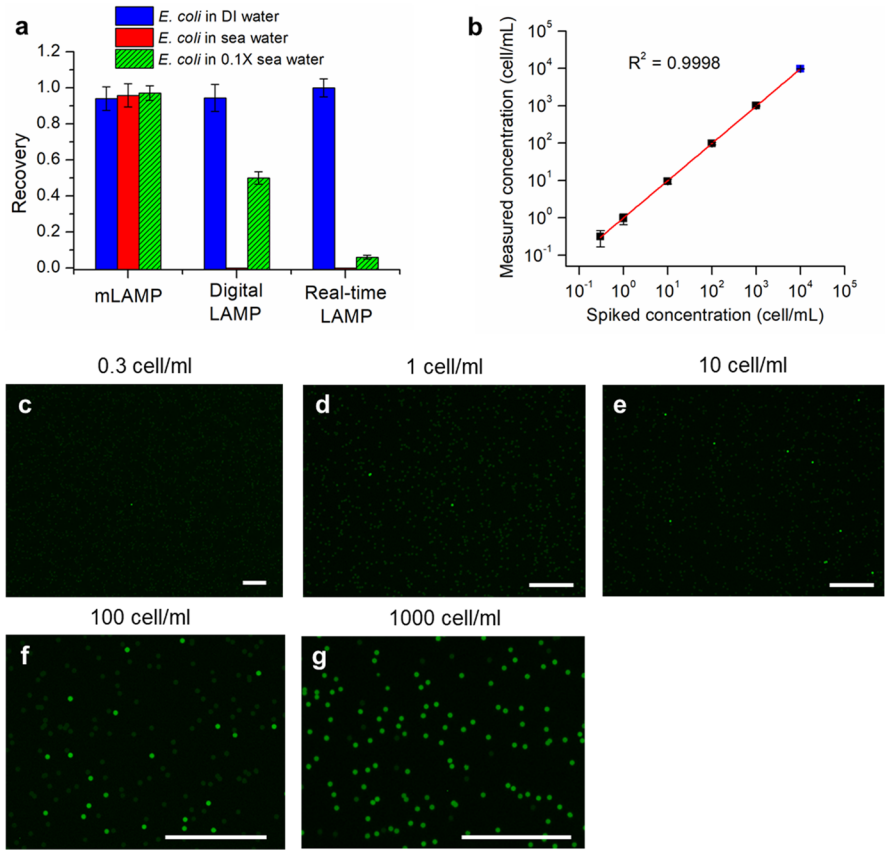

Figure 5. mLAMP performance in unprocessed environmental seawater samples. (a) Recovery of *E. coli* for different quantification methods in DI water, seawater, or 10× diluted seawater. Recovery was defined as the percentage of *E. coli* detected in comparison to the originally spiked concentration. The concentration of spiked *E. coli* in the sample was 50 cells/mL for mLAMP and digital LAMP, whereas that for real-time LAMP was 5×10^4 cells/mL. (b) Comparison of measured *E. coli* concentrations to the spiked concentrations. The black points were measured using 10 mL of seawater, and the blue point was obtained using only 1 mL of seawater. (c–g) End-point fluorescence images of membranes after mLAMP analysis of seawater with a series of spiked *E. coli* concentrations. All the scale bars are 0.5 mm.

fluorescence enumeration results also demonstrate that almost all of the *E. coli* disappeared after incubation with lysozyme in the tube at 65 °C (see Figure S13). However, for the sample containing lower bacterial concentration, lysozyme may not work well and lysis efficiency decreased (Figure S14). This issue can be addressed by the membrane system, as each single bacterium encapsulated inside a small pore has an ultrahigh concentration, regardless of the bulk bacteria concentration.

The modified LAMP mix including 2 mM NaF and 0.1 mg/mL lysozyme was loaded onto the asymmetric membrane for digital *E. coli* LAMP. As shown in Figure 4c, LAMP was successfully performed on the membrane. The pores with target bacteria inside generated a bright fluorescence, whereas those without target bacteria showed a weak background signal. The concentration of target bacteria in the sample can be obtained by direct counting of the positive pores and calibrated by Poisson distribution. The success rate for single *E. coli* LAMP was as high as 97% (Figure S15). Nucleic acid amplification in an ultrasmall chamber, especially with nanoporous structures, is particularly challenging due to severe adsorption of macromolecules or DNA.[12] However, digital nucleic acid amplification was still successfully performed in our nanofluidic partitioned system with a high density of nanochannels. As the bacteria were captured inside the pores first and LAMP reagents were loaded subsequently, the lysis process is restricted to each isolated pore, avoiding prerelease of cell information. All these results demonstrate the successful one-step single bacteria LAMP within each pore using a modified LAMP mixture.

Anti-inhibition and Performance in Unprocessed Samples. Raw environmental samples typically contain a variety of complex chemical and biological components that will affect the LAMP process. Direct detection of trace amounts of bacteria in these unprocessed samples is difficult and challenging. Herein, we attempted to detect and quantify an extremely low concentration of spiked *E. coli* in a 10 mL environmental sample directly, using the asymmetric membrane LAMP system (mLAMP). Seawater samples were collected from the Pacific Ocean near Santa Monica, CA. When the sample was analyzed by mLAMP, the large particles, sand, and planktons in the sample were retained by the prefilter on top of the asymmetric membrane (Figure S16), whereas the small inhibitory molecules were washed away through the underlying nanochannels. Meanwhile, the trace amounts of *E. coli* were concentrated in the micropores. Successful quantification of the spiked *E. coli* in seawater was achieved by mLAMP with a high recovery rate of 95%, as shown in Figure 5a (mLAMP column). The high recovery rate is attributed to full integration of the entire procedure on a membrane system, which minimizes potential sample loss. Meanwhile, no inhibition from the complex seawater matrix was observed, as there were no significant differences for *E. coli* quantification in seawater or in distilled water ($p > 0.05$). For comparison, conventional digital LAMP was also performed

DOI: 10.1021/acsnano.8b05384
ACS Nano 2018, 12, 10281–10290

for *E. coli* quantification in seawater. In this case, 22.5 μL of LAMP reagent was mixed with 2.5 μL of the seawater sample first and then loaded inside the pores of the membrane for digital amplification. As seen in Figure 5a (digital LAMP column), the LAMP reaction was completely inhibited, and not a single positive pore was observed. This effect may be due to the presence of high levels of inhibitors (heavy metals or organic matters) in seawater. It should be noted that, in this case, the concentration of inhibitors was already diluted 10 times by the LAMP reagents. The inhibition effect is still significant when a further diluted seawater sample (10 times dilution, abbreviated as 0.1×) was used. Only 50% of pores show successful single bacteria LAMP, and the observed final fluorescence was lower than normal. A severe inhibition pattern was also observed for real-time LAMP performed in a tube. Due to the poor sensitivity of real-time LAMP, a high concentration of *E. coli* (5×10^4 cells/mL) was spiked in the sample. However, the LAMP reaction was still totally inhibited when raw seawater was used (Figure 5a, real-time LAMP column). When a 10-fold diluted seawater sample was used, the fluorescence appeared but with a significant time delay. This delayed amplification resulted in an increased time-to-detection value and, therefore, underestimated the target concentration in the sample. All of these results demonstrate the excellent performance of our mLAMP in terms of anti-inhibition for direct digital bacteria detection in complex samples.

mLAMP exhibits excellent performance toward absolute quantification of *E. coli* at extremely low concentrations, ranging from 0.3 to 10000 cells/mL, in seawater, with single-cell sensitivity. As shown in Figure 5b–g, with more *E. coli* in the sample, the membrane shows more positive pores. A good linear correlation was observed between the detected absolute number of *E. coli* and the actual number of cells spiked into the sample. Because there is a large error for preparing a single cell in the sample, the lower detection limit (LDL) is defined as the concentration which would have a 95% chance of having at least one bacterium in the sample and equals the concentration of three bacteria per sample.[58] The LDL in our case was 0.3 cells/mL. At this concentration, there were around three positive pores visible on the whole membrane, corresponding to 3 bacteria in the 10 mL sample (see Figure S17).

In addition, the detection of pathogenic *Salmonella* in turtle pond water was also demonstrated by membrane-based RT-LAMP (mRT-LAMP). Reptiles, like turtles, may carry *Salmonella* bacteria, which cause diarrhea, stomach pain, nausea, vomiting, fever, and headaches.[59] Indeed, the multi-state outbreak of *Salmonella* in the United State during 2015 and 2017 was linked to contact with turtles carrying *Salmonella*.[60] We collected the sample from the California Institute of Technology (Caltech) turtle pond. The turtle pond water was more turbid with suspended green algae and mud. These particles were successfully removed by the prefilter and nanochannels (see Figure S16). Primers specific to the gene marker STY1607 were used to detect the corresponding mRNA as well as DNA.[61] Due to the variations of mRNA copies from cell to cell, it is hard to quantify target cells by detecting the number of mRNAs. However, mRT-LAMP circumvents these difficulties as each *Salmonella* bacterium was encapsulated inside a single pore, and thus, the contained nucleic acids, no matter how many, were amplified, resulting in a bright fluorescence. Absolute quantification of spiked *Salmonella* in pond water was realized for 3–10000 cells/mL, as shown in Figure S18.

CONCLUSION

In this work, we present the rapid, sensitive, and precise quantification of single pathogenic bacteria in milliliters of unprocessed environmental samples on an asymmetric membrane through simple filtration and LAMP amplification. An asymmetric membrane with micropores on one side and nanochannels on the other side was prepared within 1 min without the need for specialized equipment or harsh conditions. The membrane was capable of bacteria capture, concentration, purification, partition, lysis, and digital LAMP without off-membrane sample treatments. Even in unprocessed environmental sea and pond water with a high level of inhibitors, direct quantification of *E. coli* and *Salmonella* was realized with a sensitivity down to single cell and dynamic range of 0.3–10000 cells/mL.

Compared with other digital single-cell detection methods, the membrane LAMP system, mLAMP, exhibits many advantages: (i) Ten milliliter samples can be processed on the membrane within seconds, while still keeping minimum consumption of precious bioreagents. (ii) All assay steps including bacteria capture, concentration, purification, partition, and digital LAMP were integrated onto a piece of membrane without the need for off-membrane sample treatments. This significantly reduces potential sample loss and simplified the entire procedure. (iii) With the modified assay, mLAMP could quantify bacteria at concentrations down to 0.3 cells/mL in unprocessed environmental samples within 1 h, even though a relatively high level of inhibitors was present. (iv) All experiments were performed on low-cost and disposable commercial membranes without requiring elaborate chip fabrication or material design. (v) No pump, vacuum, centrifuge, or other laboratory hardware is required for field analysis.

We believe this simple membrane system offers many promising opportunities for laboratories, even without microfabrication facilities, to perform digital quantification, single-cell analysis, and other biochemical assays with high throughput. In the future, membranes could be directly sealed by an adhesive film and imaged by a smartphone to increase the system simplicity for point-of-care diagnostics.[62,63] In addition, advanced micro/nanochannel membranes with novel functions could also be integrated into the digital membrane system, like nanopore-based DNA sequencing, DNA translocation, molecular exchange, cell electroporation, or cell lysis.[64] Furthermore, the asymmetric membrane could be paired with paper-based analytical devices for complex sample manipulation and detection.[62,65] We believe the heterogeneous membrane can serve as an ideal low-cost and simple platform for the rapid detection and analysis of any markers in biological samples, including nucleic acids, bacteria, circulating tumor cells, stem cells, exosomes, viruses, and proteins.

EXPERIMENTAL SECTION

Chemicals and Materials. All LAMP reagents were purchased from New England Biolabs (Ipswich, MA), and all primers were ordered from Integrated DNA Technologies (Coralville, IA), unless otherwise mentioned. Calcein, $MnCl_2$, as well as acids were purchased from Sigma-Aldrich (St. Louis, MO). Lysozyme, SYBR Green, and culture media were obtained from ThermoFisher Scientific (San Jose, CA). Track-etched PC membranes, PES membranes, and Nylon

DOI: 10.1021/acsnano.8b05384
ACS Nano 2018, 12, 10281–10290

membranes were purchased from Sterlitech Corporation (Kent, WA). Sylgard 184 silicon elastomer kit, consisting of a prepolymer base and a curing agent, was obtained from Dow Corning (Midland, MI).

Cell Culture. All bacterial strains were purchased from the American Type Culture Collection (ATCC, Manassas, VA). *E. coli* (ATCC 10798) was cultivated in Luria−Bertani broth in the shaking incubator for ∼14 h at 37 °C. *Salmonella typhi* (CVD 909) was cultivated in tryptic soy broth with 1 mg/L of 2,3-dihydroxybenzoate in the incubator for ∼14 h at 35 °C. The concentration of used bacteria suspensions was measured by fluorescence enumeration or standard bacteria culture. For fluorescence enumeration, a bacterial sample was first stained with 1× SYBR Green for 30 min, followed by filtration through a commercial PC membrane with a 0.2 μm pore size. The cell number was then counted under a fluorescence microscope (Leica DMi8). For bacteria culture assays, bacteria concentrations were quantified by spreading 20 μL of samples on corresponding agar plates, incubating them for 12 h at the respective temperature, and counting the colony-forming units (CFU). DNA extraction was performed using a commercial bead beating tube (GeneRite, NJ, USA) or using the PureLink DNA extraction kit (ThermoFisher Scientific) following their instructions.

Preparation of Asymmetric Membranes. To prepare the asymmetric membrane, two symmetric track-etched PC membranes with channel size sizes of 25 μm and 400 nm were stacked and then placed on the top of a thin PDMS film, as illustrated in Figure S1. After being heated at 165 °C on a hot plate for 1 min, these two membranes were irreversibly bonded together. The PDMS films were used to prevent thermal deformation of the membranes at high temperature. PDMS films were prepared by mixing their precursor and curing agent in a ratio of 10:1 and heating the mixture to 75 °C for 1.5 h.

Some commercial PC membranes were coated with polyvinylpyrrolidone (PVP). This hydrophilic coating must be removed first because it affects the LAMP reaction. PVP removal was accomplished by dipping membranes in 10% acetic acid for 60 min, followed by heating to 120 °C for 30 min.[66]

LAMP Assay. The 25 μL of modified LAMP mix for digital single bacteria LAMP contained 1× isothermal buffer, 6 mM total $MgSO_4$, 1.4 mM dNTP, 640 U/mL *Bst* 2.0 WarmStart polymerase, 1.6 μM FIB and BIP, 0.2 μM F3 and B3, 0.8 μM LF and LB, 1.5 mg/mL BSA, 50 μM calcein, 1 mM $MnCl_2$, 2 mM NaF, and 0.1 mg/mL lysozyme. For RT-LAMP, WarmStart RTx reverse transcriptase was also added to a final concentration of 300 U/mL. The primers for *E. coli* were designed to be specific to a conserved region on the malB gene,[67] whereas primers for *Salmonella* were specific to gene marker STY1607.[61] Their sequence is shown in the Supporting Information. Primer specificity has already been demonstrated and published.[61,67] Thus, no selectivity tests (toward other bacteria) were conducted in this study.

Digital Single Bacteria Detection on Membranes. The asymmetric membrane with a sacrificial PC membrane (2 μm pore size) on top was put into a commercial filter holder (Swinnex, Kent, WA), and 1−10 mL of environmental sample with spiked bacteria was filtered through it using a syringe pushed manually. After filtration, the sacrificial prefilter membrane was thrown away, and 25 μL of modified LAMP mix was added on the top of asymmetric membrane. The wetted membrane was then sealed between two pieces of PDMS film. Subsequently, the top PDMS was peeled off, followed by adding mineral oil and a frame-seal (Bio-Rad, Hercules, CA) to cover the whole membrane. The membranes were incubated at 65 °C on a hot plate (MJ Research PTC-100, Watertown, MA) for 40 min. After amplification, the fluorescence images of the membrane were taken by a fluorescence microscope (Leica DMi8) using a 4× objective. Positive pores were counted using ImageJ (NIH) software and calibrated by Poisson distribution. The total number of pores can also be counted using ImageJ because the negative one also shows a weak fluorescence. However, in this study, the total number of pores was simply estimated based on porosity (1×10^4 pores/cm^2). Each sample was tested at least three times.

For real-time LAMP performance in the tube, the LAMP assay was premixed with 2.5 μL of seawater first and incubated at 65 °C using an Eppendorf RealPlex2. Fluorescence intensity of the reaction was monitored every minute for 60 min. For conventional digital LAMP, the LAMP assay mixture (premixed with a 2.5 μL seawater sample) was loaded into each pore of the asymmetric membrane and incubated at 65 °C for 40 min for digital LAMP analyses.

Environmental Samples. Seawater samples were collected from the Santa Monica beach in California. Cultured *E. coli* samples were spiked with a final concentration of 0.3 to 1×10^4 cells/mL and allowed to equilibrate for 1 h before analysis. The turtle pond water was collected from the turtle pond at the California Institute of Technology (Caltech), and cultured *Salmonella* was spiked in with a final concentration of 3 to 1×10^4 cells/mL.

Characterization. Top-view and cross-sectional view SEM images were obtained with a ZEISS 1550VP field-emission scanning electron microscope. Before analysis, samples were sputtered with 10 nm Pd. Wettability of the membrane was measured using a contact angle goniometer equipped with an AmScope microscope camera model MU300. A drop of LAMP mix was placed on the surface of the membranes. After 10 s, the image was captured and then analyzed using ImageJ.

COMSOL Simulation. Finite element modeling was carried out using the commercial software COMSOL Multiphysics (COMSOL Inc., Burlington, MA). In our simulations, the fluid flows were considered as water with a density of 1×10^3 kg/m^3 and a dynamic viscosity μ of 1×10^{-3} Pa·s. The fluid geometry during sample filtration was represented by a 2D model. The fluid flow passing through the asymmetric membrane was represented by two layers, each with a thickness of 25 μm and diameter of 13 mm. The diameter and center-to-center distance of the micropores in the upper layer were 25 and 225 μm, respectively. The diameter and center-to-center distance of the nanochannels in the bottom layer were 400 nm and 2 μm, respectively. The velocity of fluid at the inlet was set to 0.0318 m/s. The steady-state laminar flow profile throughout the fluid geometry was calculated first using the Navier−Stokes equation. Subsequently, a fixed amount of 1 μm particles was placed at the sample inlet for calculations of their trajectories using a particle tracing model. The density of the particles was set to 1100 kg/m^3, similar to that of *E. coli*. The trajectories of the particles were calculated, and thus the distribution of particles along the membrane was measured.

ASSOCIATED CONTENT

Supporting Information

The Supporting Information is available free of charge on the ACS Publications website at DOI: 10.1021/acsnano.8b05384.

COMSOL simulated movie showing the trajectories of particles under filtration flow through the asymmetric membrane (AVI)

Primer sequences, contact angle results, fabrication schemes, pore size distributions, detailed SEM characterization, additional fluorescence images, gel electrophoresis results, bacterial lysis results, and *Salmonella* quantification (PDF)

AUTHOR INFORMATION

Corresponding Author

*E-mail: mrh@caltech.edu.

ORCID

Xingyu Lin: 0000-0002-0950-0736

Xiao Huang: 0000-0002-3737-6939

Yanzhe Zhu: 0000-0002-2260-1830

Xing Xie: 0000-0002-2253-0964

Notes

The authors declare no competing financial interest.

DOI: 10.1021/acsnano.8b05384
ACS Nano 2018, 12, 10281−10290

ACKNOWLEDGMENTS

The authors acknowledge the financial support provided by the Bill and Melinda Gates Foundation (Grant No. OPP1111252).

REFERENCES

(1) Shannon, M. A.; Bohn, P. W.; Elimelech, M.; Georgiadis, J. G.; Marinas, B. J.; Mayes, A. M. Science and Technology for Water Purification in the Coming Decades. *Nature* **2008**, *452*, 301−310.
(2) Bridle, H.; Miller, B.; Desmulliez, M. P. Application of Microfluidics in Waterborne Pathogen Monitoring: A Review. *Water Res.* **2014**, *55*, 256−271.
(3) Ramirez-Castillo, F. Y.; Loera-Muro, A.; Jacques, M.; Garneau, P.; Avelar-Gonzalez, F. J.; Harel, J.; Guerrero-Barrera, A. L. Waterborne Pathogens: Detection Methods and Challenges. *Pathogens* **2015**, *4*, 307−334.
(4) Zhao, X.; Hilliard, L. R.; Mechery, S. J.; Wang, Y.; Bagwe, R. P.; Jin, S.; Tan, W. A Rapid Bioassay for Single Bacterial Cell Quantitation Using Bioconjugated Nanoparticles. *Proc. Natl. Acad. Sci. U. S. A.* **2004**, *101*, 15027−15032.
(5) United States Environmental Protection Agency. Recreational Water Quality Criteria; https://www.epa.gov/sites/production/files/2015-10/documents/rwqc2012.pdf (accessed June 2018).
(6) Zhang, D.; Bi, H.; Liu, B.; Qiao, L. Detection of Pathogenic Microorganisms by Microfluidics Based Analytical Methods. *Anal. Chem.* **2018**, *90*, 5512−5520.
(7) Heyries, K. A.; Tropini, C.; Vaninsberghe, M.; Doolin, C.; Petriv, O. I.; Singhal, A.; Leung, K.; Hughesman, C. B.; Hansen, C. L. Megapixel Digital PCR. *Nat. Methods* **2011**, *8*, 649−651.
(8) Joensson, H. N.; Andersson Svahn, H. Droplet Microfluidics - a Tool for Single-Cell Analysis. *Angew. Chem., Int. Ed.* **2012**, *51*, 12176−12192.
(9) Ven, K.; Vanspauwen, B.; Perez-Ruiz, E.; Leirs, K.; Decrop, D.; Gerstmans, H.; Spasic, D.; Lammertyn, J. Target Confinement in Small Reaction Volumes Using Microfluidic Technologies: A Smart Approach for Single-Entity Detection and Analysis. *ACS Sens* **2018**, *3*, 264−284.
(10) Yen, T. M.; Zhang, T.; Chen, P.-W.; Ku, T.-H.; Chiu, Y.-J.; Lian, I.; Lo, Y.-H. Self-Assembled Pico-Liter Droplet Microarray for Ultrasensitive Nucleic Acid Quantification. *ACS Nano* **2015**, *9*, 10655−10663.
(11) Novak, R.; Zeng, Y.; Shuga, J.; Venugopalan, G.; Fletcher, D. A.; Smith, M. T.; Mathies, R. A. Single-Cell Multiplex Gene Detection and Sequencing with Microfluidically Generated Agarose Emulsions. *Angew. Chem., Int. Ed.* **2011**, *50*, 390−395.
(12) Men, Y.; Fu, Y.; Chen, Z.; Sims, P. A.; Greenleaf, W. J.; Huang, Y. Digital Polymerase Chain Reaction in an Array of Femtoliter Polydimethylsiloxane Microreactors. *Anal. Chem.* **2012**, *84*, 4262−4266.
(13) Zhu, Z.; Zhang, W.; Leng, X.; Zhang, M.; Guan, Z.; Lu, J.; Yang, C. J. Highly Sensitive and Quantitative Detection of Rare Pathogens through Agarose Droplet Microfluidic Emulsion PCR at the Single-Cell Level. *Lab Chip* **2012**, *12*, 3907−3913.
(14) Tadmor, A. D.; Ottesen, E. A.; Leadbetter, J. R.; Phillips, R. Probing Individual Environmental Bacteria for Viruses by Using Microfluidic Digital PCR. *Science* **2011**, *333*, 58−62.
(15) Wang, Y.; Southard, K. M.; Zeng, Y. Digital PCR Using Micropatterned Superporous Absorbent Array Chips. *Analyst* **2016**, *141*, 3821−3831.
(16) Yeh, E. C.; Fu, C. C.; Hu, L.; Thakur, R.; Feng, J.; Lee, L. P. Self-Powered Integrated Microfluidic Point-of-Care Low-Cost Enabling (Simple) Chip. *Sci. Adv.* **2017**, *3*, e1501645.
(17) Rodriguez-Manzano, J.; Karymov, M. A.; Begolo, S.; Selck, D. A.; Zhukov, D. V.; Jue, E.; Ismagilov, R. F. Reading out Single-Molecule Digital RNA and DNA Isothermal Amplification in Nanoliter Volumes with Unmodified Camera Phones. *ACS Nano* **2016**, *10*, 3102−3013.
(18) Schoepp, N. G.; Schlappi, T. S.; Curtis, M. S.; Butkovich, S. S.; Miller, S.; Humphries, R. M.; Ismagilov, R. F. Rapid Pathogen-Specific Phenotypic Antibiotic Susceptibility Testing Using Digital LAMP Quantification in Clinical Samples. *Sci. Transl. Med.* **2017**, *9*, eaal3693.
(19) White, A. K.; VanInsberghe, M.; Petriv, O. I.; Hamidi, M.; Sikorski, D.; Marra, M. A.; Piret, J.; Aparicio, S.; Hansen, C. L. High-Throughput Microfluidic Single-Cell RT-qPCR. *Proc. Natl. Acad. Sci. U. S. A.* **2011**, *108*, 13999−14004.
(20) Kim, S. C.; Clark, I. C.; Shahi, P.; Abate, A. R. Single-Cell RT-PCR in Microfluidic Droplets with Integrated Chemical Lysis. *Anal. Chem.* **2018**, *90*, 1273−1279.
(21) Hu, Y.; Xu, P.; Luo, J.; He, H.; Du, W. Absolute Quantification of H5-Subtype Avian Influenza Viruses Using Droplet Digital Loop-Mediated Isothermal Amplification. *Anal. Chem.* **2017**, *89*, 745−750.
(22) Gong, Y.; Ogunniyi, A. O.; Love, J. C. Massively Parallel Detection of Gene Expression in Single Cells Using Subnanolitre Wells. *Lab Chip* **2010**, *10*, 2334−2337.
(23) Zhang, H.; Jenkins, G.; Zou, Y.; Zhu, Z.; Yang, C. J. Massively Parallel Single-Molecule and Single-Cell Emulsion Reverse Transcription Polymerase Chain Reaction Using Agarose Droplet Microfluidics. *Anal. Chem.* **2012**, *84*, 3599−3606.
(24) Kang, D. K.; Ali, M. M.; Zhang, K.; Huang, S. S.; Peterson, E.; Digman, M. A.; Gratton, E.; Zhao, W. Rapid Detection of Single Bacteria in Unprocessed Blood Using Integrated Comprehensive Droplet Digital Detection. *Nat. Commun.* **2014**, *5*, 5427.
(25) Ali, M. M.; Aguirre, S. D.; Lazim, H.; Li, Y. Fluorogenic Dnazyme Probes as Bacterial Indicators. *Angew. Chem., Int. Ed.* **2011**, *50*, 3751−3754.
(26) Li, Z. Y.; Huang, M.; Wang, X. K.; Zhu, Y.; Li, J. S.; Wong, C. C. L.; Fang, Q. Nanoliter-Scale Oil-Air-Droplet Chip-Based Single Cell Proteomic Analysis. *Anal. Chem.* **2018**, *90*, 5430−5438.
(27) Juul, S.; Nielsen, C. J.; Labouriau, R.; Roy, A.; Tesauro, C.; Jensen, P. W.; Harmsen, C.; Kristoffersen, E. L.; Chiu, Y.-L.; Frøhlich, R.; et al. Droplet Microfluidics Platform for Highly Sensitive and Quantitative Detection of Malaria-Causing Plasmodium Parasites Based on Enzyme Activity Measurement. *ACS Nano* **2012**, *6*, 10676−10683.
(28) Avesar, J.; Rosenfeld, D.; Truman-Rosentsvit, M.; Ben-Arye, T.; Geffen, Y.; Bercovici, M.; Levenberg, S. Rapid Phenotypic Antimicrobial Susceptibility Testing Using Nanoliter Arrays. *Proc. Natl. Acad. Sci. U. S. A.* **2017**, *114*, E5787−E5795.
(29) Wu, H.; Chen, X.; Gao, X.; Zhang, M.; Wu, J.; Wen, W. High-Throughput Generation of Durable Droplet Arrays for Single-Cell Encapsulation, Culture, and Monitoring. *Anal. Chem.* **2018**, *90*, 4303−4309.
(30) Love, J. C.; Ronan, J. L.; Grotenbreg, G. M.; van der Veen, A. G.; Ploegh, H. L. A Microengraving Method for Rapid Selection of Single Cells Producing Antigen-Specific Antibodies. *Nat. Biotechnol.* **2006**, *24*, 703−707.
(31) Ogunniyi, A. O.; Story, C. M.; Papa, E.; Guillen, E.; Love, J. C. Screening Individual Hybridomas by Microengraving to Discover Monoclonal Antibodies. *Nat. Protoc.* **2009**, *4*, 767−782.
(32) Paunescu, D.; Mora, C. A.; Querci, L.; Heckel, R.; Puddu, M.; Hattendorf, B.; Günther, D.; Grass, R. N. Detecting and Number Counting of Single Engineered Nanoparticles by Digital Particle Polymerase Chain Reaction. *ACS Nano* **2015**, *9*, 9564−9572.
(33) Zhong, Q.; Bhattacharya, S.; Kotsopoulos, S.; Olson, J.; Taly, V.; Griffiths, A. D.; Link, D. R.; Larson, J. W. Multiplex Digital PCR: Breaking the One Target Per Color Barrier of Quantitative PCR. *Lab Chip* **2011**, *11*, 2167−2174.
(34) Mazutis, L.; Gilbert, J.; Ung, W. L.; Weitz, D. A.; Griffiths, A. D.; Heyman, J. A. Single-Cell Analysis and Sorting Using Droplet-Based Microfluidics. *Nat. Protoc.* **2013**, *8*, 870−891.
(35) Lyu, F.; Xu, M.; Cheng, Y.; Xie, J.; Rao, J.; Tang, S. K. Quantitative Detection of Cells Expressing Blac Using Droplet-Based Microfluidics for Use in the Diagnosis of Tuberculosis. *Biomicrofluidics* **2015**, *9*, 044120.
(36) Kaminski, T. S.; Scheler, O.; Garstecki, P. Droplet Microfluidics for Microbiology: Techniques, Applications and Challenges. *Lab Chip* **2016**, *16*, 2168−2187.

DOI: 10.1021/acsnano.8b05384
ACS Nano 2018, 12, 10281−10290

(37) Guo, W.; Tian, Y.; Jiang, L. Asymmetric Ion Transport through Ion-Channel-Mimetic Solid-State Nanopores. *Acc. Chem. Res.* **2013**, *46*, 2834−2846.
(38) Zhang, H.; Tian, Y.; Hou, J.; Hou, X.; Hou, G.; Ou, R.; Wang, H.; Jiang, L. Bioinspired Smart Gate-Location-Controllable Single Nanochannels: Experiment and Theoretical Simulation. *ACS Nano* **2015**, *9*, 12264−12273.
(39) Li, C. Y.; Wu, Z. Q.; Yuan, C. G.; Wang, K.; Xia, X. H. Propagation of Concentration Polarization Affecting Ions Transport in Branching Nanochannel Array. *Anal. Chem.* **2015**, *87*, 8194−8202.
(40) Li, C.-Y.; Ma, F.-X.; Wu, Z.-Q.; Gao, H.-L.; Shao, W.-T.; Wang, K.; Xia, X.-H. Solution-Ph-Modulated Rectification of Ionic Current in Highly Ordered Nanochannel Arrays Patterned with Chemical Functional Groups at Designed Positions. *Adv. Funct. Mater.* **2013**, *23*, 3836−3844.
(41) Yang, Q.; Lin, X.; Wang, Y.; Su, B. Nanochannels as Molecular Check Valves. *Nanoscale* **2017**, *9*, 18523−18528.
(42) Zhang, Z.; Kong, X. Y.; Xiao, K.; Liu, Q.; Xie, G.; Li, P.; Ma, J.; Tian, Y.; Wen, L.; Jiang, L. Engineered Asymmetric Heterogeneous Membrane: A Concentration-Gradient-Driven Energy Harvesting Device. *J. Am. Chem. Soc.* **2015**, *137*, 14765−14772.
(43) Zhang, Z.; Wen, L.; Jiang, L. Bioinspired Smart Asymmetric Nanochannel Membranes. *Chem. Soc. Rev.* **2018**, *47*, 322−356.
(44) Tsao, C.-W.; DeVoe, D. L. Bonding of Thermoplastic Polymer Microfluidics. *Microfluid. Nanofluid.* **2009**, *6*, 1−16.
(45) Ko, J.; Bhagwat, N.; Yee, S. S.; Ortiz, N.; Sahmoud, A.; Black, T.; Aiello, N. M.; McKenzie, L.; O'Hara, M.; Redlinger, C.; Romeo, J.; Carpenter, E. L.; Stanger, B. Z.; Issadore, D. Combining Machine Learning and Nanofluidic Technology to Diagnose Pancreatic Cancer Using Exosomes. *ACS Nano* **2017**, *11*, 11182−11193.
(46) Chen, W.; Jin, B.; Hu, Y. L.; Lu, Y.; Xia, X. H. Entrapment of Protein in Nanotubes Formed by a Nanochannel and Ion-Channel Hybrid Structure of Anodic Alumina. *Small* **2012**, *8*, 1001−1005.
(47) Wang, C.; Li, S. J.; Wu, Z. Q.; Xu, J. J.; Chen, H. Y.; Xia, X. H. Study on the Kinetics of Homogeneous Enzyme Reactions in a Micro/Nanofluidics Device. *Lab Chip* **2010**, *10*, 639−646.
(48) Lin, X.; Yang, Q.; Ding, L.; Su, B. Ultrathin Silica Membranes with Highly Ordered and Perpendicular Nanochannels for Precise and Fast Molecular Separation. *ACS Nano* **2015**, *9*, 11266−11277.
(49) Liu, F.; Vermesh, O.; Mani, V.; Ge, T. J.; Madsen, S. J.; Sabour, A.; Hsu, E. C.; Gowrishankar, G.; Kanada, M.; Jokerst, J. V.; Sierra, R. G.; Chang, E.; Lau, K.; Sridhar, K.; Bermudez, A.; Pitteri, S. J.; Stoyanova, T.; Sinclair, R.; Nair, V. S.; Gambhir, S. S.; et al. The Exosome Total Isolation Chip. *ACS Nano* **2017**, *11*, 10712−10723.
(50) Martinez-Salas, E.; Martin, J.; Vicente, M. Relationship of Escherichia coli Density to Growth Rate and Cell Age. *J. Bacteriol.* **1981**, *147*, 97−100.
(51) Tomita, N.; Mori, Y.; Kanda, H.; Notomi, T. Loop-Mediated Isothermal Amplification (LAMP) of Gene Sequences and Simple Visual Detection of Products. *Nat. Protoc.* **2008**, *3*, 877−882.
(52) Kong, J. E.; Wei, Q.; Tseng, D.; Zhang, J.; Pan, E.; Lewinski, M.; Garner, O. B.; Ozcan, A.; Di Carlo, D. Highly Stable and Sensitive Nucleic Acid Amplification and Cell-Phone-Based Readout. *ACS Nano* **2017**, *11*, 2934−2943.
(53) Josse, J. Constitutive Inorganic Pyrophosphatase of Escherichia Coli I. Purification and Catalytic Properties. *J. Biol. Chem.* **1966**, *241*, 1938−1947.
(54) Mori, Y.; Nagamine, K.; Tomita, N.; Notomi, T. Detection of Loop-Mediated Isothermal Amplification Reaction by Turbidity Derived from Magnesium Pyrophosphate Formation. *Biochem. Biophys. Res. Commun.* **2001**, *289*, 150−154.
(55) Baykov, A. A.; Artjukov, A. A.; Avaeva, S. M. Fluoride Inhibition of Inorganic Pyrophosphatase I. Kinetic Studies in a Mg2+-Ppi System Using a New Continuous Enzyme Assay. *Biochim. Biophys. Acta* **1976**, *429*, 982−992.
(56) Zhu, K.; Jin, H.; He, Z.; Zhu, Q.; Wang, B. A Continuous Method for the Large-Scale Extraction of Plasmid DNA by Modified Boiling Lysis. *Nat. Protoc.* **2007**, *1*, 3088−3093.
(57) Abolmaaty, A.; El-Shemy, M.; Khallaf, M.; Levin, R. Effect of Lysing Methods and Their Variables on the Yield of Escherichia Coli O157: H7 DNA and Its PCR Amplification. *J. Microbiol. Methods* **1998**, *34*, 133−141.
(58) Kreutz, J. E.; Munson, T.; Huynh, T.; Shen, F.; Du, W.; Ismagilov, R. F. Theoretical Design and Analysis of Multivolume Digital Assays with Wide Dynamic Range Validated Experimentally with Microfluidic Digital PCR. *Anal. Chem.* **2011**, *83*, 8158−8168.
(59) Winter, S. E.; Thiennimitr, P.; Winter, M. G.; Butler, B. P.; Huseby, D. L.; Crawford, R. W.; Russell, J. M.; Bevins, C. L.; Adams, L. G.; Tsolis, R. M.; Roth, J. R.; Baumler, A. J. Gut Inflammation Provides a Respiratory Electron Acceptor for Salmonella. *Nature* **2010**, *467*, 426−429.
(60) Gambino-Shirley, K.; Stevenson, L.; Concepción-Acevedo, J.; Trees, E.; Wagner, D.; Whitlock, L.; Roberts, J.; Garrett, N.; Van Duyne, S.; McAllister, G. Flea Market Finds and Global Exports: Four Multistate Outbreaks of Human Salmonella Infections Linked to Small Turtles, United States—2015. *Zoonoses Public Health* **2018**, *65*, 560.
(61) Fan, F.; Yan, M.; Du, P.; Chen, C.; Kan, B. Rapid and Sensitive Salmonella Typhi Detection in Blood and Fecal Samples Using Reverse Transcription Loop-Mediated Isothermal Amplification. *Foodborne Pathog. Dis.* **2015**, *12*, 778−786.
(62) Xu, G.; Nolder, D.; Reboud, J.; Oguike, M. C.; van Schalkwyk, D. A.; Sutherland, C. J.; Cooper, J. M. Paper-Origami-Based Multiplexed Malaria Diagnostics from Whole Blood. *Angew. Chem., Int. Ed.* **2016**, *55*, 15250−15253.
(63) Huang, X.; Lin, X.; Urmann, K.; Li, L.; Xie, X.; Jiang, S.; Hoffmann, M. R. A Smartphone Based in-Gel Loop Mediated Isothermal Amplification (gLAMP) System Enables Rapid Coliphage Ms2 Quantification in Environmental Waters. *Environ. Sci. Technol.* **2018**, *52*, 6399.
(64) Experton, J.; Wilson, A. G.; Martin, C. R. Low-Voltage Flow-through Electroporation in Gold-Microtube Membranes. *Anal. Chem.* **2016**, *88*, 12445−12452.
(65) Liu, M.; Hui, C. Y.; Zhang, Q.; Gu, J.; Kannan, B.; Jahanshahi-Anbuhi, S.; Filipe, C. D.; Brennan, J. D.; Li, Y. Target-Induced and Equipment-Free DNA Amplification with a Simple Paper Device. *Angew. Chem., Int. Ed.* **2016**, *55*, 2709−2713.
(66) Cheng, I. F.; Martin, C. R. Ultramicrodisk Electrode Ensembles Prepared by Incorporating Carbon Paste into a Microporous Host Membrane. *Anal. Chem.* **1988**, *60*, 2163−2165.
(67) Hill, J.; Beriwal, S.; Chandra, I.; Paul, V. K.; Kapil, A.; Singh, T.; Wadowsky, R. M.; Singh, V.; Goyal, A.; Jahnukainen, T.; Johnson, J. R.; Tarr, P. I.; Vats, A. Loop-Mediated Isothermal Amplification Assay for Rapid Detection of Common Strains of Escherichia Coli. *J. Clin. Microbiol.* **2008**, *46*, 2800−2804.

DOI: 10.1021/acsnano.8b05384
ACS Nano 2018, 12, 10281−10290

Appendix C

SYNTHESIS AND APPLICATION OF SUPERABSORBENT POLYMER MICROSPHERES FOR RAPID CONCENTRATION AND QUANTIFICATION OF MICROBIAL PATHOGENS IN AMBIENT WATER

Wu, X., Huang, X., Zhu, Y., Li, J., and Hoffmann, M.R. (2020). "Synthesis and application of superabsorbent polymer microspheres for rapid concentration and quantification of microbial pathogens in ambient water." *Separation and Purification Technology*: 116540. https://doi.org/10.1016/j.seppur.2020.116540

Separation and Purification Technology 239 (2020) 116540

Contents lists available at ScienceDirect

Separation and Purification Technology

journal homepage: www.elsevier.com/locate/seppur

Synthesis and application of superabsorbent polymer microspheres for rapid concentration and quantification of microbial pathogens in ambient water

Xunyi Wu, Xiao Huang, Yanzhe Zhu, Jing Li, Michael R. Hoffmann*

Linde + Robinson Laboratories, California Institute of Technology, Pasadena, CA 91125, United States

ARTICLE INFO

Keywords:
Super-absorbent polymer (SAP)
Concentration method
Waterborne pathogen
3D printing
Point-of-sample collection

ABSTRACT

Even though numerous methods have been developed for the detection and quantification of waterborne pathogens, the application of these methods is often hindered by the very low pathogen concentrations in natural waters. Therefore, rapid and efficient sample concentration methods are urgently needed. Here we present a novel method to pre-concentrate microbial pathogens in water using a portable 3D-printed system with super-absorbent polymer (SAP) microspheres, which can effectively reduce the actual volume of water in a collected sample. The SAP microspheres absorb water while excluding bacteria and viruses by size exclusion and charge repulsion. To improve the water absorption capacity of SAP in varying ionic strength waters (0–100 mM), we optimized the formulation of SAP to 180 $g{\cdot}L^{-1}$ Acrylamide, 75 $g{\cdot}L^{-1}$ Itaconic Acid and 4.0 $g{\cdot}L^{-1}$ Bis-Acrylamide for the highest ionic strength water as a function of the extent of cross-linking and the concentration of counter ions. Fluorescence microscopy and double-layer agar plating respectively showed that the 3D-printed system with optimally-designed SAP microspheres could rapidly achieve a 10-fold increase in the concentration of *Escherichia coli* (*E. coli*) and bacteriophage MS2 within 20 min with concentration efficiencies of 87% and 96%, respectively. Fold changes between concentrated and original samples from qPCR and RT-qPCR results were found to be respectively 11.34–22.27 for *E. coli* with original concentrations from 10^4 to 10^6 $cell{\cdot}mL^{-1}$, and 8.20–13.81 for MS2 with original concentrations from 10^4 to 10^6 $PFU{\cdot}mL^{-1}$. Furthermore, SAP microspheres can be reused for 20 times without performance loss, significantly decreasing the cost of our concentration system.

1. Introduction

Waterborne pathogens, including various pathogenic bacteria, viruses, and protozoa, are responsible for a series of diseases, and thus have been a major public health concern worldwide [1–3]. According to the World Health Organization (WHO), global mortality attributable to water-related diseases is currently 3.4 million per year, most of which are children [4]. This issue is especially severe in developing regions of the world due to the scarcity of clean water supplies and poor sanitation conditions [1,4–6]. Sensitive detection and quantification methods for waterborne pathogens, including traditional culture-based methods, or more recently, nucleic acid amplification tests [3,7–10], are thus indispensable to ensure water safety and to protect the public health.

Testing for pathogens in environmental waters has two main challenges: (1) the concentrations of pathogens in environmental water samples are usually magnitudes lower than those in clinical samples; and (2) the small sample volume being analyzed in each assay makes the direct detection of pathogens in environmental water samples nearly impossible [1,3]. Pathogen concentrations below the detection limit of the methods mentioned above, do not guarantee the safety of water, as they may still pose a health risk considering their low infectious doses [5,11].

Numerous techniques for pathogen concentration have been developed. Traditional techniques including polyethylene glycol (PEG) coagulation and precipitation, membrane filtration, centrifugation, and evaporation are most commonly used [12,13]. However, these concentration methods require complicated setups and are often time-consuming, which means water samples have to be transported to centralized laboratories with inevitable sample degradation even under continuous cold chain [1]. For field-studies, marine biologists use three steps of Tangential Flow Filtration (TFF) to concentrate water samples with a volume of 120 L [14]. The use of filtration cartridges and membranes, as well as pumping systems, are inevitable and the first TFF step for 60-fold concentration alone takes four hours [15]. The Bag-Mediated Filtration System (BMFS) provides another in-field concentration method that uses gravity as the driving force to filter and concentrate water samples. However, filters and an elution step

* Corresponding author.
E-mail address: mrh@caltech.edu (M.R. Hoffmann).

https://doi.org/10.1016/j.seppur.2020.116540
Received 26 September 2019; Received in revised form 11 December 2019; Accepted 9 January 2020
Available online 11 January 2020

followed by PEG/NaCl precipitation were also required [16]. Some new techniques are emerging, such as in-plane evaporation [17], magnetic nanoparticle platform on chip [18] or magnetic separators [19,20]. However, these new methods are still limited to laboratory use and are incapable of handling field samples with volumes of at least 1 or 2 L [19–21].

Super-absorbent polymer (SAP) microspheres are a class of cross-linked hydrogels that can absorb and retain water up to 1000 times the initial dry weight of the SAP beads [22,23]. SAP materials are widely used in personal disposable hygiene products (e.g., diapers), and for agricultural water preservation or waste fluid spill control [24,25]. By controlling the pore sizes of the hydrogel down to several nanometers, SAPs can absorb water but at the same time exclude particles with sizes above several nanometers, such as bacteria and viruses [24,26]. In order to use SAPs for microbial sample concentration, the SAPs were synthesized as small spherical microspheres using a milli-fluidic flow system. Itaconic acid is added to the polymer to obtain negatively charged polymeric microspheres that have uniform spherical shapes, which minimize electrostatic adsorption of microorganisms on the surface of the microspheres [27].

SAP microspheres absorb water through osmosis, which is driven by polyelectrolyte counter ions attached to the polymer. However, the extent of water absorption is limited by the retention force of the polymer networks due to cross-linking. The maximum water absorbencies and water absorption rates of the SAPs are determined by the equilibrium of the osmotic forces and the retention forces. For a given SAP formulation with a fixed number of polyelectrolyte counter ions, the osmotic force generated by the SAPs decreases with an increase of ionic strength, which effectively lowers the maximum water absorbency and water absorption rate of a specific SAP formulation. Therefore, the ionic strength of environmental water samples may have a significant impact on the performance of the SAP microspheres.

Here we have adjusted the composition of the SAP microspheres to achieve optimal performances in freshwater or saline waters and further demonstrated that bacteria and viruses collected from environmental water samples can be rapidly concentrated using optimized SAP microspheres. We have further developed a 3D-printed portable, hand-pressed centrifuge system to realize the single-step concentration using SAP microspheres for onsite water concentration in limited-resource settings and without trained personnel. Our study highlights that concentration of the microbial samples using SAPs provides an alternative sample concentration method that avoids a typical multi-step procedure that is often tedious, time-consuming, and inappropriate for use in underdeveloped parts of the world.

2. Materials and methods

2.1. SAP preparation and characterization

Monomers used for synthesis of the polymeric beads were acrylamide and itaconic acid, which were dissolved in deionized water with concentrations of 180 g·L^{-1} and 20 g·L^{-1}, respectively. Bis-acrylamide (4.0 g·L^{-1}) was added to the monomer solution as a cross-linker and potassium persulfate (2.6 g·L^{-1}) was added as the initiator of the polymerization reaction [27–29]. Itaconic acid in the monomer solution was fully neutralized by sodium hydroxide prior to the polymerization. All chemicals were purchased from Sigma-Aldrich and were used as received.

SAP microspheres with diameter of 500 μm were prepared by a two-step polymerization using a milli-fluidic system as shown in Fig. 1. Droplets of the monomer solution were generated through a T-junction with an inner diameter of 1/16 in. into the carrying silicon oil of 500 cSt. For the generation of water phase droplets, oil phase and water phase were injected at 0.5 mL·min^{-1} and 0.2 mL·min^{-1}, respectively, using two syringe pumps (74905-02, Cole-Parmer, US), into the tubing with 1/16-inch inner diameter. Generated droplets first underwent

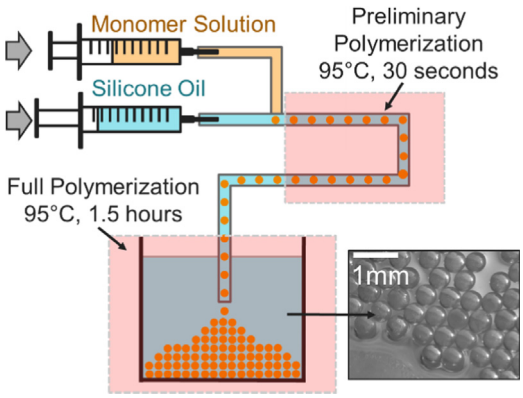

Fig. 1. A schematic illustration of the synthesis steps producing SAP microspheres.

preliminary polymerization in the tube for 30 s at 95 °C. Subsequently, full polymerization of the microspheres was achieved after the microspheres left the tube and settled in the hot oil bath at 95 °C for 1.5 h. This system can generate microspheres of diameters ranging from 500 μm to 2000 μm. Another fabrication method, inverse suspension polymerization, can be used to generate microspheres of diameters ranging from 10 μm to 500 μm, which can be used in smaller concentration systems with smaller starting sample volumes (see Fig. S1). After the polymerization, fabricated microspheres were washed using 95% ethanol to wash off residual oil. Microspheres were soaked in DI water for 24 h to remove any remaining monomers and subsequently dried under vacuum overnight. Weight analyses of dried SAP microspheres were performed using an analytical balance (AT469, Mettler, USA).

2.2. Water absorbency evaluation

The water absorbency Q (g/g) is defined as the swollen weight of SAP (g) divided by the dried weight of SAP (g). To simplify the experimental procedures and to evaluate the water absorbency more easily and precisely, larger SAP blocks (~1 × 10^{-2} g/block) (Fig. S7) were fabricated with varying monomer and cross-linker ratios (see Table 1). SAP blocks were fabricated under the same condition for SAP beads fabrication, and they share the same adsorption properties with SAP beads. Na^+ content in the polymer was changed by varying the proportion of sodium itaconate in the monomer solution. SAP blocks were tested for their absorbency in sodium chloride solutions with a series of ionic strengths of 0, 100, 200 and 500 mmol·L^{-1} [30]. The ionic strength S of all solutions was calculated using the following equation:

$$S = \frac{1}{2}\sum_{i=1}^{n} c_i z_i^2 \quad (1)$$

where c is the concentration of the dissolved salt ion in mol·L^{-1}, and z

Table 1
SAP recipes with varying cross-linking degree and sodium content.

	Acrylamide (g·L^{-1})	Itaconic Acid (g·L^{-1})	Bis-Acrylamide (g·L^{-1})
(O1) Original Recipe	180	20	4
C1	180	20	0.2
C2	180	20	0.4
C3	180	20	1
C4	180	20	2
S1	180	50	4
S2	180	75	4
S3	180	100	4

is the valence of the ion. For the dissolved salts, a complete dissociation was assumed [30]. After absorbing water overnight, polymer blocks were drained and the remaining water on the surface of the SAP was gently removed with a paper tissue. The weight of the fully swollen SAP blocks was determined, and their corresponding water absorbency (gram water absorbed by gram dried polymer) was calculated.

To measure the absorption rate, completely dried SAP microspheres were soaked in water. Their diameter changes upon swelling were recorded and measured with a light microscope (Leica M205FA, Leica Co., Germany). The water absorption rates were evaluated by three models with MATLAB (see supplementary information) and compared to the experimental results.

2.3. Microbial sample preparation

E. coli (ATCC 10798) was used as model bacteria in this study and cultured in Luria-Bertani broth (BD Difco™, USA). Before each concentration test, cells were harvested, washed and serially diluted to 10^4–10^6 cells·mL^{-1} using phosphate-buffered saline (pH 7.4) (Corning™, USA). Coliphage MS2 (ATCC 15597-B1) was chosen as model virus. The growth and purification procedures of MS2 are described in our previous work [10]. Before spiking MS2 in water samples, host *E. coli* cells were removed through centrifugation at 12000 rpm (13523 g) for 2 min (Eppendorf 5424, US). Briefly, MS2 suspension was diluted to 10^5–10^7 PFU·mL^{-1} for seeding studies. Environmental water samples were collected from a turtle pond on the Caltech campus and from the primary effluent from a local wastewater treatment plant (with ionic strengths of 15 and 20 mmol·L^{-1}, respectively [31]). The conductivities and pH values of environmental water samples were measured with an electrical pH/conductivity meter (Orion Star A215, Thermo Scientific, US) and ionic strengths were quantified using Griffin's equation [32].

2.4. Concentration experiments

A manual hand-powered tube system was designed and fabricated for field use in resource-limited settings (see Fig. 4). A 3D-printed filter with a mesh size of 300 μm (Fig. S4A) was inserted into a 50 mL commercial centrifuge tube (SuperClear™ Ultra High Performance Centrifuge Tubes, VWR, USA). The filter was fabricated using a high-resolution 3D printer (ProJet™ MJP 2500 Plus) with Visijet M2 RCL Clear Material (3D Systems, Rock Hill, SC). Subsequently, the tube was divided into two chambers: the upper chamber (filled with 0.5 g SAP microspheres) for sample concentration; and the lower chamber for concentrated sample collection. 40 mL water sample was added into the tube and was kept in the upper chamber. The sample water would not enter the lower chamber through the filter due to the surface tension of the liquid. The tube was left standing for 15 min for SAP microspheres to absorb water. Then the residual water (~4 mL) was transferred to the lower chamber by centrifugation (~500 rpm). The hand-press centrifuge was adapted from a commercially-available salad spinner (32480, OXO, USA). The filter and microspheres were taken out of the centrifuge tube. Subsequently, the concentrated sample was collected and its volume was measured. The concentrations of *E. coli* and MS2 in samples before and after concentration were measured and compared as described in Section 2.5. Concentration experiments of *E. coli* solutions with initial concentrations of 10^4, 10^5 and 10^6 cell·mL^{-1} were performed as independent triplicates. The difference before and after each microsphere-concentration experiment was compared using qPCR assays. The qPCR assays of *E. coli* solutions of 10^5, 10^6 and 10^7 cell·mL^{-1} were also performed as positive controls. Concentration experiments using MS2 with initial concentrations of 10^5, 10^6 and 10^7 PFU·mL^{-1} were performed in triplicate. The RT-qPCR assays of MS2 solutions of 10^6, 10^7 and 10^8 PFU·mL^{-1} were also performed as positive controls.

2.5. Concentration efficiency analyses

In this study, we use concentration efficiency to evaluate the performance of the concentration system. Here, we define the concentration efficiency as the percentage of microorganisms that remain in concentrated samples. Concentration efficiencies for *E. coli* and MS2 were analyzed using both of microcopy and culturing methods at the level of cell. The performance of the system was further evaluated by the fold-change using PCR-based molecular methods. *E. coli* cell concentrations were quantified using fluorescence microscopy (Leica DMi8, Leica Co., Germany) after SYBR-Green (Invitrogen™, USA) staining according to the manufacturer's protocol [10]. Fluorescence pictures were processed and the cell numbers were counted by ImageJ software (ImageJ 1.51j8, Wayne Rasband National Institutes of Health, USA). The number of *E. coli* was also evaluated by plating on Luria-Bertani agar (BD Difco™, USA). Colonies were counted after 14 h of incubation at 37 °C. Total environmental bacterial concentrations in environmental water samples (pond water and wastewater) were enumerated by fluorescence microscope counting and plate counting on LBA as well. The MS2 concentration was determined by the double agar layer method [33].

Concentration efficiencies of *E. coli* and MS2 were quantified by quantitative PCR (qPCR) and quantitative reverse transcription PCR (RT-qPCR) using a 6300 Realplex4 qPCR platform (Eppendorf, Hamburg, Germany). Relevant primer sets and probes are listed in Table S1. For *E. coli*, the qPCR assay targeting the 16 s rRNA gene was carried out in a 20-μL reaction mixture consists of 10 μL PerfeCTa® qPCR ToughMix® (Quanta BioSciences Inc.), 0.25 μM forward primer, 0.25 μM reverse primer, 0.25 μM TaqMan probe, 2 μL of template DNA, and nuclease-free-water. The qPCR thermocycling involves 3 min of initialization at 95 °C, and 40 cycles of denaturation at 95 °C for 15 s followed by annealing/extension at 55 °C for 30 s. For MS2, the RT-qPCR reactions were performed using QIAGEN OneStep RT-PCR Kit (Germantown, MD). Each 25-μL reaction mix included 800 nM forward and reverse primers, 300 nM TaqMan probe, 0.5 mg·mL^{-1} BSA, 1x RT-PCR buffer, 0.4 mM dNTP, 1 U enzyme mix, 3 μL of template RNA, and nuclease-free water.[10] The RT-qPCR thermocycling involves an initial reverse transcription step at 50 °C for 30 min, followed by an initial denaturation at 95 °C for 15 min, then 45 cycles of 94 °C for 15 s and 60 °C for 60 s. The nuclease-free water was used as negative controls for all qPCR and RT-qPCR assays. Here for each concentration assay, the concentration efficiency was evaluated by the fold change value:

$$Fold\ \ change = \frac{C(aftertheconcentration)}{C(beforetheconcentration)} \times 100\% \quad (2)$$

where $C_{(before\ the\ concentration)}$ and $C_{(after\ the\ concentration)}$ are concentrations of sample before and after concentration calculated with standard curves performed on each plate. Concentrations of *E. coli* and MS2 standard samples were respectively evaluated using the fluorescence microscopy and the double-layer agar as described in Section 2.5. All qPCR and RT-qPCR reactions performed in this study reached efficiency between 90% and 110%, indicating the high reliability of our performed assays [34]. Quantification data of samples before and after concentration experiments for the fold change calculations for both *E. coli* and MS2 can be found in Table S3 in the supporting information. All samples were run in triplicate.

2.6. Reusability test

To reuse the SAP microspheres after the concentration tests, the microspheres were washed under running tap water for two minutes to remove the remaining bacteria and viruses from the surfaces of the microspheres. The SAP microspheres were subsequently washed in 30 mL Milli-Q water and followed by being dried for subsequent reuse.

The synthesized SAP microspheres were fully loaded with water via absorption and then dried using a vacuum oven (VO914A, Thermo Scientific, USA) for 20 consecutive cycles. The gross weights and water absorbencies were measured to test their reusability after successive swelling and drying cycles.

3. Results and discussion

3.1. Synthesis of SAP microspheres

Uniform poly (acrylamide-co-itaconic acid) (P(AM-co-IA)) microspheres were fabricated using a system as illustrated in Fig. 1. Monomer solution-in-oil droplets were generated with two syringe pumps, using a T-junction. After the generation of monomer solution droplets, the P(AM-co-IA) microspheres required at least 1.5 h at 95 °C to achieve complete polymerization: the polymerization reaction was catalyzed by free radicals from persulfate generated by heating and dissociating potassium persulfate. The persulfate free radicals convert monomers of acrylamide and itaconic acid with double bonds to free radicals that react with other monomers to begin the polymerization chain reaction. The elongating polymer chains are randomly cross-linked by bis-acrylamide, resulting in a gel matrix structure [35]. The two-step polymerization system was designed such that the polymer microspheres would only undergo preliminary polymerization in the tube, so they would not fuse into each other and block the tube. When the partially polymerized microspheres left the tube, they were immersed in an oil bath for 1.5 h allowing for complete polymerization. The characteristics of washed and fully-dried SAP microspheres presented uniform spherical shape with a characteristic diameter of 500 ± 8 μm, white color, and smooth surfaces as shown in Fig. 1. Each SAP microspheres have the same formula and are formed with the same amount of monomers, being very uniform after absorbing water. The slight difference in the shape of the sphere when they are dried was most likely due to the inconsistent shape change during the drying process. When the microspheres were fully dried, their density was slightly lower than that of water due to that voids presented in the polymer structure. Variances in the porous polymer structure during drying of each polymer microspheres may also lead to slight density inconsistency between microspheres, but these slight differences in shape and density would not influence the performance of SAP microspheres on water absorption as they became uniform after they start to absorb water. Smaller size microspheres can be fabricated by inverse suspension polymerization method and shared similar SAP properties (see Fig. S1B).

3.2. Optimization of SAP for various water matrices

SAP microspheres used in the previous research with fixed composition can only work in deionized water, since both the maximum capacity, and the rate of water absorption would decrease drastically in high ionic strength water. Hence, the composition of the SAP beads needs to be adjusted to achieve optimal performances for different water matrices. SAP blocks fabricated according to the original monomer solution recipe (180 $g{\cdot}L^{-1}$ AM, 20 $g{\cdot}L^{-1}$ IA and 4.0 $g{\cdot}L^{-1}$ Bis-A) could absorb water of around 80 times their own weight (water absorbency (Q ~ 80), and a maximum absorbency of 96% was reached under 20 min in DI water (see Fig. 2). Although the polymer is stable and tolerant to different environmental conditions, the maximum water absorbency and water absorption rate of the polymer were significantly reduced in higher ionic strength water samples due to the decreased osmotic force. For environmental waters, the average ionic strength of freshwater and wastewater are around 5 $mmol{\cdot}L^{-1}$ and 50 $mmol{\cdot}L^{-1}$, respectively, and can be as high as 150 $mmol{\cdot}L^{-1}$ for untreated wastewater [36–39]. In water with an ionic strength of 100 $mmol{\cdot}L^{-1}$, the same SAP's absorbency decreased to 30% of its maximum absorbency. Less than 80% of maximum water absorbency was achieved, and equilibrium could not be reached for more than 30 min (see Fig. 2).

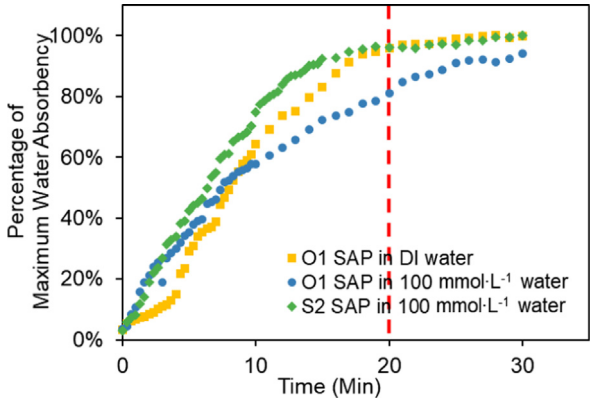

Fig. 2. Water absorbency of original microspheres (O1) and revised microspheres (S2) in DI water and saline water (100 $mmol{\cdot}L^{-1}$) over time.

Therefore, the SAP composition requires optimization to improve its performance in saline water.

The water absorbency of SAP is determined by the balance of three forces: (1) the osmosis potential between the solution within the polymer network and the external solution; (2) the electrostatic repulsion resulting from the fixed charges on the polymer chains; and (3) the elastic retractile response of the polymer network [40]. Forces (1) and (2) increase the absorption of SAP while force (3) restricts the absorption. The high sodium cation (polyelectrolyte counter ion) concentration within the polymer network provides osmotic pressure, which quickly drives water into the polymer. As the water penetrates the polymer, the sodium cation is diluted, and the concentration of sodium cation in the polymer decreases, leading to a decrease of osmotic force [22,23]. At the same time, the retention force of the polymer is increasing with the expansion of the polymer network. When the balance between the osmotic force and retention force is reached, the SAP is at equilibrium. For the cross-linked polymer, the water absorbency, Q, can be expressed as a function using elasticity gel theory of Flory [35,40], which has the following form:

$$Q^{\frac{5}{3}} = \left[\left(\frac{i}{2V_u S^{\frac{1}{2}}}\right)^2 + \left(\frac{1}{2} - X_1\right)V_1\right]V_e/V_0 \tag{4}$$

where Q: maximum water absorbency (g/g); V_e/V_0: crosslinking density of polymer (amount cross-linker/total polymer); $(1/2 - X_1)/V_1$: affinity between polymer and external solution (X_1: interaction parameter of polymer with solvent; V_1: molar volume of solvent in a real network); V_u: volume of structural unit; i: electronic/ionic charge present on the polymer backbone per polymer unit; i/V_u: fixed charge per unit volume of polymer; S: Ionic strength of external solution ($mol{\cdot}L^{-1}$). Since the affinity of the polymer to water does not change in our case, and the volume of the structural unit is fixed, the maximum water absorbency is solely controlled by the crosslinking density, fixed-charge density and external ionic strength.

Two methods were explored to improve the performance of SAP in water at different ionic strengths: one was to reduce the retention force of the polymer by decreasing the cross-linking degree; and the other was to increase the osmotic pressure by increasing the sodium content in the polymer. The recipe changes of SAP also varied the pore size of the fabricated SAP, which was still small enough to exclude bacteria and viruses with high concentration efficiencies (see Section 3.4 for results and discussion).

Fig. 3 shows the change of SAP absorption performance induced by varying cross-linking degrees and counter ion concentrations. As shown in Fig. 3A, SAP with the lowest cross-linking degree (C1) could reach water absorbency of 50 in the highest ionic strength solution (500 $mmol{\cdot}L^{-1}$), while the absorbency of the original microspheres (O1) decreased to less than 20. However, it should be noted that when

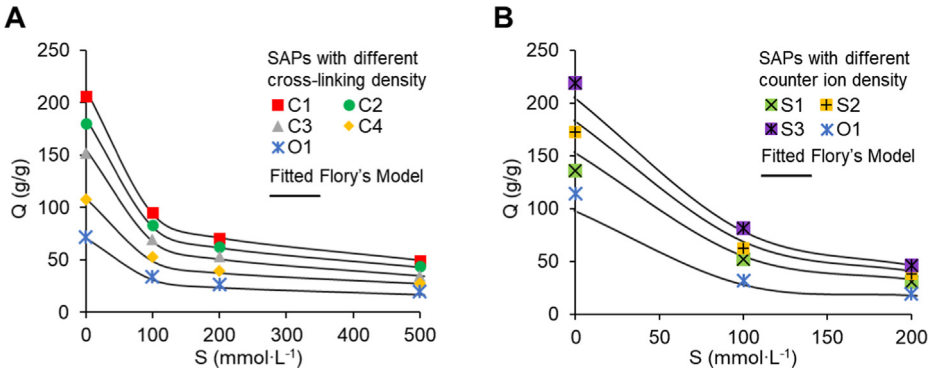

Fig. 3. Change of maximum water absorbency (Q) vs. ambient ionic strengths (S), and the impacts of changing cross-linking density (A) and counter ion density (B) on maximum water absorbency. Error bars are all smaller than 1% and are not shown on graphs.

loosening the structure of the polymer to reduce the retention force, the mechanical strength of the SAP is also reduced. If the cross-linking degree were modified to an amount smaller than 1 g Bis-A per 1000 g total monomer, then the SAP microspheres broke easily during the centrifugation step and the debris of the broken SAP microspheres entered the residual water sample, influencing the experimental results. Thus, broken SAP microspheres cannot be reused.

Increasing the Na^+ content in the polymer also significantly improved the absorption rate of SAP in saline water, by providing an increased osmotic force (see Fig. 3B). Before the centrifugation step, the microspheres needed to reach at least 90% of their maximum absorbency. At this stage, the absorption rate slows down and the weight of SAP did not change a lot (Fig. 2), which was important for the following centrifugal step. For a successful concentration step, a small volume of sample must remain after the water absorption through SAP. Therefore, a slow water absorption rate of SAP microspheres during centrifugation would be desirable. Otherwise, the SAP microspheres would continue to rapidly absorb the remaining water during centrifugation and the sample water could be totally absorbed by SAP microspheres at a fast absorption rate, leading to the failure of the concentration process. For the original SAP microspheres, less than 80% of the maximum water absorbency was obtained at 20 min in 100 $mmol{\cdot}L^{-1}$ water while still swelling rapidly. If we were to use SAP microspheres made with this recipe, the concentration process would take more than 30 min. However, the microspheres with the S2 recipe would reach 95% maximum water absorbency in 20 min, which was much faster than the microspheres with the original recipe (~35 min). The improvement of the absorption rate was further confirmed using three models (see supplementary information). By applying the models to our experimental data to calculate the diffusion coefficients, all three models show the increase of the diffusion coefficients by around 50% after using the optimized recipe. Since the resulting linear fits of $Q^{5/3}$ versus the cross-linking density and the fixed charge density (i/V_u) are consistent with the predictions of the Flory theory [39,40] (Fig. 3), the SAP formulations could be easily customized to suit different ionic strengths of the respective water matrices.

3.3. Tube concentration system

Furthermore, the previous concentration method introduced in Xie et al. (2015) required five manual and consecutive operations of using pipettes to collect concentrated samples (each step concentrating about 20% of the sample volume), which made this approach tedious, time-consuming and not applicable in field. Therefore, our study remarkably developed a portable, hand-pressed centrifuge system with one-step operation to facilitate the efficient use of SAP beads for onsite concentration for waterborne microorganism in low-resource settings, thus allowing our concentration method to be easily performed by people without any prior training. Fig. 4 schematically illustrates the tube system for microbial pathogen concentration. Each tube contains 0.5 g SAP microspheres and a 3D-printed filter. The 3D-printed filter divided the tube into two chambers and the water samples are restricted in the upper chamber before centrifugation by the filter due to the surface tension of the sample. After adding the sample, the tube only need to be left to stand for 20 min for the full absorption of water by the SAP. Non-absorbed water is transferred to the lower chamber using a hand-press centrifuge. After 20 min, more than 90% of the sample was adsorbed and continued absorption became very slow. Thus, a remaining water sample (~4 mL) could be collected by centrifugation. The hand-press centrifuge was adapted from a salad spinner, which can reach an average rotation speed of 500 rpm. This spinning speed was fast enough, as evident, as the concentration efficiency (percentage of microorganisms recovered after concentration) did not change when using a commercial centrifuge with up to 1200 rpm (data not shown). This hand-pressed spinner reduced the cost of the system and made the system totally off-grid and suitable for field use. Moreover, our system may be a promising tool in field studies, as it can rapidly concentrate environmental samples. One example of applications could be in-field sequencing when coupled with the new sequencing technology, MinION sequencer [41].

3.4. Microorganism concentration performance

The concentration factor (hereinafter referred to as the ratio of the sample volumes before and after the concentration) of SAP microspheres were maintained in a range of 1.3–2.1 for each step, so that the swollen SAP microspheres could be suspended after the concentrating step. When the concentration factor exceeded 4, the concentration efficiency decreased substantially due to that the microorganisms trapped in remaining liquids on the microsphere surface and/or in the voids among the microspheres. The concentration efficiency dropped to 38% when the concentration factor increased an order of magnitude [27]. When using the hand-pressed centrifuge centrifuging step, the concentrate was transferred to the collection chamber. This step substantially improved the concentration factors (the ratio of the sample volumes before and after concentration) and concentration efficiencies. A concentration efficiency of 87 ± 6% was achieved with a concentration factor of 9–10 for *E. coli* in DI water within 20 min (see Fig. 5). By using different SAP formulations, we were able to achieve similar concentration efficiencies of *E. coli* in water with high ionic strengths up to 100 $mmol{\cdot}L^{-1}$. S2 SAP microspheres were used for the concentration of *E. coli* in 100 $mmol{\cdot}L^{-1}$ ionic strength water and an average of 89 ± 17% concentration efficiency was achieved. Additionally, qPCR targeting 16S rRNA gene and RT-qPCR were respectively performed to evaluate the concentration efficiencies of *E. coli* and MS2. As shown in Fig. 6, the fold change values between 10-fold concentrated samples and original samples were found to be 11.34, 22.27 and 17.97, respectively, from *E. coli* solutions with initial

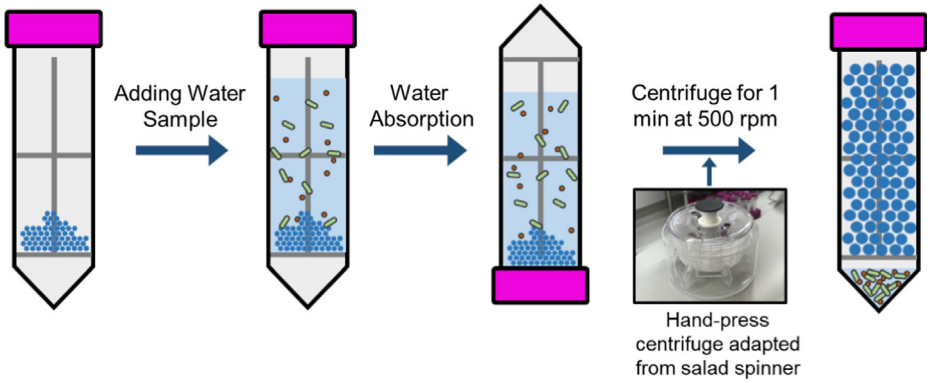

Fig. 4. The tube system designed for microbial pathogen concentration using SAP microspheres. The tube is composed of 0.5 g SAP microspheres and a 3D-printed filter. After adding the water sample, the tube is left to stand for 20 min for the full absorption of water by SAP. Non-absorbed water is pushed to the lower chamber using a hand-press centrifuge.

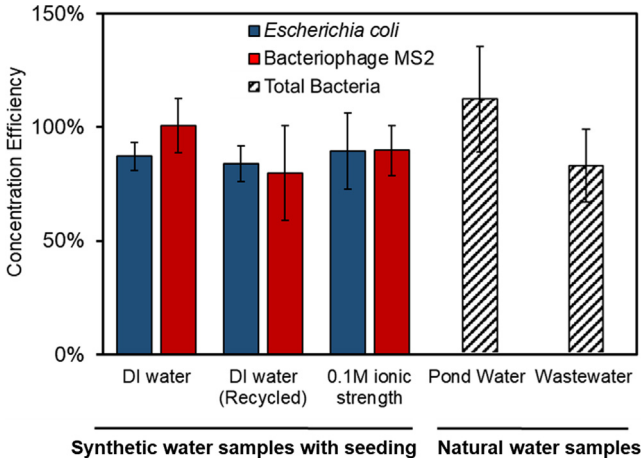

Fig. 5. Concentration efficiencies of *E. coli*, MS2 and total bacteria using the tube concentration system calculated by microscopic cell counts, plague forming unit quantification. *E. coli* and MS2 were concentrated using new SAP microspheres and recycled SAP microspheres after 20 drying- swelling cycle, and in DI and 0.1 M ionic strength water. Total bacteria were concentrated from pond water and wastewater samples.

concentrations of 10^4, 10^5 and 10^6 cell·mL^{-1}. As positive controls, the fold changes between *E. coli* solutions of 10^5 and 10^4, 10^6 and 10^5, 10^7 and 10^6 cell·mL^{-1} were 3.03, 8.50 and 9.34, respectively, which implied the concentration efficiencies of SAP microsphere-based concentration system were respectively 275%, 162% and 92% higher than they were supposed to be by qPCR assays. For the samples of 10^4, 10^5 and 10^6 cell·mL^{-1}. Fold change values between samples of 10^5 (both concentrated and serially diluted) and 10^4 cell·mL^{-1} were relatively low because the concentration of 10^4 cell·mL^{-1} is much close to the detection limit of 16S rRNA qPCR. Our results showed that the tube concentration system based on SAP microspheres could achieve satisfactory concentration efficiencies of *E. coli* solutions with a range of initial concentrations.

The bacterial concentrations of original samples did not affect the concentration efficiency as evaluated by microscopic cell counts. Experimental results showed very similar concentration efficiencies (between 85% and 90%) for water samples with different initial concentrations from 10^4 to 10^8 cells·mL^{-1}, thus allowing total concentration efficiencies of higher than 60% for 100- or 1000-time concentration, although 2 or 3 sequential concentration steps may be required. It should be noted that these sequential concentration steps may require multiple formulations of SAP microspheres due to the increasing ionic strength during concentration. It's extremely difficult to achieve 100–1000 times concentration in one step due to the difficulty in concentrated sample collection and the sample loss on the microspheres' surface.

Concentration tests using bacteriophage MS2 resulted in a similar level of concentration efficiency (see Fig. 5) evaluated by plaque forming unit quantification. The average concentration efficiency of one concentration step was 101 ± 12% in DI water using O1 SAP. For a 100-mmol·L^{-1} ionic strength water sample, the concentration efficiency of MS2 was 90 ± 10%, using S2 SAP microspheres (Fig. 5). The value of > 100% was likely caused by the well-known large standard deviation of the double agar layer method, imprecisions in

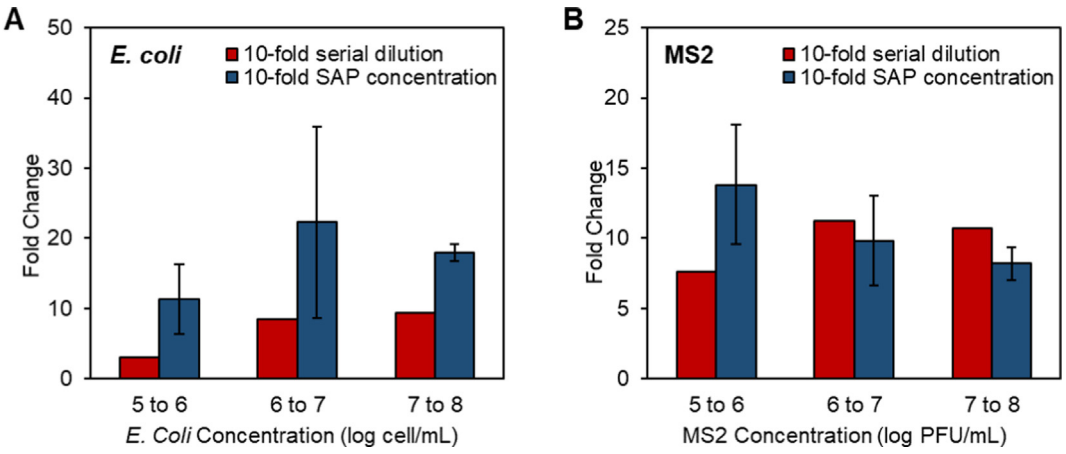

Fig. 6. Fold Changes of qPCR and RT-qPCR of *E. coli* (A) and MS2 (B) for samples in varying magnitude of orders with serially diluted samples (red bars) and concentrated samples (blue bars) using the tube concentration system; wherein standard deviations (error bars) were calculated from fold change values of triple independent concentration experiments. Fold change values were calculated from quantification data according to the standard curve performed on each plate. (For interpretation of the references to colour in this figure legend, the reader is referred to the web version of this article.)

experimental procedures and the MS2 aggregation during experiments. RT-qPCR was performed to evaluate the recovery rates of MS2. As shown in Fig. 6, the fold changes between concentrated samples and original samples were found to be 13.81, 9.83 and 8.20, respectively, for the samples with initial concentrations of 10^4, 10^5 and 10^6 PFU·mL^{-1}. Meanwhile, the fold change values between 10^6 and 10^5, 10^7 and 10^6, 10^8 and 10^7 were 7.64, 11.22 and 10.69, respectively, which implied the concentration efficiencies of SAP microsphere-based concentration system were respectively 180%, 88% and 77% comparing to what they were supposed to be by qPCR assays. Fold change values between 10-fold concentrated MS2 samples and original samples are similar to fold change values of between positive control MS2 samples with 10-fold dilution, indicating high concentration efficiencies of the tube concentration system. In summary, results from qPCR and RT-qPCR assays indicate that the SAP microsphere-based concentration method completely meets the requirements for nucleic acid amplification-based environmental monitoring and surveillance. It should be noted that compared to conventional virus concentration methods, such as ultracentrifugation, electropositive or electronegative filters or ultrafiltration [42–44], the SAP microspheres concentration method neither uses complicated instruments or expensive filters, nor requires the preconditioning of water samples.

Furthermore, the concentration efficiencies of SAP microspheres used for concentrating the native bacteria in the Caltech pond water (ionic strength 15 mmol·L^{-1}, pH = 7.75) and the wastewater from the wastewater treatment plant (ionic strength 20 mmol·L^{-1}, pH = 8.02) were investigated. As shown in Fig. 5, average bacterial concentration efficiencies of 112% and 83%, respectively, were achieved for pond water and wastewater samples. The concentration processes were completed in less than 20 min. Presence of other substances in real water samples such as natural organic matters or algae would not influence the performance of our system according to our tests on real environmental waters, which was discussed in Section 3.4.

It should be noted that we introduced itaconic acid to our customized SAP formula to add a negative surface charge and minimize the electrostatic adsorption of microorganisms. Although bacteria and viruses may not always have negative surface charge in environmental waters, which depends on their isoelectric points [45,46]. As most bacteria have low isoelectric points and will be negatively charged in environmental waters [45,47], they should be repelled by the SAP beads as what happened to our model bacterium *E. coli*. However, viruses have a broader range of isoelectric points [46]. Our model virus, MS2, has a low isoelectric point (~3.5) [46] and thus, a high concentration efficiency is expected due to electrostatic repulsion. Although accounting for a small part, there are still viruses whose surface charges in natural water may not be strong enough for electrostatic repulsion and therefore the concentration efficiency might be impaired, e.g., somatic coliphage ΦX174 (isoelectric point ~ 7) [46].

3.5. Reusability of SAP microspheres

Reusing the microspheres can significantly decrease the cost of our concentration system. After use, the microspheres can be washed and dried for subsequent applications requiring sample concentration. Simple washing with running tap water was sufficient for the reuse of SAP microspheres, as no bacteria or viruses were detected using membrane filtration from the final washing water before the next use. For more sensitive applications, SAP microspheres could be autoclaved as well. To demonstrate their reusability, the SAP microspheres were dried and rehydrated for more than 20 times. Fig. S3 shows the weight change of 100 SAP microspheres for 20 cycles of full drying and swelling. For 20 cycles, the weight change for both dried and swollen microspheres was less than 5%, whereas the decrease of water absorbency was less than 2%. The concentration efficiencies of *E. coli* and MS2 using recycled microspheres (after 20 cycles) were still up to 84 ± 7% and 90 ± 11%, respectively (Fig. 5). Slight efficiency losses during reusing recycled microspheres were most likely attributed to the inevitable breaks of some SAP microspheres during the recycling process, which became much more severe with the increase of recycling times as observed. Damaged spheres might trap much more pathogens due to the increased surface area.

4. Conclusion

In this study, tailored SAP microspheres coupled with a hand-powered tube system were developed to achieve efficient and rapid concentration for environmental microorganisms. In order to overcome the performance loss of SAP in high ionic strength water samples, we have been able to improve the water absorption ability of SAP microspheres by optimizing the degree of polymer cross-linking and controlling the counter ion concentrations using the Flory model as a guide. Optimally synthesized SAP microspheres were shown to absorb more water at higher absorption rates compared to other commercially available water-absorbing microspheres, making our synthetically-tailored SAP microspheres able to concentrate bacteria and viruses from high ionic strength water samples and environmental water samples within a short time. In addition, we developed a low-cost, portable, hand-powered portable centrifuge tube system based on our tailored SAP microspheres to facilitate concentrating water in low-resource settings in the field. Results from our study highlight that we provide a cost-effective, easy-to-use and off-grid system with tailored SAP microspheres for various water samples. We envision that this system could be applied to the field for efficient microbial concentration and promote rapid on-site microbial analysis.

CRediT authorship contribution statement

Xunyi Wu: Conceptualization, Methodology, Investigation, Formal analysis, Writing - original draft. **Xiao Huang:** Conceptualization, Methodology, Writing - review & editing. **Yanzhe Zhu:** Writing - review & editing. **Jing Li:** Methodology, Writing - review & editing. **Michael R. Hoffmann:** Conceptualization.

Declaration of Competing Interest

The authors declare that they have no known competing financial interests or personal relationships that could have appeared to influence the work reported in this paper.

Acknowledgements

The authors acknowledge the financial support provided by the Bill and Melinda Gates Foundation (grant no. OPP1111252). The authors thank Dr. Katharina Urmann, Dr. Xingyu Lin and Dr. Xing Xie for their helpful advices and discussions.

Appendix A. Supplementary material

Supplementary data to this article can be found online at https://doi.org/10.1016/j.seppur.2020.116540.

References

[1] F. Ramírez-Castillo, A. Loera-Muro, M. Jacques, P. Garneau, F. Avelar-González, J. Harel, A. Guerrero-Barrera, Waterborne pathogens: detection methods and challenges, Pathogens 4 (2015) 307–334, https://doi.org/10.3390/pathogens4020307.
[2] T.M. Straub, D.P. Chandler, Towards a unified system for detecting waterborne pathogens, J. Microbiol. Methods 53 (2003) 185–197, https://doi.org/10.1016/S0167-7012(03)00023-X.
[3] T.G. Aw, J.B. Rose, Detection of pathogens in water: From phylochips to qPCR to pyrosequencing, Curr. Opin. Biotechnol. 23 (2012) 422–430, https://doi.org/10.1016/j.copbio.2011.11.016.
[4] World Health Organization, Water for health: Taking charge, 2001. doi:10.1017/

CBO9781107415324.004.
[5] H. Bridle, Waterborne Pathogens (2014), https://doi.org/10.1016/B978-0-444-59543-0.00002-5.
[6] A. Malik, A. Yasar, A.B. Tabinda, M. Abubakar, Water-borne diseases, cost of illness and willingness to pay for diseases interventions in rural communities of developing countries, Iran. J. Public Health 41 (2012) 39–49 Export Date 9 July 2012\nSource Scopus.
[7] M.T. Madigan, J.M. Martinko, J. Parker, Brock. Biology of Microorganisms, 2012. doi:http://doi.org/10.1007/s13398-014-0173-7.2.
[8] G. Shipley, The MIQE Guidelines Uncloaked, in: PCR Troubl. Optim. Essent. Guid., 2011: pp. 149–162. doi:http://doi.org/10.1373/clinchem.2008.112797.
[9] M. Burns, H. Valdivia, Modelling the limit of detection in real-time quantitative PCR, Eur. Food Res. Technol. 226 (2008) 1513–1524, https://doi.org/10.1007/s00217-007-0683-z.
[10] X. Huang, X. Lin, K. Urmann, L. Li, X. Xie, S. Jiang, M.R. Hoffmann, Smartphone-Based in-Gel Loop-Mediated Isothermal Amplification (gLAMP) System Enables Rapid Coliphage MS2 Quantification in Environmental Waters, Environ. Sci. Technol. 52 (2018) 6399–6407, https://doi.org/10.1021/acs.est.8b00241.
[11] P. Schmid-Hempel, S.A. Frank, Pathogenesis, virulence, and infective dose, PLoS Pathog. 3 (2007) 1372–1373, https://doi.org/10.1371/journal.ppat.0030147.
[12] K.A. Stevens, L.A. Jaykus, Bacterial separation and concentration from complex sample matrices: a review, Crit. Rev. Microbiol. 30 (2004) 7–24, https://doi.org/10.1080/10408410490266410.
[13] M.A. Borchardt, B.A. Kieke, S.K. Spencer, Ranking filter methods for concentrating pathogens in lake water, Appl. Environ. Microbiol. 79 (2013) 5418–5419, https://doi.org/10.1128/AEM.01430-13.
[14] A. Sundbergh, S. Craig Cary, K.E. Wommack, R.R. Helton, K. Portune, S.J. Williamson, B.T. Glazer, An instrument for collecting discrete large-volume water samples suitable for ecological studies of microorganisms, Deep Sea Res. Part I Oceanogr. Res. Pap. 51 (2004) 1781–1792, https://doi.org/10.1016/j.dsr.2004.05.011.
[15] K.E. Gibson, K.J. Schwab, Tangential-flow ultrafiltration with integrated inhibition detection for recovery of surrogates and human pathogens from large-volume source water and finished drinking water, Appl. Environ. Microbiol. 77 (2011) 385–391, https://doi.org/10.1128/AEM.01164-10.
[16] C.S. Fagnant, L.M. Sánchez-Gonzalez, N.A. Zhou, J.C. Falman, M. Eisenstein, D. Guelig, B. Ockerman, Y. Guan, A.L. Kossik, Y.S. Linden, N.K. Beck, R. Wilmouth, E. Komen, B. Mwangi, J. Nyangao, J.H. Shirai, I. Novosselov, P. Borus, D.S. Boyle, J.S. Meschke, Improvement of the Bag-Mediated Filtration System for Sampling Wastewater and Wastewater-Impacted Waters, Food Environ. Virol. 10 (2018) 72–82, https://doi.org/10.1007/s12560-017-9311-7.
[17] J.W. Choi, S.M. Hosseini Hashemi, D. Erickson, D. Psaltis, A micropillar array for sample concentration via in-plane evaporation, Biomicrofluidics. 8 (2014) 1–9. doi:http://doi.org/10.1063/1.4890943.
[18] Y. Zhang, L.K. Riley, M. Lin, Z. Hu, Lanthanum-based concentration and micro-respirometric detection of microbes in water, Water Res. (2010), https://doi.org/10.1016/j.watres.2010.03.029.
[19] O. Rotariu, I.D. Ogden, M. MacRae, V. Bădescu, N.J.C. Strachan, An immunomagnetic separator for concentration of pathogenic micro-organisms from large volume samples, J. Magn. Magn. Mater. 293 (2005) 589–596, https://doi.org/10.1016/j.jmmm.2005.01.078.
[20] G.D. Chen, C.J. Alberts, W. Rodriguez, M. Toner, Concentration and Purification of Human Immunodeficiency Virus Type 1 Virions by Microfluidic Separation of Superparamagnetic Nanoparticles, Anal. Chem. 82 (2009) 723–728, https://doi.org/10.1021/ac9024522.
[21] S. Park, Y. Zhang, T.-H. Wang, S. Yang, Continuous dielectrophoretic bacterial separation and concentration from physiological media of high conductivity, Lab Chip. 11 (2011) 2893, https://doi.org/10.1039/c1lc20307j.
[22] S. Kiatkamjornwong, Superabsorbent Polymers and Superabsorbent Polymer Composites, ScienceAsia. 33 (2007) 39–43, https://doi.org/10.2306/scienceasia1513-1874.2007.33(s1).039.
[23] W.-F. Lee, R.-J. Wu, Superabsorbent polymeric materials. I. Swelling behaviors of crosslinked poly(sodium acrylate-co-hydroxyethyl methacrylate) in aqueous salt solution, J. Appl. Polym. Sci. 62 (1996) 1099–1114. doi:http://doi.org/10.1002/(SICI)1097-4628(19961114)62:7 < 1099::AID-APP16 > 3.0.CO;2-1.
[24] Mark Elliott, Superabsorbent Polymers, 573 (1994) 128–140. doi:http://doi.org/10.1021/bk-1994-0573.
[25] E.M. Ahmed, Hydrogel: Preparation, characterization, and applications: a review, J. Adv. Res. 6 (2015) 105–121, https://doi.org/10.1016/j.jare.2013.07.006.
[26] D. Valade, L.K. Wong, Y. Jeon, Z. Jia, M.J. Monteiro, Polyacrylamide hydrogel membranes with controlled pore sizes, J. Polym. Sci. Part A Polym. Chem. 51 (2013) 129–138, https://doi.org/10.1002/pola.26311.
[27] X. Xie, J. Bahnemann, S. Wang, Y. Yang, M.R. Hoffmann, "Nanofiltration" enabled by super-absorbent polymer beads for concentrating microorganisms in water samples, Sci. Rep. 6 (2016) 1–8, https://doi.org/10.1038/srep20516.
[28] D. Shi, Y. Gao, L. Sun, M. Chen, Superabsorbent poly(acrylamide-co-itaconic acid) hydrogel microspheres: Preparation, characterization and absorbency, Polym. Sci. Ser. A. 56 (2014) 275–282, https://doi.org/10.1134/S0965545X14030146.
[29] S. Bednarz, A. Błaszczyk, D. Błażejewska, D. Bogdał, M. Cao, Y. Durant, L.E. Coleman, N.A. Meinhardt, Z. Hehn, D. Nowak, J. Pethe, J. Li, T.B. Brill, A. Note, S. Polowiński, C.F. Sch, G. Swift, H. Company, T. Imoto, S. Nagai, K. Yoshida, P.E.L. Schofer, B.E. Tate, K. Yokota, T. Hirabayashi, T. Takashima, L.Yu. Yu, H.M. Shen, Z. L. Xu, Polymerization of itaconic acid, Polimery. 5 (1975) 1197–1205. doi:http://doi.org/10.1007/BF02283833.
[30] L.J. Böni, R. Zurflüh, M.E. Baumgartner, E.J. Windhab, P. Fischer, S. Kuster, P.A. Rühs, Effect of ionic strength and seawater cations on hagfish slime formation, Sci. Rep. 8 (2018) 1–12, https://doi.org/10.1038/s41598-018-27975-0.
[31] M.H.B. Daniel, A. Montebelo, Effects of urban sewage on dissolved oxygen, dissolved inorganic and organic carbon, and electrical conductivity of small streams along a gradient of urbanization in the Piracicaba river basin, Water, Air, Soil. 136 (2002) 189–206 http://link.springer.com/article/10.1023/A:1015287708170.
[32] R.A. Griffen, J.J. Jurinach, Estimation of activity co-efficent from the electrical conductivity of natural agnote systems in soil extracts, Soil Sc. 116 (1973) 26–30.
[33] A.M. Kropinski, A. Mazzocco, T.E. Waddell, E. Lingohr, R.P. Johnson, Enumeration of Bacteriophages by Double Agar Overlay Plaque Assay, in: 2009: pp. 69–76. doi:http://doi.org/10.1007/978-1-60327-164-6_7.
[34] A. Osselaere, R. Santos, V. Hautekiet, P. De Backer, K. Chiers, Deoxynivalenol Impairs Hepatic and Intestinal Gene Expression of Selected Oxidative Stress , Tight Junction and Inflammation Proteins in Broiler Chickens , but Addition of an Adsorbing Agent Shifts the Effects to the Distal Parts of the Small Intestine, 8 (2013) 1–7. doi:http://doi.org/10.1371/journal.pone.0069014.
[35] X.X. Chen, G.G. Shan, J. Huang, Z.Z. Huang, Z.Z. Weng, Synthesis and properties of acrylic-based superabsorbent, J. Appl. Polym. Sci. 92 (2004) 619–624, https://doi.org/10.1080/10601320701351268.
[36] F. Prieto, E. Barrado, M. Vega, L. Deban, Measurement of electrical conductivity of wastewater for fast determination of metal ion concentration, Russ. J. Appl. Chem. 74 (2001) 1321–1324, https://doi.org/10.1023/A:1013710413982.
[37] S.M. Cormier, G.W. Suter, L. Zheng, Derivation of a benchmark for freshwater ionic strength, Environ. Toxicol. Chem. 32 (2013) 263–271, https://doi.org/10.1002/etc.2064.
[38] R.A. Griffin, J.J. Jurinak, Estimation of activity coefficients from the electrical conductivity of natural aquatic systems and soil extracts, Soil Sci., 116, 26-30. http://dx.doi.org/10.1097/00010694-197307000-00005.
[39] R.S. Cates, Influence of crosslink density on swelling and conformation of surface-constrained poly(n-isopropylacrylamide), Hydrogels (2010), https://doi.org/10.1017/CBO9781107415324.004.
[40] P.J. Flory, J. Rehner Jr, Statistical mechanics of cross-linked polymer networks II. Swelling, J. Chem. Phys. 11 (1943) 521–526.
[41] A.D. Tyler, L. Mataseje, C.J. Urfano, L. Schmidt, K.S. Antonation, M.R. Mulvey, C.R. Corbett, Evaluation of Oxford Nanopore's MinION Sequencing Device for Microbial Whole Genome Sequencing Applications, Sci. Rep. (2018), https://doi.org/10.1038/s41598-018-29334-5.
[42] J.L. Cashdollar, L. Wymer, Methods for primary concentration of viruses from water samples: A review and meta-analysis of recent studies, J. Appl. Microbiol. 115 (2013) 1–11, https://doi.org/10.1111/jam.12143.
[43] D.A. Kuzmanovic, I. Elashvili, C. Wick, C. O'Connell, S. Krueger, Bacteriophage MS2: Molecular weight and spatial distribution of the protein and RNA components by small-angle neutron scattering and virus counting, Structure 11 (2003) 1339–1348, https://doi.org/10.1016/j.str.2003.09.021.
[44] H. Katayama, A. Shimasaki, H. Katayama, A. Shimasaki, S. Ohgaki, Development of a virus concentration method and its application to detection of enterovirus and norwalk virus from coastal seawater development of a virus concentration method and its application to detection of enterovirus and norwalk virus from coastal, Appl. Environ. Microbiol. 68 (2002) 1033–1039, https://doi.org/10.1128/AEM.68.3.1033.
[45] V.P. Harden, J.O. Harris, The isoelectric point of bacterial cells, J. Bacteriol. 65 (1953) 198–202.
[46] B. Michen, T. Graule, Isoelectric points of viruses, J. Appl. Microbiol. 109 (2010) 388–397, https://doi.org/10.1111/j.1365-2672.2010.04663.x.
[47] G.V. Sherbet, M.S. Lakshmi, Characterisation of *Escherichia coli* cell surface by isoelectric equilibrium analysis, BBA – Biomembr. 298 (1973) 50–58, https://doi.org/10.1016/0005-2736(73)90008-4.

A p p e n d i x D

RAPID DETECTION METHODS FOR BACTERIAL PATHOGENS IN AMBIENT WATERS AT THE POINT-OF-SAMPLE COLLECTION: A BRIEF REVIEW

Li, J., Zhu, Y., Wu, X., and Michael R. Hoffmann. (2020) Rapid detection methods for bacterial pathogens in ambient waters at the point-of-sample collection: A brief review. *Clinical Infectious Diseases*. In Press.

Clinical Infectious Diseases

SUPPLEMENT ARTICLE

Rapid Detection Methods for Bacterial Pathogens in Ambient Waters at the Point of Sample Collection: A Brief Review

Jing Li, Yanzhe Zhu, Xunyi Wu, and Michael R. Hoffmann

Linde + Robinson Laboratories, California Institute of Technology, Pasadena, California, USA

The world is currently facing a serious health burden of waterborne diseases, including diarrhea, gastrointestinal diseases, and systemic illnesses. The control of these infectious diseases ultimately depends on the access to safe drinking water, properly managed sanitation, and hygiene practices. Therefore, ultrasensitive, rapid, and specific monitoring platforms for bacterial pathogens in ambient waters at the point of sample collection are urgently needed. We conducted a literature review on state-of-the-art research of rapid in-field aquatic bacteria detection methods, including cell-based methods, nucleic acid amplification detection methods, and biosensors. The detection performance, the advantages, and the disadvantages of the technologies are critically discussed. We envision that promising monitoring approaches should be automated, real-time, and target-multiplexed, thus allowing comprehensive evaluation of exposure risks attributable to waterborne pathogens and even emerging microbial contaminants such as antibiotic resistance genes, which leads to better protection of public health.

Keywords. waterborne pathogens; exposure risk assessment; detection methods; rapidity; portability.

Access to adequate water, sanitation, and hygiene (WASH) has long been a significant public health concern and an international development policy. According to the World Health Organization, global mortality attributable to waterborne diseases is estimated to be > 2.2 million per year, among which about 1.4 million are children, resulting in nearly $12 billion per year of economic loss worldwide [1]. It is estimated that diarrhea alone amounts to 842 000 deaths per year due to unsafe WASH and includes 361 000 deaths of children < 5 years of age, mostly in low-income countries [2]. Ultrasensitive, rapid, and specific monitoring platforms for bacterial pathogens in ambient waters at the point of sample collection are essential for timely water quality surveillance and microbial risk assessment. Therefore, the development of such platforms plays a key role in predicting and assessing the risk of disease outbreaks and providing quality care in healthcare settings such as improving the effectiveness of vaccine distribution.

Microbial detection techniques are usually classified into phenotypic methods and molecular methods. Culture-based methods as the mainstream of phenotyping have the advantages of cost-effectiveness and simplicity, and remain the gold standard for bacterial monitoring and identification. However, it requires days for culture-based methods to provide conclusive results, which greatly hampers their applications in water quality monitoring [3]. Molecular analyses including conventional polymerase chain reaction (PCR)–based methods, immunology-based methods, etc, however, require lengthy processes of sample pretreatment (eg, concentration, cell lysis, purification), expensive equipment, and trained personnel in centralized laboratory facilities. The demanding requirements of molecular methods represent a major disadvantage for their application in resource-limited communities [4, 5]. In addition, the majority of currently available molecular techniques have low precision (~20%) and are poorly suited for absolute quantification, thus having limited application in low-concentration pathogen detection [6]. To tackle this problem, in addition to enhancing specificity and mitigating competitive side reactions, researchers have also been exploring the "digital detection" concept. It realizes absolute quantification through separating the sample into sufficient partitions followed by individual molecular reaction and endpoint counting of positive and negative signals in each reaction [6, 7]. In addition, biosensor is also a promising technique for future waterborne pathogen monitoring systems. Biosensor generally provides more reliable results from real-time measurements and allows rapid analysis without the requirement of complicated pretreatment steps such as the target enrichment process, which still has a lot of room to be developed [8–10].

Overall, microbial pathogen detection is urged to be ultrasensitive, rapid, simple, low-cost, field-deployable, and

Correspondence: M. R. Hoffmann, Linde + Robinson Laboratories, California Institute of Technology, 1200 E California Blvd, MC 131-24, Pasadena, CA 91125 (mrh@caltech.edu).

Clinical Infectious Diseases® 2020;71(S2):S84–90

DOI: 10.1093/cid/ciaa498

easily operable by undertrained individuals for applications in environmental surveillance. Over the past years, numerous research advances have been made in such integrated platform for detection and identification of bacterial pathogens including but not limited to *Salmonella enterica* serovar Typhi (*S.* typhi) in water. Here, we review representative technologies categorized into cell-based methods, nucleic acid amplification methods, and biosensors. We also further discuss the needs of future developments on microbial monitoring platforms in the underdeveloped parts of the world.

CELL-BASED DETECTION METHODS

Compared to molecular-based detection platforms that target specific nucleic acids or proteins, cell-based detection methods offer direct identification and measurement with relative simple workflows [11]. Utilization of commercial instruments simplifies the construction of cell-based detection platforms. Recent development of miniaturized analysis systems has further promoted the efficiency and portability of cell-based detection methods, thus enabling complex diagnostics or monitoring procedures.

Miniaturized cell cultivation techniques based on microfluidic devices and Lab-on-a-Chip technologies consume less fluid, take less volume, and usually have higher tolerance toward ambient conditions, thus reducing the total cost and time for bacterial analysis [12]. One example of miniaturized cell cultivation is a palm-size device developed by Futai et al utilizing Braille display, monolithic surface, modified culture media and transparent heater [13]. This device was successfully used to culture highly carbon dioxide (CO_2)–dependent cells in nonpreferable growing environment with limited CO_2, humidity and a non-37°C temperature. Even for uncultivatable microbial species in various environments, an isolation chip with miniature diffusion chambers was developed to achieve parallel cultivation and isolation [14]. However, these miniaturized cell cultivation routines unavoidably take a long time, can usually be labor intensive, and require skilled operators.

Compared to cell culture, flow cytometers (FCMs) for direct cell counting enable fast quantification of the total bacterial community in the environment with high reproducibility and relatively small standard deviation. More importantly, many commercial FCMs are available for adaptations and the setup of FCM is suitable for automation, making FCM a great candidate for online routine bacterial monitoring [15]. Besmer et al used an automated in situ FCM analysis platform to help characterize the temporal variation of dynamic aquatic environments enabled by a commercial FCM (C6 flow cytometer, BD Accuri, San Jose California) coupled with a fully automated staining robot [16, 17]. Going one step further, Props et al combined the use of real-time FCM and advanced fingerprinting metrics, which aided the detection and characterization of microbial dynamic changes with a high temporal resolution of 10–30 seconds [18]. Nevertheless, FCM techniques have some major drawbacks, including difficulties in distinguishing between live and dead cells and specific strains of bacteria, and in discriminating bacterial aggregates and clusters. Incorporating microscopic imaging to FCM could boost the specificity of this detection platform. For example, an automatic imaging FCM was developed with a deep learning–based phase-recovery and holographic-reconstruction framework to generate pictures of micro-object in water samples without fluorescence triggering, and the pictures generated could be used for characterization [19]. However, current holograms taken by the microscopy and reconstructed images do not have a resolution high enough for specific bacterial pathogen characterization and thus further research is needed.

Besides miniature cell cultivation and FCM, other online cell-based sensing methods have also been developed. A real-time sensor using multiangle light scattering (MALS) technology was developed by Sherchan et al. By comparing the light scattering patterns after using a laser beam to strike particulates in water (including organic particles and microbial cells) with light scattering patterns in the computerized database, data obtained was characterized and the load of injected *Escherichia coli* was back-calculated [20]. Due to the existence of fluorophores in bacterial cells such as tryptophan, phenylalanine, or nucleic acids, which emit fluorescence light after excited by ultraviolet light, Simões and Dong developed an optical microfluidic sensor based on tryptophan intrinsic fluorescence with 3D-printing prototyping [21]. Furthermore, direct 3D image recognition for online pathogen detection was enabled by the combination of a sample-holding flow cell and a field imaging system (including a light source, a magnifying lens, and a camera). An image analysis system was developed to analyze 59 parameters of the images obtained and was able to distinguish between bacteria and abiotic particles. 3D image recognition analysis also provides quantification results, which correlates well with actual bacterial counts [22]. Tables 1 and 2 summarize specific detection parameters and comments on the application and detection parameters of the above-mentioned cell-based technologies.

Many methods mentioned in the section have been successfully implanted for days or even months with full automation, and can be constructed easily with commercial instruments. However, the sensitivity of these methods can be easily influenced by different environmental factors and the detection limit is relatively high. Moreover, it is challenging to identify specific pathogens solely based on cell-level analysis, not to mention their genetic information. Therefore, further molecular level detections are needed to secure higher sensitivity and specificity.

NUCLEIC ACID AMPLIFICATION DETECTION PLATFORMS

Compared to phenotyping methods, molecular methods typically based on the quantification and identification of specific

Table 1. Pathogen Detection Methods and Their Samples Studied

Detection Method			Phenotypic or Genetic	Waterborne Microbial Agent Tested	Complex Sample Matrices Tested	Treated Volume, mL
A. Cell-based	A1. Isolation chip		Phenotypic	Total bacteria	Seawater and soil	NA
	A2. Online flow cytometry		Phenotypic	Total bacteria	Drinking water, river water, and groundwater	0.015
	A3. Real-time flow cytometry		Phenotypic	Total bacteria	Nonchlorinated municipal drinking water, river water, and pond water	0.016/min
	A4. MALS sensor		Phenotypic	*Escherichia coli*	Distilled and tap water	600
	A5. Optical microfluidic sensor based on tryptophan intrinsic fluorescence		Phenotypic	*E. coli* and *Legionella*	Distilled water	NA
	A6. Novel optical sensor		Phenotypic	Total particles	Nonchlorinated water and water from cattle slaughterhouse	200
B. NAA	PCR-based	B1. Coaxial channel-based DNA extraction and microfluidic PCR	Genetic	*E. coli*	Milk	10
	LAMP-based	B2. Self-contained microfluidic gLAMP	Genetic	*Proteus hauseri* *Vibrio parahaemolyticus* *Salmonella* subsp *enterica* *E. coli*	Serum	NA
		B3. Centrifugal microfluidic automatic wireless end-point LAMP	Genetic	*E. coli* *Salmonella* spp *Vibrio cholerae*	Chicken meat	NA
		B4. One-step single-layer membrane for digital LAMP	Genetic	*E. coli* *Salmonella* Typhi *Enterococcus faecalis*	Culture media	NA
		B5. Asymmetric double-layer membrane for digital LAMP	Genetic	*E. coli* *Salmonella* Typhi	Unprocessed environmental water	10
		B6. In-gel LAMP	Genetic	MS2	Culture media	NA
C. Biosensor	C1. MOF-bacteriophage biosensor		Phenotypic	*Staphylococcus aureus*	Pastry cream	0.6
	C2. Impedimetric paper-based biosensor		Phenotypic	Cultures from sewage sludge	Synthetic wastewater	NA
	C3. Immunomagnetic separation and colorimetric paper-based device		Phenotypic	*Salmonella* Typhimurium	Bird feces and whole milk	1
	C4. Real-time amperometric immunoassay amplified by nanomaterial		Phenotypic	*E. coli*	Water	0.2
	C5. Phage-mediated separation with quantitative PCR detection		Combined	*E. coli* O157:H7	Agricultural water and city water	1
	C6. Carbon nanotube multilayer biosensors and on-chip LAMP		Combined	*E. coli* O157:H7	Juice and milk	1

Abbreviations: LAMP, loop-mediated isothermal amplification; MALS, multiangle light scattering; MOF, metal-organic framework; NA, not available; NAA, nucleic acid analysis; PCR, polymerase chain reaction.

genomic segments of the pathogen's genomes allow rapid, highly specific, and more sensitive detection, which better fit the expectations of timely monitoring and effective surveillance of aquatic pathogens in a range of water environmental settings. In this section, advances in monitoring methods based on PCR and loop-mediated isothermal amplification (LAMP) are respectively discussed.

PCR-BASED METHODS

The major drawback of PCR-related methods usually lies in their long response time and limited portability, since they rely on fussy thermal cycling and require additional equipment to detect the amplification products [35]. Another drawback is that trained personnel with experimental skills are needed to perform the assays, thus making the PCR-based systems impractical in resource-limited settings [4, 5]. Therefore, there is an urgent demand for a mobile and automated PCR-based device to monitor water microbial quality. Microfluidics have been demonstrated to provide a higher surface-to-volume ratio and a higher rate of mass and heat transfer, thus offering better performance than conventional systems due to significantly reduced reaction time [36]. Zhang et al reported a microfluidic PCR system integrated with the sample pretreatment technique of coaxial channel-based DNA extraction that was able to detect *E. coli* in milk matrix [23]. Detailed information about this

Table 2. Pathogen Detection Methods and Their Technical Characteristics

Detection Method	Limit of Detection	Recovery Efficiency, %	Dynamic Range	Time to Answer, h	Absolute or Relative Quantification	Trained Personnel Required	Tests at Species Level	Ready for Field Test	Reference
A1	NA	Up to 50%	~500 cells	2 wk	Relative	Yes	No	No	[14]
A2	10^3 cells/mL^{-1}	NA	10^3–10^6 cells/mL^{-1}	0.25	Absolute	No	No	Yes	[16, 17]
A3	10^3 cells/mL^{-1}	NA	~10^3 cells/mL^{-1}	0.25	Absolute	No	No	Yes	[18]
A4	10^3 CFU/mL^{-1}	NA	10^3–10^6 CFU/mL^{-1}	0	Relative	Yes	No	No	[20]
A5	1.4×10^3 CFU/mL^{-1}	NA	7×10^5 to 1×10^4 CFU/mL^{-1}	0	Relative	Yes	No	Yes	[21]
A6	1.6×10^2 particles/mL^{-1}	NA	1.6×10^2–5×10^6 particles/mL^{-1}	10	Relative	No	No	Yes	[22]
B1	12 CFU/mL^{-1}	97.4–100.6	NA	1.5	Relative	No	Yes	No	[23]
B2	3 copies/μL^{-1}	NA	3–3000 copies/μL^{-1}	1.2	Relative	No	Yes	Yes	[24]
	3 copies/μL^{-1}		3–3000 copies/μL^{-1}						
	2 copies/μL^{-1}		2–2000 copies/μL^{-1}						
	3 copies/μL^{-1}		3–3000 copies/μL^{-1}						
B3	3×10^{-5} ng/μL–1 or 2.7×10^4 CFU/mL^{-1}	NA	3×10^{-5}–3×100 ng/μL^{-1}	1	Relative	No	Yes	Yes	[25]
B4	11 copies/μL^{-1}	NA	11–1.1×10^5 copies/μL^{-1}	1	Absolute	No	Yes	Yes	[26]
B5	0.3 cells/mL^{-1}	99.9	0.3–10 000 cells/mL^{-1}	1	Absolute	No	Yes	Yes	[27]
	3 cells/mL^{-1}	NA	3–10 000 cells/mL^{-1}						
B6	0.7 PFU per reaction	NA	1–1000 PFU per reaction	0.5	Absolute	No	Yes	Yes	[28]
C1	31 CFU/mL^{-1}	96–104	40–4×10^8 CFU/mL^{-1}	0.33	Relative	No	Yes	Yes	[29]
C2	1.9×10^3 CFU/mL^{-1}	NA	10^3–10^6 CFU/mL^{-1}	0.75	Relative	Yes	No	Yes	[30]
C3	10^2 CFU/mL^{-1}	8.84–21.3	NA	1.5	Relative	Yes	Yes	Yes	[31]
C4	50 CFU/mL^{-1}	NA	50–10^7 CFU/mL^{-1}	0.53	Relative	No	Yes	Yes	[32]
C5	10^2 CFU/mL^{-1}	45.4–80.2	10^2–10^6 CFU/mL^{-1}	2	Relative	Yes	Yes	Yes	[33]
C6	1 CFU/mL^{-1}	101–112.1	5–10^5 CFU/mL^{-1}	2	Relative	Yes	Yes	Yes	[34]

Abbreviations: CFU, colony-forming units; NA, not available; PFU, plaque-forming units.

system can be found in Tables 1 and 2. Some companies have directly tackled the mobility issue of PCR systems by developing handheld PCR instruments as shown in Table 3. Nguyen et al investigated the feasibility of using the Biomeme handheld quantitative PCR (qPCR) system for rapid (< 50 minute) on-site detection and monitoring of *Flavobacterium psychrophilum* in filtered water samples [37]. The study showed a close match between the results of the Biomeme handheld qPCR system and those of traditional bench qPCR, highlighting the feasibility of field-based qPCR systems in rapidly detecting and timely monitoring bacterial pathogens in water.

Table 3. Summary of Commercially Available Handheld Quantitative Polymerase Chain Reaction Systems

Company	Item	Weight, kg	Footprint, cm^2
Chai	Open quantitative PCR[a]	4	28.0 × 24.0
Ubiquitome	Freedom 4[b]	Not available	10.2 × 20.3
Ubiquitome	Liberty 16[c]	3.2	21.2 × 11.0
Amplyus	miniPCR[b]	0.45	12.7 × 5.1
Biomeme	Franklin[b]	0.91	About the size of a soda can

Abbreviation: PCR, polymerase chain reaction.

[a]Product information is from https://www.chaibio.com/openqpcr.

[b]Product information is from Reference 35.

[c]Product information is from https://insights.ubiquitomebio.com/liberty16-personal-qpcr-machine.

LAMP-BASED METHODS

LAMP is one of the most commonly used isothermal amplification methods [23, 38] and has attracted the most attention due to its high specificity, high amounts of amplification product, and superior tolerance to inhibitors [39]. Moreover, LAMP can be carried out at a constant temperature, so that it does not require a thermal cycler, which simplifies the detection procedure and allows better portability compared to PCR-based methods. Chen et al introduced a self-contained microdevice to in-gel LAMP (gLAMP) for multiplexed pathogen detection in complex clinical samples such as serum [24]. *Escherichia coli*, *Proteus hauseri*, *Vibrio parahemolyticus*, and *Salmonella* subspecies were simultaneously detected with high selectivity and sensitivity, as shown in Tables 1 and 2. Another major merit of the detection system was that the microchip preloaded with agarose solution containing LAMP reagents could maintain activity for 30 days when stored at 4°C, allowing the long-term storage and transportation of LAMP reagents, which is essential for LAMP-based point-of-use applications [24]. Sayad et al developed a wireless automatic endpoint detection system using centrifugal microfluidics for food safety examination. Foodborne pathogenic bacteria including *E. coli*, *Salmonella* species, and *Vibrio cholerae* in chicken meat were successfully detected with the sample-to-response time of < 1 hour [25]. Moreover, since

this system is performed in an entirely automated way with the help of Bluetooth wireless technology, it is accessible for field application in environmental water samples. However, for the methods described above, the adaptability to environmental water matrix rather than food or blood needs further investigation and validation; in addition, the above methods were semiquantitative and not suitable for absolute quantification. Hoffmann's laboratory has done a lot of work on developing rapid microbial pathogen detection systems based on digital LAMP (dLAMP) for absolute quantification in environmental waters [26–28]. Lin et al demonstrated that 1-step LAMP can be successfully performed on single-layer commercial polycarbonate membrane to achieve absolute quantification of the genome DNA of *E. coli*, *Enterococcus faecalis*, and *S.* Typhi [26]. Lin et al further reported the development and validation of the simpler and more robust double-layer membrane for dLAMP of bacterial pathogens in complex environmental waters. Absolute quantification of *E. coli* and *S.* Typhi spiked in unprocessed pond water and seawater could be completed within 1 hour with the sensitivity down to single cell [27]. Huang et al developed a gLAMP system enabling absolute quantification of microbial pathogens in environmental waters within 30 minutes at a very low cost of $5 per test. Bacteria (*E. coli* and *S.* Typhi) and viruses (bacteriophage MS2) were immobilized with LAMP reagents in polyethylene glycol hydrogel matrix and were then amplified [28]. Although the authors demonstrated that the above system could also be used for absolute quantification of bacterial targets including *E. coli* and *S.* Typhi, relevant detection limits were not reported, which needs further validation. More detailed information about all of the above-mentioned LAMP-based systems can be found in Tables 1 and 2. In this emerging field, a range of rapid and easy-to-operate platforms have been developed for low-concentration pathogen detection. It has great potential for future application in point-of-sample detection in field upon proper modification of consumables such as reagents and microchips.

BIOSENSORS

Biosensors are analytical devices that consist of target recognition molecules and signal transducers to detect the interaction between the recognition molecules and the specific target. Innovations in recognition molecules and signal transduction methods, as summarized in Figure 1, are emerging to achieve sensitive, rapid, and specific pathogen detection. We note that thorough reviews are available on various types of recognition molecules and signal transducers applicable to waterborne bacterial pathogen detection [40, 41]. Below we highlight novel biosensors that are portable for in-field applications or hold promise for online water quality monitoring.

The novel combination of target recognition molecules and new substrates for their immobilization has been demonstrated to boost the sensitivity of biosensors and the applicability in-field applicability. For example, Bhardwaj et al conjugated bacteriophage onto metal-organic framework (MOF) for specific quantification of *Staphylococcus aureus* [29]. The MOF, NH_2-MIL-53(Fe), functioned as a water-dispersible and stable matrix, and also as an optical transducer whose reduction in photoluminescence was proportional to target bacterial concentration. This type of stable and economical biosensor with notable quantification performance could be an attractive solution to scale up for point-of-sample-collection detection. However, it should be noted that such target-specific bacteriophage is not available for every bacterial pathogen. As an alternative class of recognition molecules, aptamers (synthetic single-stranded oligonucleotides) can fold into designed 3D structure to bind specific targets. The sequence of the aptamers can be selected in vitro through systematic evolution of ligands by exponential enrichment, and the easily synthesized aptamers have high stability, specificity, and affinity to the targets [43].

Integration of nanomaterials with paper microfluidics has led to development of convenient portable biosensor devices. Commercial test strips, such as RapidCheK and Watersafe, are available for environmental detection of *E. coli* and *Salmonella* Typhimurium. However, these commercial kits mainly use colorimetric detection based on nanoparticle aggregation caused by antibody–antigen reaction, which takes hours to give qualitative results [44]. Using an alternative detection approach, Rengaraj et al conjugated concanavalin A, the recognition molecule binding saccharide on bacterial cell surfaces, onto commercial hydrophobic paper with screen-printed conductive carbon ink for impedance measurement. This device has potential in-field applicability in terms of portable instrumentation and relative assay stability against environmental disturbance [30]. However, as typical to capillary force-driven paper microfluidics, the sample size at microliters is too small to be relevant for environmental pathogen monitoring without a prior sample concentration step. To overcome this limitation, Srisa-Art et al adopted an approach combining immunomagnetic separation using anti-*Salmonella* coated Dynabeads and paper-based sandwich immunoassay using the detection enzyme β-galactosidase, which forms a red-violet product with chlorophenol red galactopyranoside for colorimetric detection. The immunomagnetic separation enabled species-specific capture and enrichment from a 1-mL sample [31]. Although the detection device is paper-based, laboratory equipment such as vortex and pipette was still required for the immunomagnetic separation step. To adapt paper microfluidics for in-field environmental detection, the integration of pathogen-specific separation with biosensors represents both an opportunity and a challenge.

For automated and low-cost bacterial pathogen monitoring, immunoassay-based electrochemical biosensors are approaching commercialization, owing to the consistent assay performance and easily automated instrumentation [45]. For example, based on an

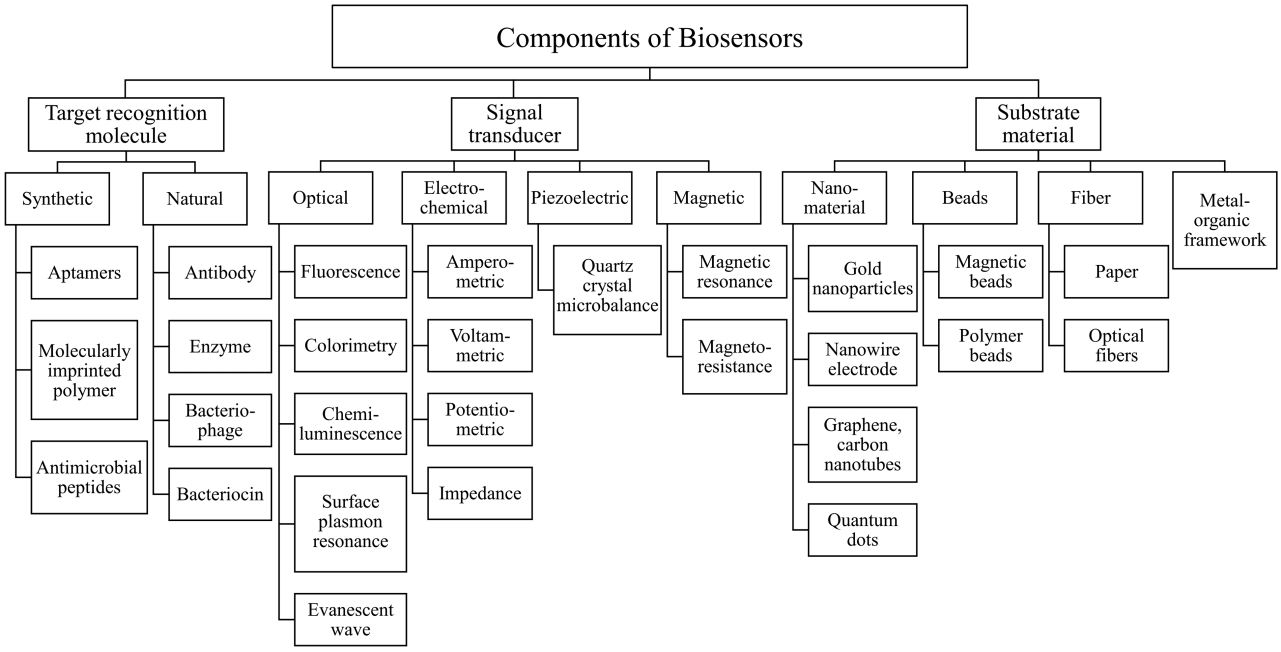

Figure 1. Recent developments in biosensors for bacterial pathogen detection. Widely used or innovative target recognition molecules, signal transducers, and substrate materials are summarized based on Justino et al [40], Kumar et al [41], and Vikesland and Wigginton [42].

electrochemical biosensor, Altintas et al developed a fully automated portable system for real-time amperometric measurements of *E. coli*–specific immunoassay on a microfluidic chip [32]. The instrument prototype with programmed fluid manipulation, electrochemical measurements, and user interface was also developed and tested, thus showing great promise for commercialization. However, since the protein-based recognition reaction is intrinsically weak and susceptible to matrix effect, the majority of these novel biosensors are still limited in sensitivity and specificity compared to nucleic acid analysis (NAA) methods. One solution would be to employ biosensors for target capture utilizing the specific target recognition, while using a nucleic acid–based method to amplify target DNA or RNA for detection. Wang et al demonstrated this approach with bacteriophage-coated Dynabeads for magnetic separation of pathogenic *E. coli* followed by qPCR detection of total bacterial DNA [33]. Li et al combined antibody-coated carbon nanotube multilayer biosensors for specific capture of *E. coli* and microfluidic chip-based LAMP detection [34]. The latter study achieved single cell detection in 1 mL complex samples such as juice and milk [33, 34]. More detailed information on above biosensors can be found in Tables 1 and 2. With the automated platforms available for LAMP and PCR, these studies demonstrated that coupled biosensor-NAA would be a promising approach for further development of a fully automated environmental pathogen detection system.

CONCLUSIONS

Portable systems for rapid, ultrasensitive, and specific environmental pathogen monitoring are essential in risk assessment, outbreak prevention, and vaccine distribution for low-resource settings. Recent advances in cell-based, nucleic acid–based, and biosensor-based platforms are reviewed here, with a focus on promising solutions for bacterial pathogen detection in ambient waters at the point of sample collection. Among the reviewed technologies, miniaturized PCR instruments is the most well-developed and commercialized method that is readily deployable in field for sensitive and specific pathogenic bacterial detection, as summarized in Table 3. For biosensors, the combination of biosensor and NAA-based detection holds promise for improved detection efficiency and thus deserves further research and commercial development. Overall, future research should focus on Lab-on-a-Chip pretreatment approaches that can be integrated with subsequent detection [46], entirely automated devices with preloaded reagents, multiplex detection systems, and online real-time monitoring. Such platforms would benefit further comprehensive and timely hazard identification, exposure risk assessment, and pollution control and management. For example, to cope with the global health crisis caused by widespread and fast-evolving antibiotic resistance genes (ARGs), point-of-sample-collection gene sequencing [47] has been developed. This technique provides information on hundreds of ARG subtypes and toxin genes for a range of water environments. Acquiring this information in-field is a pressing need not only for pathogen source tracking, but also for preventing ARG dissemination across various environments.

Notes

Financial support. This work was supported by the Bill & Melinda Gates Foundation (grant number OPP1111252 and OPP1192379).

Supplement sponsorship. This supplement is funded with support from the Coalition against Typhoid Secretariat, housed at the Sabin Vaccine Institute in Washington, DC and made possible by a grant from the Bill & Melinda Gates Foundation.

Potential conflicts of interest. The authors: No reported conflicts of interest. All authors have submitted the ICMJE Form for Disclosure of Potential Conflicts of Interest.

References

1. Ramírez-Castillo FY, Loera-Muro A, Jacques M, et al. Waterborne pathogens: detection methods and challenges. Pathogens **2015**; 4:307–34.
2. Prüss-Ustün A, Bartram J, Clasen T, et al. Burden of disease from inadequate water, sanitation and hygiene in low- and middle-income settings: a retrospective analysis of data from 145 countries. Trop Med Int Health **2014**; 19:894–905.
3. Zhang D, Bi H, Liu B, Qiao L. Detection of pathogenic microorganisms by microfluidics based analytical methods. Anal Chem **2018**; 90:5512–20.
4. Gunda NSK, Mitra SK. Rapid water quality monitoring for microbial contamination. Electrochem Soc Interface **2017**; 25:73–78.
5. Song J, Mauk MG, Hackett BA, Cherry S, Bau HH, Liu C. Instrument-free point-of-care molecular detection of Zika virus. Anal Chem **2016**; 88:7289–94.
6. Heyries KA, Tropini C, Vaninsberghe M, et al. Megapixel digital PCR. Nat Methods **2011**; 8:649–51.
7. Vogelstein B, Kinzler KW. Digital PCR. Proc Natl Acad Sci U S A **1999**; 96:9236–41.
8. Deisingh AK, Thompson M. Strategies for the detection of *Escherichia coli* O157:H7 in foods. J Appl Microbiol **2004**; 96:419–29.
9. Vikesland PJ, Wigginton KR. Nanomaterial enabled biosensors for pathogen monitoring—a review. Environ Sci Technol **2010**; 44:3656–69.
10. Yilmaz E, Majidi D, Ozgur E, Denizli A. Whole cell imprinting based *Escherichia coli* sensors: a study for SPR and QCM. Sensors Actuators B Chem **2015**; 209:714–21.
11. Mairhofer J, Roppert K, Ertl P. Microfluidic systems for pathogen sensing: a review. Sensors (Basel) **2009**; 9:4804–23.
12. Coluccio ML, Perozziello G, Malara N, et al. Microfluidic platforms for cell cultures and investigations. Microelectron Eng **2019**; 208:14–28.
13. Futai N, Gu W, Song JW, Takayama S. Handheld recirculation system and customized media for microfluidic cell culture. Lab Chip **2006**; 6:149–54.
14. Nichols D, Cahoon N, Trakhtenberg EM, et al. Use of ichip for high-throughput in situ cultivation of "uncultivable" microbial species. Appl Environ Microbiol **2010**; 76:2445–50.
15. Van Nevel S, Koetzsch S, Proctor CR, et al. Flow cytometric bacterial cell counts challenge conventional heterotrophic plate counts for routine microbiological drinking water monitoring. Water Res **2017**; 113:191–206.
16. Besmer MD, Weissbrodt DG, Kratochvil BE, Sigrist JA, Weyland MS, Hammes F. The feasibility of automated online flow cytometry for in-situ monitoring of microbial dynamics in aquatic ecosystems. Front Microbiol **2014**; 5:1–12.
17. Besmer MD, Epting J, Page RM, Sigrist JA, Huggenberger P, Hammes F. Online flow cytometry reveals microbial dynamics influenced by concurrent natural and operational events in groundwater used for drinking water treatment. Sci Rep **2016**; 6:38462.
18. Props R, Rubbens P, Besmer M, et al. Detection of microbial disturbances in a drinking water microbial community through continuous acquisition and advanced analysis of flow cytometry data. Water Res **2018**; 145:73–82.
19. Göröcs Z, Tamamitsu M, Bianco V, et al. A deep learning-enabled portable imaging flow cytometer for cost-effective, high-throughput, and label-free analysis of natural water samples. Light Sci Appl **2018**; 7:66.
20. Sherchan S, Miles S, Ikner L, Yu HW, Snyder SA, Pepper IL. Near real-time detection of *E. coli* in reclaimed water. Sensors (Switzerland) **2018**; 18:1–10.
21. Simões J, Dong T. Continuous and real-time detection of drinking-water pathogens with a low-cost fluorescent optofluidic sensor. Sensors (Switzerland) **2018**; 18:2210.
22. Højris B, Christensen SCB, Albrechtsen HJ, Smith C, Dahlqvist M. A novel, optical, on-line bacteria sensor for monitoring drinking water quality. Sci Rep **2016**; 6:1–10.
23. Zhang H, Huang F, Cai G, Li Y, Lin J. Rapid and sensitive detection of *Escherichia coli* O157:H7 using coaxial channel-based DNA extraction and microfluidic PCR. J Dairy Sci **2018**; 101:9736–46.
24. Chen C, Liu P, Zhao X, Du W, Feng X, Liu BF. A self-contained microfluidic in-gel loop-mediated isothermal amplification for multiplexed pathogen detection. Sensors Actuators B Chem **2017**; 239:1–8.
25. Sayad A, Ibrahim F, Mukim Uddin S, Cho J, Madou M, Thong KL. A microdevice for rapid, monoplex and colorimetric detection of foodborne pathogens using a centrifugal microfluidic platform. Biosens Bioelectron **2018**; 100:96–104.
26. Lin X, Huang X, Urmann K, Xie X, Hoffmann MR. Digital loop-mediated isothermal amplification on a commercial membrane. ACS Sens **2019**; 4:242–9.
27. Lin X, Huang X, Zhu Y, Urmann K, Xie X, Hoffmann MR. Asymmetric membrane for digital detection of single bacteria in milliliters of complex water samples. ACS Nano **2018**; 12:10281–90.
28. Huang X, Lin X, Urmann K, et al. Smartphone-based in-gel loop-mediated isothermal amplification (gLAMP) system enables rapid coliphage MS2 quantification in environmental waters. Environ Sci Technol **2018**; 52:6399–407.
29. Bhardwaj N, Bhardwaj SK, Mehta J, Kim KH, Deep A. MOF-bacteriophage biosensor for highly sensitive and specific detection of *Staphylococcus aureus*. ACS Appl Mater Interfaces **2017**; 9:33589–98.
30. Rengaraj S, Cruz-Izquierdo Á, Scott JL, Di Lorenzo M. Impedimetric paper-based biosensor for the detection of bacterial contamination in water. Sensors Actuators B Chem **2018**; 265:50–8.
31. Srisa-Art M, Boehle KE, Geiss BJ, Henry CS. Highly sensitive detection of *Salmonella* Typhimurium using a colorimetric paper-based analytical device coupled with immunomagnetic separation. Anal Chem **2018**; 90:1035–43.
32. Altintas Z, Akgun M, Kokturk G, Uludag Y. A fully automated microfluidic-based electrochemical sensor for real-time bacteria detection. Biosens Bioelectron **2018**; 100:541–8.
33. Wang Z, Wang D, Kinchla AJ, Sela DA, Nugen SR. Rapid screening of waterborne pathogens using phage-mediated separation coupled with real-time PCR detection. Anal Bioanal Chem **2016**; 408:4169–78.
34. Li T, Zhu F, Guo W, et al. Selective capture and rapid identification of E. coli O157:H7 by carbon nanotube multilayer biosensors and microfluidic chip-based LAMP. RSC Adv **2017**; 7:30446–52.
35. Marx V. PCR heads into the field. Nat Methods **2015**; 12:393–7.
36. Foudeh AM, Fatanat Didar T, Veres T, Tabrizian M. Microfluidic designs and techniques using lab-on-a-chip devices for pathogen detection for point-of-care diagnostics. Lab Chip **2012**; 12:3249–66.
37. Nguyen PL, Sudheesh PS, Thomas AC, Sinnesael M, Haman K, Cain KD. Rapid detection and monitoring of *Flavobacterium psychrophilum* in water by using a handheld, field-portable quantitative PCR System. J Aquat Anim Health **2018**; 30:302–11.
38. Zhang C, Xu J, Ma W, Zheng W. PCR microfluidic devices for DNA amplification. Biotechnol Adv **2006**; 24:243–84.
39. Notomi T, Okayama H, Masubuchi H, et al. Loop-mediated isothermal amplification of DNA. Nucleic Acids Res **2000**; 28:E63.
40. Justino CIL, Duarte AC, Rocha-Santos TAP. Recent progress in biosensors for environmental monitoring: a review. Sensors (Switzerland) **2017**; 17:2918.
41. Kumar N, Hu Y, Singh S, Mizaikoff B. Emerging biosensor platforms for the assessment of water-borne pathogens. Analyst **2018**; 143:359–73.
42. Vikesland PJ. Nanosensors for water quality monitoring. Nat Nanotechnol **2018**; 13:651–60.
43. Zhao YW, Wang HX, Jia GC, Li Z. Application of aptamer-based biosensor for rapid detection of pathogenic *Escherichia coli*. Sensors (Switzerland) **2018**; 18:1–16.
44. Ge X, Asiri AM, Du D, Wen W, Wang S, Lin Y. Nanomaterial-enhanced paper-based biosensors. Trends Anal Chem **2014**; 58:31–9.
45. Furst AL, Francis MB. Impedance-based detection of bacteria. Chem Rev **2019**; 119:700–26.
46. Zhu Y, Huang X, Xie X, et al. Propidium monoazide pretreatment on a 3D-printed microfluidic device for efficient PCR determination of "live: versus dead" microbial cells. Environ Sci Water Res Technol **2018**; 4:956–63.
47. Hu YOO, Ndegwa N, Alneberg J, et al. Stationary and portable sequencing-based approaches for tracing wastewater contamination in urban stormwater systems. Sci Rep **2018**; 8:1–13.